Isophthalic Acid Derivative Metal-Organic Frameworks for Gas Capture and Separation

A thesis presented in partial fulfilment of the requirements of the degree of

Master of Science
in
Chemistry

at Massey University, Manawatu, New Zealand

Victoria-Jayne Scott
2022

To all those who think they can’t do it.

‘For I can do everything through Christ who gives me strength.’

– Philippians 4.13

Abstract

Gas capture and separation is a relevant, dynamic field of research because gases play a vital role in our society from the synthesis of polymers and plastics to the production of fuel. Furthermore, there is an ever-increasing concentration of greenhouse gases, namely CO_2 and methane, in the atmosphere, which is leading to climate change. Various types of adsorbents and absorption-based methods have been utilized for gas capture and separation, however many of these methods are expensive and have a high energy penalty. Metal-organic frameworks (MOFs) are a class of adsorbents which can be made inexpensively, and they can be recycled with a low energy input, thus making them desirable materials for gas capture and separation.

This thesis focuses on MOFs with small pores for gas capture and separation. The MOFs are made with isophthalic acids, which are inexpensive starting materials. The MOFs were found using the Cambridge Structural Database, analysed using a simulation software known as PoreBlazer, and then synthesized for gas adsorption analysis. Many reported synthetic procedures could not be replicated, but this led to the discovery of many new MOF materials. Together with the MOFs that could be reproduced in our laboratory, many MOFs were found with good uptakes and good selectivities for various interesting gas pairs. This thesis not only introduces several new MOFs but shows the variability of using the isophthalic acid ligand core to produce many MOF materials. Overall, several important discoveries of new MOF materials for important gas separations were made.

Contributions

All the work in this thesis was completed by Victoria-Jayne Scott

Except:

- Q_{st} calculations for a few gases which were performed by Elnaz Jangodaz.
- For help with single crystal structure collection and refinement by Dr. Seok June Lee (Subo).
- The synthetic method of UC-MUF-201, which was found by Mutjalin Limlamthong.

Acknowledgements

I would like to take the opportunity to thank the large number of people who helped and supported me throughout my MSc journey. Firstly, I would like to thank my supervisor Shane Telfer for knowing that I was capable of doing an MSc and for providing me the opportunity to do so. I have greatly appreciated all your enthusiasm, support, guidance, and knowledge. Thank you for always answering all of my questions and for never making me feel stupid for asking them. Thank you for being a fantastic supervisor.

I would like to thank Dr. Seok June Lee (Subo) for all his advice and wisdom, especially in the crystallographic department, and Elnaz Jangodaz for her help with Q_{st} calculations. I would also like to thank Bernhard Auer, Yiming Zhang, Ludwig Petters, Dr. Marco Pandullo, Ghadir Dahalan, Dr. Joel Cornelio, Dr. Adil Alkas, Dr. Omid Qazvini, Dr. Nisansala Bandara and all other past Telfer Group members for their technical advice and scientific discussions.

I would like to thank my family and friends for their continual support and encouragement throughout my MSc. I would like to especially thank my wonderful husband, Jacob, for his love and unwavering faith in me. You have been incredibly supportive and always there for me; to listen, to give advice, and to help me.

Lastly, I would like to thank my heavenly Father; for bringing me to where I am, for giving me strength when I was weak, and for never leaving my side.

Abbreviations

4,4’-bipy	4,4’-bipyridine
ASA	accessible surface area
BET	Brunauer-Emmett-Teller
BDC	benzene 1,4-dicarboxylic acid
CCDC	Cambridge Crystallographic Data Centre
CSD	Cambridge Structural Database
DEF	*N*,*N*-diethylformamide
DHTP	2,5-dihydroxyterephthalic acid
DMA	*N*,*N*-dimethylacetamide
DMF	*N*,*N*-dimethylformamide
DSL	dual-site Langmuir
DSLF	dual-site Langmuir-Freundlich
EtOH	ethanol
H_2ipa / ipa	isophthalic acid / isophthalate
H_2ipa-NH_2 / ipa-NH_2	5-aminosophthalic acid / 5-aminoisophthalate
H_2ipa-Br / ipa-Br	5-bromoisophthalic acid / 5-bromoisophthalate
H_2ipa-OH / ipa-OH	5-hydroxyisophthalic acid / 5-hydroxyisophthalate
H_2ipa-CH_3 / ipa-CH_3	5-methylisophthalic acid / 5-methylisophthalate
H_2ipa-OMe / ipa-OMe	5-methyoxyisophthalic acid / 5-methoxyisophthalate
H_2ipa-NO_2 / ipa-NO_2	5-nitroisophthalic acid / 5-nitroisophthalate
HKUST	Hong Kong University of Science and Technology
IAST	Ideal Adsorbed Solution Theory
IR	infrared (spectroscopy)
IRMOF	isoreticular metal-organic framework
IUPAC	International Union of Pure and Applied Chemistry
LCD	largest cavity diameter

MEA	monoethanolamine
MOF	metal-organic framework
MOP	metal organic polyhedra
MUF	Massey University Framework
NMR	nuclear magnetic resonance (spectroscopy)
NU	Northwestern University
PLD	pore limiting diameter
PSD	pore size distribution
PXRD	powder X-ray diffraction
SBU	secondary building unit
SCXRD	single crystal X-ray diffraction
SSL	single-site Langmuir
SSLF	single-site Langmuir-Freundlich
TGA	thermogravimetric analysis
TMA	trimesic acid

Publications and thesis structure

Publications relevant to this thesis

Qazvini, O. T.; Scott, V.-J.; Bondorf, L.; Ducamp, M.; Hirscher, M.; Coudert, F.-X.; Telfer, S. G., Flexibility of a Metal–Organic Framework Enhances Gas Separation and Enables Quantum Sieving. *Chem. Mater.* **2021,** *33* (22), 8886-8894
(The results from this paper are not presented in my thesis results however the paper is cited in the introduction).

Additional publications

None

Table of Contents

Chapter 1 – Introduction

1.1 Introduction to Gas Capture and Separation

Gas storage, separation and purification are important industrial processes as they produce chemical materials for the production of polymers, plastics, and, especially, fuel.[1] Modern society requires a lot of energy to function and the use of fossil fuels, such as natural gas, crude oil or coal, provides a lot of this required energy.[2] However, the use of fossil fuels has led to increases in environmental issues such as global warming, due to the increased amounts of carbon dioxide (CO_2) and methane (CH_4) in the atmosphere. Therefore, controlling the concentration of gases such as these entering the atmosphere is ideal. The gas streams produced from the burning of such fossil fuels are riddled with impurities and thus require separation. The gas streams that are used in industry, such as light hydrocarbons, also require separation and purification before use.[2]

1.1.1 Noncovalent Forces and Important Gas Parameters

Before delving into important gas separations and the uses of gases in industry, it is necessary to explain some important gas properties. These properties help to explain why some gas pairs are hard to separate. These key characteristics can be described as dipole and quadrupole moments, polarizability, and kinetic diameter.

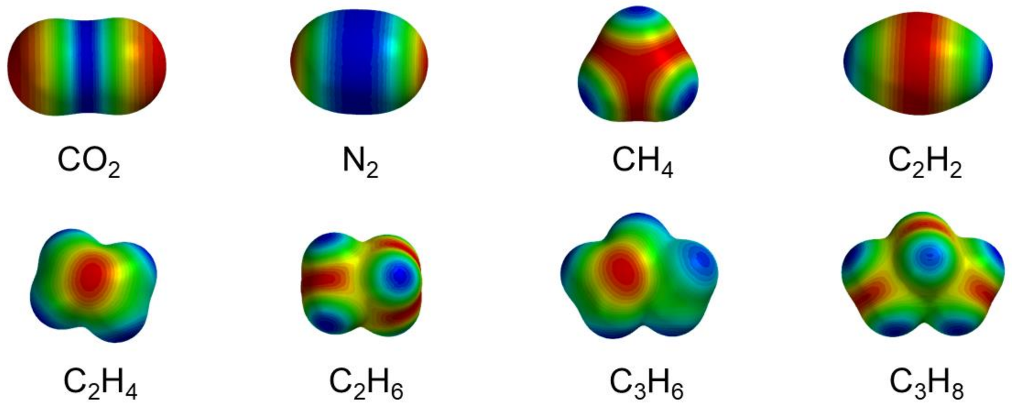

Figure 1.1 Electrostatic potential maps for selected gases. Blue signifies depleted electron density with a coloured scale of increasing electron density up to red which signifies enhanced electron density. These maps were calculated in Spartan with Hartree-Fock 6-311+G** calculations. The electron density scale is molecule dependent and is based on the absolute calculated minimum and maximum electron density values.

Most chemical bonds are polar; therefore they have a more positive end and a more negative end. Such bond polarities can result in a molecule, as a whole, having more positive regions and more negative regions. This kind of electron distribution is known as a dipole, with the magnitude of the dipole being the dipole moment.[3] Dipole moments depend not just on bond polarities but on the shape of a molecule. CO_2 for example does not have a dipole moment as the polar C=O bonds cancel each other out due to the linear molecular shape. However, water has a dipole moment due to its bent shape.[3] Quadrupole moments are also based around bond polarities. In simple terms, a quadrupole is made of two antiparallel dipoles, which are aligned so that there is no net dipole.[4, 5] Much like for dipoles, the magnitude of a quadrupole is the quadrupole moment. There are two kinds of quadrupole arrangements – two dipoles side-by-side or two dipoles head-to-head which both dipoles point in opposite directions.[4] CO_2 has a quadrupole moment as the ends have a more negative charge and the middle is more positive, thus like two dipoles which are head-to-head.

The electron cloud of a molecule is also important for polarizability. An electron cloud can be distorted by dispersion forces and the ease of distortion of a molecule's electron cloud is known as the polarizability.[3] The distorted electron cloud creates a temporary dipole. The larger the electron cloud, the easier it is to distort and thus it is more polarizable.[3] The distribution of the electron clouds of various gas molecules can be visualized in Figure 1.1. Different colours show the more negative and more positive regions, as captioned in the figure.

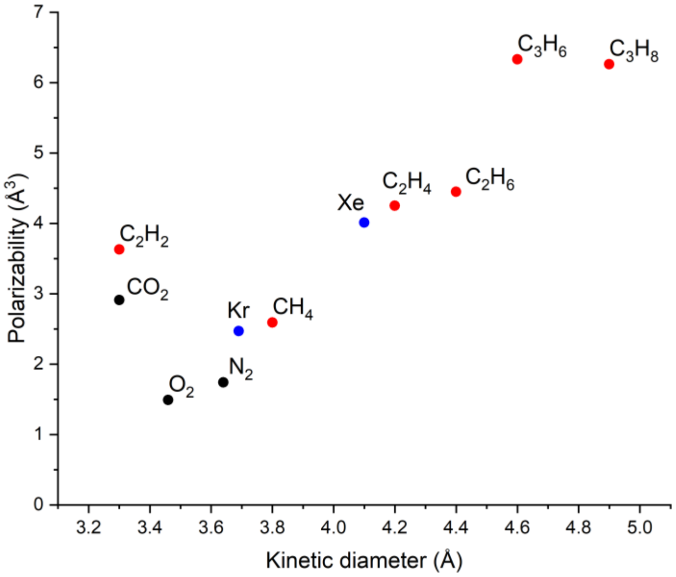

Figure 1.2 Kinetic diameter versus polarizability for selected gases discussed in section 1.1.[6-13] Colours: black: atmospheric gases, red: hydrocarbons, blue: noble gases. Figure inspired from Chen's 2019 review.[14]

Another key parameter is the kinetic diameter of gases (Figure 1.2). The kinetic diameter is the effective size of a gas molecule and is generally larger than the actual molecular size as kinetic diameter accounts for molecular motion.[15] In this thesis, when the size of a gas molecule is mentioned, it will mean the kinetic diameter of the gas.

1.1.2 Carbon Capture and Separation

Carbon dioxide (CO_2) is a key industrial gas that is produced in a variety of ways such as from the combustion of hydrocarbons (flue gas), natural gas wells, or as an off-gas from automotive combustion or petroleum refineries.[16, 17] However, the primary source of CO_2 production is from fossil fuels. With the steady increase in the use of fossil fuels since the start of the industrial era, the amount of CO_2 in the atmosphere has increased.[18] As of 2019, the global energy-related CO_2 emissions reached up to approximately 33 gigatonnes.[19] CO_2 is known to be a primary greenhouse gas which has significant impacts on global warming.[18] For this reason, CO_2 sequestration, known as carbon capture, has become a very important topic in research fields.

Carbon dioxide has several applications as it can be used to carbonate beverages, as a carrier for spray paints or vegetable oils, in portable fire extinguishers, in the welding industry or it can be reacted with ammonia to produce urea for fertilizers.[16] Furthermore, there are emerging technologies that will make better use of large quantities of CO_2 such as CO_2 hydrogenation to produce single carbon (C_1) products such as methanol, formic acid or methane, or C_{2+} products such as olefins or longer-chain alcohols.[20] Furthermore, other methods of CO_2 utilization include using it to make biofuels, polymers for plastics, or in seawater desalination.[21]

Figure 1.3 Key atmospheric gases for separation. Atom colours: carbon: black, oxygen: red, nitrogen: periwinkle blue, and hydrogen: pale peach.

There are currently fours type of carbon capture and separation methods that are under investigation with these being: pre-combustion capture, post-combustion capture, oxyfuel combustion and direct air capture.[18, 22]

1.1.2.1 Precombustion Capture

Fuels (such as coal, biomass, or natural gas) are reacted with air or oxygen, in a partial oxidation process known as gasification, to produce hydrogen gas (H_2) and carbon monoxide (CO).[17, 18, 22] The formed gas is known as syngas.[17] The CO produced is further reacted in a shift converter to make CO_2 and more H_2.[18] Therefore, the key gas pair here that needs to be separated is CO_2 and H_2. Using current separation methods, this separation is expensive and involves high temperatures.[18]

1.1.2.2 Postcombustion Capture

In postcombustion capture, CO_2 is to be removed from flue gas emitted from combustion plants.[17, 18] The composition of the flue gas depends fuel type and combustion conditions, however, generally, the main component of flue gas is nitrogen (N_2) which accounts for approximately 73 – 77 % of flue gas, followed by CO_2 of approximately 8 – 15% and water vapour of around 5 – 7 %.[17, 19, 22] Flue gas can also contain oxygen (O_2), CO, nitrous oxides (NO_x), sulphur dioxide (SO_2), hydrogen sulphide (HS), and hydrocarbons.[17] For this form of capture, the key gas pair for separation is CO_2 and N_2. These gases are hard to separate due to their similar sizes (CO_2: 3.30 Å and N_2: 3.64 Å) and shape (Figure 1.2 and Figure 1.3). However, they do have some different characteristics such as different polarizability (CO_2: 2.91 Å^3 and N_2: 1.74 Å^3), as seen in Figure 1.2 and quadrupole moment (CO_2: -4.30×10^{-26} esu cm^2 and N_2: 1.47×10^{-26} esu cm^2) which aides in separation.[6, 14, 19, 23] This type of carbon capture is one of the easiest to employ in industry as a power plant could be fitted with the appropriate chemical processors to capture the CO_2. This is currently employed in some plants, however, the ones used are to trap gas impurities, such as NO_x or SO_2 rather than CO_2.[18]

1.1.2.3 Oxyfuel Combustion

Fuels are ignited with nearly pure O_2 to generate, almost exclusively, CO_2.[18, 22] The almost pure CO_2 is an advantage of this technique and makes it ideal for capture and direct storage. However, a downfall of this technique is that pure O_2 is required, which means it needs to undergo its own separation and purification process beforehand.[18] The O_2 used for combustion is generally sequestered from air therefore, the key gas pair here is O_2 and N_2 as air is mostly made of N_2. O_2 and N_2 are difficult to separate due to their similar sizes (O_2: 3.46 Å and N_2: 3.64 Å) and similar properties, such as polarizability (O_2: 0.97-1.07 Å^3 and N_2: 1.74 Å^3, Figure 1.2) and quadrupole moment (Figure 1.3).[13, 22]

1.1.2.4 Direct Air Capture

In this method, CO_2 is directly sequestered from the air.[19, 22] As of 2018, the current levels of CO_2 in the air were 400 ppm, which is below the harmful level. However, due to the ever increasing amount of CO_2 in the atmosphere, removal of CO_2 is important to avoid reaching toxic levels.[22] Direct air capture has the potential for climate change remediation as it can take the CO_2 directly from the air.[24, 25] The key gas pair for separation in this method would also be CO_2 and N_2 due to high atmospheric N_2 levels.

1.1.3 Hydrocarbon Separation

Natural gas and crude oil are the main sources of hydrocarbon intermediates, such as methane, acetylene, ethane, ethylene, propane, and propylene, which are important precursors and products in both the petrochemical and polymer industries.[26, 27] For application purposes these gases need to be of high purity, but they often contain contaminants, therefore separation methods are required, especially for certain gas pairs.

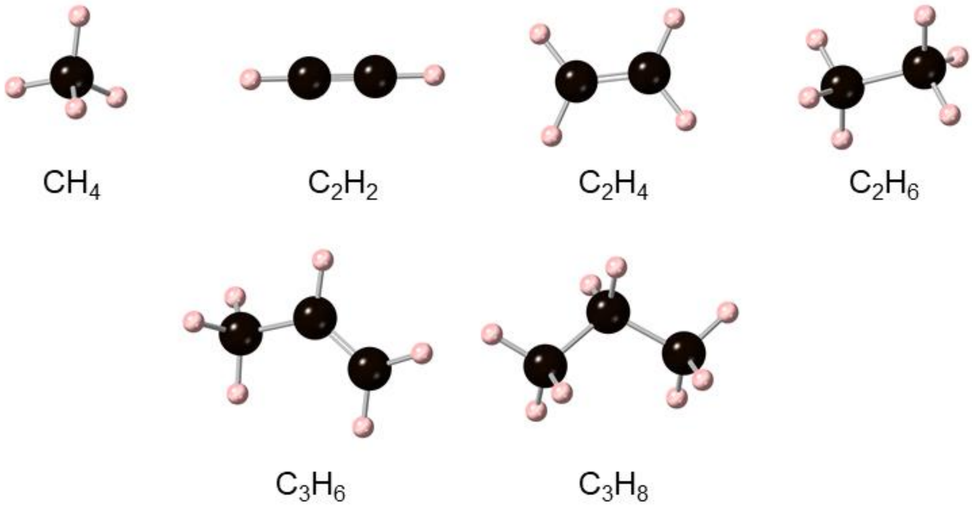

Figure 1.4 Key hydrocarbon gases for separation. Atom colours: carbon: black, and hydrogen: pale peach.

Methane (CH_4) is the main component of natural gas and is also a by-product in all gas streams from crude oil processing. CH_4 is considered as a cleaner alternative to fossil fuels because when it is oxidized it releases a lower amount of CO and CO_2 compared to fossil fuel combustion.[19, 26, 27] However, to utilize CH_4 as a possible fuel source, it needs to have any impurities removed.[19] Thus, one of the key gas pairs for separation is CH_4 and CO_2. These gases have similar sizes (CO_2: 3.30 Å and CH_4: 3.80 Å) and polarizabilities (CO_2:

2.91 Å^3 and CH_4: 2.59 Å^3), as seen in Figure 1.2, which makes separation more difficult. Their quadrupole moments do differ as methane doesn't have one, which assists separation.[6, 14, 27] Furthermore, much like CO_2, CH_4 is a greenhouse gas which needs to have its atmospheric concentration reduced. This presents CH_4 and N_2 as a key gas pair for separation. CH_4 and N_2 have similar kinetic diameters (CH_4: 3.80 Å and N_2: 3.64 Å) but different polarizabilities (CH_4: 2.59 Å^3 and N_2: 1.74 Å^3, Figure 1.2) and quadrupole moments.[6, 14, 19]

Ethane (C_2H_6) is a precursor in the cracking production of ethylene (C_2H_4).[26, 27] Ethylene is used widely in reactions to make polymers such as polyvinyl chloride or polystyrene.[26] Ethylene can also be used to make ethylene glycol which can make synthetic fibres and antifreeze.[26] One of the main impurities in the production of ethylene is acetylene (C_2H_2).[14] The presence of acetylene can be detrimental to ethylene polymerization reactions as acetylene can poison reaction catalysts, is highly explosive, and can form metal acetylides which can block gas stream pathways.[14, 27] Thus the removal of acetylene from ethylene mixtures is desired, thus making it a key gas pair in research. The current method for separating ethylene and acetylene is cryogenic distillation (see section 1.2.2 for more details) which is highly energy-intensive.[2] However, it is difficult to separate ethylene and acetylene due to their similar sizes (C_2H_4: 4.20 Å and C_2H_2: 3.30 Å) and polarizability (C_2H_4: 4.25 Å^3 and C_2H_2: 3.33 – 3.93 Å^3) as seen in Figure 1.2 and Figure 1.4. However, their quadruple moments do differ slightly (C_2H_4: 1.50 x 10^{-26} esu cm^2 and C_2H_2: 7.50 x 10^{-26} esu cm^2).[6, 9, 14] The separation of ethane and ethylene is also important in case there is any unreacted ethane after cracking, thus making this another key gas pair. Because ethane and ethylene have similar boiling points (C_2H_6: 185 K and C_2H_4: 169 K), separation via distillation is difficult.[27] These two gases also have similar sizes (C_2H_6: 4.40 Å and C_2H_4: 4.20 Å), polarizability (C_2H_6: 4.43 – 4.47 Å^3 and C_2H_4: 4.25 Å^3, Figure 1.2) and quadruple moments (C_2H_6: 0.650 esu cm^2 and C_2H_4: 1.50 x 10^{-26} esu cm^2), further complicating separation.[6, 9]

Acetylene is more than just an impurity as it can be used for the synthesis of plastics and polyurethanes, or for welding and cutting metal.[19] In the cracking of hydrocarbons or natural gas to produce acetylene, CO_2 is produced as an impurity with H_2 and CH_4.[19, 27] This results in another key gas pair for separation: acetylene and CO_2, but like the hydrocarbons mentioned former, CO_2 and acetylene have similar properties, such as their size (C_2H_2: 3.30 Å and CO_2: 3.30 Å) and polarizability (C_2H_2: 3.33 – 3.93 Å^3 and CO_2: 2.91 Å^3), as seen in Figure 1.2.[6, 19] Their quadrupole moments (C_2H_2: 7.50 x 10^{-26} esu cm^2 and CO_2: -4.30 x 10^{-26} esu cm^2) are different however, which aids in the separation process.[6]

Propane (C_3H_8) is a product of natural gas liquids or steam cracking in petroleum refining and is used to produce propylene (C_3H_6).[16, 26, 27] Propylene can be either polymerized alone, such as for making polypropylene plastics, or it can be copolymerized, such as with ethylene.[19, 26] Propylene can also be used in making chemicals such as isopropanol or glycerol.[26] Propylene gas streams used for polymerization must have a very high purity (> 99.9 %), as impurities can poison the reaction catalyst however, traces of propane remain after cracking, making propane and propylene a key gas separation pair.[19] These gases have similar boiling points (C_3H_8: 231 K and C_3H_6: 225 K) meaning that they are difficult to separate via distillation methods.[27] Propane and propylene are also similar in size (C_3H_8: 4.90 Å and C_3H_6: 4.60 Å) and polarizability (C_3H_8: 6.29 – 6.37 Å^3 and C_3H_6: 6.26 Å^3) which further complicates separation (Figure 1.2 and Figure 1.4).[10, 11, 14]

1.1.4 Xenon/Krypton Separation

Xenon and krypton are noble gases which have important industrial uses. Xenon can be used in flash photography, spacecraft propellant, and in some forms of lamps.[16, 19] Xenon also has many medical uses such as being used an as anaesthetic due to its non-toxic properties, non-laser phototherapy and MRI and CT scanning.[28] Krypton can be used, sometimes with argon, in incandescent lamps as it decreases degradation of the lamp filament, in lasers and for stimulating plant growth as the light emitted from krypton lamps is known to aid in stimulating photosynthesis.[16] Furthermore, both xenon and krypton have applications in insulation and electronics.[2, 19] Currently, cryogenic distillation is the main method for separation of xenon/krypton mixtures, which is highly energy-intensive and expensive.[2, 19] Xenon and krypton are difficult to separate due to their similar shape and size (Xe: 4.10 Å and Kr: 3.69 Å) but they do have differing polarizabilities (Xe: 4.01 Å and Kr: 2.47 Å) (Figure 1.2 and Figure 1.5).[7, 12]

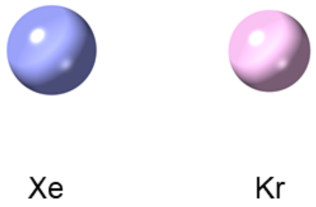

Figure 1.5 Xenon and krypton. Atom colours: xenon: violet and krypton: pale pink

1.2 Current Methods for Gas Separation

Gas separation and purification are an important part of gas preparation for industrial application. These separations account for 50 % of industrial energy and 10 – 15 % of global energy consumption.[1, 15, 19, 27] There are currently a range of methods employed for the capture, separation, and purification of gas mixtures, however, as outlined above, these gas separations are difficult to perform due to similarities in the gas properties, and often these methods are costly and energy-intensive. In this section, the current methods for gas capture, separation and purification will be outlined, alongside emerging methods.[27]

1.2.1 Absorption-Based Methods

Absorption-based methods are one of the most widely established gas capture processes, especially for CO_2 capture. One such method is amine scrubbing which is the most mature technology used for postcombustion capture of CO_2 and H_2S and has been utilized commercially since the 1930s.[29, 30] In amine scrubbing, CO_2 is captured by a closed loop cycle of adsorption and desorption (stripping) cycles with aqueous amine media.[29, 30] CO_2 is absorbed by the aqueous amine solution at around 40 °C by reacting with the amine to form either a carbamate species (primary or secondary amines) or bicarbonate ions (tertiary amines).[29-31] In the stripping stage, the solution is then heated to around 100-120 °C with water vapour to regenerate the amine so it can be used again.[29, 32] The water vapour used is condensed from the stripper vapour to release the CO_2.[29] A range of primary, secondary and tertiary alkanolamines are utilized in amine scrubbing.[30, 32] Monoethanolamine (MEA) is the traditionally used amine, but new compounds are being used more frequently. Furthermore, there is constant research and development of amine technologies, such as Shell CANSLOV, which utilizes amine technology for SO_2 and CO_2 capture.[32, 33]

Some of the advantages of amine scrubbing include the high purity streams of CO_2 produced (> 95 %), non-reliance on human operators which reduces labour costs, and the amine solvent can be recycled which reduces material costs.[34] However, this well-established method for CO_2 capture does come with its downfalls. One of the greatest disadvantages is the large energy cost required to regenerate the amine; greater than half of the total capture cost.[30, 31] The use of MEA and some other amines have disadvantages such as low CO_2 loading capacity, the formation of toxic products, reduced efficiency upon degradation (thermal or oxidative), and the corrosion of pipes and other equipment.[29, 32] Ergo, while amine scrubbing is a highly established technique for CO_2 capture, it has many limitations.

1.2.2 Cryogenic Distillation

Cryogenic distillation involves the use of extremely low temperatures (below 120 K) to separate gases.[35] Cryogenic distillation is mainly used to separation of air into its constituent gases (nitrogen, oxygen and argon), in the separation of CO_2 from gas mixtures, and in the separation of light alkenes from alkanes, such as ethylene purification and propylene purification.[35, 36] Simply put, the gas feed enters the cryogenic distillation tower, which is at a low temperature and high pressure. The gas mixture is separated due to differences in their boiling points i.e. one gas will liquefy and leave through the bottom, and the other will remain gaseous and leave through the top.[34, 35, 37, 38] This is shown by the simplified schematic in Figure 1.6. The distillation columns contain trays to aid in separation and the number of trays is dependent on the difficulty and desired purity of separation.[38]

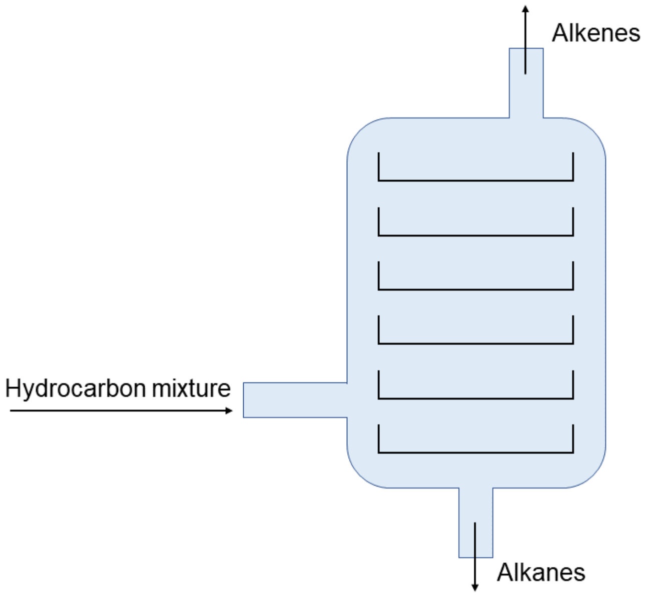

Figure 1.6 A simplified schematic depicting a cryogenic distillation tower for the separation of alkenes and alkanes.[37]

For CO_2 capture, an advantage of cryogenic distillation is that there is a high recovery rate of CO_2 and the product is liquid CO_2.[34] For air separation, cryogenic distillation results in high purity gas (95% when separating O_2 and N_2) and high gas recovery (95%).[39] One of the main disadvantages of cryogenic distillation is that it is highly energy-intensive as a lot of energy is required to maintain such low temperatures.[34, 37] In terms of CO_2 capture, another drawback is that cryogenic separation cannot be used on its own to sequester CO_2 from flue gas, because first other gases such as O_2, NO_x, SO_x and water vapour must be removed before the cryogenic process can begin.[34] Due to the low temperatures used, if contaminants such as water, oil or unwanted gases are present, they can freeze and clog up the pipes, which can result in system failure or corrode equipment.[34, 35] Other disadvantages include possible risks such as overpressurization, oxygen deficiency in the work environment, and flammability.[35]

1.2.3 Membranes

The use of membranes for gas separation has been commercially implemented since the 1980s.[40] In terms of gas separation, membranes are a barrier between two phases. Gases are allowed through the barrier due to a difference in pressure.[40, 41] The main mechanism of gas separation membrane technology involves three steps: 1) absorption of the gas into the membrane at the higher pressure side of the membrane, 2) diffusion of the gas through the membrane, and 3) desorption of the gas at the lower pressure side of the membrane.[40, 41] There are different kinds of membranes, based on their material type, such as polymeric, inorganic, carbon-based, zeolitic, solubility-controlled, facilitated transport, or mixed-matrix membranes.[36, 40] The most commonly implemented commercial membrane is polymeric.[36, 42] Commercially, membranes have several applications such as the recovery of hydrogen from ammonia plants, the separation of CO_2 and natural gas, the separation of nitrogen from air, and the separation of C_2-C_4 alkenes from nitrogen in petrochemical and polyolefin plants, with other separations in the works for future applications.[42, 43]

There are many advantages to membranes over other methods of separation. One such advantage is the low cost compared to conventional methods as membrane technologies have simple, compact, and easy to use equipment that contains no moving parts. Membranes also do not require phase changes, have a small carbon footprint, and have a low energy use.[41, 42] Some disadvantages of membranes are that they require high operating pressure, and they are susceptible to poisoning by contaminants such as heavy metals, water or small particles. Membranes also have restrictive operating temperatures as they cannot withstand high temperature, have a lack of corrosion resistance, and the selectivity or permeability of membranes can degrade over time.[42, 44]

1.2.4 Porous Materials

Porous materials allow for adsorption-based methods of gas capture and separation. There are a number of different types of porous materials including zeolites, activated carbons, silica gels, molecular sieve carbons, porous polymers, and metal-organic frameworks (MOFs).[45-47] These materials all have different properties to each other in terms of crystallinity, stability, and diversity.[46] Some of these materials are already established in the field of gas capture and separation, such as zeolites and activated carbons, whilst others, such as MOFs, are emerging methods.

Zeolites are a well-established class of porous materials.[48] Zeolites are crystalline materials known as aluminosilicates as they are formed by a periodic array of TO_4 octahedra, where T = Si or Al.[31] The framework of zeolites is negatively-charged therefore charge balancing cations are found in the frameworks, commonly alkali cations such as Na^+ or K^+.[31] Zeolites contain uniform micropores or mesopores with the pore sizes ranging of 3 – 10 Å.[45, 46] Zeolites occur commonly in nature, for example chabazite and mordenite (Figure 1.7), however synthetic zeolites can also be made. Naturally-formed zeolites tend to have smaller pores and pore volumes than synthetic zeolites.[48] Zeolites have a number of favourable qualities, such as good regenerability, good thermal and chemical stability, they are incombustible, have large surface areas, and high adsorption capacity.[31, 46-48] However, even though zeolites are one of the more established methods for gas storage and separations, there are drawbacks; they can be sensitive to acid/base and they can only operate under mild conditions as elevated temperatures or the presence of water can be detrimental to adsorption.[31, 46, 48] The cost of zeolites can be both an advantage or a disadvantage depending on the desired zeolite. Sometimes costs are low, for example if natural zeolites are used or the raw materials used to make synthetic zeolites are cheap, and sometimes the cost is high, for example if the synthetic procedure is expensive, energy-intensive, time-consuming, or toxic.[49]

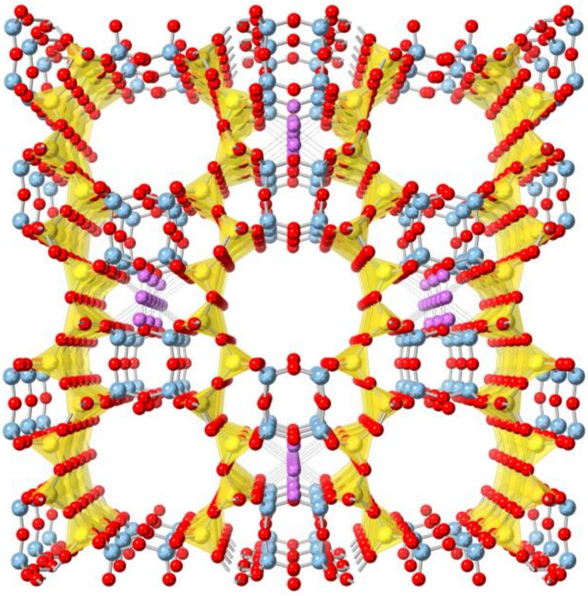

Figure 1.7 Crystal structure of mordenite. Atom colours: oxygen: red, aluminium: blue, silicon: yellow, and sodium: lilac. [50]

Activated carbon is another well-established adsorption-based method for gas storage and separation. Air purification is one of the many uses for activated carbon, alongside water treatment and solvent recovery.[51] These materials contain pores ranging from 3 – 100 Å with pore sizes varying not just between different types of activated carbons but within the material itself.[31, 45, 47, 52] Activated carbon can be formed from a range of possible sources, such as coal, industrial by-products such as petroleum or coke pitch, or a range of biomass sources like coconut shells or sawdust.[31] This is one of the advantages of using activated carbon. To make activated carbon materials, there are two stages: carbonization, where the precursor material is heated until a carbon skeleton (char) is left behind, and activation, where the char is functionalized by physical or chemical treatments.[31] There are many advantages of activated carbon including its large surface area, pore volume, low cost, good stability and decent reusability.[45, 47] However, there are also disadvantages such as decreased adsorption ability under humid conditions, high desorption temperatures, incomplete desorption, irreversible binding of gases, and flammability.[47] Another significant drawback is the lack of pore uniformity and that while the surface of the pores can be chemically altered, it is difficult to alter the structure of activated carbons.[51, 52]

An emerging type of porous material in the field in gas storage and separation is a class of compounds called metal-organic frameworks (MOFs). MOFs are a type of coordination network which have permanent porosity which allows for the uptake and separation of gas molecules.[53] This class of porous materials will be expanded upon in section 1.3 and 1.4.

1.3 Metal-Organic Frameworks (MOFs)

Metal-organic frameworks, commonly known by the acronym of MOFs, are a sub-class of coordination networks.[53] According to the International Union of Pure and Applied Chemistry (IUPAC), the definition of a MOF is *'a coordination network with organic ligands containing potential voids'* and a coordination network is a type of coordination compound which extends with repeating entities in more than one direction.[53] As another description, MOFs are made with metal-based nodes that are connected by strong coordination bonds to charged organic ligands.[54, 55] They are generally crystalline structures but are not necessarily.[53, 56] There is no defined nomenclature for MOFs however they are usually nicknamed from either (1) their place of origin, such as HKUST-1 which originates from the Hong Kong University of Science and Technology[57] or NU-1000 which originates from Northwestern University[58], or (2) by their components such as $Cu(4,4'\text{-}bpy)_{1.5}\cdot NO_3(H_2O)_{1.25}$[59] (4,4'-bipy = 4,4'-bipyridine) or Ni-BDC (BDC = 1,4-benzene dicarboxylic acid).[60] The latter nickname is known at the reticular formula.[55]

1.3.1 Brief History of MOFs

The earliest examples of coordination compounds can be reported back to the 1800s, with a pigment called Prussian Blue and it is known to be one of the first recognized coordination compounds.[54] However, the development of coordination networks really began late in the 1950s.[54] However, it wasn't until 1995 that the term 'metal-organic framework' was first introduced by Omar Yaghi.[54, 59] This compound had a cationic framework that was made of Cu^+ nodes, with a distorted trigonal planar geometry that had not yet been observed in other compounds with similar types of coordination.[59] The nodes were connected to 4,4'-bipy linkers resulting in a structure that had rectangular shaped voids.[59] Thus, the era of MOFs began.

Due to the instability of using single metal ions as nodes, polynuclear clusters were sought after instead. As mentioned in the name, polynuclear clusters contain multiple atoms, which could be multiple metal ions or could be coordinating atoms such as oxygen or nitrogen attached to the metal ion. These polynuclear clusters can be referred to as a secondary building units (SBUs) however, an SBU is not a chemical entity but rather hypothetical unit which is used to make MOF structures easier to understand. SBUs provide higher stability, rigidity, and directionality than single metal nodes.[54] This led to the development of well-known, and some of the earliest known, MOF structures with high stabilities upon solvent removal and permanent porosity: MOF-2 (1998), MOF-5 (1999), and HKUST-1 (1999).[57, 61, 62]

MOF-2 is made of dinuclear Zn^{2+} paddlewheel clusters (SBUs) with the oxygens of the cluster coming from the carboxylate groups of the BDC ligands and from coordinated water molecules. The BDC ligands associate to the nodes via di-monodentate behaviour.[61] MOF-2 was the first framework that maintained its structure upon solvent removal and its permanent porosity was shown by N_2 uptake at 77 K.[61]

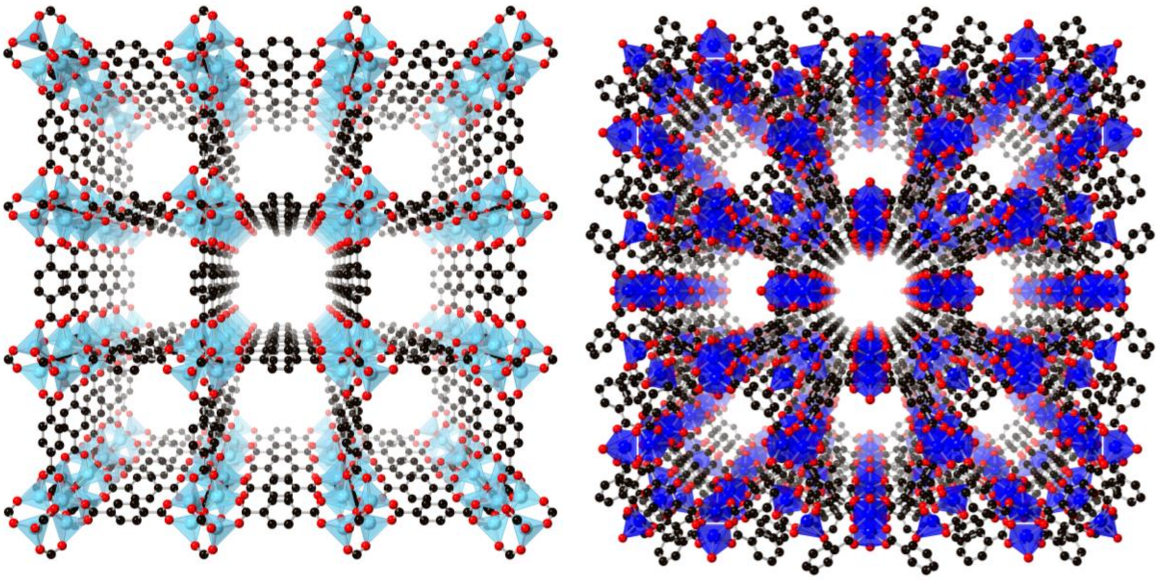

Figure 1.8 (Left) Structure of MOF-5. (Right) Structure of HKUST-1. Atom colours: carbon: black, oxygen: red, zinc: pale blue, copper: royal blue, and hydrogen: peach. Hydrogen atoms omitted for clarity.

In the following year, Yaghi's group released the structure of MOF-5, which is likely to be the most well-known MOF. The SBU of this MOF is made of a single oxygen atom which is further bound to four Zn^{2+} atoms, which results in a Zn_4O tetrahedron. [62] This allows for expansion along Cartesian coordinates in a 3-dimensional way, which is done by the addition of the BDC ligands at the edge of each Zn tetrahedron, resulting in the framework structure of MOF-5 (Figure 1.8).[62] MOF-5 has three-dimensional channels that intersect with each other with 12.9 Å inter-cluster distance and a pore aperture of 8 Å.[54, 62] The high stability of this MOF was shown by heating it to 300 °C with there being no effect on its crystallinity or structure. N_2 at 77 K isotherms of MOF-5 showed a higher uptake than MOF-2, and assuming monolayer coverage, the apparent Langmuir surface area was estimated to be 2,900 $m^2\ g^{-1}$, which further confirms the permanent porosity of MOF-5 and was an early indicator of the high surface areas that MOFs can have.[62]

HKUST-1 was also released in 1999 by William's group. HKUST-1 is made of dimeric Cu^{2+} paddlewheel SBUs with the equatorial oxygen atoms being donated from the TMA (trimesic acid) carboxylate groups. The Cu^{2+} ions are coordinated with a pseudooctahedral geometry with axial coordinated water ligands.[57] Much, like MOF-5, HKUST-1 has intersecting three-dimensional channels, with the framework having a honeycomb arrangement with hexagonal pore apertures which are made up of six SBUs and six TMA ligands, resulting in an inter-cluster distance of 18.6 Å.[57] The framework structure can be seen in Figure 1.8. N_2 at 77 K isotherms gave a Langmuir surface area of 917 $m^2\ g^{-1}$.

From 1999 onward came the exponential increase in the number of MOFs discovered and published. Due to the wide variety of metals and organic ligands available, a near infinite number of MOFs can be achieved.

1.3.2 Isoreticular Principle and Multivariate MOFs

The formation of MOFs is dependent on many variables, such as temperature, solvent, metal to ligand ratio, and synthesis method. In saying that, the rules of reticular chemistry can be applied as MOFs fall under the subheading of reticular chemistry because they are compounds which form strong bonds to make extended structures with a repeating net-like structure (topology).[54, 55, 63] The isoreticular principle is an important feature within reticular chemistry as it results in the formation of a series of compounds with the same topology. These are generally achieved by altering the ligands, generally the ligand length (for example Figure 1.9), to achieve a family of MOFs with the same topology but differing pore sizes.[54]

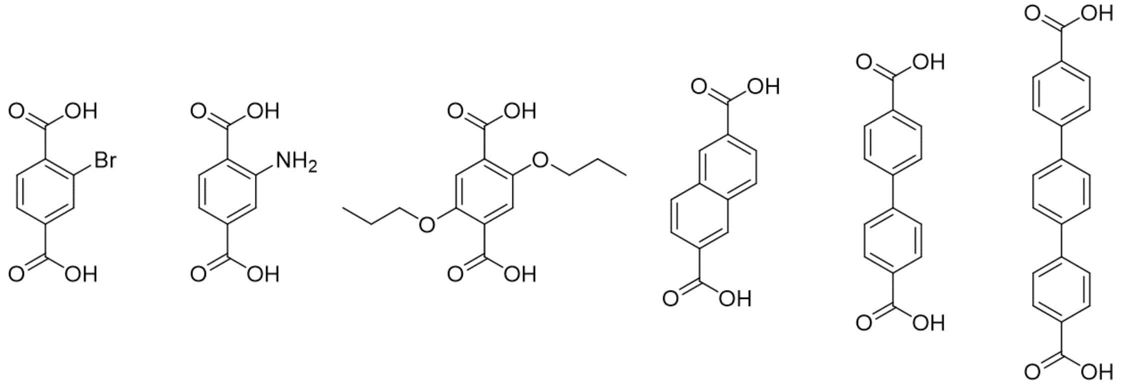

2 **3** **4** **8** **10** **16**

Figure 1.9 Ligand structures for IRMOFs 2, 3, 4, 8, 10 and 16, respectively. See Figure 1.10 for the IRMOF structures.

An example of this is the IRMOF (Isoreticular Metal-Organic Framework) series produced by Yaghi's group, as seen in Figure 1.9 and Figure 1.10.[64, 65] This series of MOFs have the same topology as MOF-5 but with different ligands. The ligands are altered in different ways. One way is by adding different functional groups to BDC such as Br, NH_2, or $O(CH_2)_2CH_3$ as seen by ligands 2, 3 and 4 (Figure 1.9), which makes IRMOFs 2, 3 and 4 respectively (Figure 1.10). Alternatively, the BDC linker can be expanded through to the addition of benzene rings to make longer ligands as shown by ligands 8, 10 and 16 (Figure 1.9) which make IRMOFs 8, 10 and 16 respectively (Figure 1.10).[64] As the linker size increases, so does the size of the pores, whilst still maintaining the framework topology.

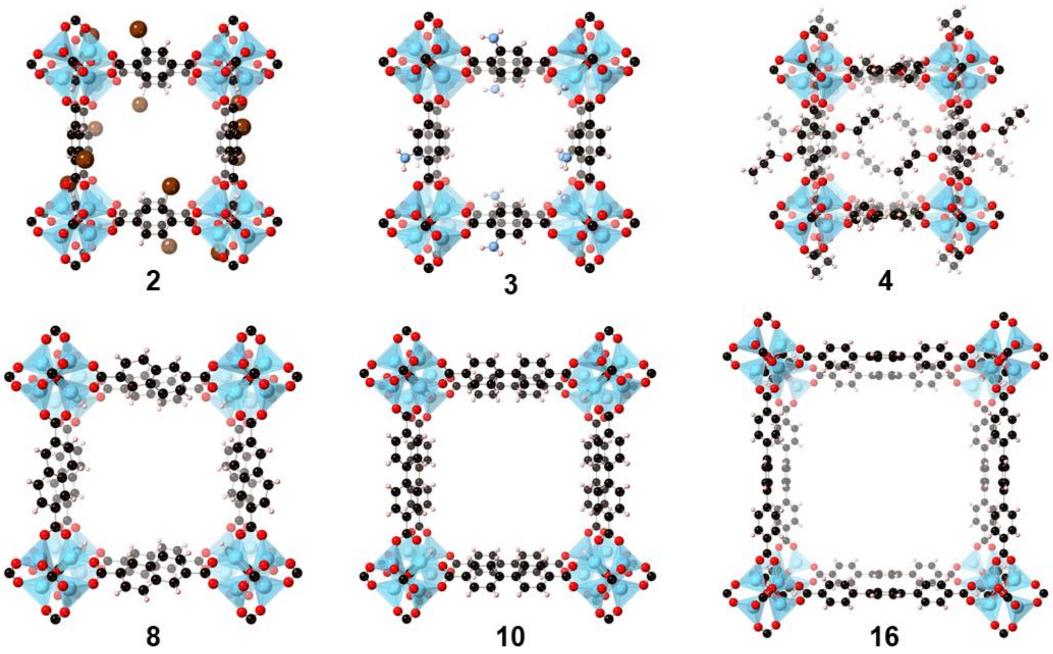

Figure 1.10 Structure of IFMOFs 2, 3, 4, 8, 10, 16, respectively. Atom colours: carbon: black, oxygen: red, zinc: pale blue, hydrogen: peach, bromine: brown and nitrogen: periwinkle blue.

The isoreticular principle applies to more than just changing ligand functionalization or length. Changing the metal ions present can also produce an isoreticular series, as seen by the MOF-74 series (Figure 1.11).

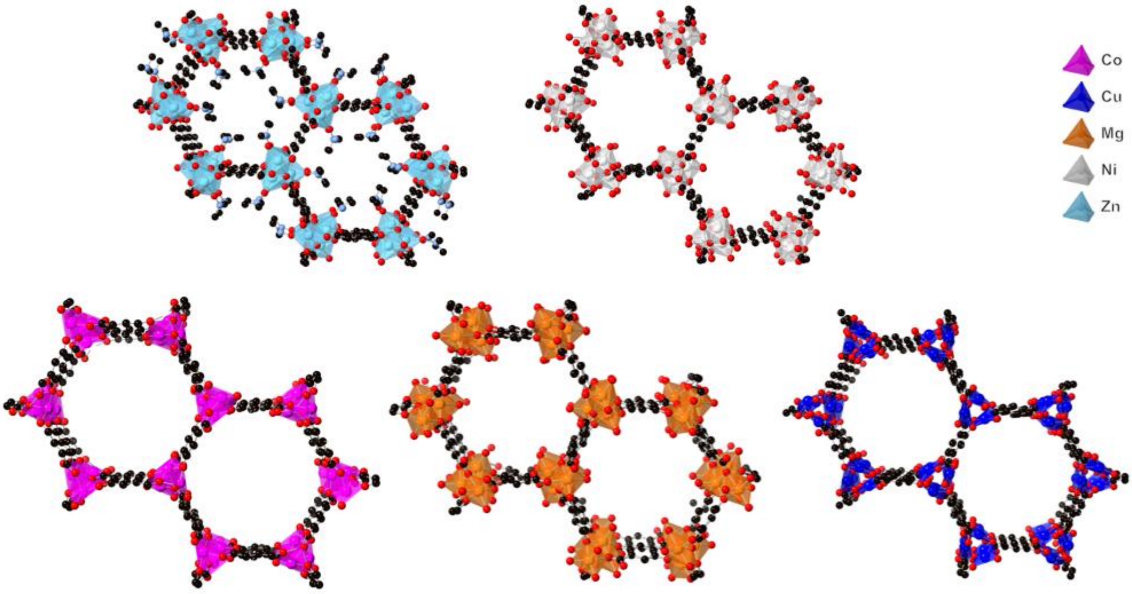

Figure 1.11 Structures of the MOF-74 series. Atom colours: carbon: black, oxygen: red, nitrogen: periwinkle blue, zinc: pale blue, nickel: chrome, cobalt: magenta, magnesium: orange, and copper: royal blue. Hydrogen atoms omitted for clarity.

The metal centres in this series adopt an octahedral geometry, with the oxygen donors being from the carboxylate or hydroxyl groups on the 2,5-dihydroxyterephthalic acid (DHTP) ligand.[66] This forms a framework with honeycomb-shaped three-dimensional channels, and the SBUs forming helical rods.[66] At the metal centres, there is generally a coordinated solvent molecule which can be removed upon activation to generate an open metal site. These sites point into the pore, which can be seen in the first structure in Figure 1.11 as DMF is coordinated. The first MOF-74 structure that was reported contained zinc, and over the course of several years, isoreticular structures were reported containing nickel, cobalt, magnesium, and copper (Figure 1.11).[66-70] Yaghi's group also showed that MOF-74 can contain more than one metal at a time in the framework and still have the same topology. They were able to insert up to ten metals into the MOF (Ba, Ca, Cd, Co, Fe, Ni, Mg, Mn, Sr, and Zn) as observed by elemental analysis.[71] This mixed metal MOF is an example of a multivariate MOF as the ten metals are inserted into random places throughout the MOF however the overall topology is retained. The introduction of heterogeneity into the framework can be either through different metal ions forming the same SBUs (as is the case here) or through having multiple linkers present which have the same coordinating groups but differing chemical composition, for example a MOF made with both BDC and BDC-Br.[54]

1.3.3 Key Characteristics of MOFs

MOFs contain a number of optimal characteristics that make them appealing for use in a variety of applications. One of the most advantageous characteristics of MOFs is their permanent porosity as the pores are where the important chemistry occurs. Permanent porosity is when the MOF will remain porous upon changes to its environment such as solvent, temperature or solvent-removal.[54] MOFs can also have their exact structures determined via X-ray diffraction. This is highly advantageous as it allows for atomic-level precision leading to a better understanding of the inner workings of the behaviour of the MOF.

Another advantage of MOFs is the range that can be made due to the variety of metals and ligands available. Transition metals, such as Zn^{2+} and Co^{2+}, are the main metals used in MOFs, however other metals such as alkaline earth metals like Mg^{2+} or lanthanide ions can be included.[62, 66, 68, 69, 72] The wide variety of organic ligands available is limited only by the laws of organic chemistry and the imagination. MOF ligands can be ditopic (containing two coordination sites), tritopic (three coordination sites) or more, which further increases the number of ways that ligands can coordinate to SBUs, thus resulting in more MOF structures.

MOF structures can also be multicomponent, where there is more than one type of ligand present, or multivariate, as mentioned in the previous section, both of which increase MOF possibilities.

MOFs have a variety of other optimal characteristics such as their robustness, resistance to thermal or chemical degradation (stability), and they can be cheap and easy to make.[45, 73] They are also more designable and tunable than other porous materials which is highly advantageous and this includes the ability to post-synthetically modify MOFs.[45, 46, 73]

Combining all of the aforementioned abilities, MOFs are dynamic field of chemistry with a vast range of applications. MOFs can be used for catalysis as ligands can be functionalized to contain catalytic groups for specific reactions.[74-76] MOFs can be used for their luminescent properties that come from either the metal centres (such as lanthanides) or due to aromatic or conjugated π systems.[72, 77] Such luminescent MOFs can be used in sensing such as for the detection of ions, vapours, or changes in pH or temperature.[72] One of the biggest applications of MOFs is in the field of gas capture, storage, and separation, which will be further outlined in section 1.4.

1.4 Use of MOFs in Gas Capture and Separation

As introduced above, MOFs are becoming increasingly investigated for their application in gas capture, storage, and separation. This is due to the porous nature of MOFs being ideal adsorbents for gas storage and the ability of ligand functionalization to result in a range of interactions with different gas molecules, allowing for efficient separation.[6, 19, 78, 79] This section will outline the mechanisms of separation in MOFs, introduce why small pore MOFs are efficient at gas separation along with some examples, and will end with the introduction to some experimental and computational techniques.

1.4.1 Methods of Separation in MOFs

Gases can be separated in MOFs using several different mechanisms which can roughly be divided into two sections: equilibrium and non-equilibrium processes.[1] It is important to note that these two types of separation processes are not mutually exclusive, as separation can be a combination of these types.

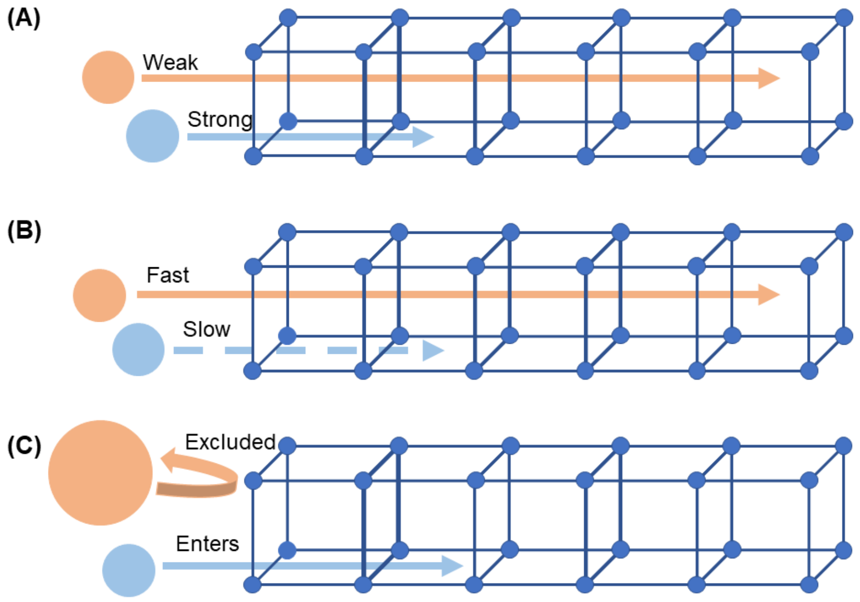

Figure 1.12 Types of separation. (A) Thermodynamic separation. (B) Kinetic separation. (C) Molecular sieving. The blue framework represents a MOF.

Equilibrium processes are generally governed by thermodynamics; such separations are often called thermodynamic separations (Figure 1.12A). This is the most common type of gas separation in MOFs and often occurs in MOFs with large pores.[14, 80] For thermodynamic separation, all gases can enter the pores, as shown in Figure 1.12, however, gases will adsorb to the surface of the pore based on their adsorption affinity.[1, 15, 81] Gases with a higher affinity will adsorb more strongly, such as the blue “molecule”, and gases with a lower affinity will bind more weakly, such as the orange “molecule”.[15] The strength of the binding affinity is determined by the types of interactions the adsorbing gas can make with the MOF surface, such as van der Waals contacts, hydrogen-bonding or dipole-dipole interactions. These interactions can be determined by the framework through pore size and shape, functional groups on the ligands and their arrangement in the pore, or by the metal nodes, for example if a node contains open metal sites.[15] The properties of the gas are also important in thermodynamic separation, such as polarizability, size, shape, and dipole/quadrupole moment.[45]

In non-equilibrium processes, separation relies on the rate of diffusion of gases through the pores.[1, 45, 81] This type of separation is also known as kinetic separation (Figure 1.12B).[14] Gases that have a higher mobility will occupy the pore preferentially to other gases.[14] This is seen in Figure 1.12B as the orange “molecule” has a higher mobility, as shown by the solid orange arrow, whereas the blue “molecule” has a lower mobility, as shown by the dashed blue arrow. The size of the MOF pore governs this kind of separation process and the smaller the pore, the more amplified the kinetic separation is.[1] As the pore size decreases, the diffusion of gases becomes more hindered and molecular diffusion will transform into surface diffusion which is more dependent on the kinetic diameter and molecular weight of the gas.[81] If the pore size continues to be reduced, it will reach a point where one of the gas components can no longer enter the pore, thus resulting in size-exclusion separation.[81] Pore size is not the only factor that influences kinetic separation; temperature and pressure are also influencing factors for both the gas and the framework.[81]

Size-exclusion separation, also known as molecular sieving, generally falls under the category of non-equilibrium processes as gases that are too large to fit into the pores are excluded, as seen by the orange "molecule" in Figure 1.12C, whilst smaller gases are allowed entry, as seen by the blue "molecule".[1, 81] In some cases, the rate of diffusion of a gas is so low that it doesn't enter the pore, however it could still fit into the pore. This is due to there being a small pore window that leads to a larger pore. The gas doesn't enter the pore as it 'bounces off' due to this small pore aperture, even though the gas could hypothetically still fit into the pore, if it could get through the small pore window.[45] MOFs are generally quite rigid structures, even at elevated temperatures before they break down, which helps size-exclusion separation. The shape of the gas is also an influencing factor of size-exclusion separation.[15, 45]

1.4.2 Small Pore MOFs for Gas Separation

As mentioned above, the size of MOF pores is an influencing factor on separation ability. For this reason, microporous (< 20 Å) and ultra-microporous (< approximately 7 Å) MOFs are becoming increasingly more investigated for their gas separation properties.[19, 80] Large-pore MOFs generally have a higher surface area and thus a higher uptake, however they often have lower selectivity values (the preference of one gas over another). On the other hand, small-pore MOFs generally have higher selectivity but lower uptake ergo, the most efficient MOFs for gas adsorption would have a balance between these properties.[14] Ultra-microporous MOFs tend to have a higher density than average MOFs, which makes their volumetric capacity on par with materials that are more porous.[24] Furthermore, denser frameworks are often more mechanically resistant than highly porous MOFs.[24]

All of the types of separation methods outlined in section 1.4.1 apply to small pores MOFs. One of the biggest advantages of such MOFs is that the pore sizes are of the same scale as the sizes of the gases.[80] The gases outlined in section 1.1 are between 3.2 and 5.0 Å for their kinetic diameter, and the size of MOF ultra-micropores, as aforementioned, is less than 7.0 Å, making the gases fit nicely inside the pores. This will increase the strength of the interactions made, allowing for better separation.[19, 24] Good size complimentary can also allow for kinetic sieving to occur as larger gases can be physically prevented from diffusing into the pore.[24] Small pore MOFs can be made using several different approaches such as using short ligands, interpenetration using larger ligands, ligand functionalization, post-synthetic modification, or installing partitioning linkers.[1, 19, 82]

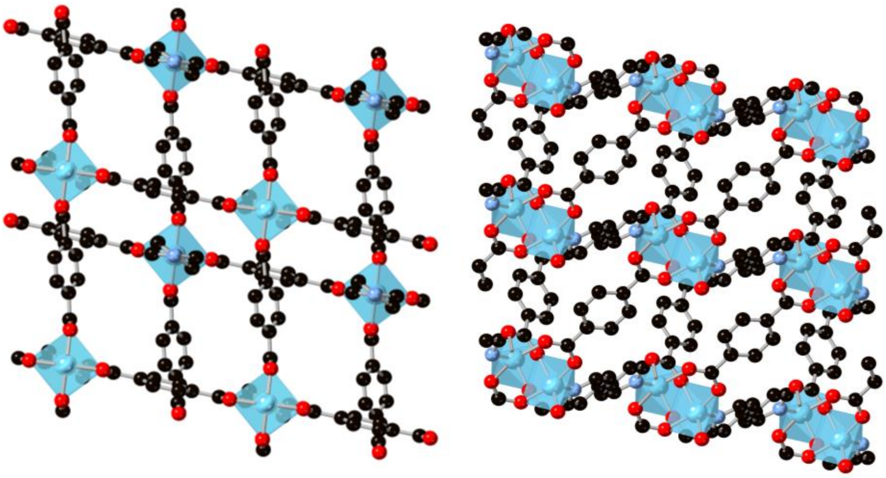

Figure 1.13 Structures of MOF-508 in the open phase (left) and the dense phase (right). Atom colours: carbon: black, oxygen: red, nitrogen: periwinkle blue and zinc: pale blue. Hydrogen atoms omitted for clarity.

In 2008, Bastin and et. al. introduced the first microporous MOF for the separation of CO_2 by fixed-bed adsorption.[83] This MOF, named MOF-508, has the formula $Zn(BDC)(4,4'\text{-bipy})_{0.5}$. MOF-508 is an interpenetrated MOF with two forms labelled *a*, which is the open phase and *b*, which is the dense phase (Figure 1.13).[84] The *b* phase is made upon guest exclusion however the structure switches back to the open, *a* phase upon guest inclusion.[84] In the open form, MOF-508 has one-dimensional channels of 4.0 x 4.0 Å which makes it both microporous and the ideal size for separation of CO_2, N_2, and CH_4 as they are all near this size.[83] MOF-508 shows selectivity towards CO_2 and this MOF introduced microporous MOFs as possible separators for gas mixtures.

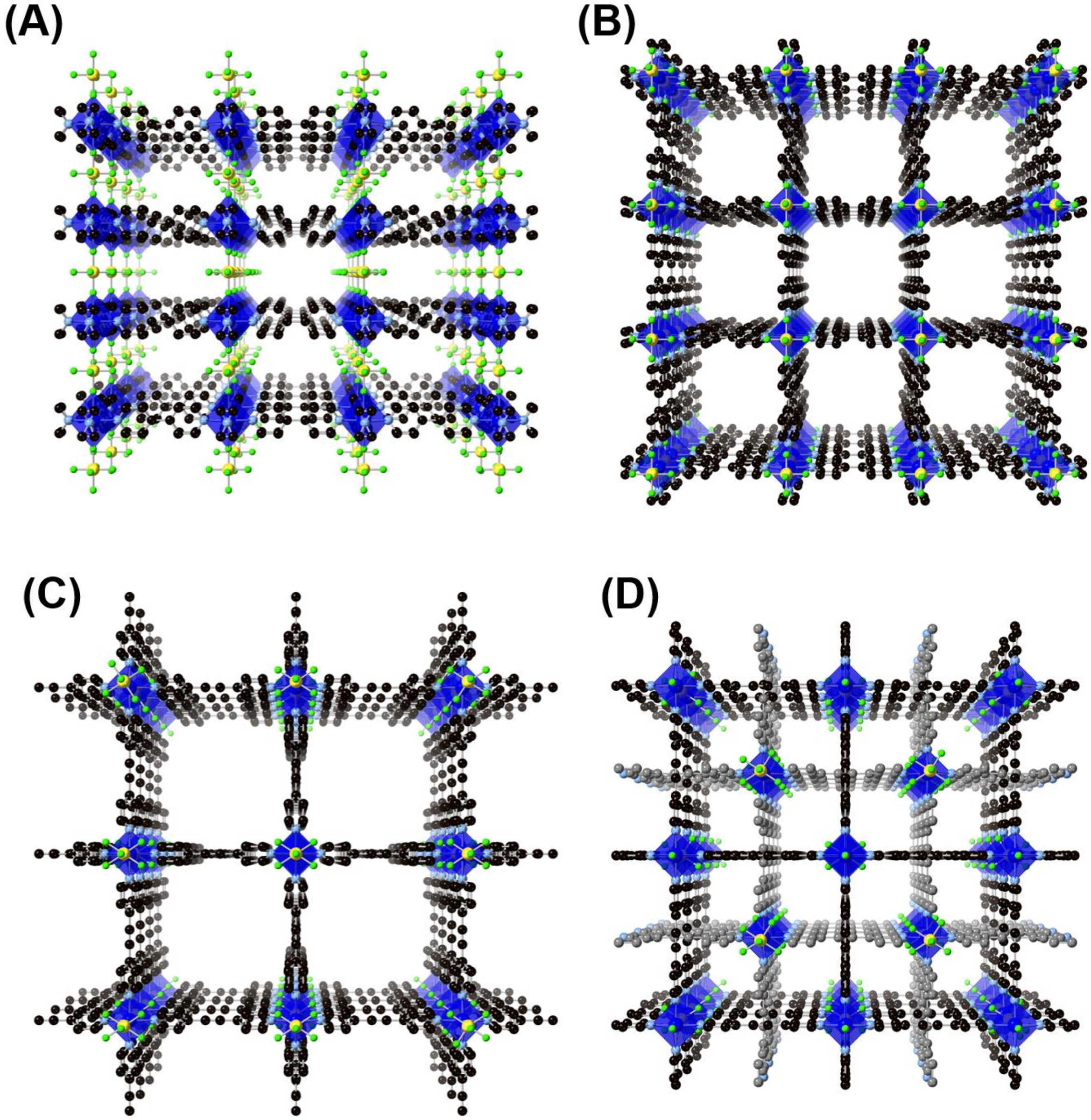

Figure 1.14 (A and B) Structure of SIFSIX-1-Cu from two orientations. (C) Structure of SIXSIX-2-Cu. (D) Structure of SIFSIX-2-Cu-i with two carbon colours to show the interpenetration. Atom colours: carbon: black and grey, nitrogen: periwinkle blue, copper: royal blue, silicon: yellow and fluorine: green. Hydrogen atoms omitted for clarity.

A group of small pore MOFs is the SIFSIX family. These MOFs are another example of the isoreticular principle as the metal ions, organic ligands or pillar anions can be replaced, creating various MOFs with the same topology.[1, 15, 22, 82] Furthermore, many of the MOFs in this family display high separation selectivities and uptakes.[1, 82] SIFSIX-1-Cu was the first in the series to be made, however its name was given after publication.[85] SIFSIX-1-Cu contains Cu^{2+} as the metallic node alongside SiF_6^{2-} anions; these two alternate in an extending chain as seen in Figure 1.14A and B.[85] In the equatorial positions of the Cu^{2+}, 4,4'-bipy ligands are coordinated through the nitrogen, which form a two-dimensional grid, and the SiF_6^{2-} ions expand the structure axially to made it three-dimensional. The network contains two types of channels: one with dimensions of 8.0 x 8.0 Å and the other with dimensions of 6.0 x 2.0 Å, thus classifying this MOF as microporous.[85] SIFSIX-1-Cu displays high methane uptake, of around 145 cm^3/g, and high acetylene uptake of around 190 cm^3/g.[1, 85]

Also in the SIFSIX family are SIFSIX-2-Cu and SIFSIX-2-Cu-i, as seen in Figure 1.14C and D. These MOFs have the same topology as SIFSIX-1-Cu however they are made with a longer ligand, 4,4'-dipyridylacetylene, which results in larger channels, as seen by SIFSIX-2-Cu which has channels of 13.1 x 13.1 Å.[82, 86] Howbeit, larger pores can result in interpenetrated MOFs, which is seen with SIFSIX-2-Cu-i. The interpenetration of this MOF decreases the pore channel dimensions down to 5.2 x 5.2 Å.[82, 86] Both MOFs display good uptake of CO_2, with SIFSIX-2-Cu-i displaying a higher uptake than its non-interpenetrated counterpart (41 cm^3/g versus 121 cm^3/g). Both MOFs show good selectivity for CO_2/CH_4 and CO_2/N_2 gas mixtures again with SIFSIX-2-Cu-i outperforming SIFSIX-2-Cu. This is likely because pores of SIFSIX-2-Cu-i are of similar dimensions to CO_2, thus resulting in better complimentary and stronger interactions.[80, 86]

1.4.3 Introduction to Experimental and Computational Techniques

This section will outline a number of techniques that are used to characterize gas uptake and separation abilities of porous materials. A microporous MOF called MUF-15 will be used as a worked example throughout this section to display the analysis techniques used. MUF-15 is made of Co^{2+} hexanuclear clusters, with these nodes being connected by isophthalic acid (H_2ipa) ligands.[87] This MOF displays good selectivity for ethane over ethylene.[87] The structure of this MOF is described in better detail in section 1.5.2.

1.4.3.1 Gas Adsorption Theory

Adsorption is known as the condensation of a gas (or liquid) onto an interface, such as the surface of a solid.[54, 88, 89] The opposite of adsorption is desorption, where the gas (or liquid) on the solid surface is removed. All the aforementioned processes can be summarized using the term sorption.[88] The adsorbable gas is known as the adsorptive, once it enters the adsorbed state it is known as the adsorbate, and the solid surface is known as the adsorbent.[54, 88] There are two kinds of adsorption: chemisorption and physisorption. In chemisorption, chemical bonds are made between the adsorbate and the absorbent. This changes the properties of the adsorbate, which strongly adheres to the surface, and only a monolayer (a singular layer of molecules on the surface) is formed.[54, 88, 90] In physisorption, weak intermolecular interactions are made between the adsorbate and adsorbent. The physiosorbed adsorbate retains its identity upon adsorption and desorption and physisorption can result in multilayer surface coverage.[54, 88-90]

Gases can interact with porous materials via chemisorption or physisorption. For this thesis, physisorption will be investigated. Gases physisorb to MOFs through a wide range of attractive and repulsive non-covalent interactions such as van der Waals contacts, hydrogen bonding or electrostatic interactions. These kinds of interactions are influenced by the gas properties outlined in section 1.1.1.1 like polarizability, dipole moment and quadrupole moment. Because gases adsorb to the surface of MOF pores, these properties become important in determining the strength of the interaction and thus influencing gas uptake.

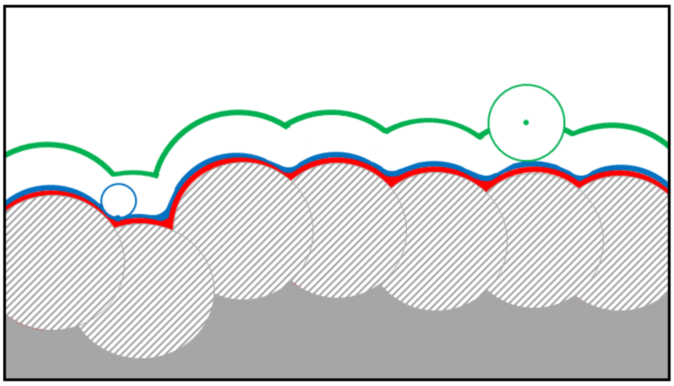

Figure 1.15 Types of surfaces on an adsorbent: the van der Waals surface (red), the Connolly surface (blue) and the accessible surface (green). Figure adapted from Thommes et. al. and Sarkisov et. al. The grey circles represent the surface atoms, and the dark grey is the bulk of the adsorbent. [88, 91]

The surface of a solid is an important part of gas sorption theory and it can be defined in three ways: the van der Waals surface, the Conolly surface, and the accessible surface.[88, 91] These can be seen in Figure 1.15. The van der Waals surface is defined as the edge of the van der Waals spheres of the surface atoms and is where the occupied space and the empty space meet, as shown by the red line in Figure 1.15.[88, 91] The blue line in Figure 1.15 shows the Connolly surface. The Connolly surface is accessible by physisorption and is defined by a point on the end of a spherical probe (blue circle in Figure 1.1) that is rolling across the surface.[88, 91] Lastly, the green line in Figure 1.15 represents the accessible surface which is determined by the middle of a spherical probe (green circle), of a certain size, that rolls over the surface. Connolly surface and the accessible surface are probe-size dependent, as shown by the different sized probes. Smaller probes will lead to larger surface areas and thus pore volumes. These definitions are outlined in the paper by Sarkisov et. al and are used in the computational program known as PoreBlazer.[91] This calculates structural properties of porous materials, and it will be outlined more in Chapter 2 as it is a vital part of this thesis project.[91]

1.4.3.2 Gas Adsorption Equipment and Adsorption Isotherms

Gas adsorption analysers are used to measure the gas uptake of porous materials, such as MOFs, and an example of such instrumentation, called a Quantachrome iQ2, can be seen in Figure 1.16 (right).

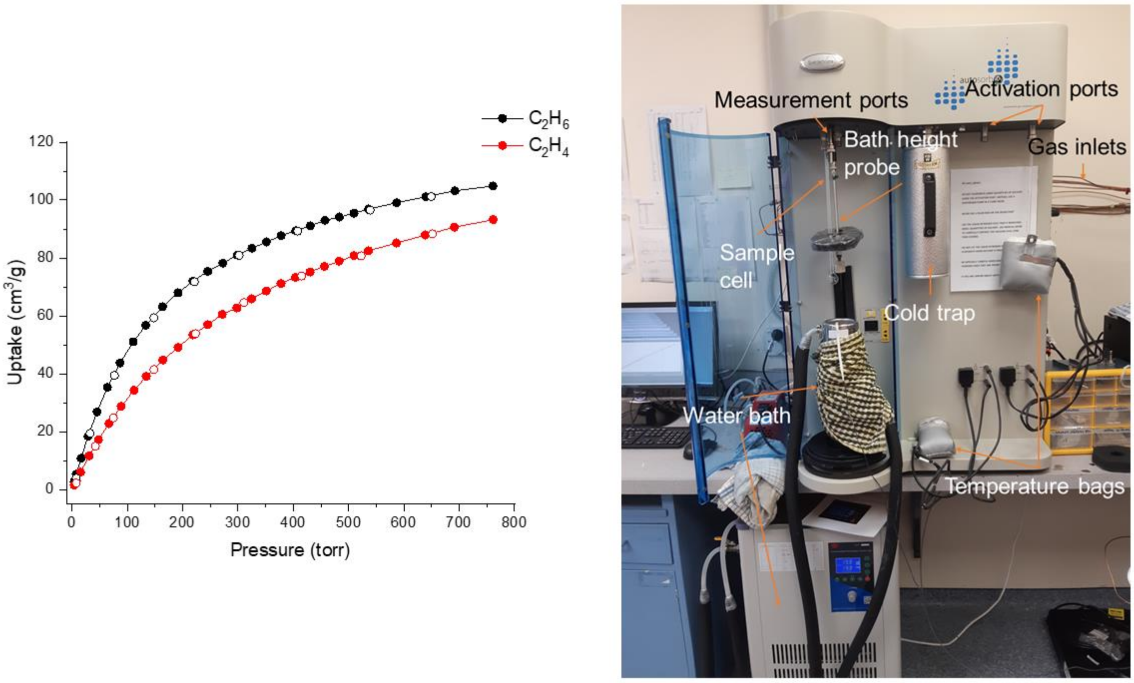

Figure 1.16 (Left) C_2H_6 (ethane) and C_2H_4 (ethylene) gas adsorption isotherms for MUF-15 at 293 K.[87] Coloured circles are adsorption points and open circles are desorption points. (Right) Annotated diagram of a Quantachrome iQ2 gas adsorption instrument.

The activation ports are where all solvent is removed from the MOF pores. This occurs under vacuum and at a chosen temperature. The sample cell/s are heated by the temperature bags. Once fully activated, the sample/s are moved to the measurement ports where they are kept at a chosen temperature by the water bath. On the measurement ports is where the MOF is exposed to the chosen gas and measurement takes place, hence its name. For measurement, the manifold of the instrument will dose a certain amount of gas into the sample cell. Using the ideal gas law, the expected gas pressure can be calculated.[88] This is compared to the measured pressure and the difference in pressure is used to calculate uptake. This pressure difference is due to the adsorption of gas by the MOF. The amount adsorbed by a certain mass of material is dependent on the equilibrium pressure and the temperature, thus resulting in an adsorption isotherm, which is a graph of successively increasing gas pressure versus the uptake of the MOF (at a certain temperature).[88, 89] This is main method used to display the uptake of a gas by a MOF or other porous material. An example of a typical isotherm for a MOF can be seen in Figure 1.16 (left) with MUF-15 being used as a case study.[87]

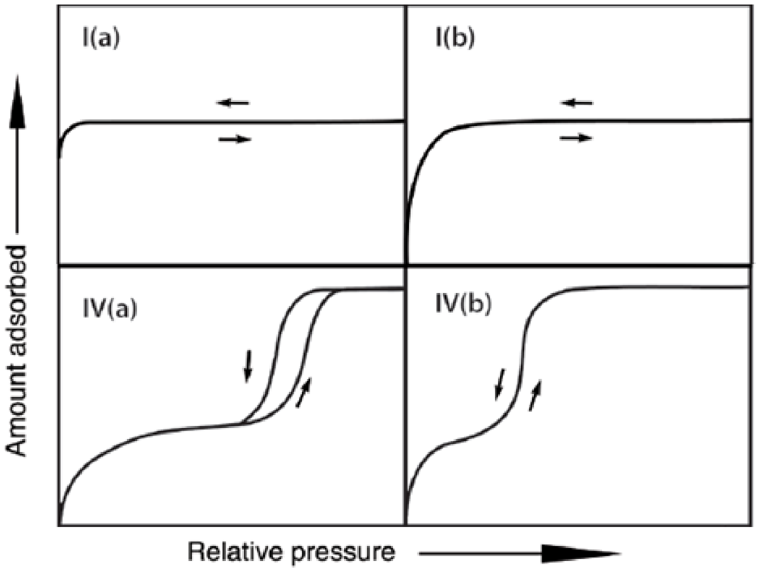

Figure 1.17 Main types of gas sorption isotherms in MOFs. Figure adapted from IUPAC gas sorption guidelines.[88]

IUPAC has classified six types isotherms, named I through VI, which can be applied to the gas uptake of a variety of porous materials.[54, 88, 89] Generally, the type of isotherm displayed is dependent on the pore size of the material however, MOFs do not strictly follow this pattern as most MOFs display either Type I or Type IV isotherms. Type I isotherms are reversible, concave in regard to pressure, and the amount adsorbed reaches a plateau of saturation. Materials with these types of isotherms generally have strong interactions between the adsorbate and the adsorbent and a decrease in the pore width results in a higher adsorption energy and a decrease in the pressure at which the pores are filled.[88-90] Type IV isotherms, which are also known as stepped isotherms, have an initial concave region which corresponds to monolayer coverage then the inflection to the quasi-linear and convex regions which corresponds to multilayer coverage reaching a saturation plateau. The difference between Type IV(a) and Type IV(b) is that the former displays hysteresis, which is where the adsorption and desorption curves do not match.[54, 88, 89] Hysteresis in MOFs is generally not ideal. Hysteresis in MOFs can be due to slow diffusion or a framework shift. Stepped isotherms are generally associated with changes to the framework structure, which result in changes in uptake such as a pore opening wider to accommodate more gas.[92, 93]

1.4.3.3 Isosteric Heat of Adsorption (Q_{st})

The isosteric heat of adsorption, denoted Q_{st}, is a measure of the change in enthalpy (heat released) when an adsorbate is adsorbed to a surface from the bulk phase.[94, 95] Q_{st} is dependent on the binding strength of an adsorbate and adsorbent, thus a larger Q_{st} value means that more gas will be adsorbed to the surface, at a given pressure, and thus that gas has a strong affinity to the surface.[24, 95] Furthermore, Q_{st} can be used to determine the regeneration energy which is the energy required for desorption.[95] Q_{st} can be determined by using either direct calorimetry or by using adsorption isotherms for the same gas at two or three different temperatures.[94, 95] For this thesis, we will use the latter method. These temperatures should ideally be no more than 20 K apart as a larger difference will introduce errors.[95] Q_{st} is dependent on gas loading, as the surface coverage of the material plays a role in the Q_{st} value for that specific loading, thus Q_{st} is often plotted against uptake.[95]

In practice, a virial fitting is applied to the isotherms, using the following equation:

$$lnP = lnN + \frac{1}{T}\sum_{i=0}^{m} a_i N^i + \sum_{i=0}^{n} b_i N^i \qquad \textbf{Eq. 1}$$

where N_i is the adsorbed amount and a_i and b_i are virial coefficients. Generally, the more parameters used, the better the virial fit to the data. The closer the R^2 value is to 1, the better the fitting. Following this, an integrated version of the Clausius-Clapeyron equation is used to calculate Q_{st} [94, 95]:

$$Q_{st} = -R\sum_{i=0}^{m} a_i N^i \qquad \textbf{Eq. 2}$$

where R is the universal gas constant, a_i is the virial coefficient from Eq. 1, and N_i is the adsorbed amount. The Clausius-Clapeyron equation has two assumptions; the first being that the unabsorbed gas displays ideal behaviour, and the second being that the molar volume of the adsorbed species is negligible.[95] There is also the assumption that Q_{st} will not change over a sufficiently narrow temperature range i.e. within 10 to 20 K.[95]

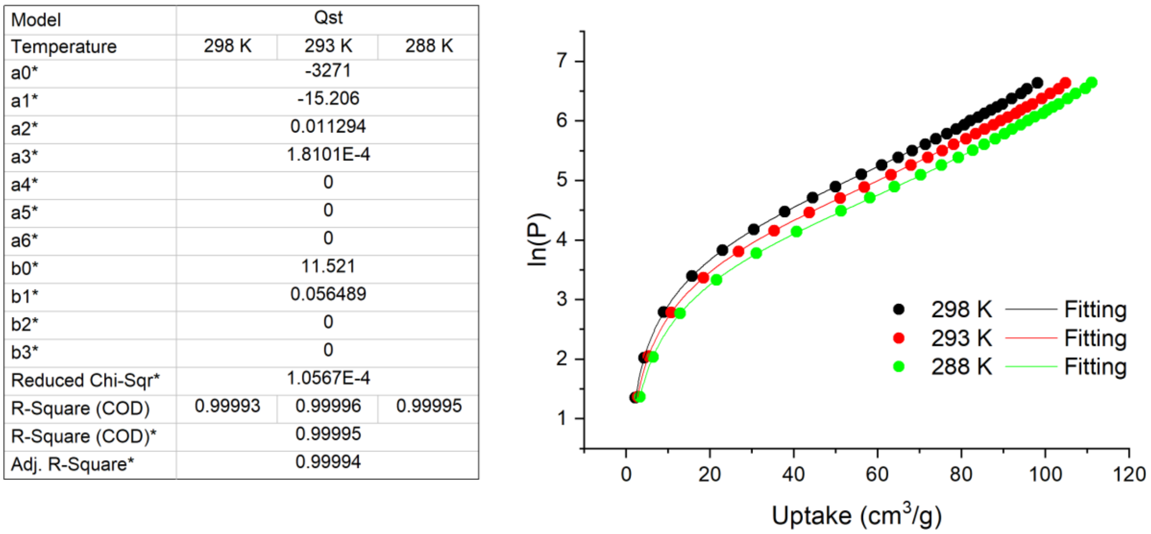

Model	Qst		
Temperature	298 K	293 K	288 K
a0*	-3271		
a1*	-15.206		
a2*	0.011294		
a3*	1.8101E-4		
a4*	0		
a5*	0		
a6*	0		
b0*	11.521		
b1*	0.056489		
b2*	0		
b3*	0		
Reduced Chi-Sqr*	1.0567E-4		
R-Square (COD)	0.99993	0.99996	0.99995
R-Square (COD)*	0.99995		
Adj. R-Square*	0.99994		

Figure 1.18 Virial equation fittings for ethane isotherms of MUF-15 at three temperatures: 298, 293 and 288 K.

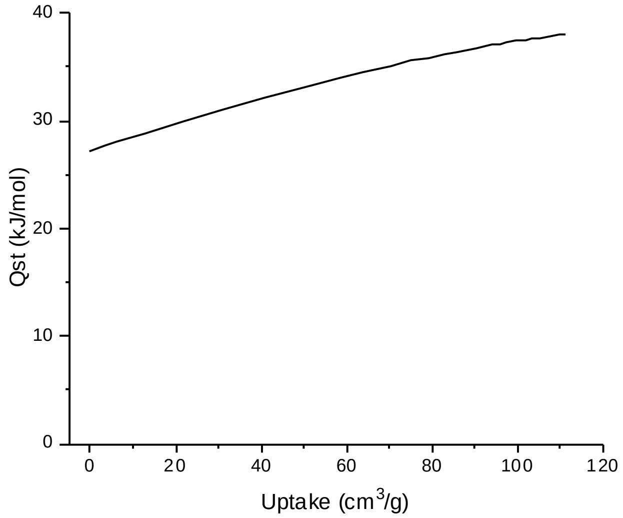

Figure 1.19 Isosteric heat of adsorption plot for ethane for MUF-15.

MUF-15 can be used as a case study for calculating Q_{st}. As previously mentioned, the data is fitted using a virial equation at two or more temperatures, as seen in Figure 1.18. Four a_i parameters and two b_i parameters were used, and their values can be seen in the table in Figure 1.18. The R^2 value is 0.99995 which shows that the virial fitting is a very good fit. The a_i coefficients are then be used to calculate Q_{st} using Eq. 2. This is then plotted as a function of uptake (Figure 1.19). Q_{st0} can also be determined, which is the isosteric heat of adsorption for the initially adsorbing gas molecule (zero coverage). In Figure 1.19, the Q_{st} trend is positive with an increasing uptake, however, Q_{st} usually has a negative trend. This is because the sites on the surface with the highest affinity will be filled first (at low pressures).[24, 95] A positive trend suggests that the MOF may be flexing, initial gas uptake promotes cooperative gas adsorption, or new binding sites are created once some gas has adsorbed to the surface.[24]

1.4.3.4 Ideal Adsorption Solution Theory (IAST)

The Ideal Adsorbed Solution Theory (IAST) was first introduced in 1965 by Myers and Prausnitz.[96, 97] The theory is based on the assumptions that the adsorbent is thermodynamically inert and homogenous, all adsorptive molecules have equal access to the adsorbent, that the adsorbed phase acts as an ideal solution, and that two gases in a mixture behave the same way they would in a pure form.[24, 96, 97] For MOFs, IAST is used to determine the selectivity (preference) of a MOF material for the adsorption of one gas over another. IAST can be calculated using pure component isotherms for different gases to predict the amount of each gas species adsorbed onto the surface when in equilibrium with a gas mixture.[98] It is assumed that temperature remains constant and that the pure component isotherms are measured at the same temperature.[98]

In practice, the gas isotherms are fitted accordingly by an appropriate model, such as the Henry or Langmuir (single site or dual site) models, as seen in Eq. 3 to Eq. 5. In some circumstances, the Langmuir-Freundlich (single site or dual site) model can be used, which contains an exponential on the pressure term. The equations for these isotherm fittings are as follows, where y is the excess gas uptake (in cm^3/g), P is the equilibrium pressure (kPa), k is the Henry constant, and b and q are dependent on the isotherm.[94, 98, 99] The q parameter is the uptake at saturation.

Henry isotherm:

$$y = kP \qquad \textbf{Eq. 3}$$

Single-site Langmuir (SSL) isotherm:

$$y = \frac{qbP}{1 + bP} \qquad \textbf{Eq. 4}$$

Dual-site Langmuir (DSL) isotherm:

$$y = \frac{q_1 b_1 P}{1 + b_1 P} + \frac{q_2 b_2 P}{1 + b_2 P} \qquad \textbf{Eq. 5}$$

After fitting, the q, b, and t values are put into the IAST software package which performs differential equations to ultimately produce the IAST selectivity, S, of a gas pair (named 1 and 2) by the following equation:

$$S = \frac{q_1/q_2}{p_1/p_2} \qquad \textbf{Eq. 6}$$

where q_1 and q_2 are the molar loadings of the adsorbed gases and p_1 and p_2 are the partial pressures of gases 1 and 2 in the feed gas stream.[99] The higher the value of S the more selective an adsorbent is towards a certain gas.

Whilst IAST is the best method for determining selectivity in MOFs, it is highly dependent on the isotherm fittings (Eq. 3 to Eq. 5).[98, 100, 101] A wrong fitting can result in inaccurate IAST values, as can situations where the IAST assumptions are no longer valid, such as molecular sieves, flexible MOFs or those where the adsorbates distribute themselves unevenly within the pores.[98, 101] Therefore it is paramount to be careful with fittings and to use the best model for an isotherm to ensure correct IAST values. For this reason, dual-site Langmuir (DSL) and single-site Langmuir (SSL) fittings will be used, ideally DSL. DSL seems to result in quite accurate IAST values.[102] DSL fittings will be performed first, then if it does not appear to fit the data well, SSL fits will be used. An example of a poor DSL fit would be if q_2 was abnormally low (< 1), thus moving to the SSL model would be best as the low q_2 is indicating that there is no need to model a second site. The numbers produced from the fittings will be closely analysed, as indicated above, to see if they look like reasonable values i.e. not very large or very small and have errors that are less than ≈ 10% of the value. This indicates that the model is appropriate, alongside a high R^2 value; the closer the R^2 value is to 1, the better the fit.

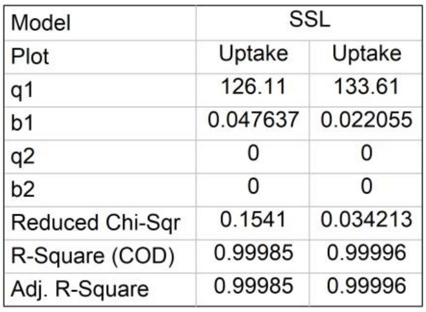

Model	SSL	
Plot	Uptake	Uptake
q1	126.11	133.61
b1	0.047637	0.022055
q2	0	0
b2	0	0
Reduced Chi-Sqr	0.1541	0.034213
R-Square (COD)	0.99985	0.99996
Adj. R-Square	0.99985	0.99996

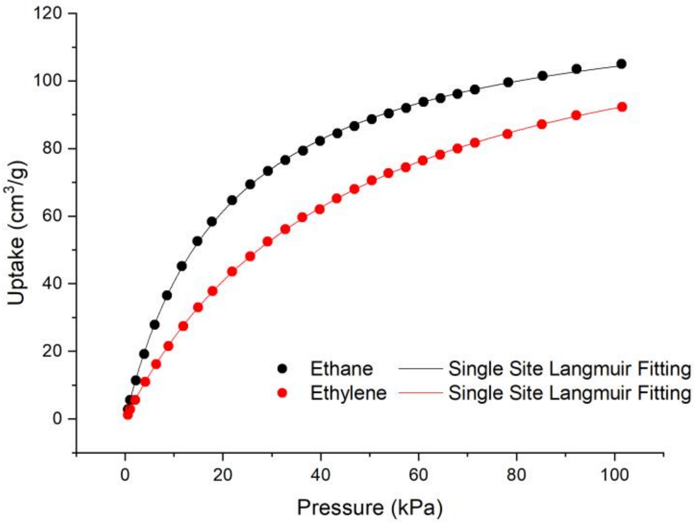

Figure 1.20 Single site Langmuir fits for pure component isotherms of ethane and ethylene for MUF-15 at 293 K.

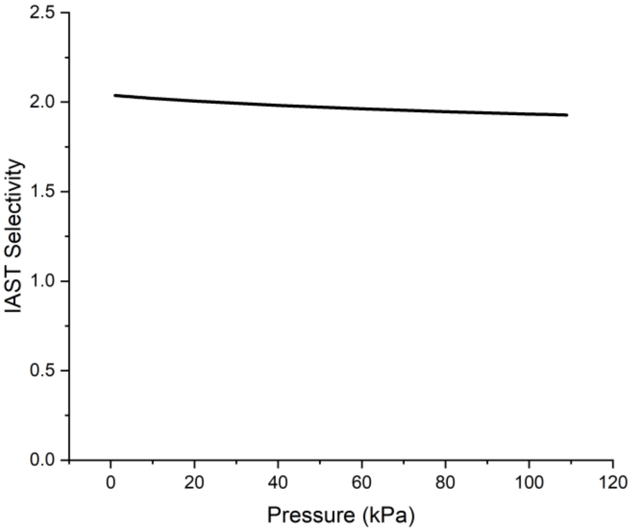

Figure 1.21 IAST selectivity as a function of pressure.

MUF-15 will again be used as a case study to show how IAST is calculated for a MOF. As mentioned earlier, MUF-15 is selective for ethane over ethylene therefore isotherms of these two gases at a certain temperature are used to show this selectivity. An SSL fitting (Eq. 4) is used to fit the data and it can be seen that the q1 and b1 values are reasonable as is the R^2 value. The values for *q*, *b* and *t* are then input into a software package that determines IAST. IAST is then plotted as a function of pressure (Figure 1.21).

1.5 MOFs Built Up Using Isophthalate Ligands

Isophthalic acid (H_2ipa) is a small ligand that has been used in the formation of thousands of MOFs, be it by itself, in a derivative form, or as a co-ligand in multicomponent MOFs. This section will introduce H_2ipa based MOFs and the three MOFs which became the ‘parents’ of this thesis project.

1.5.1 Background

Isophthalic acid (H_2ipa), otherwise known as 1,3-benzendicarboxylic acid, consists of a benzene ring and two carboxylate groups at the 1’ and 3’ positions.[103] This ligand has been used in many MOFs as it can create a range of diverse structures, especially when substituents are placed in the 5′ position or this ligand is used as a co-ligand. According to the Cambridge Structural Database (CSD), there are just under 9,000 MOFs containing the H_2ipa motif. The H_2ipa ligand commonly creates structures with zig-zag or wave-like channels, however it can form other structures such as helical or herring-bone structures.[103-

[105] Compared to many of the ligands used in MOF formation, H_2ipa is a small ligand therefore the MOFs that are made can be classified as microporous or ultra-microporous. The ligand can also coordinate in a variety of ways through either both oxygen atoms of the carboxylate group or only one, through bridging modes, non-bridging modes, and bidentate chelating modes, as seen in Figure 1.22.[103, 106, 107]

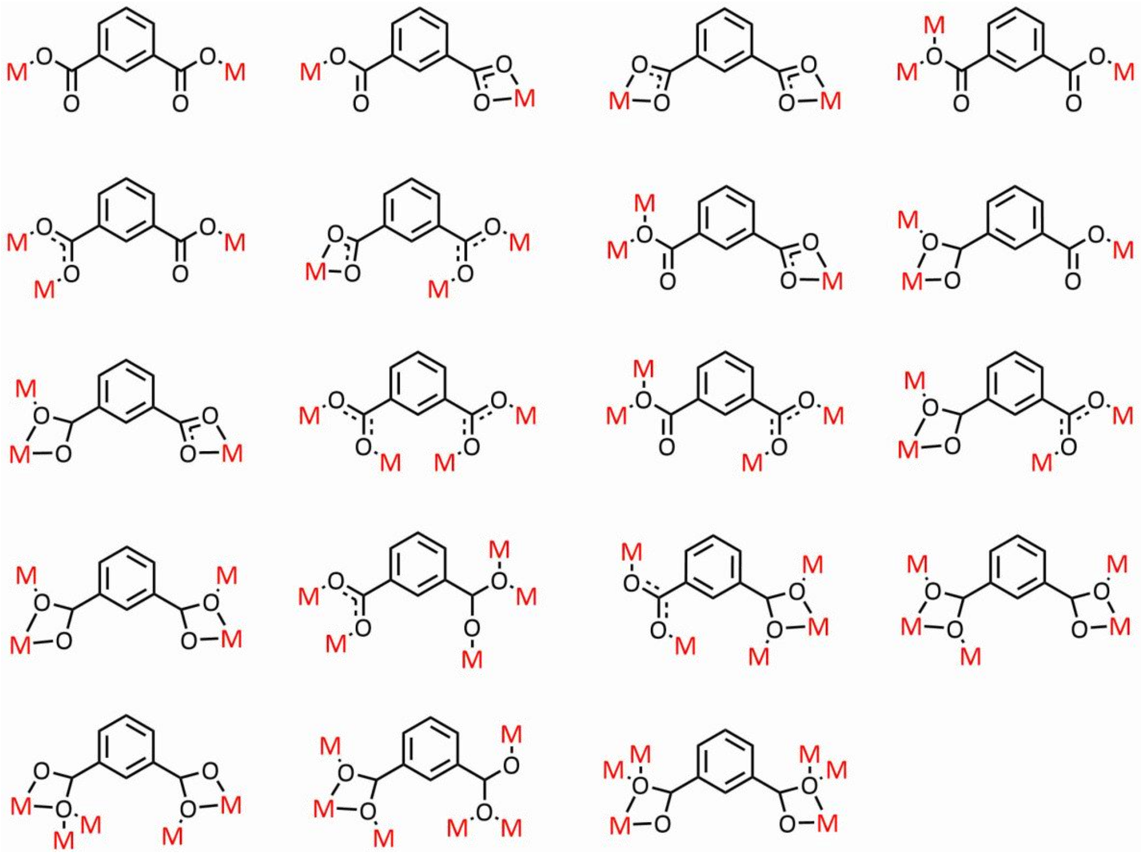

Figure 1.22 Various bridging modes for the isophthalate ligand where M is a metal centre. Figure adapted from Gonçalves et. al.[103]

The 5′ position can be substituted with functional groups, such as F, Cl, I, Br, OH, NO_2, NH_2, CH_3, OCH_3, CN, SO_3, and PO_3H, to create ipa derivatives.[103, 108-110] The functional groups would affect MOF formation due to their size (and therefore steric effects), polarity or ability to interact with nearby groups, such as through hydrogen bonding or van der Waals interactions. These groups would impact pore size, shape, and environment which would in turn impact the application of such MOFs.

These H_2ipa ligands are useful as they can be used to make single-ligand MOFs (as will be the focus of this thesis), or they can also be used to create multicomponent MOFs with other ligands.[104-109] They can be used as spacers or pillaring agents. This ligand can also coordinate to a range of metal ions, which further increases the number of possibilities of

MOFs available to be formed. The most common metal ions used are Zn^{2+}, Co^{2+}, Cd^{2+}, Cu^{2+}, and lanthanide ions (such as Er^{3+}, Dy^{3+} or Ho^{3+}), however, there are some examples of main group metals, such as Mg^{2+} and Al^{2+}.[103, 111-113] There are also a few examples of heterometallic ipa derivative MOFs containing transition metals and/or alkali metal ions.[114-116] Combining the range of 5′ derivative ligands with the range of coordination modes, possible metals that ipa ligands can coordinate to, and the range of possible pore structures, there are a large number of H_2ipa-based MOFs that can be made. Furthermore, MOFs formed with pure H_2ipa ligands are likely to be ultra-microporous, which suggests that these MOFs could be useful for gas separation purposes as the pore sizes would be on par with the sizes of gases. Functionalization of the 5′ position of such MOFs would potentially change the gas adsorption characteristics, providing interesting aspects for research.

When discussing this ligand, there are three forms of the name which will be used throughout this project. As introduced above, H_2ipa will be used when discussing the doubly protonated form (isophthalic acid). When only one carboxylate group is protonated, then the ligand will be referred to as Hipa, and when neither group is protonated (isophthalate), the ligand will be called ipa. When discussing the various 5′ derivatives of H_2ipa, the same nomenclature will be used alongside the name of the functional group, which will be attached to the end. For example, 5-aminoisophthalic acid would be called H_2ipa-NH_2 and the isophthalate version would be called ipa-NH_2.`

1.5.2 Project Parent MOFs: MUF-15, MUF-16, and MUF-17

Recently published from our group, are three ipa MOFs with good separation abilities. These MOFs are known as MUF-15, MUF-16, and MUF-17 (MUF = Massey University Framework).[6, 78, 79, 87, 117, 118] These MOFs display different gas uptakes and separation abilities which is interesting as they are all based around the same H_2ipa parent ligand.

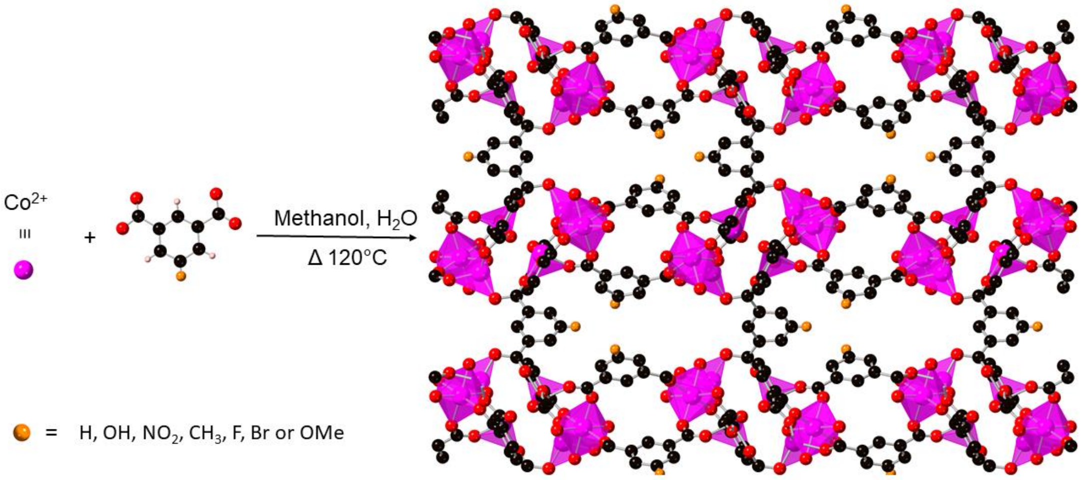

Figure 1.23 Precursors and structure of MUF-15. Atom colours: carbon: black, oxygen: red, hydrogen: peach, cobalt: magenta, and 5′ substituents: orange. Hydrogen atoms omitted from the structure for clarity.

MUF-15, as mentioned in the case study in section 1.4.3, is selective for ethane over ethylene. The MOF is made of Co^{2+} hexanuclear clusters, with the oxygen atoms coming from the carboxylate groups on the ipa ligands and from coordinated water molecules.[87] These clusters are linked together by the ipa ligands resulting in zig-zag shaped one-dimensional channels, with different sized apertures of 8.5 x 3.5, 7.0 x 3.8 and 3.2 x 1.2 Å.[87] The structure of MUF-15 can be seen in Figure 1.23. MUF-15 has a relatively high uptake (for a small pore MOF) of both ethane and ethylene, of 105 cm^3/g and 93 cm^3/g respectively, at 293 K and 1 bar.[87] The IAST selectivity for MUF-15 for a 50/50 mixture of ethane and ethylene is around two. This, combined with its uptake, is very good and comparable to other ethane selective MOFs.[87, 119, 120] The 5′ position of the ipa ligands points toward the middle of the pores, thus making this position ideal for functionalization with different substituents such as hydroxyl, nitro, methyl, fluoro, bromo or methoxy groups (Figure 1.23).[79, 118] This creates a family of MUF-15 MOFs that are very similar to each other. They all share the Co^{2+} hexanuclear cluster, however the ligand arrangement differs slightly between the MOFs.[79] Comparing them all to MUF-15, MUF-15-F is isoreticular, MUF-15-Br and MUF-15-CH_3 are supramolecular isomers, and MUF-15-OMe is a topological isomer.[79, 118] The structure of MUF-15-OH and MUF-15-NO_2 could not be determined, due to their lack of stability, thus their exact structural relationship to MUF-15 is not known. In this series, the functionalization of the ligands changes their gas uptakes and the gases they ‘prefer’ i.e. have a higher uptake of.[79] This indicates that the functional group on the ligand influences gas uptake. Furthermore, the functional group can induce the flexibility. MUF-15-NO_2 shows slight flexibility for CO_2 and ethane uptake and MUF-15-OMe shows significant flexing for CO_2, acetylene, ethane and ethylene.[79, 118] This indicates that gas uptake pries the framework into a more open form to take up more gas, resulting in a jump in uptake in the gas adsorption isotherm.[118]

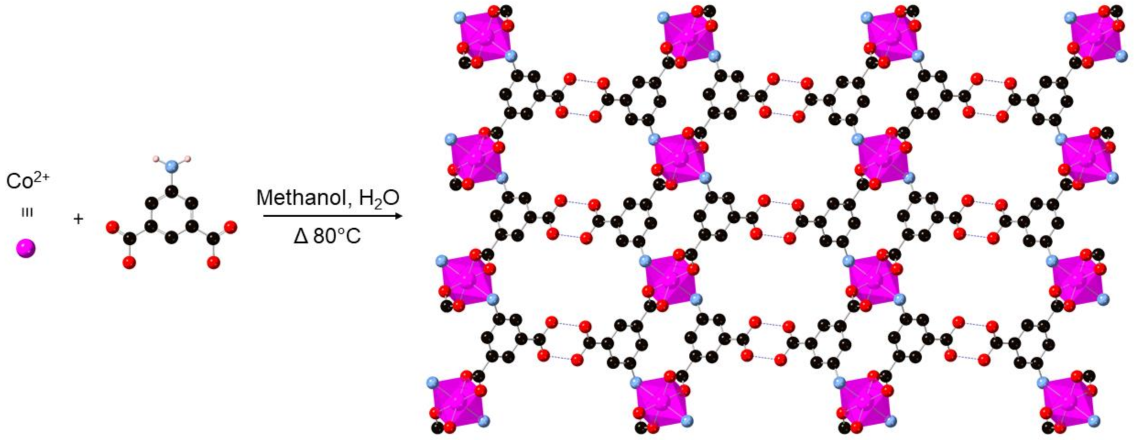

Figure 1.24 Precursors and structure of MUF-16 (Co). Atom colours: carbon: black, oxygen: red, hydrogen: peach, nitrogen: periwinkle blue, and cobalt: magenta. Hydrogen atoms omitted from structure for clarity.

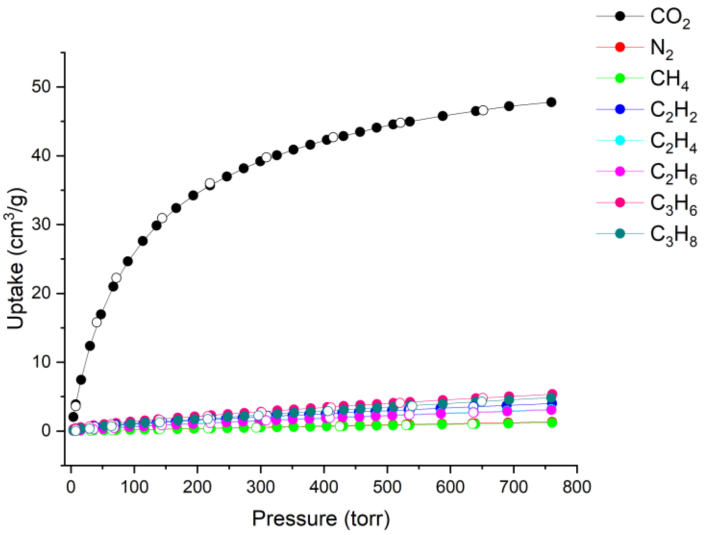

Figure 1.25 MUF-16 (Co) adsorption isotherms at 293 K.

MUF-16 is made from 5-aminoisophthalic acid (H_2ipa-NH_2). MUF-16 can contain either Co^{2+}, Mn^{2+}, or Ni^{2+} metal centres. The metal ions adopt an octahedral geometry with two nitrogen atoms coming from a ligand amino group, arranged trans to each other, and four oxygen atoms from the carboxylate groups which are arranged equatorially to the nitrogen donors.[6] The metal ions are aligned in a one-dimensional chain, and the Hipa-NH_2 ligands connect these chains together into two-dimensional sheets.[6, 117] These sheets are then grown into a three-dimensional framework by the hydrogen bonding between carboxylate groups on adjacent layers. The structure of MUF-16 (Co) can be seen in Figure 1.24. The resultant framework has one-dimensional channels of 3.6 x 7.6 Å.[6, 117] These channels are the perfect size to accommodate small gas molecules, such as CO_2, of which this framework is highly selective for, as evidenced in the isotherms in Figure 1.25. MUF-16 (Co) has an uptake of 48 cm^3/g for CO_2 (at 293 K and 1 bar).[6] This is a significantly higher uptake than all other gases exposed to MUF-16 (Co), which have uptakes between 1.2 cm^3/g (for methane) and 5.4 cm^3/g (for propene).[6]

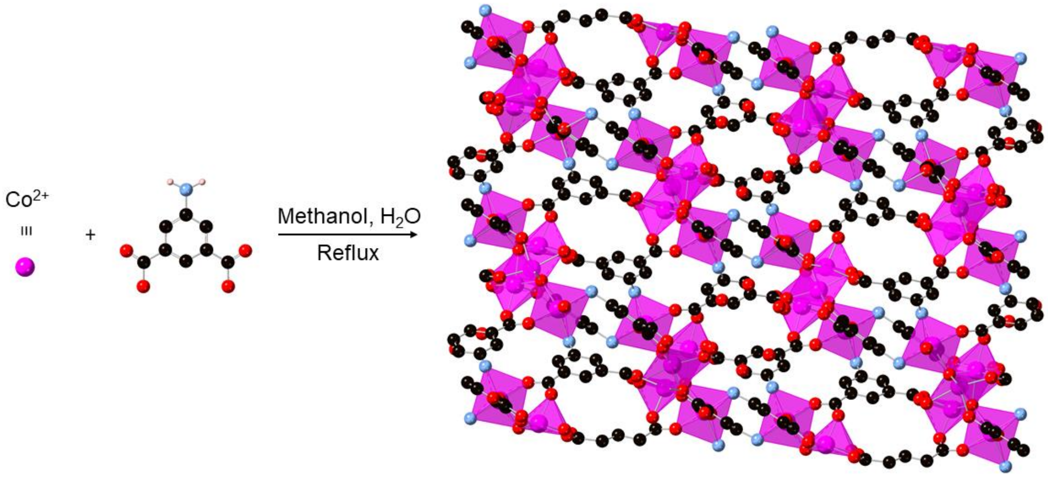

Figure 1.26 Precursors and structure of MUF-17. Atom colours: carbon: black, oxygen: red, hydrogen: peach, nitrogen: periwinkle blue, and cobalt: pink. Hydrogen atoms omitted from structure for clarity.

The third MOF in this series is called MUF-17. This MOF is made up of pentanuclear clusters containing five Co^{2+} ions, bridging OH groups, coordinated water molecules and the oxygen and nitrogen atoms from the carboxylate and amino groups, respectively, on the ipa-NH_2 ligands.[78] The clusters act as 12-connected nodes, which are connected through ipa-NH_2 ligands, and expand outward to form zig-zag shaped one-dimensional channels. The structure is seen in Figure 1.26. These channels contain large cavities with an aperture size of 4.7 x 4.8 Å, which are connected though narrower channels of 3.1 x 3.5 Å.[78] MUF-17 is selective towards acetylene in the presence of CO_2 and ethylene, with an uptake of 112 cm^3/cm^3 for acetylene, compared to 93 cm^3/cm^3 for CO_2 and 79.70 cm^3/cm^3 for ethylene, at 293 K and 1 bar.[78]

1.5.3 Project Outline and Aims

As introduced, the H_2ipa ligand, both 5′ functionalized and in its original state, is a highly versatile ligand which can create a wide variety of MOFs which have differing structures. Furthermore, MUFs 15-17 showed that MOFs based off the H_2ipa ligand can have good gas uptakes and selectivities. This resulted in the birth of this project; to use the H_2ipa ligand, in either its original form or 5′ functionalized form, to make a range of MOFs with good gas uptakes and selectivities for different key gas pairs. The aim of this project is to target MOFs which have already been reported in the literature but have not been subjected to gas adsorption analysis. In practise we know that following literature procedures will often lead to new MOF phases, which is the other aim of this project; to investigate any new phases that are discovered over the course of this project. Chapter 2 will outline the entire methodology of this project, while Chapter 3 will mainly discuss the results of using known MOFs for gas adsorption analysis. Chapters 4 and 5 will discuss most of new MOF phases that were discovered, and finally, Chapter 6 will conclude the project and introduce any future work.

Chapter 2 – Selecting MOFs for Synthesis and Analysis

2.1 Introduction

As stated in Chapter 1, this chapter will discuss the entire methodology of this project. PoreBlazer formed a vital part of this thesis work as it was used to determine and give a starting point for which H_2ipa derivative MOFs would be explored for this project. This chapter will outline how PoreBlazer works, including the property information it produces and how it was used to determine which MOFs will be of interest for this project. Then this chapter will show which MOFs of interest have been chosen as a starting point and it will outline the synthetic and analytic methodology of this project.

2.2 PoreBlazer

Computer simulations are useful in the analysis of MOFs as they can provide a lot of information into the structure and properties of a MOF. PoreBlazer, developed by Sarkisov and Harrison, is the first simulation package of its kind for the computational characterization of both crystalline and amorphous materials, ordered or disordered.[91, 121] The code used by PoreBlazer is a Fortran 90 code which is based on a grid/lattice representation of the porous space.[91, 121] PoreBlazer gives information about the pore volume, largest cavity diameter (LCD), pore limiting diameter (PLD), accessible surface area (ASA), network percolation and a few other parameters, some of which will be outlined in detail further in this section.[91, 121] There are other computational simulation packages besides PoreBlazer such as ZEOMICS, MOFomics, Zeo++, RASPA, and PorosityPlus which use different approaches and interfaces to calculate the same kinds of properties as PoreBlazer.[91, 121]

The algorithm that PoreBlazer uses to calculate structural properties is made up by dividing the porous material system into cubelets. One of the first calculations determines the distances between the middle of each of the cubelets and the middle of each of the atoms. This lattice of cubelets is used to determine all the structural properties via various algorithms, such as the following examples. To determine pore volume, a spherical probe must be able to sit in the centre of a cube and not have any overlap with a surface atom.[91] The percolation of a porous material is calculated using the Hoshen-Kopelman algorithm by determining a path that a spherical probe can take through the system without overlap of surface atoms.[91] To determine the accessible surface area, a Monte Carlo algorithm is used.

In this method, for each atom, points are generated at random around the atom surface. Each point is tested to see if it is within a collision distance from any other atom; if it is not, then that point is part of the accessible surface.[91]

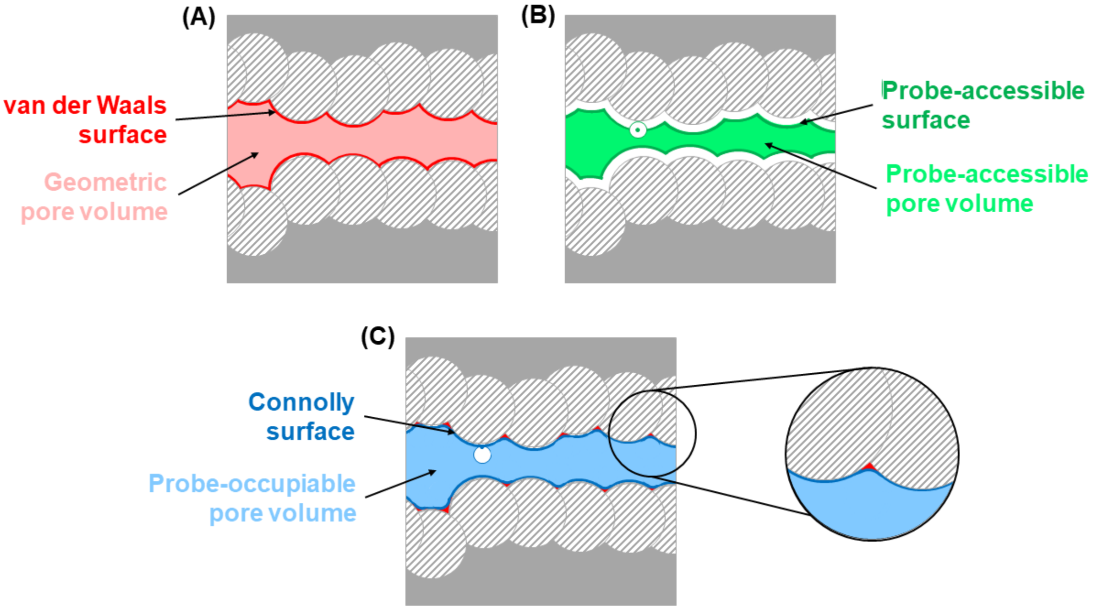

Figure 2.1 Schematic depicting the types of surfaces and pore volume definitions on an adsorbent. (A) van der Waals surface and geometric pore volume. (B) Probe-accessible surface and probe-accessible pore volume. (C) Connolly surface and probe-occupiable pore volume. The striped circles represent the surface atoms, and the dark grey is the bulk of the adsorbent, with the gap between the striped circles representing a horizontal channel. [88, 91] Figure adapted from Sarkisov et al.[91]

The pore volume and surface area calculated by PoreBlazer must be strictly defined. The surface of a solid can be defined in three different ways: the van der Waals surface, the probe-accessible surface, and the Conolly surface, each of which have corresponding pore volume definitions (Figure 2.1).[88, 91] The definitions of the three surfaces can be found in Chapter 1, section 1.4.3.1 and in Figure 1.15. The red shaded area in Figure 2.1A corresponds to the geometric pore volume, which is the space enclosed by the van der Waals surface (red line) and is accessible to a minute point probe.[91] The volume enclosed by the probe-accessible surface (green line) is known as the probe-accessible pore volume, as shown by the green shaded area in Figure 2.1B, as it is accessible to a probe of that specific size.[91] Lastly, the volume enclosed by the Connolly surface (blue line), as shown by the blue shaded area in Figure 2.1C, is the probe-occupiable pore volume which corresponds to the volume that the spherical probe can occupy[91]. The size of both the probe-accessible and probe-occupiable pore volumes is dependent on the size of the probe used. For the PoreBlazer calculations, a nitrogen probe is used (radius of 2.8 Å), and the ASA value produced is the accessible surface area (green) mentioned in Figure 2.1B. PoreBlazer also reports the geometric pore volume as shown by the red shaded region in Figure 2.1A.

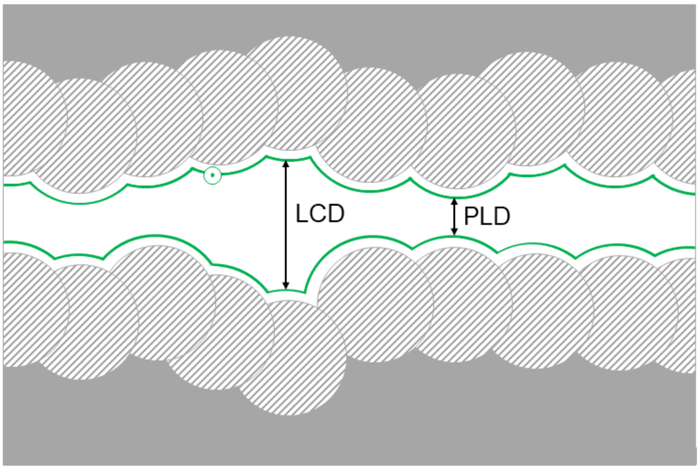

Figure 2.2 Schematic depicting the largest cavity diameter (LCD) and the pore limiting diameter (PLD). The green line depicts the probe-accessible surface.

Two more important properties calculated by PoreBlazer are largest cavity diameter (LCD) and pore limiting diameter (PLD). The largest probe that can cross the porous material in at least one dimension in a continuous pathway is known as the PLD (Figure 2.2).[91] The largest pore in the material is known as the LCD (Figure 2.2).[91] PoreBlazer appears to use the van der Waals surface to calculate PLD and LCD as changing the probe radius does not influence the PLD and LCD values.

PoreBlazer works by inputting several files into a folder within the program then using a run batch (run.bat) file which contains the code to calculate the structural parameters. The files required by PoreBlazer are as follows[91, 122]:

1. Defaults.dat file. This is provided by the PoreBlazer package and contains information about:
    a. The default universal force field (UFF) used.
    b. The helium atom sigma (Å) and epsilon (K) values, alongside the nitrogen atom sigma (Å), and the temperature (K).
    c. The cut-off distance (Å) and the number of trials performed for a surface area calculation.
    d. Cubelet size (Å).

   e. The anticipated size of the largest possible pore diameter and the bin size for the pore size distribution (PSD), both in Å.
   f. Random number seed.
2. UFF.atoms file. This is also provided by the PoreBlazer package and contains values for the diameter (Å), epsilon (K) and molecular weight (g mol^{-1}) of 98 elements.
3. xyz file. This was made using Olex2 for each MOF based on the cif file. This file contains the x, y, z coordinates for the atoms in the MOF structure. The files were edited so that no solvent was present in the pores.
4. input.dat file. This is different for each MOF. It requires the name of the MOF xyz file, followed by the a, b, c unit cell lengths (Å), and ending with the α, β, γ unit cell angles (°).
5. run.bat file. This performs the calculations.

Once all five files are in a folder within PoreBlazer, clicking on the run.bat file starts the calculations. Once completed, a results.txt file is created which contains all of the parameters that PoreBlazer calculates, alongside pore size distribution (PSD) files for MOFs that are deemed porous

2.3 Results and Discussion

Due to the large number of H_2ipa and H_2ipa derivative MOFs that can be made, it was paramount to devise a way to sort through all the MOFs to find a starting point. This resulted in the following method for this thesis project. This method can be visualized in Figure 2.3. Steps 1 to 3 were completed by me before the official commencement of this project.

1. The CSD was searched for MOFs containing ipa or its 5′ derivatives. A MOF subset was used so only MOF structures came up as results. The structure of ipa, and its 5′ derivatives was input into the search engine and any MOFs with that motif came up as results. The search parameters were refined so that the MOF contained ipa itself and not the ipa motif as part of a larger ligand. There were around 9,000 results of MOFs containing the ipa ligand however, these were further narrowed down using parameters such as not allowing a metal to nitrogen bond (which eliminated many frameworks with co-ligands). This parameter did not work for ipa-NH_2, however as the amine can coordinate to metals, ergo this parameter could not be used for ipa-NH_2. Furthermore, certain 5′ (R) functional groups were searched such as R = H, N, O, S, P or more specifically, CH_2OH or a halogen, which further narrowed down the results.

2. 507 MOFs were found in Step 1 and were compiled in an Excel spreadsheet and sorted according to their R groups. For each MOF, the CCDC (Cambridge Crystallographic Data Centre) code, CCDC deposition number, journal name, publication year, DOI, metal centre, formula, and density were collected alongside whether or not the paper analysed the sorption properties of the MOF. For each MOF, the cif file and paper was collected and saved.
3. All 507 MOFs were input into PoreBlazer to calculate the PLD, LCD and ASA. A nitrogen probe was used for the calculations. Only 12 MOFs produced no PoreBlazer data. For some, this was because the atoms they contained were not present in the UFF.atoms file, such as iodine or lithium, and the others did not run for unknown reasons.
4. Two lists were formed as starting points for this thesis project. They were known as the ‘Priority List’ and the ‘Larger Pore List’.
    a. MOFs with similar PLD, LCD and ASA values to MUF-15, MUF-16, and MUF-17 were collated. There were around 50 MOFs total. This list was narrowed down by choosing MOFs with more straightforward syntheses or those which contained metals that were already available in our laboratory, such as Zn^{2+} or Co^{2+}. MOFs that contained more exotic metals, such as V or Np, and/or hazardous metals, such as Cd or U were ruled out. This resulted in a shorter list which was nicknamed the ‘Priority List’ as it was a list of MOFs that were the starting point for this project. Majority of these MOFs have PLD and LCD values that are similar to MUF-16 as this MOF has the best separation ability out of the three parent MOFs. This list is found in Table 2.1.
    b. The ‘Larger Pore List’ was formed by collating MOFs which an LCD > 6 Å i.e. pore sizes greater than MUF-15, MUF-16, and MUF-17, hence the nickname ‘Larger Pore’. These MOF pores are still quite small as they are ≤ 10 Å thus we expect they may have good separation performance. From there, the synthetic protocols were analysed with the same criteria as in step 4a to narrow down the list. This list is found in Table 2.2.
5. Synthesis attempts of MOFs in first the ‘Priority List’ then in the ‘Larger Pore List’ were made. There are three possible outcomes of this step:
    a. The MOFs cannot be synthesized.
    b. The desired MOF was made.
    c. A different MOF was made.

For the latter two outcomes, the MOF needed to be made in pure phase and in a sufficient amount (> 30 mg) to move on to step 6.

6. Gas sorption was performed on the MOFs to test their uptake and thus separation abilities. The MOF would be screened for a range of gases, including CO_2, N_2, CH_4, acetylene, ethane, ethylene, propane, propylene, Xe, and Kr. Within this step, there are two possible outcomes:
    a. Good gas sorption. This would include modest to high uptakes and good separation between one or more key gas pairs.
    b. Poor gas sorption. This would include low gas uptakes and/or poor separation, which is indicative of low porosity.

   Following gas sorption, Q_{st} would be calculated for gases with a high uptake and IAST would be calculated for key gas pairs that showed good differences in uptake.

Further characterization was performed on successful MOFs, such as stability tests, thermogravimetric analysis (TGA), and single crystal X-ray diffraction (for new MOFs).

Whilst this project starts with synthesizing previously published MOFs, new MOFs are still being looked out for, as mentioned in the stepwise methodology (step 5c). If an unexpected phase showed up, it was investigated to see if it is porous. Even better if it is a new MOF. Furthermore, literature protocols were altered to try produce new phases or isoreticular families of MOFs by differing metals or ligand functional groups.

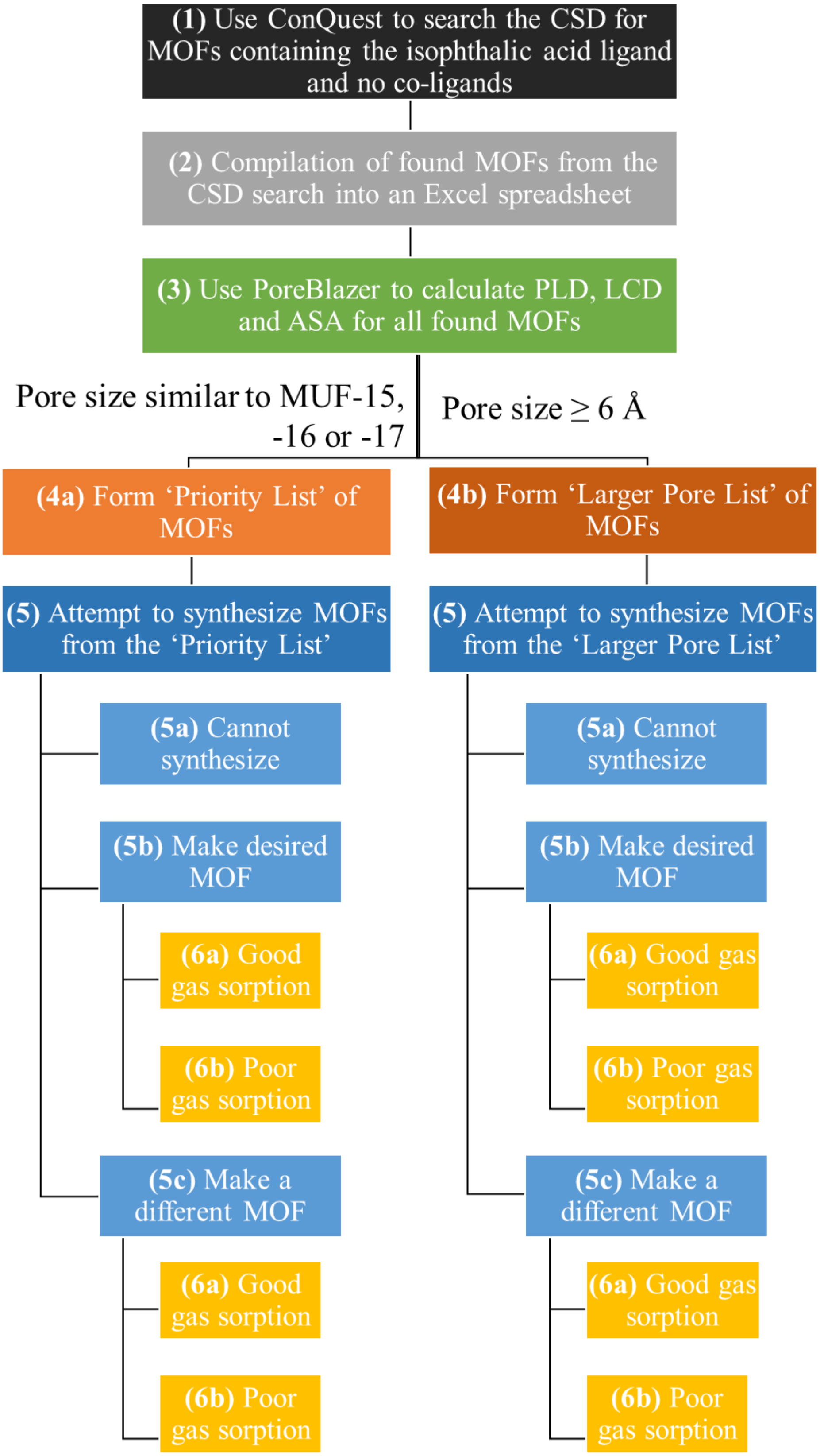

Figure 2.3 Flowchart describing the methodology of this thesis project from conception to synthesis to gas sorption. Each step has its own colour with blue being synthesis-related steps.

Table 2.1 PoreBlazer parameters for the ‘Priority List’ MOFs including the parameters calculated for MUFs 15, 16, and 17 for comparison.

CCDC Code	Metal Centre	R=?	Year	LCD (Å)	PLD (Å)	ASA (m^2/g)	Ref
MUF-15	*Co*	*H*	*2019*	*5.07*	*3.23*	*432*	[87]
NAGKOY	Zn	NO_2	2016	5.43	3.96	423	[123]
XADDOX	Co	H	2010	5.85	3.43	725	[124]
HOMQEI	Cu	OH	2019	4.72	3.34	374	[125]
TOWLOI	Fe	H	2014	4.87	2.44	-	[126]
MUF-16	*Co*	*NH_2*	*2020*	*3.47*	*2.74*	*0*	[6]
JETJOI	Zn & Na	H	2005	3.45	2.73	0	[115]
ACOHUW03	Mn	NH_2	2012	3.54	2.34	-	[127]
TILHEC	Co & Na	H	2007	3.32	2.75	0	[128]
LARPIF	Fe & Na	H	2012	3.29	2.73	0	[129]
SABXEB	Co & Tb	NO_2	2008	3.46	2.60	-	[130]
SABYUS	Co & Eu	NO_2	2008	3.56	2.52	-	[130]
EMIDEJ02	Ca	H	2018	3.52	1.53	-	[131]
RUGXOI01	Zn	OH	2017	3.64	1.58	-	[132]
MUF-17	*Co*	*NH_2*	*2019*	*4.49*	*2.24*	*0*	[78]
OGUPIQ	Co	NH_2	2009	4.30	2.74	0	[133]
COXFOL	Co	H	2009	4.69	2.87	113	[134]
XOBGUT	Eu	NO_2	2019	4.60	2.93	53.7	[135]
LOWQIX	Zn	H	2001	4.08	2.28	-	[136]

Table 2.2 PoreBlazer parameters for the 'Larger Pore List' MOFs.

CCDC Code	Metal Centre	R=?	Year	LCD (Å)	PLD (Å)	ASA (m^2/g)	Ref
QULMOA	In	SO_3	2009	10.05	2.66	-	[137]
IPIREG	Zn	NH_2	2016	9.51	8.19	601	[138]
KIXKOS	Co	H	2007	8.27	2.64	-	[139]
NAGKEO	Zn	Br	2016	8.12	3.39	1240	[123]
TACYED	In	H	2010	7.98	5.73	1470	[140]
QULMIU	In	NH_2	2009	7.21	4.03	391	[137]
WAMRIN	Mg	NH_2	2012	7.16	5.59	1450	[113]
AJIHOQ	Cu	H	2003	7.07	6.25	584	[141]
TOWMID	Fe	OMe	2014	7.07	2.34	-	[126]
TAGQUQ	Cu	NO_2	2016	7.02	6.45	362	[142]
FILYEG	Co	H	2013	6.67	3.8	1350	[143]
TOWMEZ	Fe	Br	2014	6.45	2.28	-	[126]
EDOTUN	Co & Zn	H	2007	6.35	4.49	201	[114]
OFEJAM	Cu	H	2013	6.28	3.6	456	[144]
RUGXUO	Zn	OH	2015	6.13	4.91	702	[132]

In Table 2.1 and Table 2.2, sometimes ASA is reported as zero. This is not due to a lack in porosity, as known porous MOFs can give ASA values of zero. It is due to the MOF having a PLD smaller or very close to the size of a nitrogen probe, thus N_2 will be unable to diffuse through the network, making ASA and the probe-occupiable volume zero.[91] Those with a dash for ASA did not give any value. These all have a small PLD (< 2.70 Å) therefore the likely reason is the same as above; the PLD is smaller than the size of the nitrogen probe.

As there are many MOFs on the 'Priority List' and the 'Larger Pore List', one may expect that this project will result in many of those MOFs being successful results, i.e. having good gas uptake and separation capabilities. However, MOF synthesis is highly sensitive, and it is likely that many of the MOFs on these lists will not be reproducible, or they may only be reproducible in a mixed phase. The MOFs may also not be stable upon activation or not be as porous as advertised. Thus we only expect a small handful, likely three or four, to be successful results. We have seen this in this project and the following chapters will outline these results.

2.4 Conclusion

This chapter outlines how the computer simulation software named PoreBlazer was used to create the 'Priority List' and the 'Larger Pore List'. The results of these lists will be the focus of Chapter 3, whilst also being the fundamental basis of Chapters 4 and 5. This chapter shows the wide variety of MOFs that can be made with the base ligand, with a wide range of pore sizes, accessible surface areas and metals that are incorporated. This search has also shown the relevance and importance of the H_2ipa ligand as the papers reporting its use in MOF chemistry have been reported since the early 2000s and is still being reported in recent years.

Chapter 3 – MOFs on the 'Priority' and 'Larger Pore' Lists

3.1 Introduction

In Chapter 1, H_2ipa was introduced as a highly versatile ligand which can coordinate in various ways to various metals to produce a wide range of MOFs.[103] MOFs containing only this ligand, or only 5′ derivatives of this ligand, were analysed in Chapter 2 using PoreBlazer. The results were compared with MUF-15, -16 and -17, which are exceptional ipa-derived MOFs for gas adsorption and separation. This resulted in the 'Priority List' of potentially high-performance MOFs. In addition, those with pores > 6 Å were collated to produce the 'Larger Pore List'. These two lists became the starting line for this project. Even though all of these MOFs are known, their gas adsorption abilities had not been measured. This is the goal of this project, as outlined in Chapter 2. We anticipate that in some cases the literature synthetic methods will be difficult to reproduce so these lists are also likely to produce other interesting MOFs for gas adsorption analysis.

This chapter outlines the results from the 'Priority List' and 'Larger Pore List'. We will analyse in detail both the successful results and the less-successful results and discuss how PoreBlazer ties in with the experimental data gathered. This chapter will also highlight gas pair selectivities calculated for certain MOFs and compare them to some benchmark values set by selected MOFs in the literature.

3.2 Results and discussion

3.2.1 'Priority' List Results

The 'Priority List', as first outlined in Chapter 2, can be found in Table 3.1 with information about if the MOF was successfully synthesized alongside any other additional notes.

Table 3.1 PoreBlazer parameters for the ‘Priority List’ MOFs including the parameters calculated for MUFs 15, 16, and 17 for comparison. Key: ✓ means synthesized, ✗ means could not be synthesized, – means did not attempt, and ✦ means an inconclusive result.

CCDC Code	Metal Centre	R=	LCD (Å)	PLD (Å)	ASA (m^2/g)	Made ✓/✗	Notes
MUF-15 [87]	*Co*	*H*	*5.07*	*3.23*	*432*	N/A	
NAGKOY [123]	Zn	NO$_2$	5.43	3.96	423	✗	Reagents unavailable
XADDOX [124]	Co	H	5.85	3.43	725	✦	Unable to reproduce
HOMQEI [125]	Cu	OH	4.72	3.34	374	-	Based on a metal organic polyhedra*
TOWLOI [126]	Fe	H	4.87	2.44	-	✗	Non-crystalline phase
MUF-16 [6]	*Co*	*NH$_2$*	*3.47*	*2.74*	*0*	N/A	
JETJOI [115]	Zn & Na	H	3.45	2.73	0	✓	
ACOHUW03[127]	Mn	NH$_2$	3.54	2.34	-	✗	Made different phase
TILHEC [128]	Co & Na	H	3.32	2.75	0	✗	Mixed phase only
LARPIF [129]	Fe & Na	H	3.29	2.73	0	✗	Mixed phase only
SABXEB [130]	Co & Tb	NO$_2$	3.46	2.60	-	✗	Mixed phase only
SABYUS [130]	Co & Eu	NO$_2$	3.56	2.52	-	✗	Mixed phase only
EMIDEJ02 [131]	Ca	H	3.52	1.53	-	✓	
RUGXOI01 [132]	Zn	OH	3.64	1.58	-	✓	Unable to scale up
MUF-17 [78]	*Co*	*NH$_2$*	*4.49*	*2.24*	*0*	N/A	
OGUPIQ [133]	Co	NH$_2$	4.30	2.74	0	✗	Mixed phase only
COXFOL [134]	Co	H	4.69	2.87	113	✦	Unable to reproduce
XOBGUT [135]	Eu	NO$_2$	4.60	2.93	53.7	✗	
LOWQIX [136]	Zn	H	4.08	2.28	-	✗	Made different phase

*The difference between this structure (called a metal organic polyhedra AKA MOP) and a MOF is that the MOP is a discrete cage, unlike a MOF which can build infinitely.[125]

The synthesis of the majority of the MOFs in the ‘Priority List’ could not be reproduced in our laboratory. The successfully made MOFs were XADDOX, JETJOI and EMIDEJ02, of which their results will be outlined in sections 2.2.3, 2.2.4 and 2.2.6 respectively. RUGXOI01 was also synthesized at a small scale, however, scale up for gas adsorption experiments did not work. For the syntheses that did not work, either no crystals would grow, amorphous phases would form, a mixed phase of the desired MOF alongside another phase or a mixed phase of two completely new phases would form instead. When the published synthetic protocol did not work, different reaction variables were altered to see if that would produce the desired MOF. These altered reactions either produced a mixed phase, or an alternative non-porous phase. An example of the latter is ACOHUW03 synthesis attempts often produced a non-porous MOF called WEGDAP.

3.2.2 ‘Larger Pore’ List Results

Much like the ‘Priority List’, the ‘Larger Pore List’ was introduced in Chapter 2 and details about this list can be found in Table 3.2 with information about if the MOF was successfully synthesized (made) and any other additional notes.

The MOFs that were successfully made from the ‘Larger Pore List’ were WAMRIN, EDOTUN, OFEJAM and RUGXUO. The results of WAMRIN, EDOTUN, and RUGXUO will be outlined in section 3.2.7. In the paper that published OFEJAM, the structure contained a polyoxometalate.[144] When using that method without the templating polyoxometalate, a different phase was produced, which had an inconclusive PXRD pattern as it did not fully match the expected phase.[144, 145] For this reason, OFEJAM was not investigated further for this project, however, its synthetic method was used to develop several more MOFs which will be explained in greater detail in Chapters 4 and 5. TAGQUQ was not successfully synthesized (with the paper method or different methods), however, an analogue with H_2ipa was made using a protocol devised from a student in a different research group (Mutjalin Limlamthong). The results of this analogue will be outlined in section 3.2.6.

Much like the ‘Priority List’, the ‘Larger Pore List’ had many MOFs that could not be made. For this list, there were a few MOFs where the synthesis protocols had other organic compounds present that were not incorporated into the structure. For some of these, we did not have those compounds in the laboratory and thus the synthesis was either not attempted or it was attempted without the organic compound.

Table 3.2 PoreBlazer parameters for the ‘Larger Pore’ MOFs. Key: ✓ means synthesized, × means could not be synthesized, – means did not attempt and ✦ means an inconclusive result.

CCDC Code	Metal Centre	R=	LCD (Å)	PLD (Å)	ASA (m^2/g)	Made ✓/×	Notes
QULMOA [137]	In	SO_3	10.05	2.66	-	×	
IPIREG [138]	Zn	NH_2	9.51	8.19	601	-	Did not have solvent amounts in method
KIXKOS [139]	Co	H	8.27	2.64	-	×	
NAGKEO [123]	Zn	Br	8.12	3.39	1240	×	Reagents unavailable
TACYED [140]	In	H	7.98	5.73	1470	×	Non-crystalline phase
QULMIU [137]	In	NH_2	7.21	4.03	391		
WAMRIN [113]	Mg	NH_2	7.16	5.59	1450	✓	
AJIHOQ [141]	Cu	H	7.07	6.25	584	×	Copper oxide
TOWMID [126]	Fe	OMe	7.07	2.34	-	×	Non-crystalline phase
TAGQUQ [142]	Cu	NO_2	7.02	6.45	362	✦	Made with different ligand
FILYEG [143]	Co	H	6.67	3.8	1350	×	Reagents unavailable
TOWMEZ [126]	Fe	Br	6.45	2.28	-	×	Non-crystalline phase
EDOTUN [114]	Co & Zn	H	6.35	4.49	201	✓	
OFEJAM [144]	Cu	H	6.28	3.6	456	✦	Inconclusive
RUGXUO [132]	Zn	OH	6.13	4.91	702	✓	

3.2.3 MUF-15 Analogues

XADDOX is one of the MOFs from the ‘Priority List’ was reproduced.[124] MUF-200 is a new phase that was formed while trying to make TILHEC (another MOF on the ‘Priority List’). Upon further examination and SCXRD analysis, it was determined that these MOFs are almost identical in structure to MUF-15.[87] In addition, there are two more known Co^{2+}/ipa MOFs that are also practically identical to MUF-15; these are known as FILYEC and FILYEG.[143]

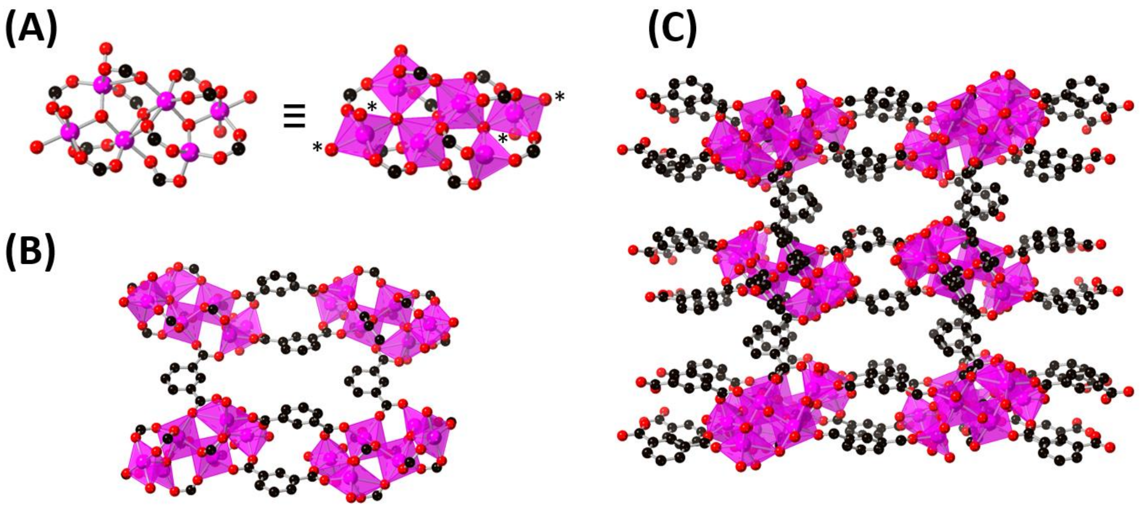

Figure 3.1 Framework of XADDOX used as a representative portrayal of the MUF-15 analogues. (A) Structure of the hexanuclear cluster with an asterisk beside the variable terminal positions. (B) Assembly of the ipa ligands to connect the hexanuclear clusters. (C) Framework viewed along the c axis. Atom colours: carbon: black, oxygen: red, and cobalt: magenta. Hydrogen atoms omitted for clarity.

All five of these MOFs contain a hexanuclear cluster made of six Co^{2+} ions, ten bridging dianionic ipa ligands and two μ_3-OH ligands. These clusters are connected together by ipa bridges to form a three-dimensional framework. XADDOX is given as a representative framework in Figure 3.1.

Table 3.3 Parameters of the MUF-15 analogues.

	Crystal System	Space group	Coordinated solvent	Disordered (Yes/No)	PoreBlazer Values (Å)
MUF-15 [87]	Orthorhombic	*Pnna*	2 H_2O	Yes	PLD: 3.23 LCD: 5.01
XADDOX[124]	Orthorhombic	$P2_12_12$	5 H_2O	No	PLD: 3.43 LCD: 5.85
MUF-200	Orthorhombic	*Pnn2*	4 DMF	No	PLD: 2.28 LCD: 4.08
FILYEG[143]	Monoclinic	$P2_1/c$	2 H_2O	Yes	PLD: 3.80 LCD: 6.97
FILYAC[143]	Orthorhombic	*Pnna*	2 H_2O, 2 DMF	No	PLD: 3.20 LCD: 4.40

The difference between these five MOFs is in the nature of the occupancies on each of the two outer Co^{2+} ions of the hexanuclear clusters. There are four available sites that can be filled with coordinated solvent which differs between the five MOFs, as shown in Table 3.3. Furthermore, for MUF-15 and FILYEG, only two of the four sites are filled, with the two bound solvent molecules being disordered over the sites.[87, 143] These MOFs also have different crystal systems and space groups, even though the overall framework is the same. These different coordinated solvent molecules influence the pore sizes calculated by PoreBlazer.

More details about the properties of XADDOX and MUF-200 are presented below. XADDOX could not be reliably reproduced in our lab (*vide infra*), however MUF-200 could. The reagents were unavailable to make FILYEG and FILYAC is added for structural comparison only. Comparing the gas adsorption abilities of XADDOX, MUF-200, and MUF-15, there is variation between the uptake values and the order of gases with the highest uptakes. This shows that the activation conditions play a significant role in the gas adsorption abilities of these MOFs, noting that the coordinated solvent may be fully or partially lost during the activation procedure. XADDOX and MUF-15 have the same activation conditions of heating under vacuum at 120 °C for 20 hours, whilst MUF-200 was heated to 100 °C for 24 hours.

3.2.3.1 XADDOX

XADDOX (Cheng et. al., 2010) is made by a solvothermal reaction with $Co(OAc)_2{\cdot}5H_2O$ and H_2ipa resulting in a MOF with the formula of $[Co_6(\mu_3\text{-}OH)_2(ipa)_5(H_2O)_5]{\cdot}8H_2O$.[124] More detail about the experimental procedure and PXRD patterns can be found in the appendix.

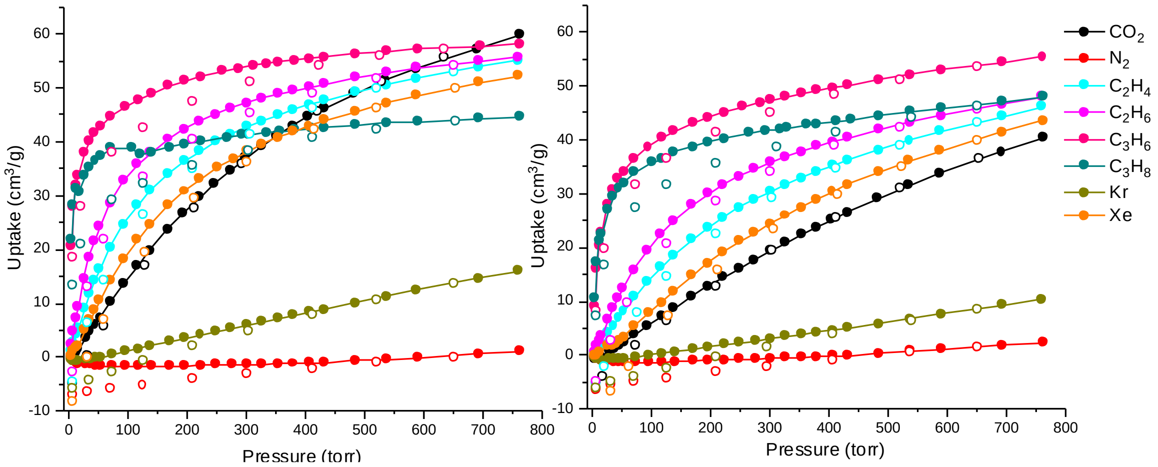

Figure 3.2 Adsorption isotherms of XADDOX at 273 K (left) and 293 K (right). Coloured circles represent adsorption points and open circles represent desorption points.

XADDOX strongly adsorbs CO_2 (40.3 cm^3/g), ethane (47.9 cm^3/g), ethylene (46.1 cm^3/g), propane (47.9 cm^3/g), and propylene (55.4 cm^3/g), all at 293 K and 760 torr. As introduced in Chapter 1, CO_2 and N_2 are a key gas pair, thus the high CO_2 uptake compared to the low N_2 uptake (2.33 cm^3/g, at 293 K and 760 torr) is ideal. Another key gas pair is Xe/Kr, of which XADDOX displays promising selectivity due to the lower Kr uptake compared to the Xe uptake (10.4 cm^3/g for Kr compared to 43.5 cm^3/g for Xe). The C_3 pair also displays decent differences in uptake, which is ideal as this pair is hard to separate by conventional means.

The isotherms do, however, display a degree of hysteresis, mainly for the C_3 gases, especially propane at 273 K. These isotherms were originally meant to be preliminary data, with the intention of collecting a better set of isotherms at a later date, however XADDOX is quite difficult to synthesize. Even upon varying the reaction conditions and following the exact same protocols as that of the paper itself, and of the successful method, most times resulted in an amorphous phase, or a mixed phase. Thus, while XADDOX has good gas uptakes, this MOF would have difficulty with practical application as it is hard to reproduce, hence why in the ‘Priority List’ it is classified as an inconclusive result.

It is also noteworthy that these isotherms display ‘negative’ uptake. This is not a true result as there cannot be a negative uptake, but this is rather due to limitations of the instrument due to there being a small sample size and low gas uptake. Thus, more sample will be required, in future work, to obtain better isotherms.

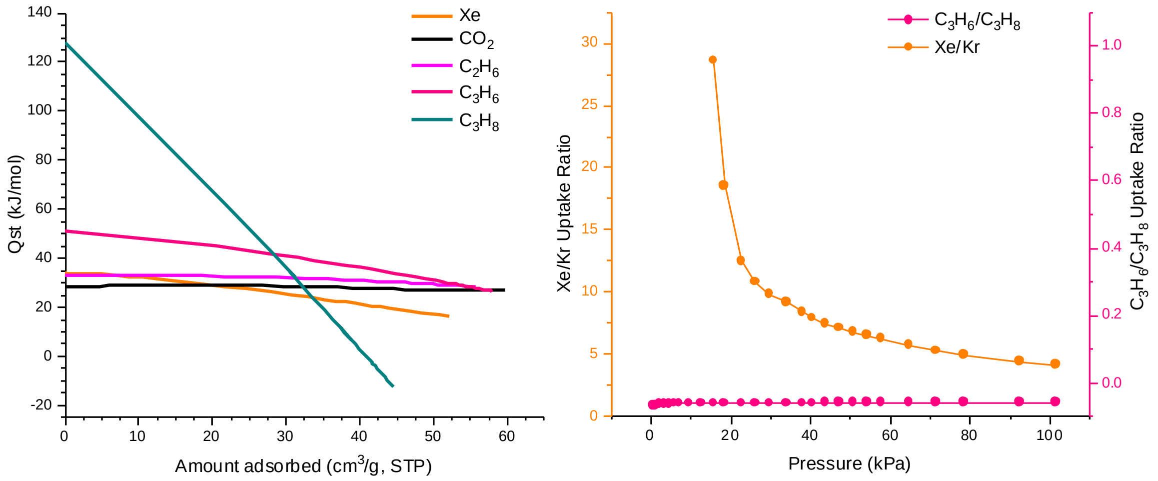

Figure 3.3 (Left) Q_{st} plots for Xe, CO_2, ethane, propylene, and propane uptake of XADDOX. (Right) Uptake ratio vs pressure of propylene/propane and Xe/Kr for XADDOX at 293 K. The axis and corresponding gas pair are colour coordinated;

Q_{st} values were calculated for the top five adsorbing gases using the isotherms collected at 273 and 293 K (Figure 3.3). All gases displayed a negative trend with propane having the highest Q_{st} at zero coverage of 128 kJ/mol. While such a high Q_{st} indicates that that gas interacts very strongly with XADDOX, it is much higher than expected for physisorption and is probably a consequence of imperfections in the experimental data. The second highest Q_{st0} was propylene at 50.8 kJ/mol, followed by Xe at 33.8 kJ/mol, ethane at 32.4 kJ/mol, and lastly, CO_2 at 27.7 kJ/mol. The similar values of Xe, ethane and CO_2 indicate they all have similar binding strengths to XADDOX.

Due to the lack of decent isotherm data, IAST was not determined for the key gas pairs of interest. However, for the C_3 gases and Xe/Kr, the uptake ratios were determined to give a preliminary idea at the selectivity of XADDOX (Figure 3.3). For the C_3 gases at around 100 kPa, there is an uptake ratio of 1.15, showing that propylene is slightly preferred over propane. For Xe/Kr, the uptake ratio was highly dependent on the pressure. Very low pressure data points were removed due to Kr having ‘negative’ uptakes in this region (*vide supra* for explanation). At lower pressure, there is a high uptake ratio, for example at 15.5 kPa the ratio is 28.6, with this ratio decreasing exponentially until it is around 4.19 at 100 kPa. This shows that whilst Xe uptake is continually preferred over Kr, it is especially preferred at low pressure. IAST is generally used to compare the selective performance of a MOF. Due to the lack of IAST values for XADDOX, no literature comparison will be made.

3.2.3.2 MUF-200

Whilst trying to make TILHEC, which is a MOF that is found on the ‘Priority List’, a new phase was produced, which we named MUF-200 (MUF = Massey University Framework).[128] MUF-200 crystallizes in a *Pnn2* space group, with unit cell dimensions of 21.4 x 28.6 x 10.9 Å, with 90° angles. The formula for MUF-200 is $[Co_6(\mu_3\text{-}OH)_2(ipa)_5(DMF)_4]$. More crystallographic detail can be found in the Table 3.4.

PoreBlazer calculations were performed using the SCXRD data for MUF-200. Using the direct SCXRD structure, MUF-200 has an LCD of 4.08 Å, PLD of 2.28 Å, and no value for ASA was given due to the small PLD. The BET (Brunauer-Emmett-Teller) surface area was calculated from experimental data (N_2 at 77 K isotherm) and was determined to be 405 m^2/g (Figure A.42).

Table 3.4 SCXRD data collection and structure refinement details for MUF-200.

Formula	$[Co_6(\mu_3\text{-}OH)_2(ipa)_5(DMF)_4]$
Empirical Formula	$C_{13}H_{12.5}Co_{1.5}NO_{6.5}$
Formula weight	375.13
Temperature (K)	273
Crystal system	orthorhombic
Space group	*Pnn2*
a (Å)	21.388(3)
b (Å)	28.631(4)
c (Å)	10.8700(14)
$\alpha = \beta = \gamma$ (°)	90
Volume (Å^3)	6656.2(15)
Z	16
ρ_{calc} (g/cm^3)	1.497
μ (mm^{-1})	12.121
F(000)	3040.0
Radiation	CuKα (λ = 1.54178)
2Θ range for data collection (°)	5.158 to 149.318
Index ranges	$-26 \leq h \leq 25$, $-35 \leq k \leq 35$, $-13 \leq l \leq 12$
Reflections collected	79190
Independent reflections	13179 [R_{int} = 0.0633, R_{sigma} = 0.0502]
Data/restraints/parameters	13179/115/781
Goodness-of-fit on F^2	1.038
Final R indexes [I>=2σ (I)]	R_1 = 0.0614, wR_2 = 0.1655
Final R indexes [all data]	R_1 = 0.0785, wR_2 = 0.1840
Largest diff. peak/hole (e Å^{-3})	0.70/-0.79
Flack parameter	0.5

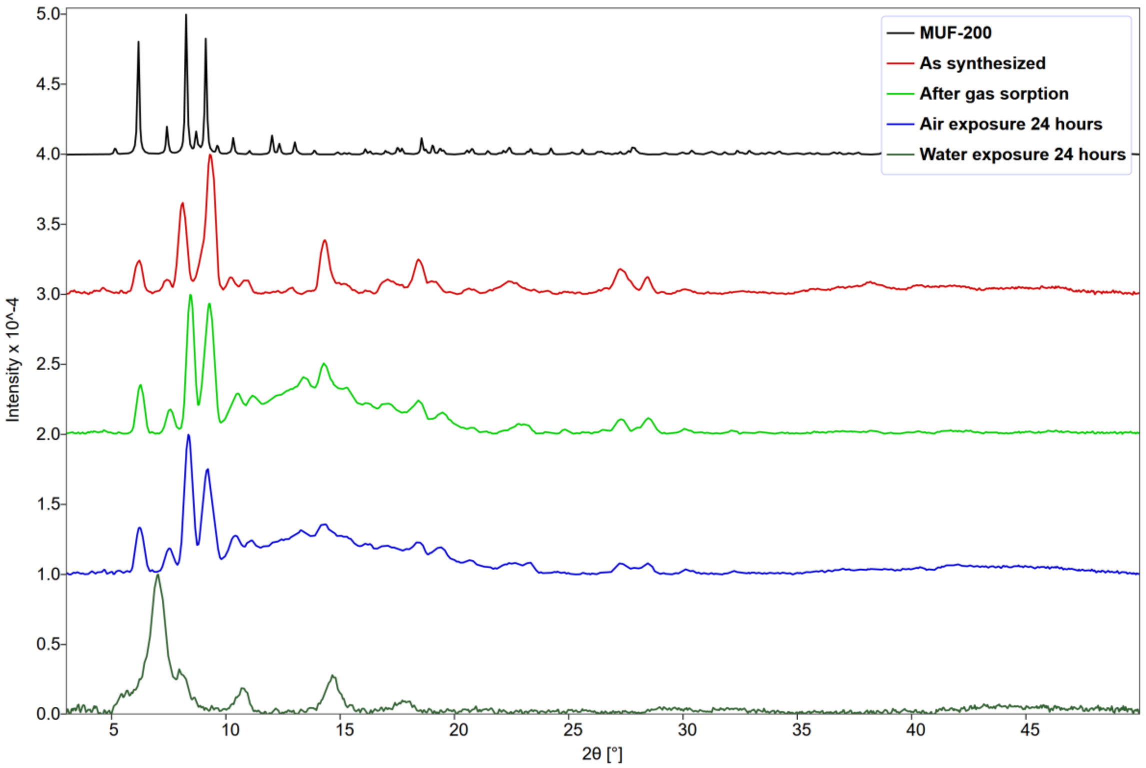

Figure 3.4 PXRD patterns of MUF-200 simulated (black), as synthesized (red), after gas adsorption (lime), after exposure to air for 24 hours (royal blue), and after water exposure for 24 hours (dark green).

Comparison of experimental PXRD patterns to the simulated pattern from the SCXRD data can be seen in Figure 3.4. There is a decent match between the simulated and experimental patterns, however there is a peak at 14.3° that does not quite fit. The patterns also show fluctuations in peak height, which was also observed between batches. Peak positions can also vary slightly due to sample treatment before measurement. Due to the slight differences in the experimental patterns compared to the SCXRD pattern, it was hypothesized that removal the coordinated DMF could cause variation (such removal could occur upon activation). ^{1}H nuclear magnetic resonance (NMR) spectroscopy on a dissolved a sample showed 1.3 DMF molecules for every five ipa ligands indicating that the majority of the DMF is removed upon activation (Figure A.46). For this reason, PoreBlazer was run with a structure that had no DMF and it showed an LCD of 5.45 Å, PLD of 3.60 Å, and an ASA of 701.7 m^2/g. Whilst this is not the fully correct model, as some DMF will still be present, this is close to the actual structure that was exposed to the gases. PoreBlazer determined a higher BET than the experimental data, which is expected as it was assuming no DMF present, where there actually would still be some.

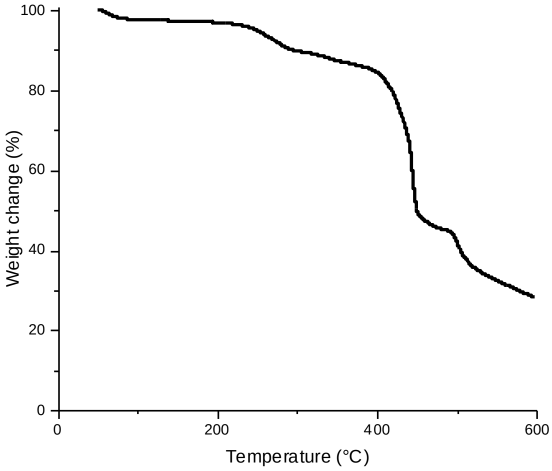

Figure 3.5 TGA curve for MUF-200.

The framework is stable after gas adsorption and when exposed to the laboratory atmosphere, however it is unstable in water (Figure 3.4). TGA analysis showed that MUF-200 is stable until around 250 °C before it starts to decompose (Figure 3.5).

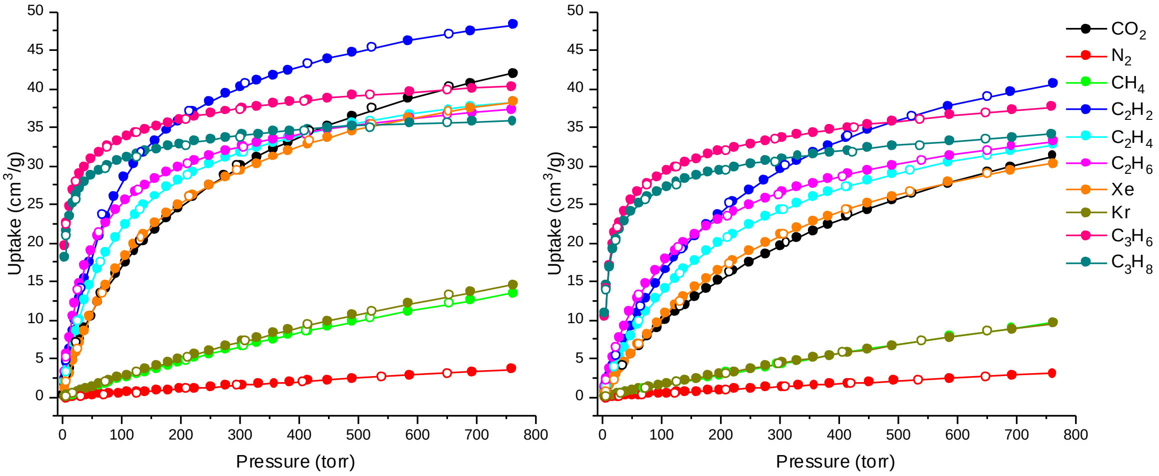

Figure 3.6 Adsorption isotherms of MUF-200 at 273 K (left) and 293 K (right). Coloured circles represent adsorption points and open circles represent desorption points.

MUF-200 has similar uptakes to XADDOX with the highest gases being the C_2 and C_3 gases, alongside CO_2 and Xe (all at 293 K and 760 torr). These can all be seen in Figure 3.6. Acetylene had the highest uptake at 40.7 cm^3/g, followed by propylene (34.9 cm^3/g) and propane (34.1 cm^3/g). Ethane and ethylene had almost identical uptakes at 33.1 and 32.8 cm^3/g

respectively. These uptakes were closely followed by CO_2 at 31.2 cm^3/g and Xe at 30.3 cm^3/g. No hysteresis was observed in these isotherms.

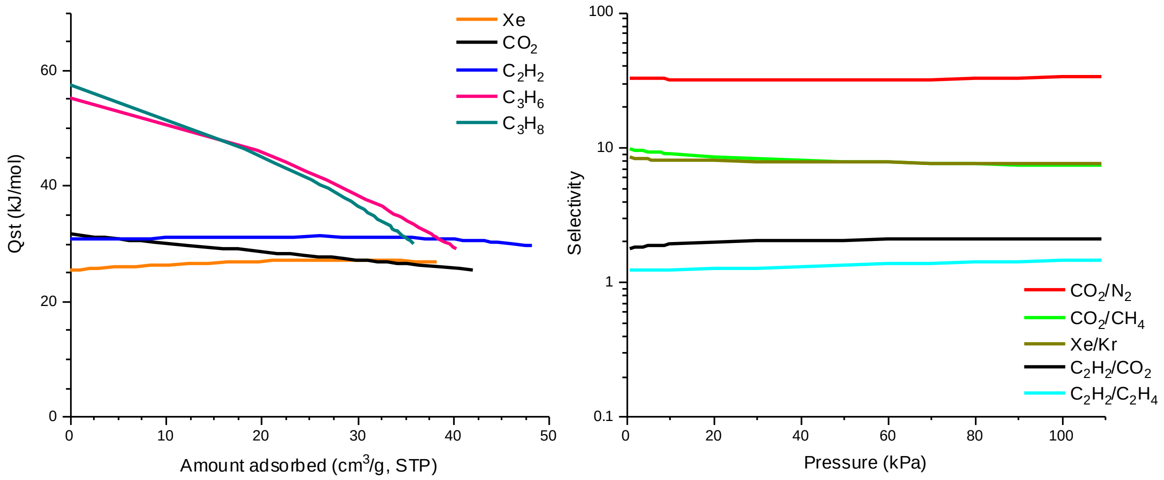

Figure 3.7 (Left) Qst plots for Xe, CO_2, acetylene, propylene, and propane uptakes of MUF-200. (Right) IAST selectivity of 50:50 mixtures of CO_2/N_2, CO_2/CH_4, Xe/Kr, C_2H_2/CO_2, and C_2H_2/C_2H_4. A logarithmic scale was used for the y axis.

Due to there being a number of gases with high uptakes and thus a few interesting gas pairs, Q_{st} was calculated for five of the highest adsorbing gases using pure component isotherms collected at 273 and 293 K (Figure 3.7). At zero coverage, the Q_{st} values were 26.8 kJ/mol for Xe, 25.3 kJ/mol for CO_2, 29.6 kJ/mol for acetylene, 55.0 kJ/mol for propylene and 57.4 kJ/mol for propane. The C_3 gases both have much higher Q_{st0} values, suggesting they are the gases which interact the strongest with the framework, as expected.

There are several key gas pairs that are of interest for MUF-200 which were followed up by IAST analysis. The gas pair with the highest selectivity was CO_2/N_2 with a selectivity of 32.8 at 100 kPa. Followed by CO_2/CH_4 selectivity of 7.28, then Xe and Kr selectivity of 7.51. The lowest two selectivity values were for acetylene/CO_2 at 2.08 and acetylene/ethylene at 1.43. All gas pairs were analysed for a 50:50 mixture. For comparison to a non-extensive literature search, MUF-200 displays a relatively low CO_2/N_2 selectivity, when using a 15:85 mixture.[146] MUF-200 also displays relatively low CO_2/CH_4 selectivity, as many benchmark materials have higher CO_2 capacity.[146] Compared to Xe/Kr literature, MUF-200 displays moderate to low uptakes and selectivities.[147, 148] MUF-200 has low selectivity and uptakes for both acetylene/CO_2 and acetylene/ethylene gas mixtures.[149-151] Therefore overall, MUF-200 does not display new benchmark selectivities though nonetheless it is selective for a range of key gas pairs.

3.2.4 JETJOI

JETJOI was published by He et. al. in 2005.[115] It was made via a solvothermal reaction with $Zn(NO_3)_2 \cdot 6H_2O$, H_2ipa, and NaOH in *N*, *N*-dimethylformamide (DMF) resulting in colourless rod-shaped crystals.[115] JETJOI has a formula of $NH_2(CH_3)_2[ZnNa(ipa)_2]$.

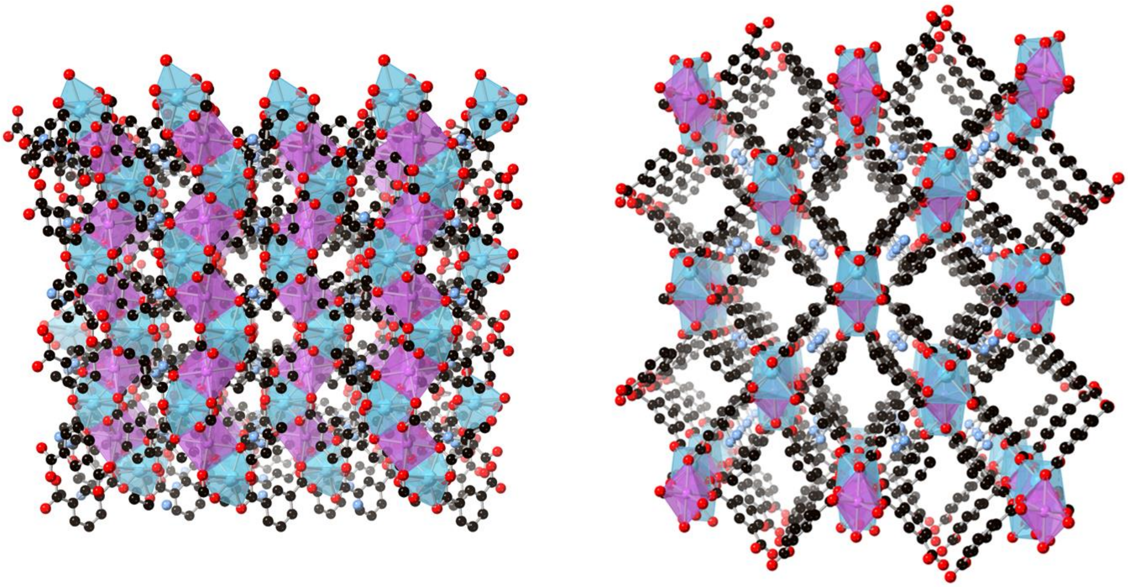

Figure 3.8 Structure of JETJOI viewed along the a axis (left) and the c axis (right). Atom colours: carbon: black, oxygen: red, nitrogen: periwinkle blue, zinc: pale blue, and sodium: lilac. Hydrogen atoms omitted for clarity.

The structure for JETJOI can be seen in Figure 3.8. The Zn^{2+} ions have a tetrahedral geometry, and the Na^+ ions have an octahedral geometry. These build into infinite rod-shaped SBUs, with the Zn^{2+} alternating with the Na^+.[115] Each rod is linked to another through ipa ligands and there are also dimethylamine cations present which play a templating role.[115] More detail about the experimental procedure and PXRD patterns can be found in the appendix.

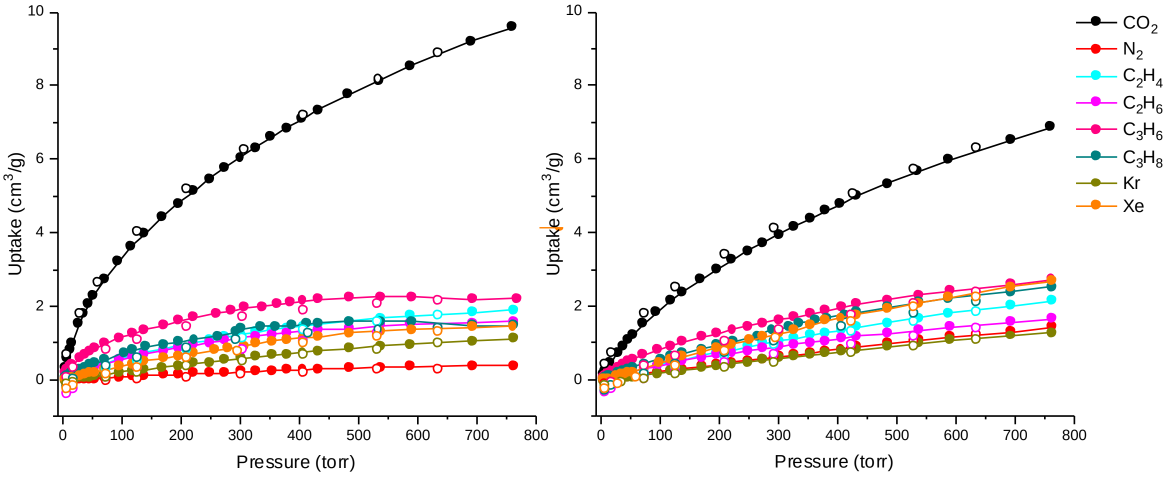

Figure 3.9 Adsorption isotherms of JETJOI at 273 K (left) and 293 K (right). Coloured circles represent adsorption points and open circles represent desorption points.

JETJOI displayed moderate gas uptakes (Figure 3.9). Unlike XADDOX, for JETJOI only one gas has a high uptake, whereas the rest are considerably lower. This type of uptake was observed with MUF-16 where only one gas is highly preferred. CO_2 has the highest uptake for JETJOI with 6.87 cm^3/g (at 293 K and 760 torr), with all the other gases having lower uptakes, with the second highest gas uptake being for propylene at 2.72 cm^3/g. This is ideal behaviour for gas adsorption experiments as one gas is high preferred over all the other gases, here the gas being CO_2.

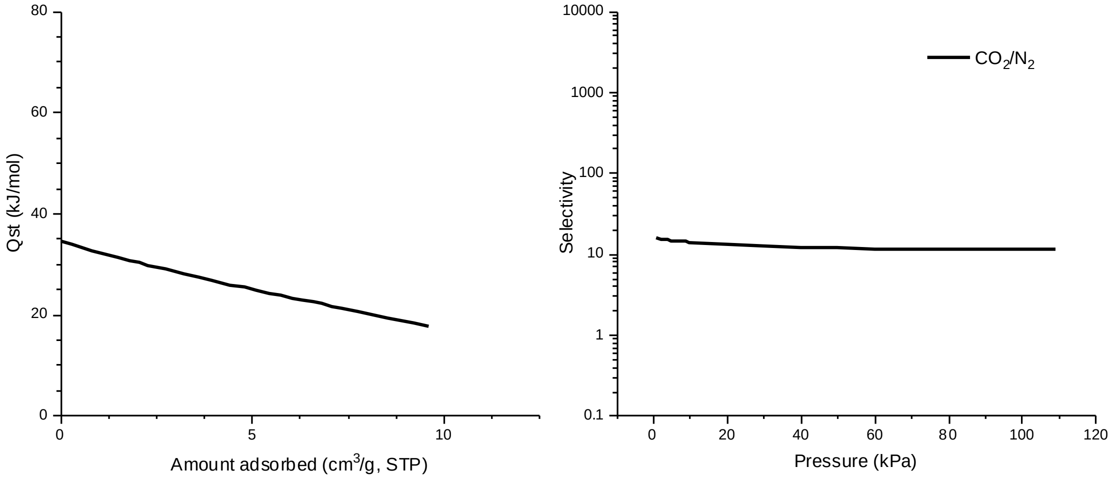

Figure 3.10 (Left) Q_{st} plots for CO_2 uptake of JETJOI. (Right) IAST selectivity of a 50:50 mixture of CO_2 and N_2. A logarithmic scale is used for the y axis.

The Q_{st} of JETJOI for CO_2 was calculated using pure component isotherms collected at 273 and 293 K and can be seen in Figure 3.10. The Q_{st} value at zero coverage is 34.5 kJ/mol and it decreases as uptake increases, which is expected for Q_{st} as the sites with the highest affinity get filled first. Due to the clear difference in CO_2 uptake to the other gases, the IAST selectivity of CO_2/N_2 was calculated as this is a key gas pair. At 100 kPa, JETJOI has a selectivity of 1075 for this gas pair (in a 50:50 mixture). Compared to a non-comprehensive literature search, the IAST of JETJOI for CO_2/N_2 is low, as is the uptakes.[146]

3.2.5 UC-MUF-201 (TAGQUQ Analogue)

This MOF, named UC-MUF-201, was found by another student from a different university (University of Canterbury, UC), using the MUF-15 protocol, hence the joint name. It has the same PXRD pattern as TAGQUQ but it is made from H_2ipa, not H_2ipa-NO_2.[142] UC-MUF-201 was made by a solvothermal reaction of $Cu(OAc)_2{\cdot}H_2O$ and H_2ipa in a solution of MeOH and water at 120 °C. This yielded a blue powder product with a formula of $[Cu_2(ipa)_2(H_2O)_2]$. More details about the experimental procedure can be found in the appendix.

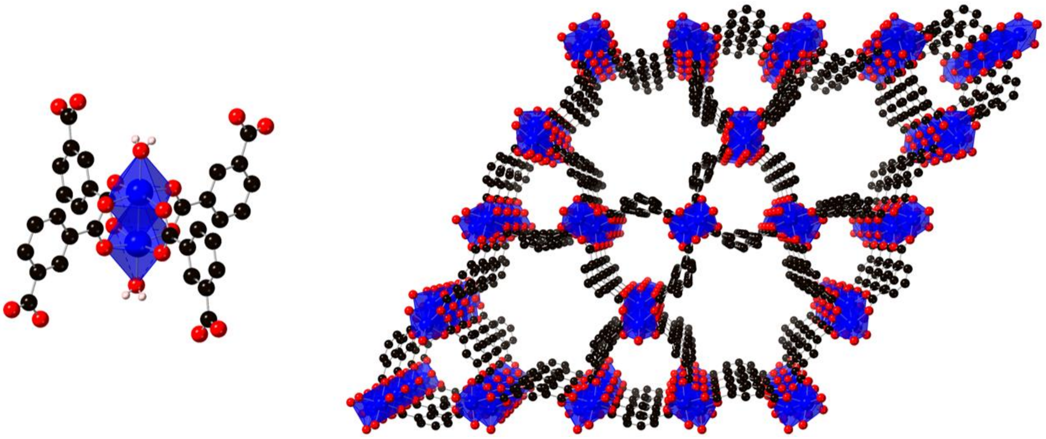

Figure 3.11 (Left) Coordination at the paddlewheel cluster of UC-MUF-201. (Right) Framework of UC-MUF-201 viewed along the c axis. Atom colours: carbon: black, oxygen: red, hydrogen: peach, and copper: royal blue. Most hydrogen atoms are omitted for clarity.

The Cu^{2+} ions in UC-MOF-201 both have an octahedral geometry and form a paddlewheel cluster with four ipa ligands connecting the two Cu^{2+} ions together (Figure 3.11). Each Cu^{2+} ion has a water molecule bound in the axial position. The ipa ligands bridge the paddlewheels with one carboxylate binding to set of Cu^{2+} ions in a paddlewheel, while the other carboxylate binds to the Cu^{2+} ions of a different paddlewheel. This builds the structure into two-dimensional layers, with non-covalent interactions connecting these layers into a three-dimensional framework. There are two kinds of pore environments in UC-MUF-201; one made of six ipa ligands and six paddlewheel clusters, and the other made of three ipa ligands and three paddlewheel clusters. This structure is the same as TAGQUQ except that ipa is present rather than ipa-NO_2.[142]

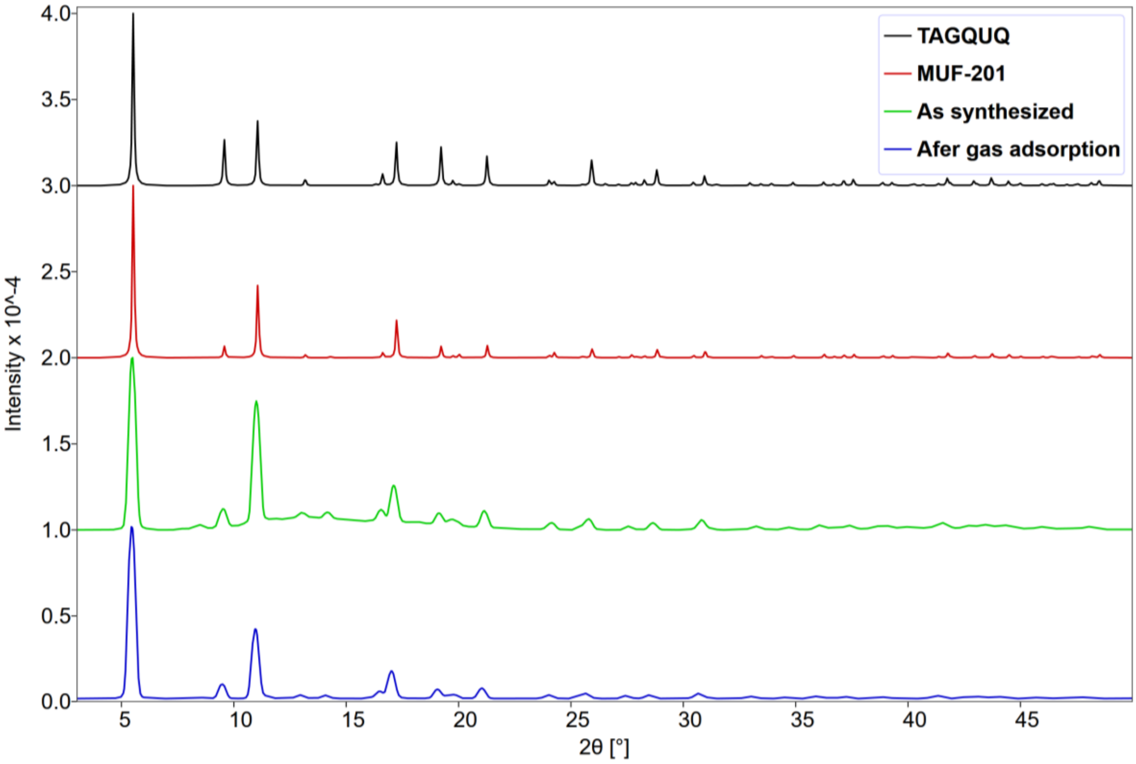

Figure 3.12 PXRD patterns of TAGQUQ simulated (black), UC-MUF-201 simulated (red), as synthesized (lime), and after gas sorption (royal blue).

The simulated PXRD patterns of TAGQUQ and UC-MUF-201 show that they are isoreticular analogues of each other (Figure 3.12). The majority of the as synthesized pattern matches the simulated structure however there is one small peak at 8.4° that does not quite match. . The structure was retained after gas adsorption measurements.

UC-MUF-201 was run through PoreBlazer which calculated an LCD of 8.04 Å, a PLD of 7.31 Å and an ASA of 688 m^2/g. All of these values are larger than those for TAGQUQ (LCD: 7.02 Å, PLD: 6.45 Å, and ASA: 362 m^2/g) which is expected as the UC-MUF-201 ligand has a smaller 5′ functional group than TAGQUQ. BET analysis with a N_2 at 77 K isotherm showed a surface area of 434 m^2/g, which is lower than the calculated surface area.

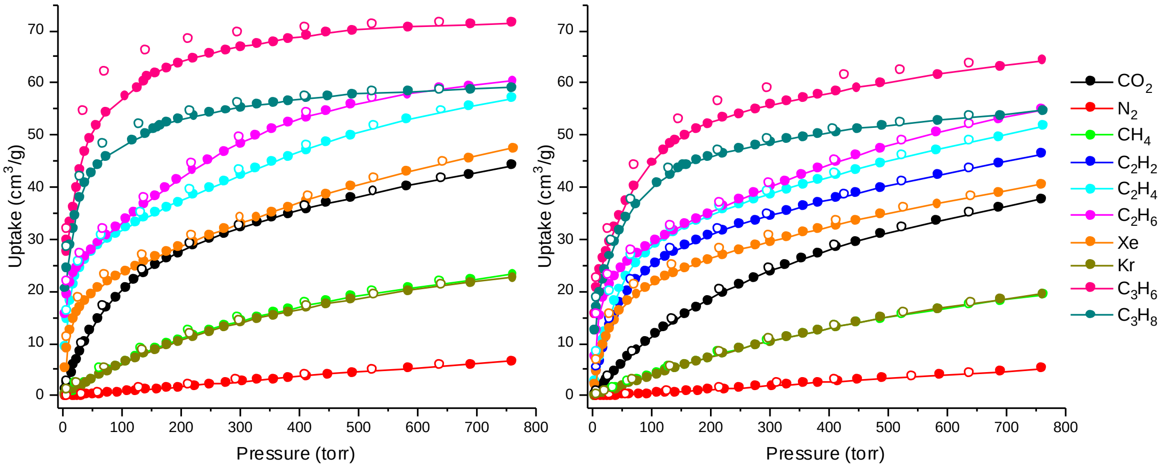

Figure 3.13 Adsorption isotherms of UC-MUF-201 at 273 K (left) and 293 K (right). Coloured circles represent adsorption points and open circles represent desorption points.

UC-MUF-201 displays relatively high gas uptakes for a small pore MOF (Figure 3.13). The gases with the highest uptakes are propylene (64.3 cm^3/g) and propane (54.6 cm^3/g), followed closely by ethane (54.9 cm^3/g) and ethylene (51.6 cm^3/g). These results are recorded at 293 K and 760 torr. Acetylene had the next highest uptake at 46.4 cm^3/g, followed by Xe at 40.5 cm^3/g and CO$_2$ at 37.8 cm^3/g. Minor hysteresis was observed in the propylene and propane isotherms.

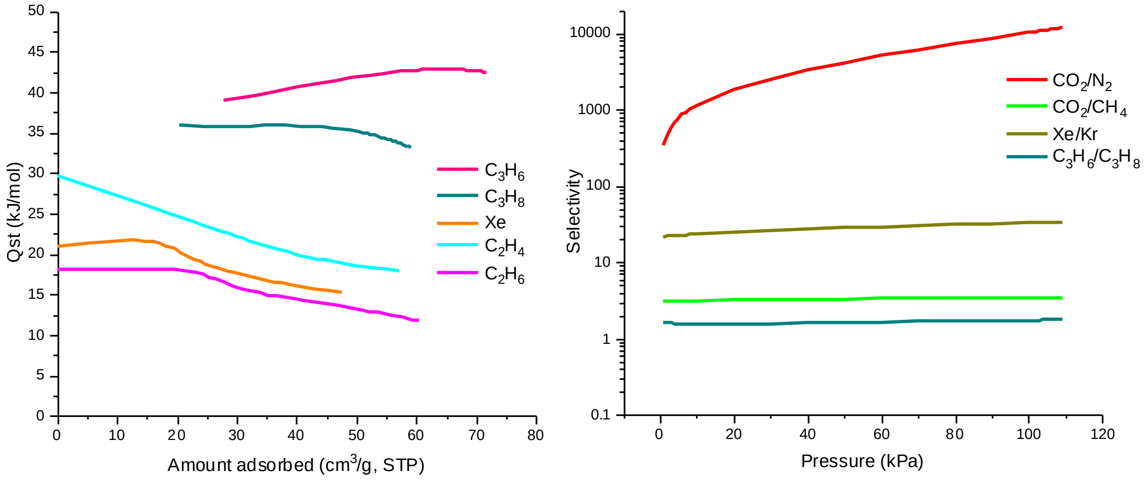

Figure 3.14 (Left) Qst plots for propylene, propane, Xe, ethylene, and ethane uptakes of UC-MUF-201. (Right) IAST selectivity of 50:50 mixtures of CO$_2$/N$_2$, CO$_2$/CH$_4$, Xe/Kr, and C$_3$H$_6$/C$_3$H$_8$. A logarithmic scale was used for the y axis.

Due to there being a few key gas pairs with high uptakes, Q_{st} was calculated for the five highest adsorbing gases using pure component isotherms collected at 273 and 293 K (Figure 3.14**)**. All gases have a mostly negative Q_{st} trend except for propylene which has a slight positive trend. The negative trends indicate that the strongest adsorbing sites get filled first, whilst the positive trends suggest there may cooperative binding once gases adsorb in the pores. At zero coverage, the Q_{st} values are 20.8 kJ/mol for Xe, 29.6 kJ/mol for ethylene, and 18.0 kJ/mol for ethane. Q_{st0} was not determined for the C_3 gases due to the lack of low pressure data points. Despite that, it can be seen that the C_3 gases interact more strongly with UC-MUF-201 than the C_2 gases or Xe. This is consistent with the higher uptakes of the C_3 gases.

There were several key gas pairs that showed promise for good selectivity, thus IAST analysis was performed for UC-MUF-201. The gas pair with the highest selectivity was for CO_2/N_2 with a selectivity of 10170 at 100 kPa. This was followed by Xe/Kr selectivity of 32.5, then CO_2/CH_4 at 3.46 and lastly the C_3 gases at 1.74 (all at 100 kPa). These are all for 50:50 mixtures and can be found in Figure 3.14. In comparison to a preliminary literature search, UC-MUF-201 displays very good CO_2/N_2 selectivity but CO_2/CH_4 selectivity is quite low, as is the CO_2 uptake compared to the best materials in literature.[146] The Xe/Kr selectivity is quite good, alongside a decent uptake.[147, 148] The selectivity between the C_3 gases is low, however the uptakes of both gases are quite good.[152] Thus, the most interesting gas pairs for separation by UC-MUF-201 are CO_2/N_2 and Xe/Kr. While these selectivities are not new benchmark values, these two separations are comparable to some of the better materials in literature.

3.2.6 EMIDEJ02, WAMRIN, EDOTUN, and RUGXUO

Whilst some of the MOFs in this project were successful, displaying good to moderate gas uptakes and selectivities, we expected that not all of the MOFs would have this kind of behaviour. EMIDEJ02, WAMRIN, EDOTUN, and RUGXUO are examples of this. EMIDEJ02 is from the ‘Priority List’ whilst WAMRIN, EDOTUN, and RUGXUO are from the ‘Larger Pore List’.

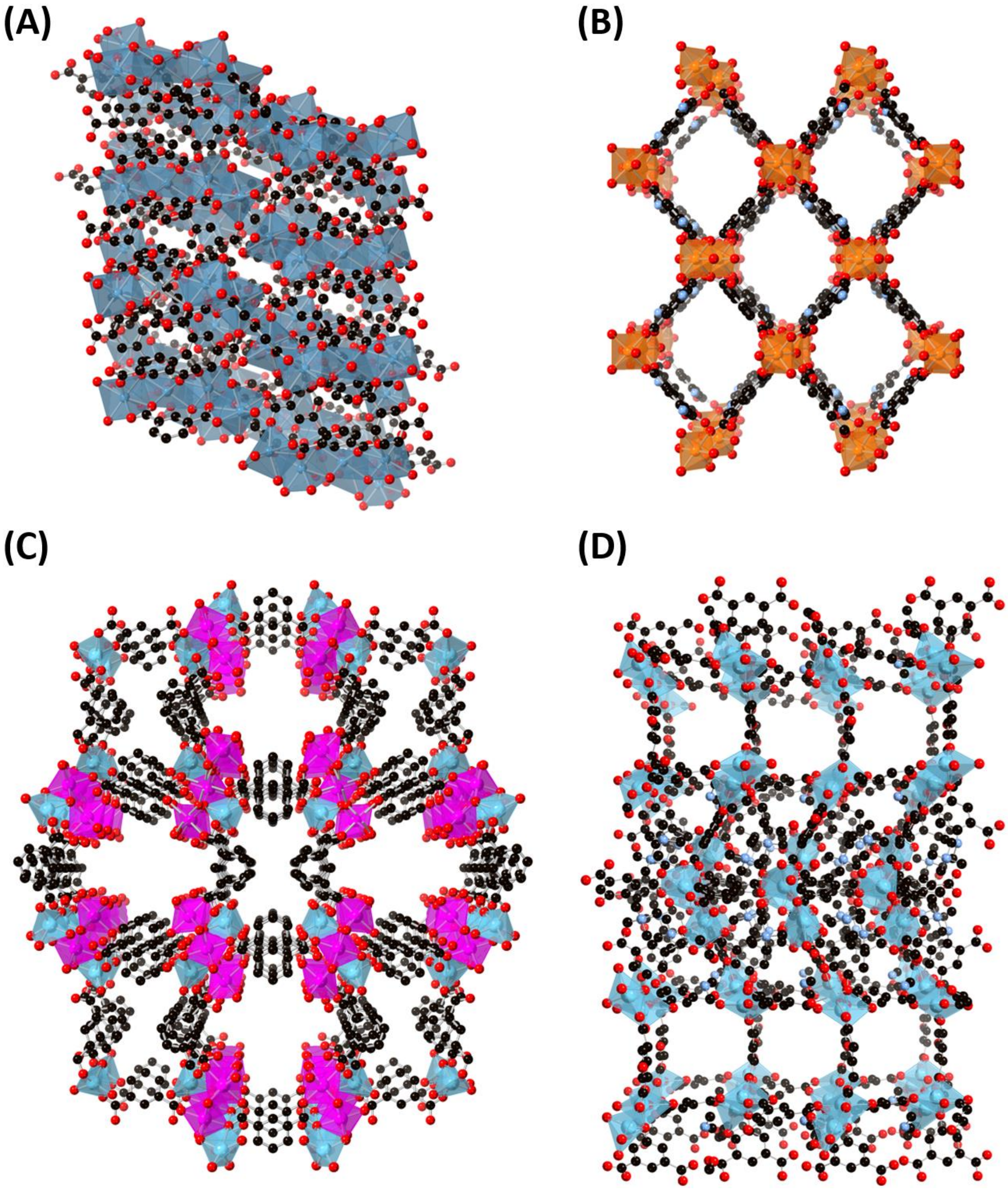

Figure 3.15 Structures (A) EMIDEJ02, (B) WAMRIN, (C) EDOTUN, (D) RUGXUO viewed along the b axis. Atom colours: carbon: black, oxygen: red, nitrogen: periwinkle blue, calcium: dusty blue, magnesium: orange, zinc: pale blue, and cobalt: magenta. Hydrogen atoms omitted for clarity.

EMIDEJ02 was published by Al-Terkawi et. al. in 2018 and has a formula of [Ca(ipa)(H_2O)$_{3.4}$].[131] This MOF was made by ball-milling Ca(OH)$_2$ with H$_2$ipa and is built up from eight- and nine-fold coordinated Ca^{2+} ions.[131] Carboxylate oxygens from the ligands, alongside water molecules, bridge the Ca^{2+} ions together to create one-dimensional helical strands, which are connected through hydrogen bonding.[131] The structure can be seen in Figure

3.15A. According to PoreBlazer, EMIDEJ02 has an LCD and PLD of 3.52 and 1.53 Å respectively, with the LCD being on par with MUF-16 (3.47 Å). However, EMIDEJ02 displayed poor gas uptakes for five gases, with the highest being for CO_2 at 1.37 cm^3/g at 293 K, with significant hysteresis (Figure A.31).

WAMRIN is a Mg^{2+} and H_2ipa-NH_2 MOF which was published by Wang et. al. in 2012 with a formula of $[Mg_3(H_2O)_4(\text{ipa-NH}_2)_2(\text{Hipa-NH}_2)_2]\cdot 4DMA$.[113] This MOF is made by a solvothermal reaction and is built up from octahedrally coordinated Mg^{2+} trinuclear clusters.[113] This results in a eight-fold coordinated SBU with bridging ipa-NH_2 ligands, which create the three-dimensional framework.[113] This framework contains rhombic one-dimensional channels along the b axis, as seen in Figure 3.15B, with a PoreBlazer calculated LCD and PLD of 7.16 and 5.59 Å respectively. In terms of both LCD and PLD, WAMRIN contains one of the largest pore volumes of the 'Larger Pore' MOFs, however this does not necessarily correspond to high uptakes. Of the five gases analysed (at 293 K), the highest uptake was CO_2 at 3.94 cm^3/g (Figure A.32). There was some hysteresis observed for all gases, but it was not quite as large as for EMIDEJ02.

Thirdly, EDOTUN was published by Chen et. al. in 2007 with a formula of $[Co_3Zn_3(\text{ipa})_4(\mu_3\text{-OH})_2(\mu_2\text{-OH})_2(H_2O)_4]\cdot 4.5H_2O$.[114] This MOF is made by a hydrothermal reaction and is built up from octahedrally coordinated Co^{2+} ions and tetrahedrally coordinated Zn^{2+} ions.[114] These metals form Co_3Zn_2 heteropentanculear clusters.[114] The clusters are connected by ipa ligands which adopt various coordination modes, to generate a two-dimensional grid, which stacks to build a three-dimensional MOF (Figure 3.15C).[114] According to PoreBlazer, EDOTUN has an LCD and PLD of 6.35 and 4.49 Å respectively, which are relatively large pores. Much like with WAMRIN, EDOTUN had low gas uptakes across the five gases tested (at 293 K) with the highest being CO_2 at 3.35 cm^3/g, with hysteresis displayed (Figure A.33). The other gases did not have much hysteresis. EDOTUN was fragile as activation caused the MOF to collapse.

Lastly, RUGXUO was published by Hill et. al. in 2015 with a formula of $[Me_2NH_2][Me_4N]_2[Zn_4(\text{ipa-OH})_2(\text{Hipa-OH})_{2.5}]\cdot 3DMF$.[132] RUGXUO is made by a solvothermal reaction and is built up from five- and six-fold coordinated Zn^{2+} ions.[132] Both the hydroxyl and carboxylate groups on the ligand coordinate to the Zn^{2+} ions, through different coordination modes, which builds the structure into a three-dimensional framework, alongside the templating Me_4N^+ and $Me_2NH_2^+$ cations.[132] The structure of this MOF can be seen in Figure 3.15. According to PoreBlazer, RUGXUO has an LCD and PLD of 6.13 and 4.91 Å, respectively, which are moderately large pores for this project. RUGXUO was tested for five gases at 293 K and showed very low uptakes with significant hysteresis (Figure A.34). The highest uptake was for CO_2 at 1.79 cm^3/g. Upon closer inspection, Hill et al. reported that RUGXUO is ‘effectively non-porous after activation’, even though the structure is retained.[132] This lack of porosity is evidenced by the low uptakes.

The results from EMIDEJ02, WAMRIN, EDOTUN, and RUGXUO are interesting as they display that while simulation software like PoreBlazer gives a good indication of pore sizes, experimental work is very much required to see if a MOF will have good gas uptakes or not. According to PoreBlazer, both WAMRIN and EDOTUN had plenty large enough pores to accommodate gases and would thus be expected to have relatively high uptakes, but in practice neither did. This shows that even though PoreBlazer determined a large pore size, there are other variables in play which determine uptake. The flipside is also true. PoreBlazer reported an LCD similar to MUF-16 for EMIDEJ02, however looking at the structure of the MOF (Figure 3.15A), there are very narrow channels, which are far too small to accommodate gases, which is shown by the very low gas uptakes. PoreBlazer works best when the MOF in question strictly obeys its SCXRD structure, as this is what PoreBlazer uses to determine PLD and LCD. However, in reality, a MOF structure can vary due to solvent removal, flexing, or sample treatment, thus the results from PoreBlazer become less accurate and experimental data is more heavily relied upon. RUGXUO is a good example of this, because in theory, it would have high gas uptakes however activation renders the MOF non-porous.

3.3 Conclusion

This chapter outlined the results of working through the ‘Priority’ and ‘Larger Pore’ lists. Majority of the MOFs on these lists could not be synthesized, which shows how sensitive MOF reactions can be to particular laboratory conditions. This chapter outlined the successful results of MOFs from the lists (XADDOX and JETJOI) but also delved into the less-successful MOFs (EMIDEJ02, WAMRIN, EDOTUN, and RUGXUO) and why they likely had the results that they did. These results show that PoreBlazer information, whilst still valuable, relies on a strict dependence on the SCXRD structure, but in reality, structures can vary. Trying to synthesize the MOFs on these lists showed that unexpected new MOFs can be found along the way, in this case MUF-200 and UC-MUF-201. Both MUF-200 and UC-MUF-201 displayed good gas adsorption abilities, alongside being easy to synthesize and they are air stable. MUF-200 and UC-MUF-201 were not the only new phases discovered, as Chapters 4 and 5 will divulge.

Chapter 4 – Low Porosity MOFs

4.1 Introduction

One of the most advantageous characteristics about MOFs is their permanent porosity. Their ability to be crystalline whilst still containing porous voids goes against the norm for molecular materials. Nature favours the formation of dense, symmetrical structures as they are held together by more interactions and are thus more thermodynamically favoured.[54, 153] However, majority of MOFs do not follow this trend and instead are open and porous. The permanent porosity that is found in MOFs is what makes them such attractive materials to work with. In saying that, not all MOFs are porous.[154, 155] Some have densely packed structures with small, virtually non-existent pores. Non-porous, or low porosity, MOFs can be formed by interpenetration or using small linkers that result in tight packing and thus very small voids.[156-158] Examples of the latter include some MOFs made with H_2ipa and its 5′ derivatives.[157, 158] The MOFs that will be discussed in this chapter are all low-porosity MOFs that have been discovered along the course of this project.

As outlined in Chapter 3, many of the MOFs on the 'Priority List' and the 'Larger Pore List' could not be synthesized. This resulted in altering the synthetic conditions in attempt to make the desired MOF. Oftentimes, this did not work and instead, another MOF phase was produced. These MOFs are still worthwhile exploring as even unexpected results can be good; for example, see MUF-200 in Chapter 3. Many of the new MOFs found, as introduced above, have low porosity. All of the MOFs reported in this chapter were checked against the CSD to see if they have been reported before and all bar one has not. Thus the aim of this chapter is to discuss several new MOF materials that were discovered whilst trying to make MOFs from the 'Priority List' and the 'Larger Pore List'. Detailed crystallographic data, PXRD patterns, and all gas adsorption isotherms can be found in the appendix as these MOFs are not suitable for the application of this project and are thus only briefly mentioned.

4.2 Results and Discussion

4.2.1 MUF-202

This MOF, named MUF-202, was found when altering the synthetic conditions used to produce MUF-15-NO_2.[79] It is formed by ball-milling $Co(OAc)_2 \cdot 5H_2O$ and 5-nitroisophthalic acid (H_2ipa-NO_2) in butanol and isopropanol before transferring into a Teflon-lined autoclave reaction vessel with some water and heating to 120°C for 20 hours. The resultant pink, plate crystals have a monoclinic space group, $P2_1/C$, and a formula of [Co(ipa-NO_2)(H_2O)$_3$]. The unit cell dimensions are 11.1 x 14.0 x 7.56 Å with a β angle of 109°.

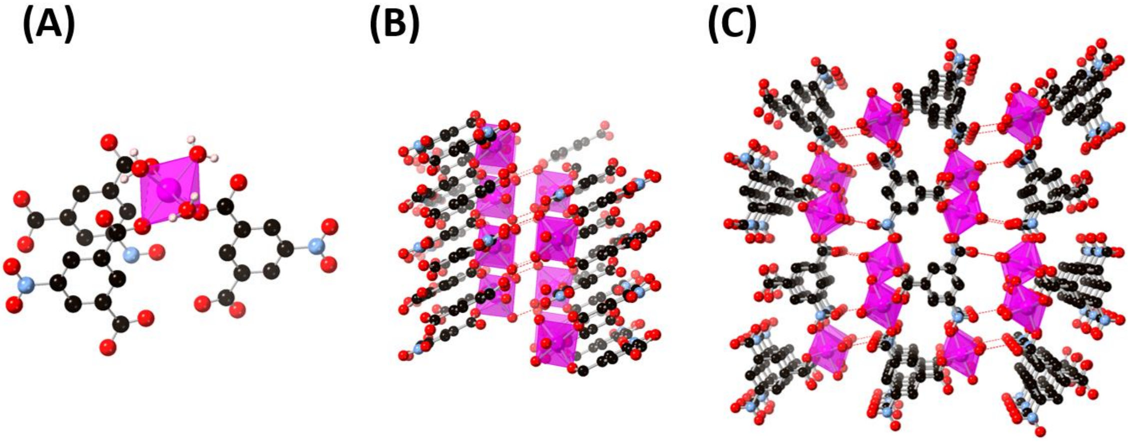

Figure 4.1 (A) Coordination at the metal node of MUF-202. Framework MUF-202 viewed along the b axis (B) and the c axis (C). The red dotted lines denote hydrogen-bonding. Atom colours: carbon: black, oxygen: red, nitrogen: periwinkle blue, cobalt: magenta, and hydrogen: peach. Hydrogen atoms omitted for clarity in (B) and (C).

The Co^{2+} ion has an octahedral geometry and is coordinated to three water molecules and the oxygen atoms of three different ipa-NO_2 molecules (Figure 4.1A). On the ipa-NO_2 ligand, one carboxylate bridges two Co^{2+} ions, while the other carboxylate only coordinates to one. The nitro group remains uncoordinated. Two-dimensional rows of ligand and Co^{2+} then form, with the rows connecting to each other via hydrogen bonding between the bound water molecules (red lines on Figure 4.1B and C). The bridging carboxylate groups on the ipa-NO_2 ligand connect the two-dimensional sheets into a three-dimensional framework (Figure 4.1B and C).

PoreBlazer calculations on MUF-202 showed that the framework has an LCD of 1.68 Å, a PLD of 0.84 Å and no ASA value was determined (due to the small PLD). This alone indicates that MUF-202 is likely to have low gas uptakes, as the pores are too small to accommodate gas molecules. Gas adsorption experiments were nonetheless undertaken. The highest gas uptake was for CO_2 with an uptake of 2.38cm^3/g and the second highest being 2.09 cm^3/g for propylene. These low values are consistent with surface adsorption to the exterior surface as PXRD patterns also show that the MOF collapsed upon activation (Figure A.26).

4.2.2 MUF-203

MUF-203 was found when trying to make LOWQIX, which is a MOF from the ‘Priority List’. The reaction conditions that made MUF-203 ended up being considerably different to the published method for LOWQIX. In theory, LOWQIX crystals form by combining $ZnCl_2$ with H_2ipa in DMF, with the addition of methylamine in acetonitrile.[136] The crystals then grow undisturbed at room temperature.[136] For MUF-203, $Zn(NO_3)_2 \cdot 6H_2O$ and H_2ipa were dissolved in DMF and acetonitrile in a vial and heated to 85°C for 48 hours. The resultant colourless, prismatic crystals have a cubic space group of $F\bar{4}3m$ and a formula of $[Zn_4O(ipa)_3]$. The unit cell dimension is 15.5 Å.

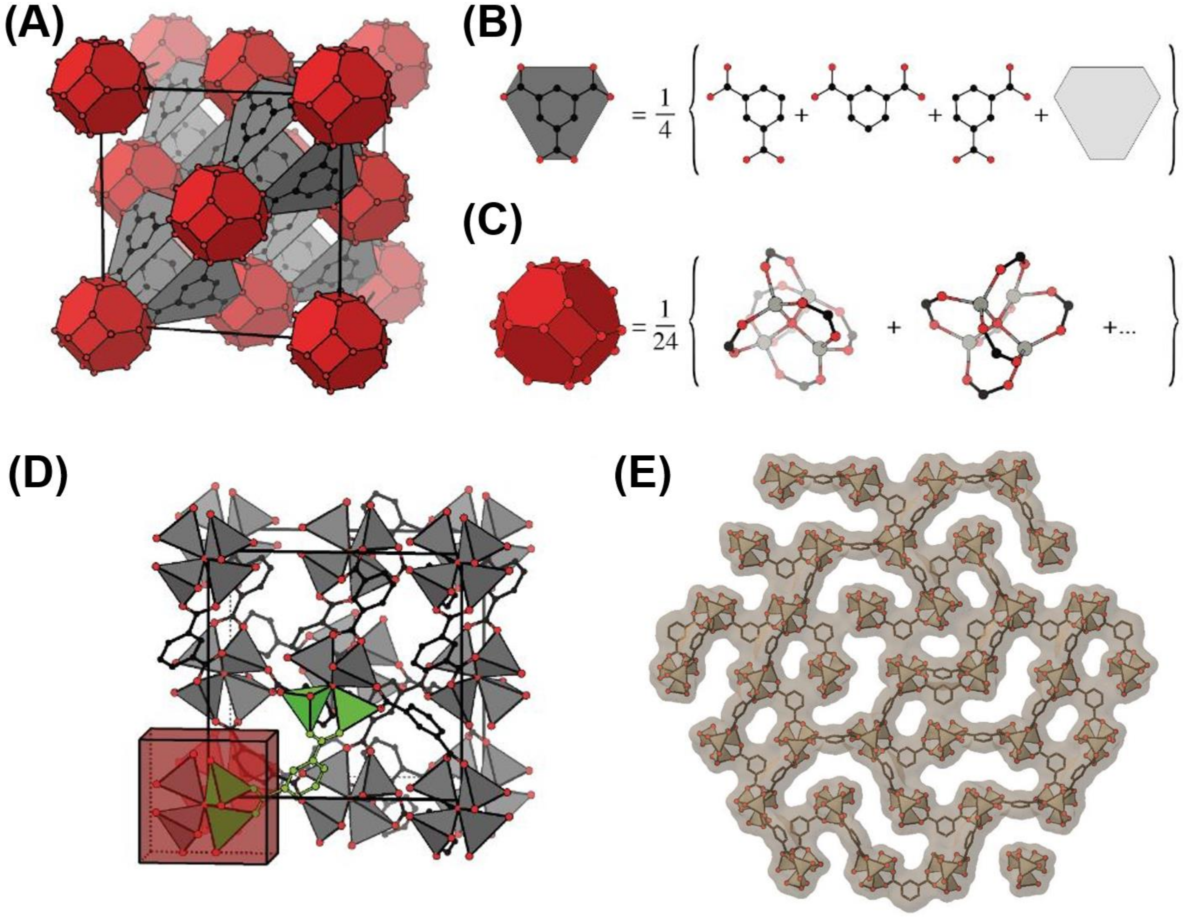

Figure 4.2 (A) Framework of MUF-203 including the disorder. (B) Possible arrangements of the ipa ligand and the schematic tile used to depict them. (C) Metal cluster with the disorder and possible arrangements without disorder. (D) One possible model of MUF-203 without disorder. (E) One possible model of the pore network of MUF-203 without disorder. Atom colours: carbon: black, oxygen: red, and zinc: grey. Hydrogen atoms omitted for clarity. Figure from Meekel et. al.[159]

Upon writing up this thesis, it was discovered that another group had simultaneously and independently discovered this MOF, which they named TRUMOF-1.[159] Due to the difficulty in modelling and presenting the disorder in MUF-203 (*vide infra*), Figure 4.2 is an adaptation from the figures in the paper by Meekel et. al..[159]

The Zn^{2+} ions all coordinate with tetrahedral geometry and form a Zn_4O cluster. These clusters are connected via ipa ligands which build the structure up into a three-dimensional framework. However, MUF-203 is much more complicated than that, as shown in Figure 4.2. This MOF is highly disordered thus all the oxygen and carbon atoms have partial occupancies, which means that the ligands and oxygen atoms on the clusters are not always present or are not always in that orientation. For the ipa ligand, there are three possible arrangements, each at 120° to each other (Figure 4.2B). These ligands are also present at each particular site 25% of the time.[159] There is also disorder at the metal cluster, where each of the possible 12 sites is occupied 50% of the time (Figure 4.2C).[159] An average structure, without modelling the disorder, is shown in Figure 4.2A whereas one of the many, many possible structures is modelled in Figure 4.2D. Due to the different types of disorder in MUF-203 and thus hundreds of possible structures, PoreBlazer calculations could not be performed as it would not be representative of the actual framework. Furthermore, the pore network and pore environments are highly variable, due to the disorder (Figure 4.2E) which would render PoreBlazer results inaccurate.

Gas adsorption experiments showed fairly low gas uptakes. The highest uptake was for acetylene at 12.9 cm^3/g followed by CO_2 at 12.2 cm^3/g. There was not significant separation evident for any key gas pairs except for CO_2 and N_2 (with a N_2 uptake of 1.24 cm^3/g) and ethane (6.42 cm^3/g) and ethylene (9.94 cm^3/g). There was also hysteresis in many of the isotherms. This hysteresis is due to restricted diffusion, likely due to the small pore windows. Due to the low overall uptakes, this MOF was not investigated any further. Interestingly, the Meekel et. al. preprint also presents a few gas adsorption isotherms. They recorded much higher uptakes of around 55 cm^3/g for CO_2 and around 25 cm^3/g for CH_4.[159] They used a different activation protocol, suggesting that this affects the adsorption performance of the MOF. Since they only report CO_2 and CH_4 isotherms (at 273 and 293 K) alongside H_2 and N_2 (at 77 and 87 K), future work could be done on MUF-203 with their activation protocol and different gases to explore the potentially interesting selectivity.

4.2.3 MUF-204

MUF-204 was found when altering the synthetic conditions of WAMRIN, which had both H_2ipa and H_2ipa-NH_2 present.[113] To ensure that only H_2ipa-NH_2 was incorporated into the WAMRIN structure, the H_2ipa was removed from the synthesis. This instead formed MUF-204, which is structurally unrelated to WAMRIN. MUF-204 was made via a solvothermal reaction of $Mg(OAc)_2{\cdot}4H_2O$ and H_2ipa-NH_2 in a solution of *N*,*N*-dimethylacetamide (DMA), ethanol and water in a Teflon-lined autoclave reaction vessel at 110 °C for 3 days. The resultant peach, plate crystals have a triclinic space group of *P-1* and a formula of [Mg(ipa-NH_2)(H_2O)$_2$]. The unit cell dimensions are 7.55 x 8.19 x 8.93 Å with angles of 99.2, 101, and 116°.

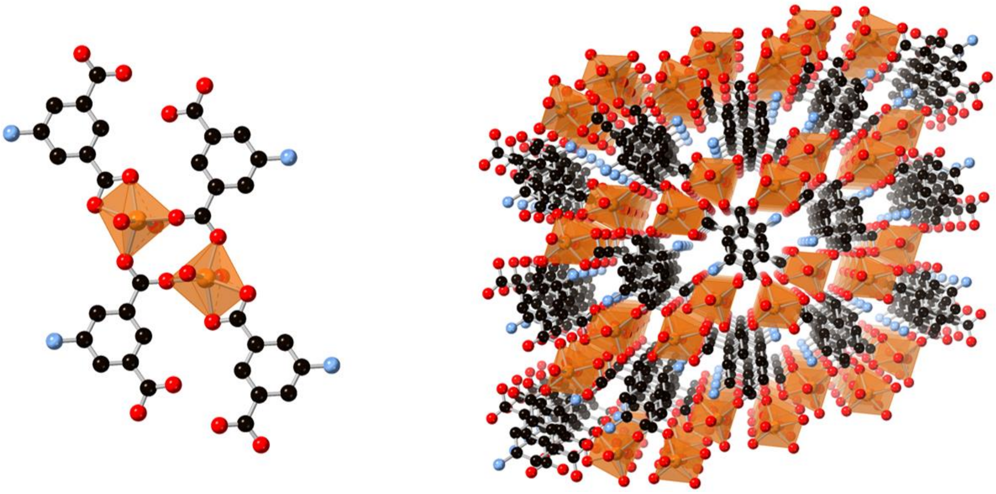

Figure 4.3 (Left) Coordination at two metal nodes of MUF-204. (Right) Framework of MUF-204 viewed along the a axis. Atom colours: carbon: black, oxygen: red, nitrogen: periwinkle blue, and magnesium: orange. Hydrogen atoms omitted for clarity.

The Mg^{2+} ion has a pseudo-octahedral geometry with two water ligands coordinated, in the axial positions, and four oxygens from the carboxylate groups of three different ipa-NH_2 ligands, in the equatorial positions (Figure 4.3 left). On the ipa-NH_2 ligands, one carboxylate group bridges two different Mg^{2+} ions, whilst the other binds to a third Mg^{2+} ion. The amino group remains uncoordinated. Combining the metal and ligand arrangement results in the formation of two-dimensional sheets which connect into a three-dimensional framework (Figure 4.3 right) via hydrogen bonding between the coordinated water molecules and the amino groups on the ligand.

PoreBlazer calculations on MUF-204 showed that the framework has an LCD of 1.66 Å, a PLD of 0.83 Å and no ASA value was determined (due to the small pore sizes). This MOF has very similar pore sizes to MUF-202 and is thus expected to have low gas uptakes. Only two isotherms were collected for this MOF: CO_2 and N_2, with uptakes of 2.47 and 1.69 cm^3/g, respectively at 293 K. Some 'negative' uptakes were observed, which is physically impossible but is due to the low uptakes and instrument error. Hysteresis was also observed, which would be due to restricted diffusion because of the small pores. These low uptakes back up the low porosity seen in both the SCXRD structure and the PoreBlazer calculations.

4.2.4 MUF-205

MUF-205 was discovered when trying to synthesize analogues of WAMRIN with different 5′ functional groups. Whilst WAMRIN itself had poor gas adsorption abilities; the framework does have large pore sizes. Therefore, a different pore environment, created by using a different ligand, could improve the gas adsorption abilities. Therefore, 5-bromoisophthalic acid (H_2ipa-Br) was used in place of H_2ipa-NH_2 in the same synthetic protocol as MUF-204 except that a Schott bottle was used as the reaction vessel. The resultant colourless plate crystals have a monoclinic space group of *P2₁/m* and a formula of $[Mg_3(ipa\text{-}Br)_3(H_2O)(DMA)_2(EtOH)]\cdot H_2O$. The unit cell has dimensions of 9.49 x 22.1 x 20.4 Å, with a β angle of 101°.

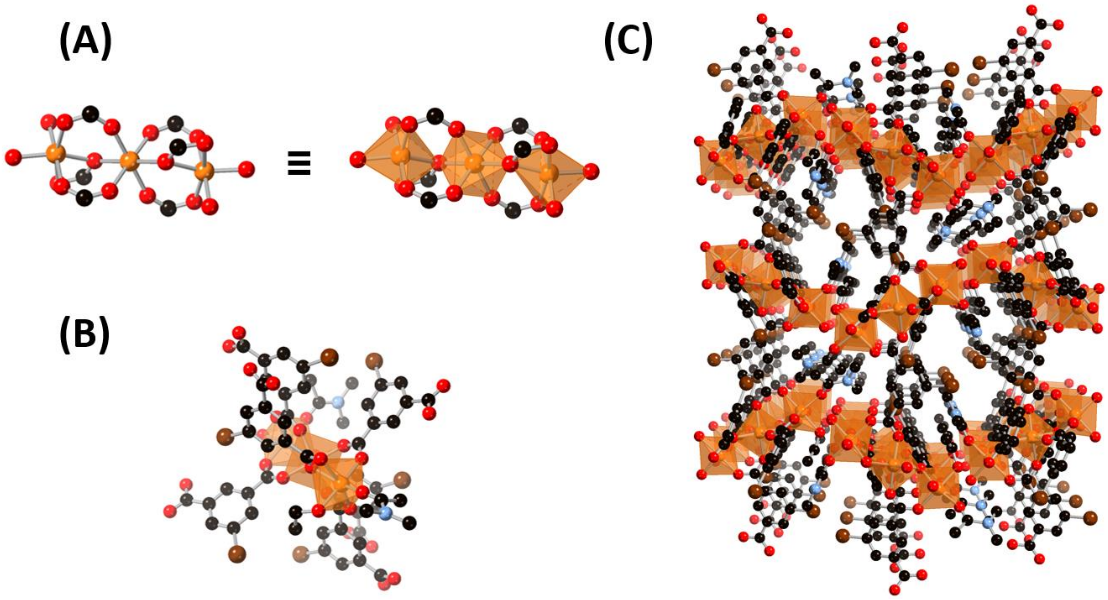

Figure 4.4 (A) Trinuclear cluster of MUF-205. (B) Ligand coordination to the trinuclear cluster. (C) Framework of MUF-205 viewed along the a axis. Atom colours: carbon: black, oxygen: red, nitrogen: periwinkle blue, magnesium: orange and bromine: brown. Hydrogen atoms omitted for clarity.

There are three distinct Mg^{2+} ions, all of which have an octahedral geometry. They connect together to form a trinuclear cluster connected by six bridging ipa-Br ligands (Figure 4.4A). Mg2 is the central Mg^{2+} ion and has six different ipa-Br ligands attached through their carboxylate groups. All of these six ligands bridge to connect Mg2 to Mg1 and Mg3. Mg1 is connected to three different ipa-Br ligands, one coordinated water molecule and one DMA molecule. The water and DMA molecules are on the periphery of the cluster. Mg3 is connected to three different ipa-Br ligands and one coordinated DMA molecule, however instead of the water, Mg3 has an ethanol molecule attached. Again, the DMA and ethanol are on the periphery. The DMA attached to Mg3 displayed positional disorder as the entire moiety could be in two different positions. For Figure 4.4, only one of these orientations was modelled. Coordination of ligands to the trinuclear cluster is shown in Figure 4.4B. The carboxylate groups on the ipa-Br ligands have two coordination modes: one carboxylate bridging two Mg^{2+} ions, and one carboxylate coordinating to one Mg^{2+} ion whilst also bridging two Mg^{2+} ions. Bridging ipa-Br ligands connect the trinuclear clusters together to form a three-dimensional framework (Figure 4.4C).

PoreBlazer calculations on MUF-205 showed that the framework has an LCD of 2.75 Å, a PLD of 1.37 Å and no ASA value was determined due to the small PLD. These values are quite low and suggest that MUF-205 may have low uptakes, which it does. Two attempts at gas adsorption experiments were performed on MUF-205 with different activation conditions to see if that influenced the gas uptakes. Initially, the MOF was activated from ethanol and subsequently it was activated from acetone. From ethanol, the highest uptake was for CO_2 at 1.13cm^3/g followed by CH_4 at 1.02 cm^3/g. From acetone, CO_2 remained the highest at 2.16 cm^3/g, however the second highest this time was H_2 at 1.60 cm^3/g. Some ‘negative’ uptakes were observed, due to instrument error and low uptakes. These low uptakes are not due to framework collapse as the crystallinity and structure was retained after both activation protocols. Whilst the new activation conditions did not greatly improve the uptake, it did increase it a little bit which shows that activation conditions can influence the final gas uptake. Future work could focus on the activation conditions to achieve higher gas uptakes.

4.2.5 Copper MOFs Using the OFEJAM Protocol

OFEJAM (found on the ‘Larger Pore List’) is made with H_2ipa, however, upon attempting to synthesize this MOF the PXRD pattern was inconclusive, and the material was not investigated further (as mentioned in Chapter 3).[144] Nonetheless, the synthetic protocol was used to see if analogues could be made by changing the 5′ functional group. This resulted in the formation of other MOF phases. Three of these will be outlined in this chapter while the rest will be outlined in Chapter 5.

4.2.5.1 With 5-nitroisophthalic acid (H_2ipa-NO_2)

This MOF was made by a solvothermal reaction of $Cu(NO_3)_2{\cdot}3H_2O$ and H_2ipa-NO_2 in a solution of DMF, ethanol and water at 85 °C for 24 hours. Gas adsorption experiments were undertaken; however this MOF did not have high uptakes. The highest uptake was for propylene at 3.59 cm^3/g, followed by CO_2 at 3.51 cm^3/g and ethylene at 2.91 cm^3/g. There was some hysteresis observed, due to restricted diffusion, and also some ‘negative’ uptakes, due to low uptakes and instrument error. The low uptakes suggest that there is adsorption primarily to the exterior surface of the MOF, and no further experiments were performed. No structure was determined for this MOF as it only grew in powder form (and not as single crystals) and, due to the low uptakes, we were not incentivised to push for a structure. This also precluded PoreBlazer calculations.

4.2.5.2 With 5-aminoisophthalic acid (H_2ipa-NH_2)

This MOF was made by combining $Cu(NO_3)_2{\cdot}3H_2O$ and H_2ipa-NH_2 in DMF at 65 °C for six hours to produce a pale green powder. Gas adsorption experiments displayed that this material does not have high uptakes. All of the isotherms were noisy and had significant hysteresis alongside ‘negative’ uptakes due to instrument limitations. CO_2 had the highest uptake of 0.96 cm^3/g followed by ethylene at 0.39 cm^3/g. These low uptakes suggest that this material is either non-porous or collapsed under activation and thus no more experiments were performed. This MOF only grew as a powder and due to the low uptakes, we were not incentivised to push for a SCXRD structure. This also precluded PoreBlazer calculations.

4.2.5.3 MUF-206

MUF-206 was also discovered when altering the synthetic conditions used for OFEJAM. Originally, it co-crystallized with the aforementioned MOF, however further alterations of the synthesis resulted the isolation of MUF-206. MUF-206 is formed by a solvothermal reaction of $Cu(NO_3)_2{\cdot}3H_2O$ and H_2ipa-NH_2 in DMF with a drop of ethanol at 100°C for four hours. The resultant dark green, block crystals have an orthorhombic space group of *Pmna* and a formula of [Cu_2(ipa-NH_2)$_2$(DMF)$_2$]. The unit cell has dimensions of 15.0 x 7.74 x 10.6 Å.

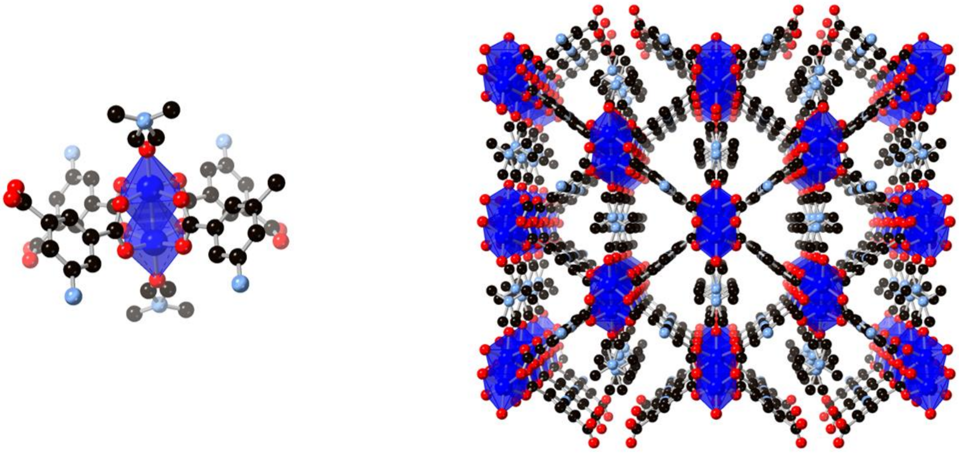

Figure 4.5 (A) Coordination at the paddlewheel cluster of MUF-206. (B) Framework of MUF-206 viewed along the b axis. Atom colours: carbon: black, oxygen: red, nitrogen: periwinkle blue, and copper: royal blue. Hydrogen atoms omitted for clarity.

The Cu^{2+} ions both have octahedral geometry and form a paddlewheel cluster with four ipa-NH_2 ligands connecting two Cu^{2+} ions together through their carboxylate groups (Figure 4.5 left). Each paddlewheel also has two DMF molecules bound to the axial sites. Paddlewheel bridging, by each ipa-NH_2 bridging two paddlewheels, builds the structure up into a three-dimensional framework (Figure 4.5 right).

PoreBlazer calculations on MUF-206 showed that the framework has an LCD of 2.32 Å, a PLD of 1.16 Å, and no ASA value was determined due to the small PLD. These values suggest that the MOF is likely non-porous, however, gas adsorption experiments were still performed. Four isotherms were collected which all show hysteresis, and some showed ‘negative’ uptakes. The highest uptake was for CO_2 at 1.43 cm^3/g followed by CH_4 at 0.61 cm^3/g, ethylene at 0.47 cm^3/g and N_2 at 0.41 cm^3/g. The low uptakes agree with the low PoreBlazer numbers. Interestingly, the coordinated DMF ligands point into the pores of MUF-206. In some studies, coordinated solvent molecules can be removed upon activation.[160] If that were to happen in this case, there would likely be an increase in uptake due to the pore size increasing. Infrared (IR) spectroscopy on a solid sample and ^{1}H NMR spectroscopy on a dissolved sample was used to see if the DMF was removed or not after activation (Figure A.47, Figure A.49 and Figure A.50). Both techniques showed that DMF is still present, however peak integrations showed that there is approximately 0.09 DMF molecules per ipa-NH_2 ligand. In MUF-206’s structure, there is a

1:1 ratio of DMF to ipa-NH_2, suggesting that most but not quite all of the DMF is removed upon activation. The same crystal structure and crystallinity is retained after activation suggesting that the MOF is stable upon DMF removal. PoreBlazer calculations were performed on MUF-206 without DMF and they showed that DMF-free MUF-206 has an LCD of 5.57 Å, a PLD of 4.52 Å, and an ASA of 826 m^2/g which is more than large enough to accommodate gas molecules. Therefore, future work could be done on MUF-206 to improve the activation protocol to fully remove the DMF.

4.3 Conclusion

These MOFs presented in this chapter were all found while trying to synthesize different MOFs or when trying to create an isoreticular series of MOFs. This chapter outlines how MOF synthesis can be unpredictable; resulting in new and different phases to those expected, which was anticipated at the outset of this project. While these new MOFs displayed low porosities and gas uptake, they could have possible uses for other applications such as luminescent or magnetic applications, or more work could be done on these MOFs to improve their gas uptake abilities.

Chapter 5 – Copper MOFs

5.1 Introduction

As introduced back in Chapter 1, the isoreticular principle states that a series of MOFs with the same topology can be made using different ligands that share the same backbone.[54] This concept, in theory, is a simple way to be able to make new MOFs. Whilst the isoreticular principle has worked for many different MOFs, expanding the scope from just one MOF into a family of MOFs, in practice, it does not always work. As shown many times throughout this thesis, MOF synthesis is quite unpredictable. Thus, one may apply the isoreticular principle to try and produce a family of MOFs, however, in practise, alternative frameworks may arise.

OFEJAM, a MOF made from copper ions and H_2ipa, was introduced in Chapters 3 and 4. However, in the original article, OFEJAM contains a polyoxometalate, which sits inside the pores.[144] As the polyoxometalate would block the pores for gas adsorption, we removed it from the synthetic protocol to generate an experimental starting point. This protocol is a simple method which could easily be altered to produce an isoreticular series. To achieve this H_2ipa ligands with different 5′ functional groups were used in place of H_2ipa. The 5′ functional groups investigated were CH_3, OMe, Br, OH, NO_2 and NH_2, of which the latter two were discussed in Chapter 4.

The aim of this chapter is to discuss some of the MOFs that were made using the modified OFEJAM protocol. Three of the four mentioned in this chapter are isoreticular to each other and all of these MOFs appear to be new phases (they are not in the CSD database, and none appear to have been published before). This chapter will also compare the IAST selectivities calculated for these MOFs to some benchmark MOFs from literature (from a non-extensive literature search). For all MOFs, more details about the synthetic procedures, and Q_{st} and IAST analyses can be found in the appendix.

5.2 Results and Discussion

5.2.1 MUF-207, MUF-208 and MUF-209.

MUF-207, MUF-208 and MUF-209 were produced by dissolving $Cu(NO_3)_2{\cdot}3H_2O$ and either 5-methylisophthalic acid (H_2ipa-CH_3), 5-methoxyisophthalic acid (H_2ipa-OMe), or H_2ipa-Br in a solution of DMF, ethanol and water then heating to 85 °C for 24 hours. H_2ipa-

CH_3 resulted in blue plate crystals of MUF-207, H_2ipa-OMe resulted in blue aggregated crystals of MUF-208, and H_2ipa-Br resulted in blue plate crystals of MUF-209. SCXRD structures of MUF-207 and MUF-209 showed that this MOF series crystallizes in the monoclinic *C2/m* space group with unit cell dimensions around 14.1 x 18.8 x 16.8 Å with a β angle of 113° (Table 5.1). The general formula for this series is $[Cu_2(ipa\text{-}X)_2(H_2O)_2]$ (where X= CH_3, OMe or Br). MUF-208 grew as aggregates, which prevented SCXRD analysis. However, given the similarity of their PXRD patterns it was concluded that MUF-208 is isoreticular to MUF-207 and MUF-209 (Figure 5.3 and Figure 5.8).

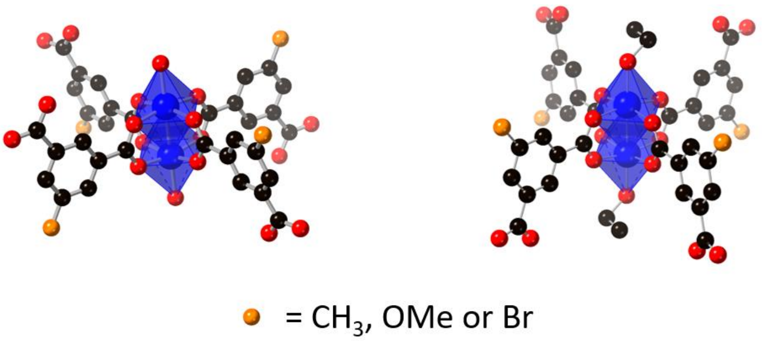

Figure 5.1 Coordination at two of the possible paddlewheel clusters of MUF-207 to MUF-209, where the left paddlewheel has axial coordinated water and the right has coordinated ethanol (the ethanol disorder is modelled). Atom colours: carbon: black, oxygen: red, orange: CH_3, OMe or Br, and copper: royal blue. Hydrogens omitted for clarity.

The Cu^{2+} ions of this MOF series both have an octahedral geometry and form a paddlewheel cluster with four ipa-X ligands connecting two Cu^{2+} ions together through their carboxylate groups (Figure 5.1). In the axial positions of the paddlewheels there is coordinated solvent. The MUF-207 paddlewheels have either water or ethanol coordinated. The ethanol is disordered as the carbon bound to the oxygen can be in one of two positions (with an occupancy of 0.5). The paddlewheels of MUF-209 have only water coordinated. Each ipa-X bridges two paddlewheels, building the structure up into a three-dimensional framework (Figure 5.2).

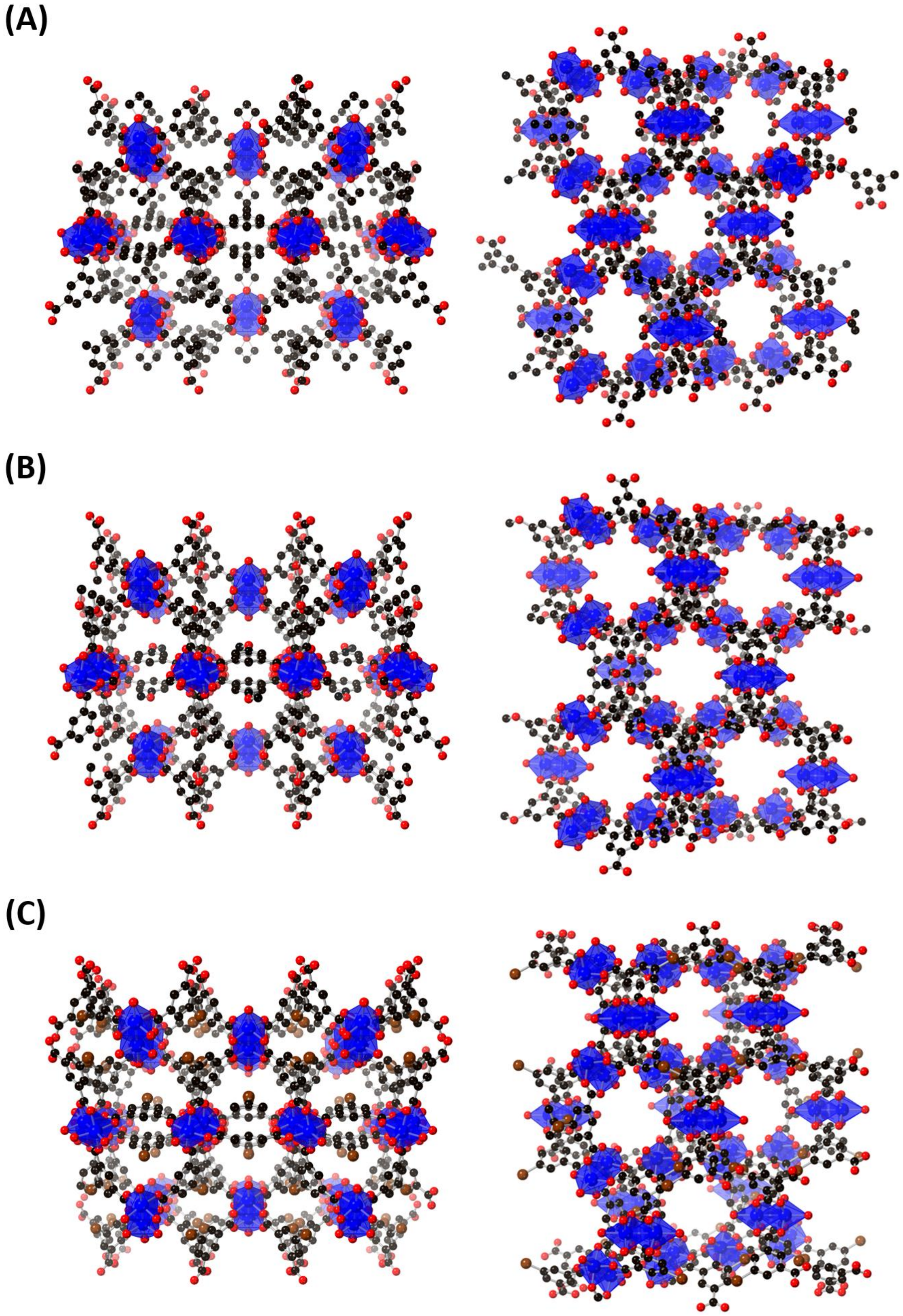

Figure 5.2 In two orientations, the frameworks of MUF-207 (A), MUF-208 (B) and MUF-209 (C) are displayed. The coordinates are simulated for MUF-208 but determined by SCXRD for MUF-207 and MUF-209. Atom colours: carbon: black, oxygen: red, bromine: brown, and copper: royal blue. Hydrogens omitted for clarity.

The structure of MUF-208 shown in Figure 5.2 was made by altering the cif file of MUF-207 to change the methyl groups into methoxy. This allowed for models to be made. The methoxy functional group displayed some disorder when added to the structure, as the methyl portion has free rotation. Therefore one orientation was modelled for the figures and calculations. It was unknown if in MUF-208 there was both ethanol and water coordinated, like in MUF-207, or just water, like in MUF-209. Therefore, for simplicity, it was treated as if there was just water bound.

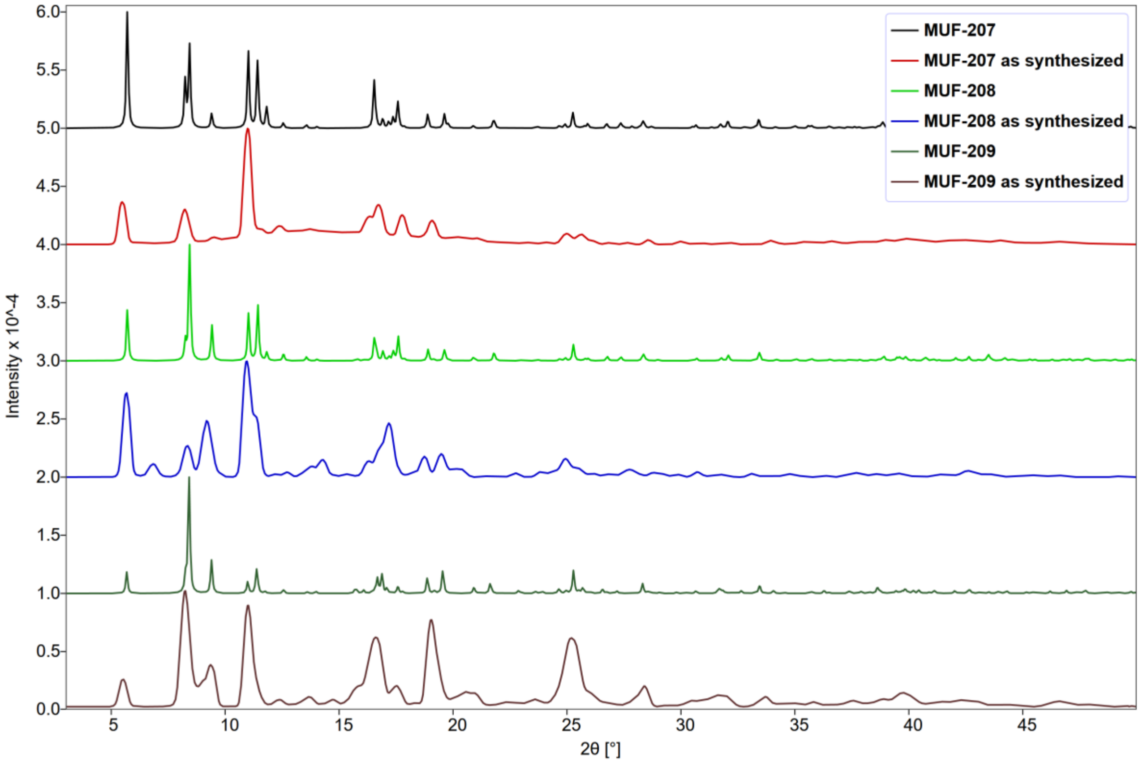

Figure 5.3 PXRD patterns of MUF-207 simulated (black) and as synthesized (red), MUF-208 simulated (lime) and as synthesized (royal blue), and MUF-209 simulated (dark green) and as synthesized (brown).

PXRD patterns highlight the isoreticular nature of MUF-207 to MUF-209, with some variations observed due to the different functional groups and coordinated solvents (Figure 5.3).

Table 5.1 SCXRD data collection and structure refinement details for MUF-207 and MUF-209.

Name	MUF-207	MUF-209
Formula	$[Cu_2(ipa\text{-}CH_3)_2(EtOH)(H_2O)]$	$[Cu_2(ipa\text{-}Br)_2(H_2O)_2]$
Empirical formula	$C_{14.5}H_{12}Cu_{1.5}O_{7.5}$	$C_8H_5BrCuO_5$
Formula weight	50.26	324.57
Temperature (K)	200.0	150.0
Crystal system	monoclinic	monoclinic
Space group	*C2/m*	*C2/m*
a (Å)	14.1094(6)	14.0967(8)
b (Å)	18.7763(7)	18.8104(11)
c (Å)	16.7390(7)	16.8645(11)
$\alpha = \gamma$ (°)	90	90
β (°)	112.391(2)	112.682(3)
Volume (Å^3)	4100.2(3)	4126.0(4)
Z	64	12
ρ_{calc} (g/cm^3)	1.303	1.568
μ (mm^{-1})	2.302	5.675
F(000)	1624.0	1884.0
Radiation	CuKα ($\lambda = 1.54178$)	CuKα ($\lambda = 1.54178$)
2Θ range for data collection (°)	5.71 to 132.024	5.68 to 118.778
Index ranges	$-16 \leq h \leq 16$, $-21 \leq k \leq 20$, $-19 \leq l \leq 19$	$-15 \leq h \leq 15$, $-20 \leq k \leq 20$, $-17 \leq l \leq 18$
Reflections collected	25320	19709
Independent reflections	3482 [$R_{int} = 0.0452$, $R_{sigma} = 0.0382$]	2994 [$R_{int} = 0.0525$, $R_{sigma} = 0.0402$]
Data/restraints/parameters	3482/300/231	2994/139/213
Goodness-of-fit on F^2	1.261	1.126
Final R indexes [I>=2σ (I)]	$R_1 = 0.1430$, $wR_2 = 0.3447$	$R_1 = 0.0840$, $wR_2 = 0.2065$
Final R indexes [all data]	$R_1 = 0.1486$, $wR_2 = 0.3469$	$R_1 = 0.0929$, $wR_2 = 0.2105$
Largest diff. peak/hole (e Å^{-3})	1.74/-1.41	1.76/-1.24

5.2.1.1 MUF-207 Properties

PoreBlazer calculations on MUF-207 gave an LCD of 7.00 Å and a PLD of 2.32 Å. No ASA value was determined due to the small PLD. An experimental BET surface area of 301 m^2/g was determined from a CO_2 isotherm at 195 K. Slow diffusion prevented the uptake of N_2 at 77 K.

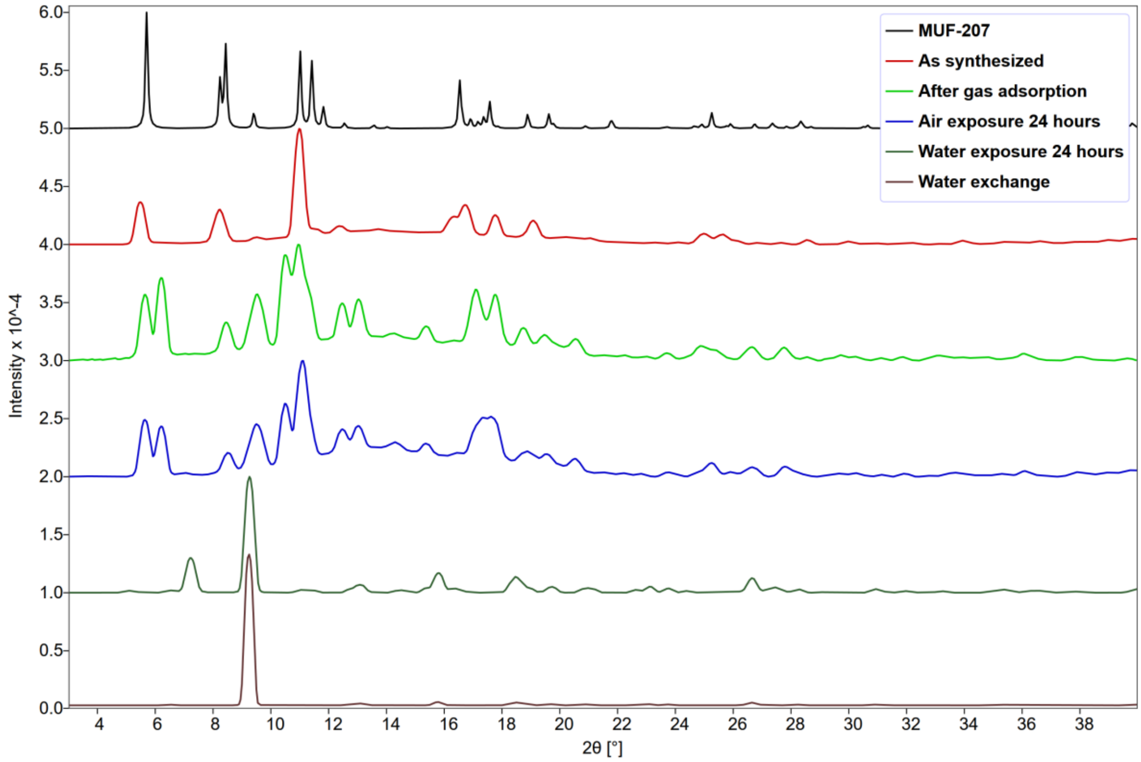

Figure 5.4 PXRD patterns of MUF-207 simulated (black), as synthesized (red), after gas adsorption (lime), after exposure to air for 24 hours (royal blue), after exposure to water for 24 hours (dark green), and after solvent exchange to water (brown).

A comparison of the experimental and simulated PXRD patterns of MUF-207 show a good match with slight shifts after gas adsorption and exposure to the atmosphere (Figure 5.4). The PXRD patterns show a shift in the structure of MUF-207 upon immersion in water (after gas adsorption) and upon solvent exchange from ethanol into water. These two structures appear very similar except the water exposure sample has additional peaks at 5.11, 7.22, 11.1, and 11.4°.

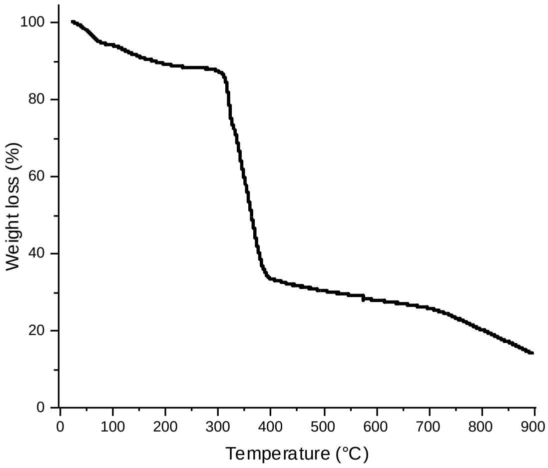

Figure 5.5 TGA curve for MUF-207.

TGA analysis shows that the MOF is stable until around 325 °C where it starts to decompose (Figure 5.5). The weight loss prior to the point corresponds to the removal of solvent trapped in the pores.

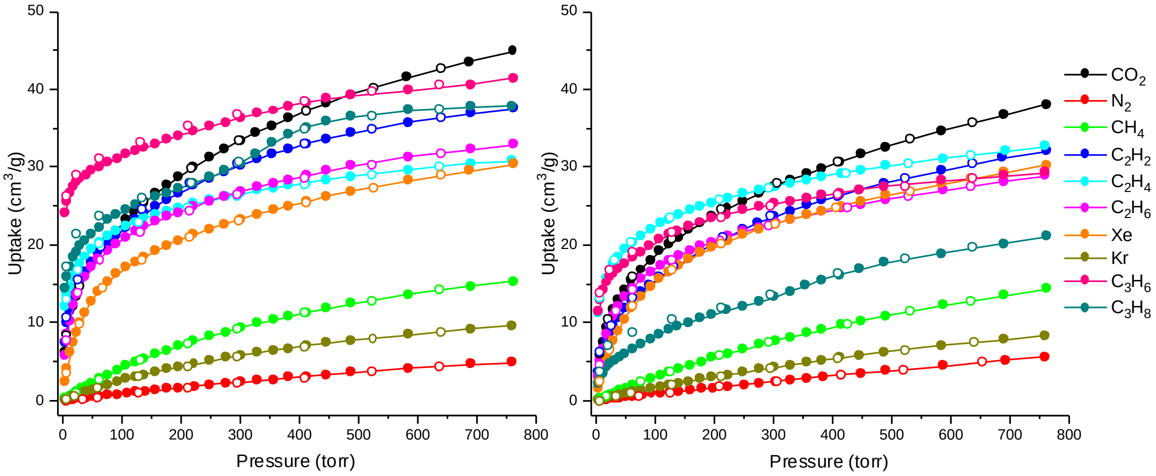

Figure 5.6 Adsorption isotherms of MUF-207 at 273 K (left) and 293 K (right). Coloured circles represent adsorption points and open circles represent desorption points.

MUF-207 displays high uptakes for a number of gases (Figure 5.6). At 293 K and 760 Torr, the highest uptake is seen for CO_2 (38.1 cm^3/g), followed by ethylene (32.7 cm^3/g), acetylene (32.1 cm^3/g), Xe (30.2 cm^3/g), propylene (29.4 cm^3/g), and ethane (28.8 cm^3/g). No hysteresis was observed in these isotherms. Both propylene and propane show hints of flexibility as these isotherms have subtle steps.

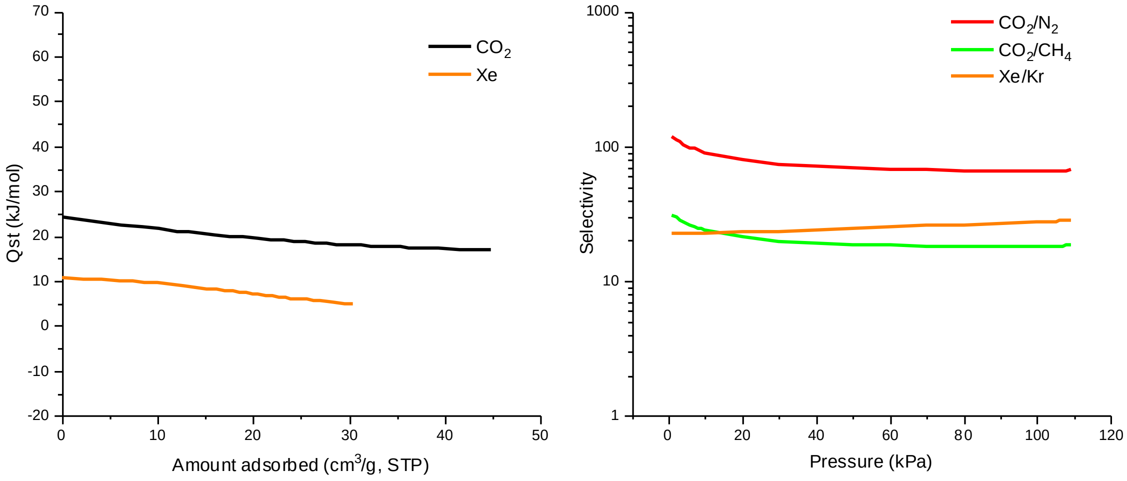

Figure 5.7 (Left) Q_{st} plots for CO_2 and Xe uptakes of MUF-207. (Right) IAST selectivity of 50:50 mixtures of CO_2/N_2, CO_2/CH_4, and Xe/Kr. A logarithmic scale is used for the y axis

Even though there were a number of highly adsorbing gases for MUF-207, Q_{st} was calculated for only two of the highest using the 273 and 293 K isotherms. These are all found in Figure 5.7. At zero coverage, the Q_{st} values were 24.3 kJ/mol for CO_2 and 10.6 kJ/mol for Xe. While propylene displayed high uptakes, Q_{st} was not determined due to the lack of low pressure data points which resulted in higher values than expected for physisorption. Acetylene and ethylene also presented irregular Q_{st} values. Remeasurement of these isotherms (and also propane for interest) with more low pressure data points would result in more reliable Q_{st} values.

IAST selectivities were determined for 50/50 mixtures of three key gas pairs: CO_2/N_2, CO_2/CH_4, and Xe/Kr (Figure 5.7). Of these, CO_2/N_2 had the highest IAST at 66.2, followed by Xe/Kr at 27.5, then CO_2/CH_4 at 18.2 (all at 100 kPa). Comparing both the uptake and the IAST values to a preliminary literature search, MUF-207 has low CO_2/N_2 selectivity, low to moderate CO_2/CH_4 selectivity and moderate Xe/Kr selectivity.[146-148] Overall, even though MUF-207 does not have any ground-breaking selectivities, it has advantages of being quick and easy to synthesize and stable when dried.

5.2.1.2 MUF-208 Properties

PoreBlazer calculations on the model of MUF-208 gave an LCD of 6.02 Å and a PLD of 2.61 Å. No ASA value was determined due to the small pore size. These numbers are reasonable compared to those calculated for MUF-207 suggesting that the structural model is acceptable. An experimental BET surface area of 371 m^2/g was determined from a CO_2 isotherm at 195 K.

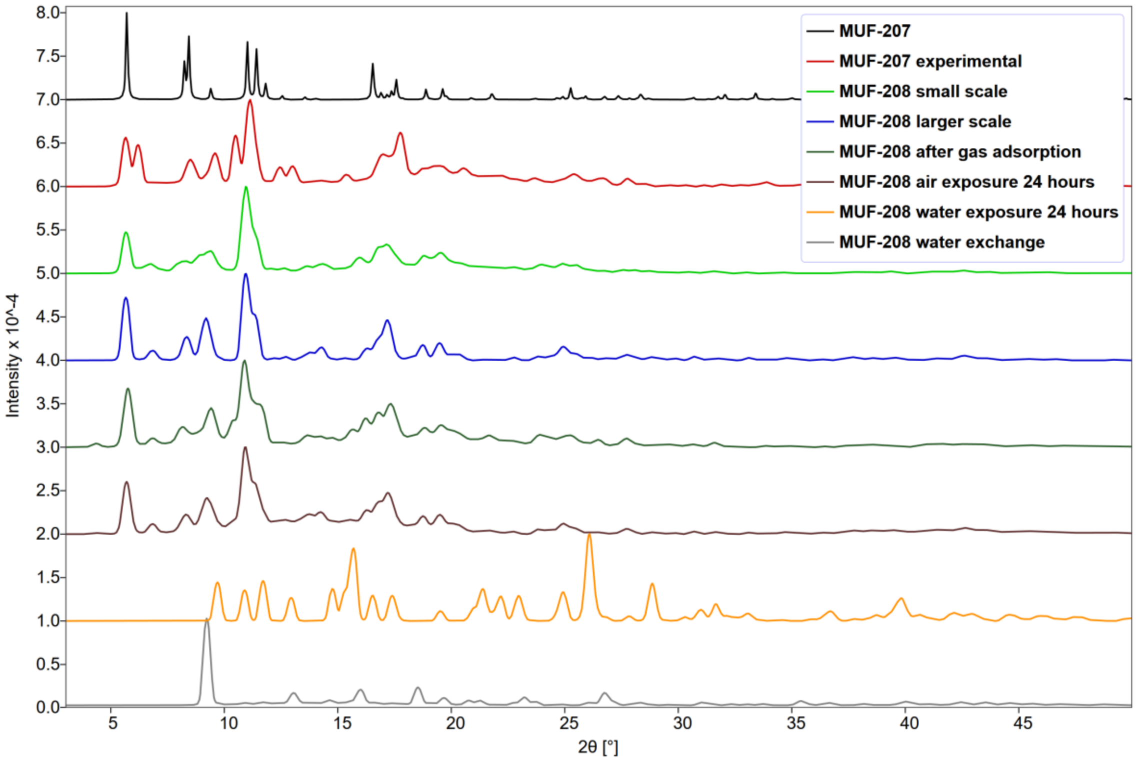

Figure 5.8 PXRD patterns of MUF-207 simulated (black), MUF-207 experimental (red), MUF-208 small scale (lime), MUF-208 larger scale used for gas adsorption (royal blue) after gas adsorption (dark green), after exposure to air for 24 hours (brown), after exposure to water for 24 hours (orange), and after solvent exchange to water (grey).

Figure 5.8 displays the PXRD patterns of MUF-208 compared to MUF-207. There is fairly good similarity between the patterns with the main peaks shifting slightly. Both samples were soaked in DBF to help the patterns match each other better to validate that these MOFs are isoreticular to each other. However, there are additional peaks in the MUF-207 PXRD pattern at 6.18, 10.5 and 17.8°, and additional peaks in the MUF-208 PXRD pattern at 6.80 and 15.9°.

MUF-208 also appears to retain its structure after gas adsorption and exposure to the atmosphere. Upon exposure to water after gas adsorption or by solvent exchange from ethanol, the structure changes. The structure after water exchange is similar to the water exchange structure for MUF-207, however there is an additional peak in MUF-207 at 6.52° and additional peaks in MUF-208 at 10.9, 11.7, 17.4, and 24.9°.

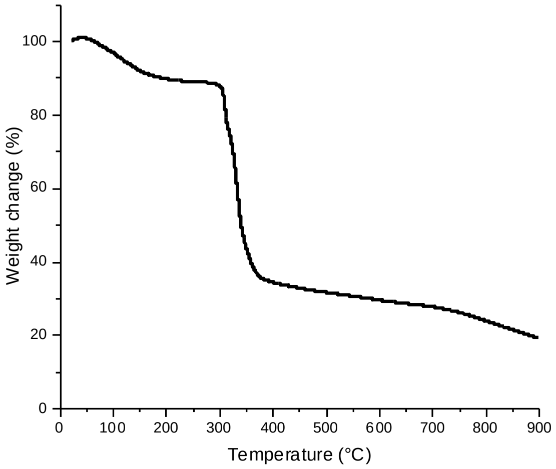

Figure 5.9 TGA curve for MUF-208.

TGA analysis (Figure 5.9) shows that MUF-208 is stable until around 325°C until it starts to decompose. Drops in weight before this stage would correspond to the removal of solvent molecules, such as water, trapped in the pores. This is very similar to the TGA curve for MUF-207.

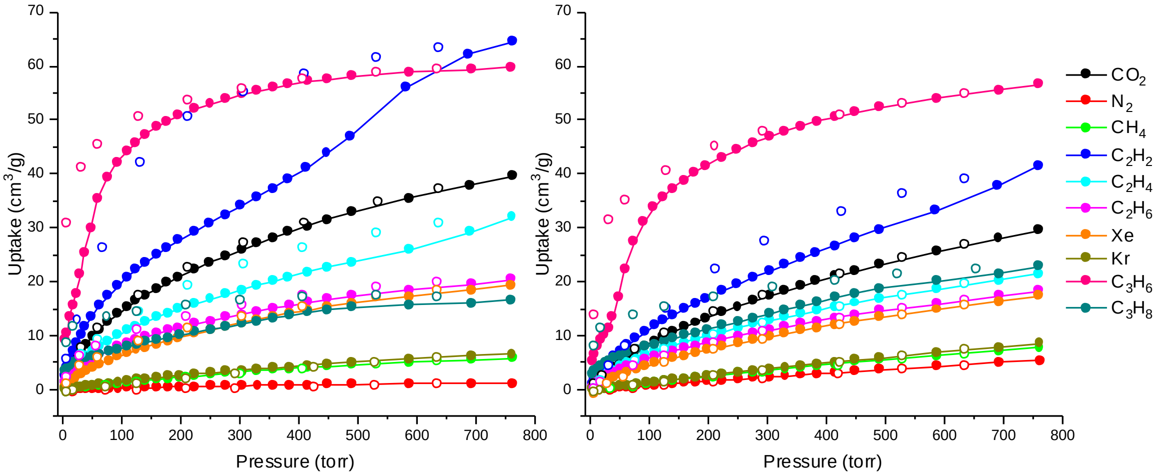

Figure 5.10 Adsorption isotherms of MUF-208 at 273 K (left) and 293 K (right). Coloured circles represent adsorption points and open circles represent desorption points.

MUF-208 displayed generally higher uptakes than MUF-207 (Figure 5.10). Much like MUF-207, the order of the highest adsorbing gases changes between 293 K and 273 K. At 293 K and 760 torr, the highest adsorbing gas was propylene (56.5cm^3/g), followed by acetylene (41.5 cm^3/g), CO_2 (29.5 cm^3/g), propane (22.8 cm^3/g), and ethylene (21.4 cm^3/g). The step in the acetylene isotherm shows that the framework is flexible, which leads to considerable hysteresis. The propane and propylene isotherms also indicate some flexibility, with minor steps and hysteresis.

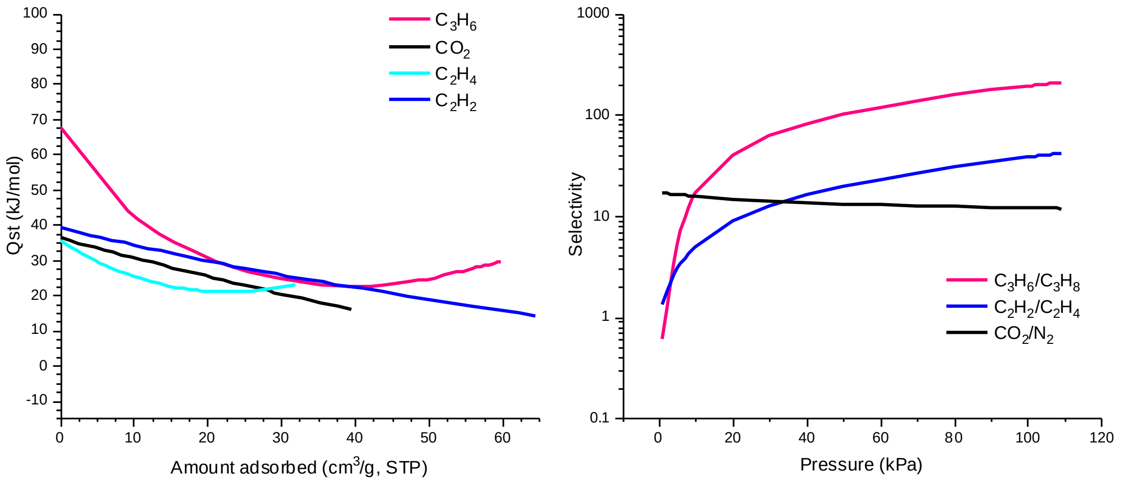

Figure 5.11 (Left) Qst plots for propylene, CO_2, ethylene, and acetylene uptakes of MUF-208. (Right) IAST selectivity of 50:50 mixtures of C_3H_6/C_3H_8, C_2H_2/C_2H_4 and CO_2/N_2. A logarithmic scale is used for the y axis.

The Q_{st} of the highest adsorbing gases was calculated using the 273 and 293 K isotherms (Figure 5.11). The Q_{st} at zero coverage was calculated to be 67.5 kJ/mol for propylene, 36.2 kJ/mol for CO_2, 35.5 kJ/mol for ethylene, and 39.3 kJ/mol for acetylene. Propylene displays a high binding affinity for MUF-208 which is expected due to its high uptakes and slow kinetics **(**Figure 5.12). All gases display a negative trend however propylene and ethylene have a slight positive trend at high pressures, suggesting there may be some cooperative binding between co-adsorbed gas molecules.

Since several key gas showed good differences in uptake, IAST calculations were performed. These key pairs were: C_3H_6/C_3H_8, C_2H_2/C_2H_4 and CO_2/N_2 (Figure 5.11). The C_3 gases display the highest IAST at 192, followed by the C_2 gases at 38, then lastly by CO_2/N_2 at 11.9 (all at 100 kPa with 50/50 composition). These values show that MUF-208 displays very good C_2 and C_3 selectivity and modest CO_2/N_2 selectivity compared to a selection of literature benchmarks.[146, 150, 152] An advantage of the C_2 and C_3 uptakes and IASTs is that neither appear to be at saturation and are thus likely to keep increasing at higher pressures.

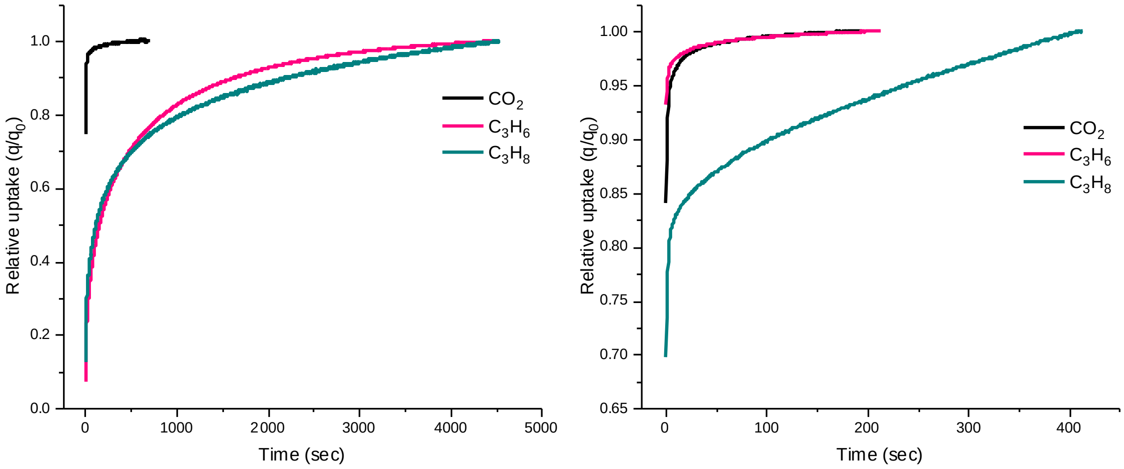

Figure 5.12 Rate of gas uptake by MUF-208 for CO_2, propylene and propane measured at low pressure (left) and high pressure (right). Low pressure measurements were taken at 130 torr for CO_2, 90 torr for propylene and 85 torr for propane. High pressure measurements were taken at 736 torr for CO_2, 743 torr for propylene and 695 torr for propane.

Due to the good C_3 selectivity of MUF-208, kinetics experiments were run to investigate the rates of gas uptake (Figure 5.12). This data was collected at both low and high pressures. CO_2 was used as a comparison since it has rapid uptake kinetics. Propylene showed slow uptake at low pressure, similar to propane, but a fast uptake at high pressure, similar to CO_2. Propane shows slow uptake low pressure and an even slower uptake at high pressure. The slow propane uptake explains the hysteresis observed in the adsorption isotherm as the pores take a long time to fill with gas to reach equilibrium. It also shows that kinetic selectivity may work in agreement with thermodynamic selectivity to enhance the separation of propane and propylene by this MOF.

In conclusion, MUF-208 displays very good selectivities for C_2 and C_3 gases with a good difference in kinetic rates for the C_3 gases. This MOF is also quick and easy to synthesize and is stable in air and after activation.

5.2.1.3 MUF-209 Properties

PoreBlazer calculations were performed on MUF-209 which showed that that MOF has an LCD of 6.12 Å, a PLD of 2.42 Å and no ASA value was determined due to the small PLD. The pore dimensions and environments of MUF-207 to MUF-209 are subtly different, which highlights the power of the isoreticular approach in MOF design. BET calculations were performed using a CO_2 at 195 K isotherm and determined that the surface area of MUF-209 is 149 m^2/g.

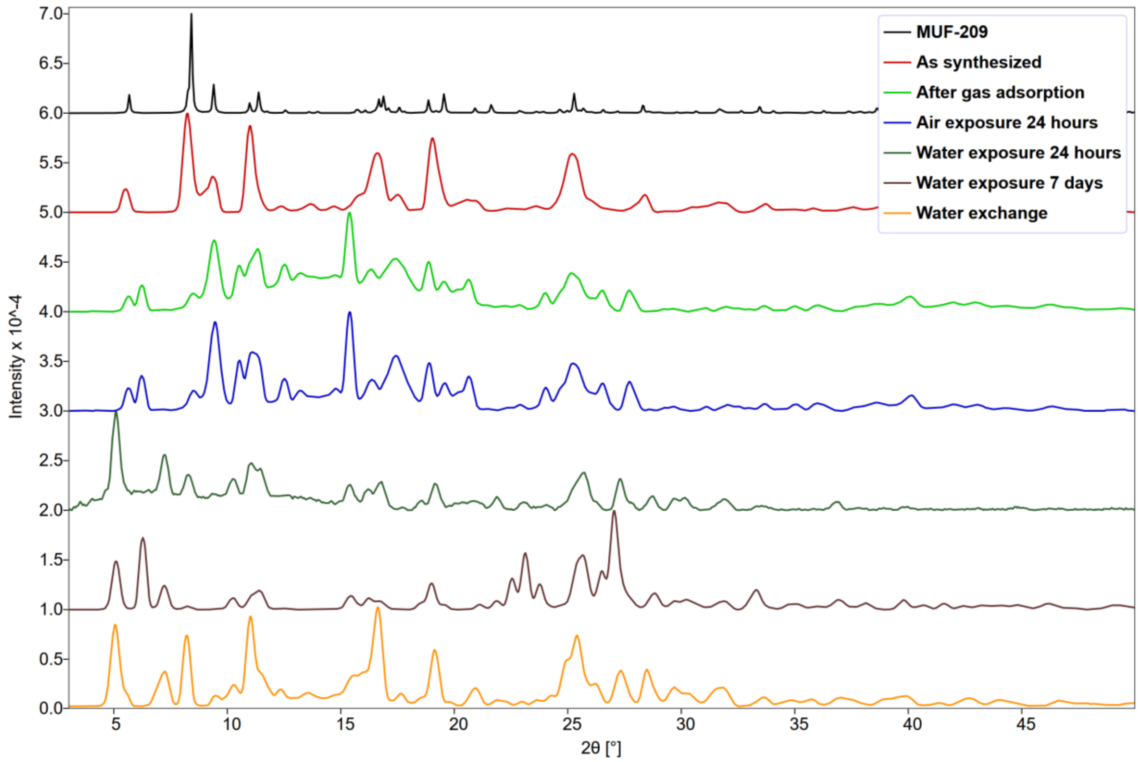

Figure 5.13 PXRD patterns of MUF-209 simulated (black), as synthesized (red), after gas adsorption (lime), after exposure to air for 24 hours (royal blue), after exposure to water for 24 hours (dark green), after exposure to water for 7 days (brown) and after solvent exchange to water (orange).

A comparison of experimental to simulated PXRD patterns can be found in Figure 5.13. There is a good match between the as synthesized and simulated PXRD patterns. However, there does appear to be a shift in peak intensities and the appearance of new peaks at 6.23, 10.5 and 13.2° after gas adsorption. These changes are retained upon exposure to the laboratory atmosphere. The MOF also appears to change structure upon exposure to water (after gas adsorption) and this structure continues to shift until seven days of soaking. Interestingly, even though the structure changes upon exposure to water after gas adsorption, the structure of MUF-209 remains the same after solvent exchange from ethanol to water. The additional peaks at 7.25, 10.3 and 27.3° can be attributed to water adsorption in the pores.

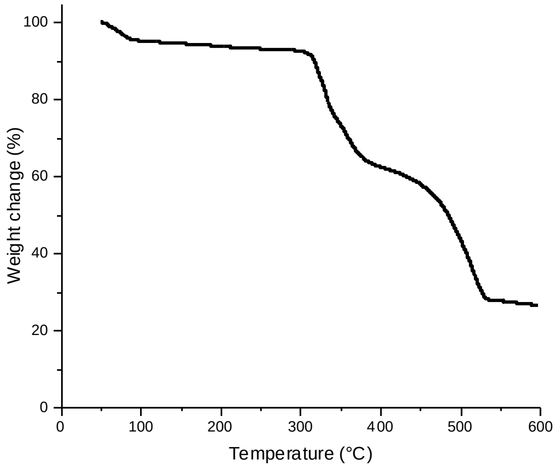

Figure 5.14 TGA curve for MUF-209.

MUF-209 is stable until around 325 °C at which point it starts to decompose (Figure 5.14). The drop in weight before 100 °C corresponds to the removal of solvent trapped in the pores.

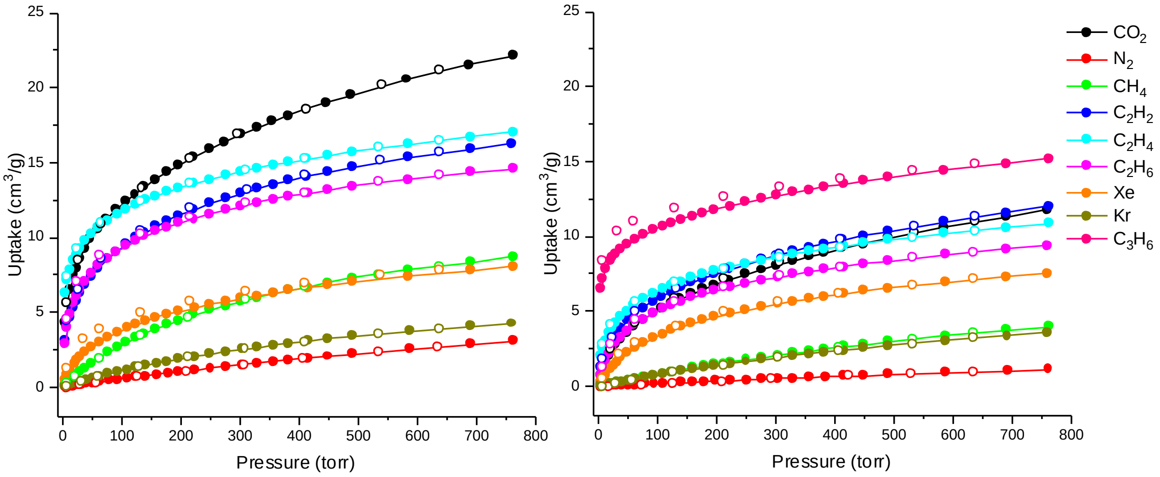

Figure 5.15 Adsorption isotherms of MUF-209 at 273 K (left) and 293 K (right). Coloured circles represent adsorption points and open circles represent desorption points.

MUF-209 shows lower uptakes gas than MUF-207 and MUF-208 (Figure 5.15). As previously observed, the order of gases with the highest uptake changes depending on the temperature. At 293 K and 760 torr, the highest uptake is for propylene (15.2 cm^3/g), followed closely by acetylene (12.0 cm^3/g) and CO_2 (11.8 cm^3/g), then ethylene (10.9 cm^3/g). Interestingly, even though propylene had the highest uptake at 293 K, no adsorption points could be measured at 273 K. No isotherms at either 273 or 293 K were able to be measured for propane. A possible reason for this is that there is slow diffusion of these large gases into the pores of MUF-209. The rate of diffusion is thus so slow that an isotherm cannot be collected.

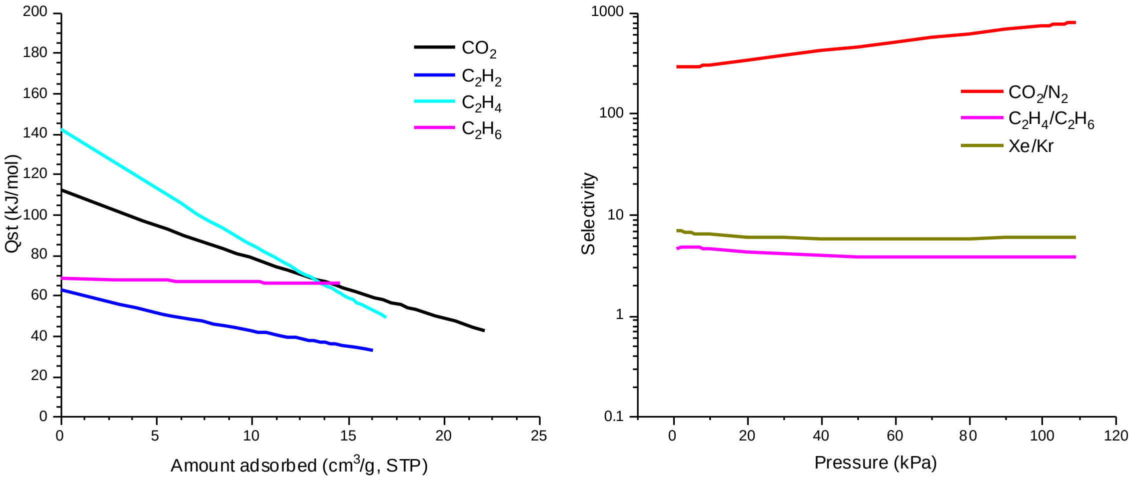

Figure 5.16 (Left) Q_{st} plots for CO_2, acetylene, ethylene, and ethane uptakes of MUF-209. (Right) IAST selectivity of 50:50 mixtures of CO_2/N_2, C_2H_4/C_2H_6 and Xe/Kr.

Q_{st} values were determined for four of the highest adsorbing gases of MUF-209: 112 kJ/mol for CO_2, 62.4 kJ/mol for acetylene, 142.2 kJ/mol for ethylene, and 68 kJ/mol for ethane (Figure 5.16). These values are all much higher than expected for physisorption and further investigation is warranted. We speculate that the framework changes structure around this temperature, which amplifies the uptake at 273 K and precludes Q_{st} calculations by conventional methods.

As there were a few key gas pairs with interesting uptakes, IAST selectivities were calculated for CO_2/N_2, ethylene/ethane and Xe/Kr. CO_2/N_2 has the highest selectivity of 730, followed by Xe/Kr of 5.86 and ethylene/ethane of 3.72. Compared to the uptakes and selectivities of benchmark materials in a preliminary search, MUF-209 displays good CO_2/N_2 selectivity (the IAST selectivity itself is very good but the uptakes are quite low), but modest ethylene/ethane and Xe/Kr selectivities.[147, 148, 161]

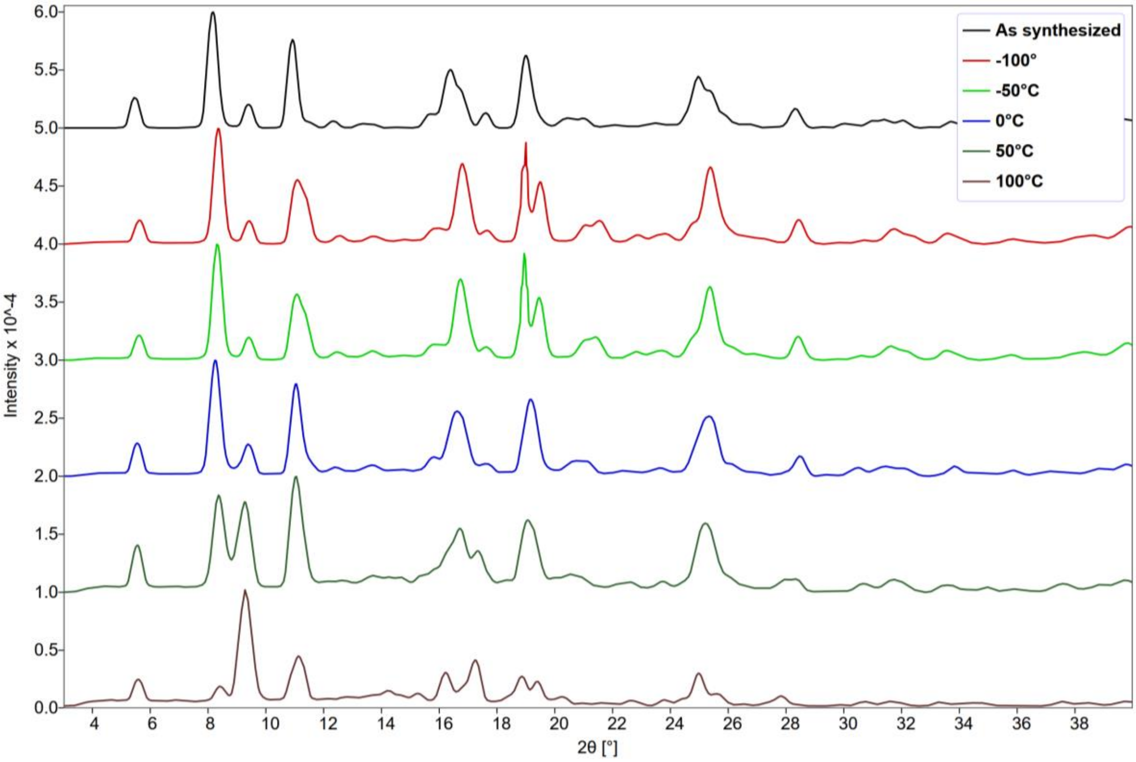

Figure 5.17 PXRD patterns of MUF-209 as synthesized (black), at -100°C (red), at -50°C (lime), at 0°C (royal blue), at 50°C (dark green), and at 100°C (brown).

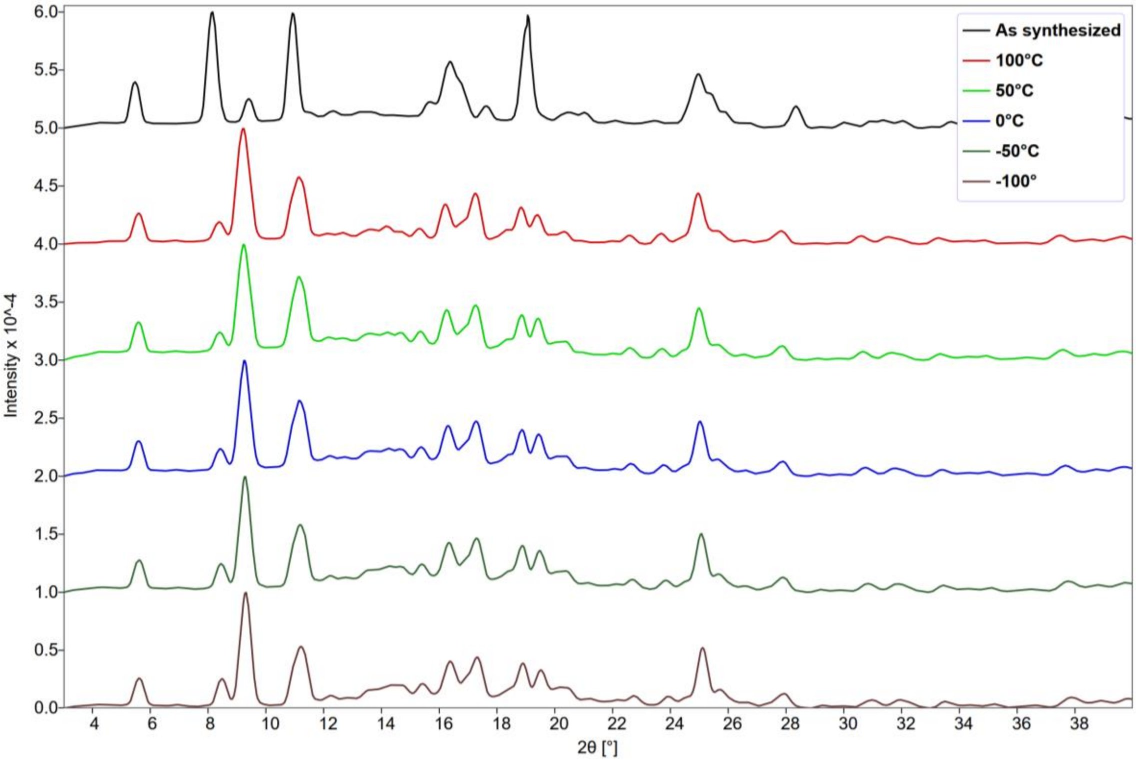

Figure 5.18 PXRD patterns of MUF-209 as synthesized (black), at 100°C (red), at 50°C (lime), at 0°C (royal blue), at -50°C (dark green), and at -100°C (brown).

The temperature-dependent hypothesis mentioned previously was investigated by checking the PXRD patterns at different temperatures to see if any changes occur which could be indicative of the MOF flexing or entirely changing its structure after activation (Figure 5.17 and Figure 5.18). First the sample was cooled to -100 °C then slowly heated to +100 °C with PXRD patterns taken at 25 °C intervals (only 50°C intervals are shown in the figures). The pattern started to shift at 50 °C and was completed by 100 °C (Figure 5.17). To test if the structural change was reversible, the opposite experiment was performed i.e. starting at +100 °C and cooling to -100 °C (Figure 5.18). This experiment showed that the change is irreversible, as upon cooling the new structure remained the same. SCXRD experiments were performed at 75°C to try capture this structure. While a clear picture did not emerge, the "high temperature' unit cell could be determined (32.1 x 18.8 x 12.9Å, with a β angle of 101°), which was different to the original cell (14.1 x 18.8 x 16.9 Å, with a β angle of 113°). Interestingly, this shifted structure is not a great match to the structure of MUF-209 after gas adsorption as the new peaks seen after gas adsorption do not correspond to the new or shifted peaks in the "high temperature" structure. MUF-209 was heated at 100 °C under vacuum for activation thus after gas adsorption, one would expect the PXRD pattern to match the high temperature ones here. This suggests that the vacuum and thus solvation of the MOF could play a role in its structure. While these experiments open more doors than they close, it introduces the interesting behaviour of MUF-209 which would be worth further investigation.

5.2.2 MUF-210

We attempted to extend this isoreticular series of MOFs by using 5-hydroxyisophthalic acid (H_2ipa-OH). This resulted in green crystals (named MUF-210), unlike H_2ipa-CH_3, H_2ipa-OMe, and H_2ipa-Br, which formed blue crystals. The only change to the general synthetic procedure was the omission of water.

SCXRD analysis of MUF-210 shows that the MOF crystallizes in the monoclinic $P2_1/c$ space group, with unit cell dimensions of 7.68 x 10.7 x 15.1 Å, with a β angle 93.2°. The formula of MUF-210 is $[Cu_2(ipa\text{-}OH)_2(DMF)_2]$. Additional crystallographic details can be found in Table 5.2.

Table 5.2 SCXRD data collection and structure refinement details for MUF-210.

Formula	$[Cu_2(ipa\text{-}OH)_2(DMF)_2]$
Empirical formula	$C_{11}H_{11}CuNO_6$
Formula weight	316.75
Temperature (K)	293.15
Crystal system	monoclinic
Space group	$P2_1/c$
a (Å)	7.679(4)
b (Å)	10.690(4)
c (Å)	15.099(5)
$\alpha = \gamma$ (°)	90
β (°)	93.155(18)
Volume ($Å^3$)	1237.6(8)
Z	4
ρ_{calc} (g/cm^3)	1.700
μ (mm^{-1})	2.735
F(000)	644.0
Radiation	CuKα (λ = 1.54184)
2Θ range for data collection (°)	10.144 to 96.182
Index ranges	$-7 \le h \le 7$, $-10 \le k \le 10$, $-14 \le l \le 14$
Reflections collected	4180
Independent reflections	1154 [R_{int} = 0.1412, R_{sigma} = 0.1530]
Data/restraints/parameters	1154/93/175
Goodness-of-fit on F^2	1.077
Final R indexes [$I>=2\sigma$ (I)]	R_1 = 0.0998, wR_2 = 0.2505
Final R indexes [all data]	R_1 = 0.1962, wR_2 = 0.3128
Largest diff. peak/hole (e $Å^{-3}$)	0.64/-0.56

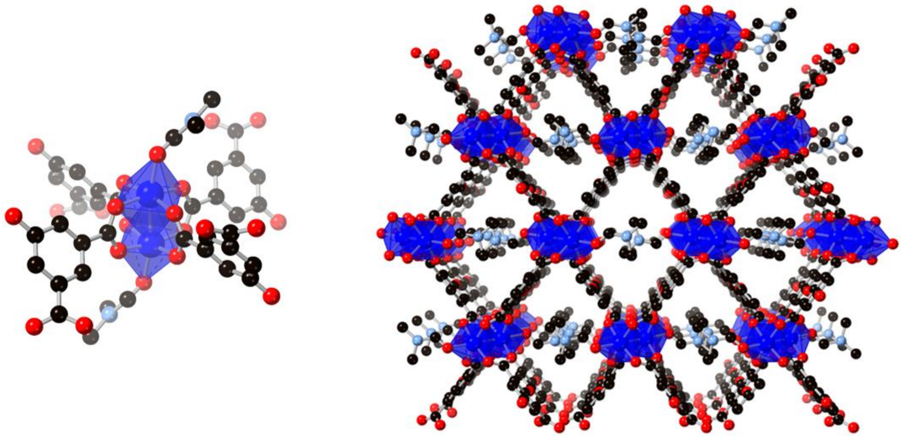

Figure 5.19 (Left) Coordination at the paddlewheel cluster of MUF-210. (Right) Framework of MUF-210 viewed along the a axis. Atom colours: carbon: black, oxygen: red, nitrogen: periwinkle blue, and copper: royal blue. Hydrogens omitted for clarity.

Much like MUF-207 to MUF-209, the Cu^{2+} ions have an octahedral geometry and form a paddlewheel cluster with four ipa-OH ligands coordinated in the equatorial positions (Figure 5.19). However, instead of water in the axial positions, MUF-210 has coordinated DMF molecules which point inside the pores. Each ipa-OH ligand coordinates to two paddlewheels through its two carboxylate groups, thus bridging the paddlewheels and building the structure up into a three dimensional framework (Figure 5.19). The hydroxyl groups on the ligand remain uncoordinated.

MUF-210 tended to grow either as a powder or as crystal aggregates, which made it very difficult to collect SCXRD data. Single crystals were eventually synthesized. The PXRD pattern simulated from the SCXRD structure is compared to experimental PXRD patterns below (Figure 5.20). Many of the peaks match however there are several extra peaks in the experimental pattern compared to the simulated pattern when the MOF was prepared on a larger scale. The differences arise due to non-zero intensities of the reflections around 5.9, 8.3, 12.7, 13.3, and 21.7° in the experimental patterns, which are predicted to have zero intensity using the SCXRD model. This likely arises from differences in solvent occupying the pores. There are unexpected minor peaks in the experimental pattern (6.6 and 9.05°), which may arise from an impurity phase. The PXRD patterns show that MUF-210 maintains its structure and crystallinity after gas adsorption and after exposure to the laboratory atmosphere. However, the framework is not stable when immersed in water (Figure 5.20).

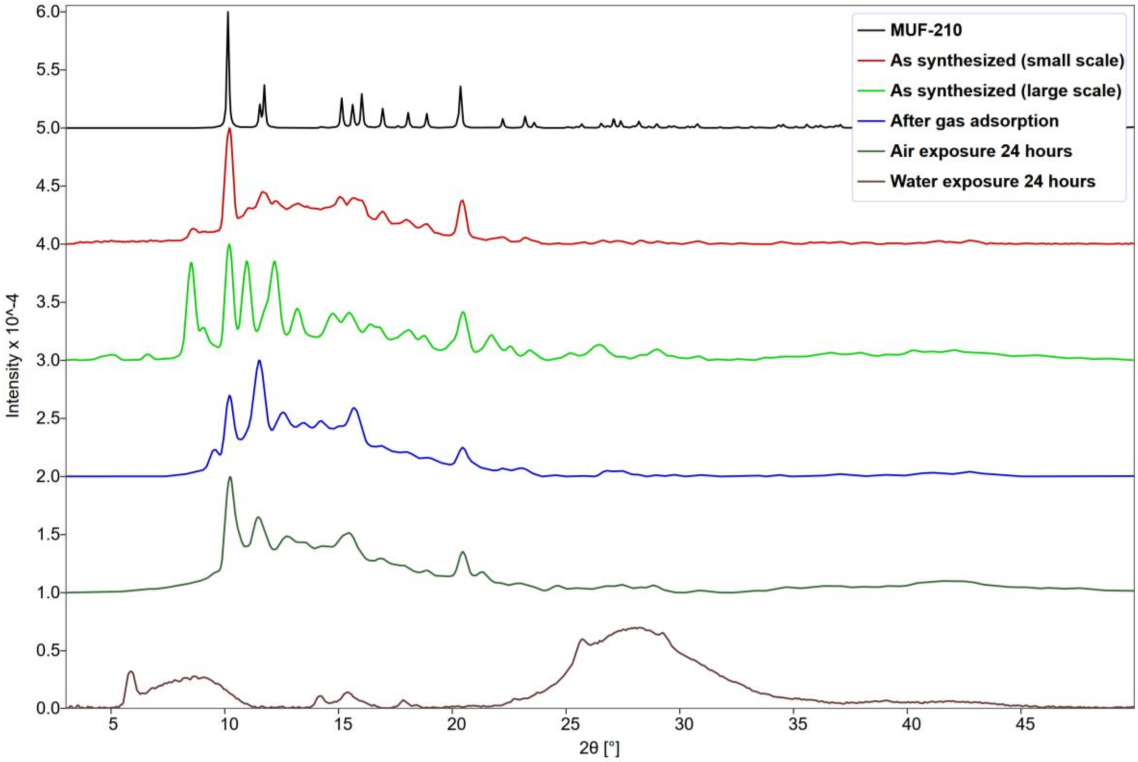

Figure 5.20 PXRD patterns of MUF-210 simulated from the SCXRD structure (black), as synthesized (red and lime), after gas adsorption (royal blue), after exposure to air for 24 hours (dark green), and after exposure to water for 24 hours (brown).

We determined the pore size distribution (PSD) using a CO_2 at 273 K isotherm. For PSD, a N_2 at 77 K isotherm is normally used, however an appropriate model for the small pore sizes could not be found. Using the CO_2 at 273 K isotherm, the calculated pore size was 5.73 Å with a surface area of 110 m^2/g (Figure A.45). This pore size can be compared to the PoreBlazer results from the SCXRD data but with the DMF removed from the axial paddlewheel sites. This gave an LCD of 5.59 Å and a PLD of 4.53 Å, which is similar to the calculated PSD, which indicates a good match between the experimental PSD and the SCXRD structure. Clearly the DMF is removed upon activation, which was confirmed by IR spectroscopy on a solid sample and ^1H NMR spectroscopy on a dissolved sample (Figure A.48, Figure A.51 and Figure A.52). It is worth noting that leaving the coordinated DMF in place results in an LCD of 2.03 Å and PLD of 1.25 Å, which is much smaller than the PSD calculated from the adsorption isotherm.

The surface area of MUF-210 was determined by BET analysis of the N_2 at 77 K isotherm (Figure A.44). This BET surface area is 233 m^2/g which, as expected, is higher than that calculated from the CO_2 at 273 K isotherm. The ASA calculated by PoreBlazer for DMF-free

MUF-210 (939 m^2/g) is considerably higher than both of these, which provides scope for further work.

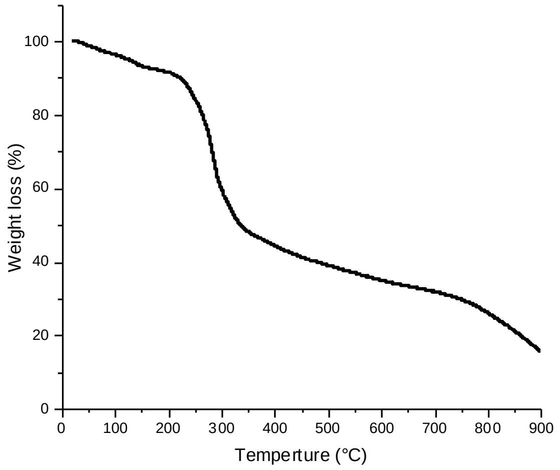

Figure 5.21 TGA curve for MUF-210.

MUF-210 is stable upon heating to 300°C until it starts to decompose (Figure 5.21). Weight loss up to this point can be attributed to the removal of solvent from the pores.

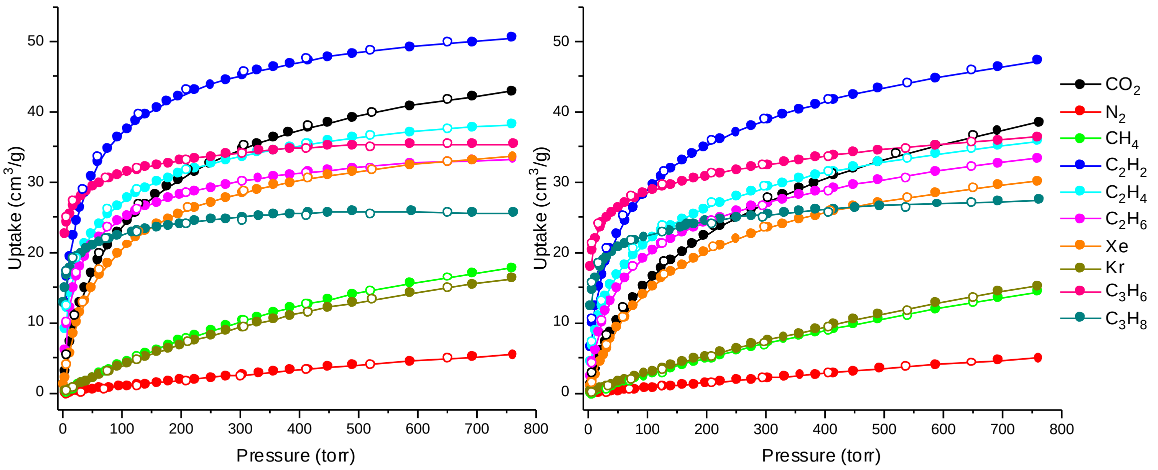

Figure 5.22 Adsorption isotherms of MUF-210 at 273 K (left) and 293 K (right). Coloured circles represent adsorption points and open circles represent desorption points.

Gas adsorption isotherms at 273 and 293 K show that MUF-210 has decent uptakes across a range of gases (Figure 5.22). The highest adsorbing gas (at 293 K and 760 torr) is acetylene (47.2 cm^3/g), followed by CO_2 (38.6 cm^3/g), propylene (36.4 cm^3/g), ethylene (35.9 cm^3/g) and ethane (33.4 cm^3/g). There is no hysteresis observed in the isotherms. These isotherms indicate that there are several key gas pairs worth investigating with IAST, such as the C_3 gases or acetylene/CO_2.

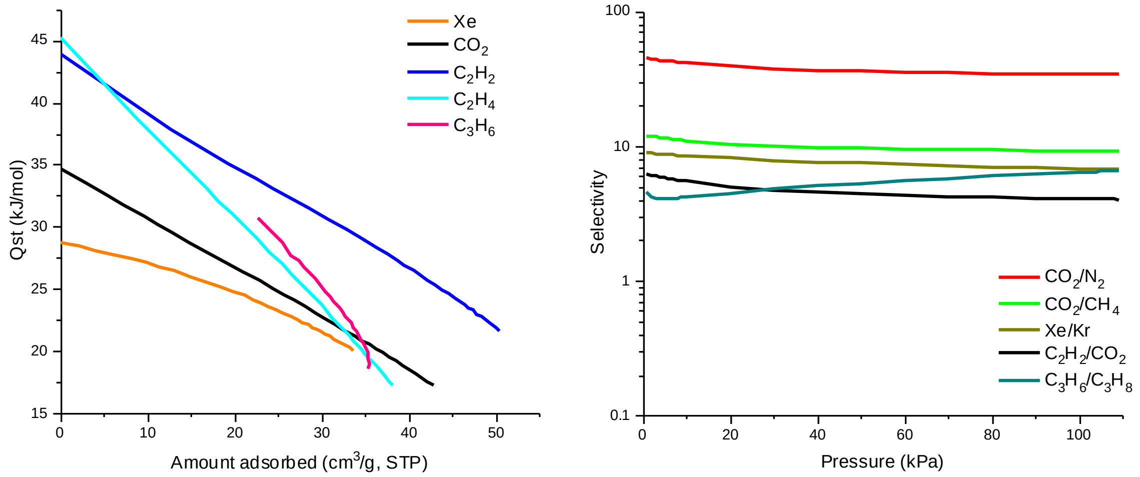

Figure 5.23 (Left) Qst plots for Xe, CO_2, acetylene, ethylene, and propylene uptakes of MUF-210. (Right) IAST selectivity of 50:50 mixtures of CO_2/N_2, CO_2/CH_4, Xe/Kr, C_2H_2/CO_2, and C_3H_6/C_3H_8 at 293 K.

Q_{st} values were determined for five of the highest adsorbing gases of MUF-210 (Figure 5.23) using 273 and 293 K isotherms. The Q_{st} at zero coverage was calculated to be 28.7 kJ/mol for Xe, 34.7 kJ/mol for CO_2, 43.9 kJ/mol for acetylene, and 45.2 kJ/mol for ethylene. Q_{st0} was not determined for propylene due to the lack of data points at very low pressures. All gases display a negative trend for Q_{st} which is expected.

IAST selectivities using 293 K isotherms were calculated for five key gas pairs for MUF-210 (Figure 5.23). These pairs are CO_2/N_2, CO_2/CH_4, Xe/Kr, C_2H_2/CO_2, and C_3H_6/C_3H_8. Of these five, CO_2/N_2 has the highest selectivity (at 100 kPa) of 34.3, followed by CO_2/CH_4 at 9.24, then Xe/Kr at 6.79, then propylene/propane at 6.36, and lastly acetylene/CO_2 at 4.04. These values combined with the corresponding gas uptakes were compared to a preliminary literature search. This showed that MUF-210 displays moderate CO_2/N_2 selectivity, low CO_2/CH_4 selectivity, low Xe/Kr selectivity, low-moderate acetylene/CO_2, and low-moderate propylene/propane selectivity.[146-149, 152] While MUF-210 does not set a new benchmark for gas separations, it is easy to synthesize, has a low cost, and is stable in air and after gas adsorption.

5.3 Conclusion

This chapter discussed four new copper-based MOFs, MUF-207 – MUF-210, that were found using the synthesis of a MOF from the ‘Larger Pore List’. The first three of these MOFs form an isoreticular series with different 5′ functional groups protruding into the pores to tune the pore environments and thus gas uptakes and selectivities. MUF-207 displays moderate selectivities while MUF-208 displays very good propylene/propane and acetylene/ethylene selectivities, and MUF-209 displays good CO_2/N_2 selectivity. MUF-210, which is the MOF in this chapter that is not part of the isoreticular family, displays low to moderate selectivities. All of these MOFs are easy to synthesize, are air stable, and can potentially be scaled up.

Chapter 6 – Conclusions and Future Work

6.1 Conclusions

The overall aim of this project was to explore MOFs derived from isophthalic acids for the adsorptive separation of key gas pairs. To achieve this goal, we formed the 'Priority List' and 'Larger Pore List' as starting points. Some of these MOFs were made and other new phases were discovered over the course of the project.

PoreBlazer was a very important tool in this project as the values it produced were pivotal in forming the two lists. This project showed that PoreBlazer is a very useful guide in finding materials that may show good gas uptake. However, PoreBlazer relies heavily on the experimental structure being exactly the same as the SCXRD structure and that this remains static. In practice this is not always the case since activation can bring about structural changes. This shows that PoreBlazer is a good guide, however it should be one of many variables kept in consideration when targeting MOFs for gas adsorption studies.

Another important conclusion from this project is that many literature protocols are not reproducible. This was a disappointing discovery as it meant that the majority of the MOFs on our lists could not be reproduced, which hindered the discovery of high-performance materials. In spite of this, reported protocols do provide an experimental basis for discovering new phases, which led to some exciting results.

Overall, the approach adopted to tackle this research was successful as it allowed for a streamlined process with clear objectives. The lists not only provided clear starting points, but they narrowed down what is a vast pool of MOFs allowing the focus to be made on ones that have the potential to separate important gas pairs. This approach also allowed us to explore new phases that formed, of which there were many. And, as the previous chapters have outlined, several of these new phases had good results which could be further investigated in the future. Thus, this thesis is able to report many positive results and has generated exciting avenues for future work.

6.2 Future Work

- Though counted as a successful MOFs from the 'Priority List', XADDOX which has a formula of $[Co_6(\mu_3\text{-}OH)_2(ipa)_5(H_2O)_5]\cdot 8H_2O$, has proven difficult to reproduce and scale up. Thus, more work could be done on this synthesis to reproduce and scale it up to be able to collect a better set of isotherms. IAST calculations and a literature comparison can then be done on the new isotherms.

- XADDOX displays high uptakes for ethylene and ethane, thus suggesting that acetylene may have high uptakes too. Therefore, if more XADDOX was made, then acetylene isotherms could be measured, as well as CH_4, which was also missed out.
- UC-MUF-201 displays good C_3 selectivity and relatively high uptakes, indicating that it would be worthwhile performing kinetics studies to explore if there is a degree of kinetic selectivity that is complementary to the thermodynamic selectivity.
- Meekel et. al. reported CO_2 and CH_4 isotherms which had higher uptakes than we found for MUF-203.[159] Thus, future work could be done on the activation conditions of MUF-203 to first replicate the reported uptakes (likely by using the reported activation conditions), then to test the range of gases we have available to see if MUF-203 displays any promising selectivities.
- Further work could be done on optimising the activation conditions of MUF-205 and MUF-206 to increase their gas uptakes. MUF-205 has already indicated improved gas adsorption abilities with different activation conditions, and MUF-206 has pore sizes that are favourable to accommodate gas molecules and is thus likely to have improved uptakes. Optimization can include changing the solvent that MOF is activated from and/or the activation temperature.
- When exchanged from ethanol to water, MUF-207 formed singular bright blue crystals (Figure 6.1). SCXRD analysis could be performed on these crystals to see if they have an interesting, stable structure. Furthermore, if it is a stable structure, gas adsorption studies could be undertaken.

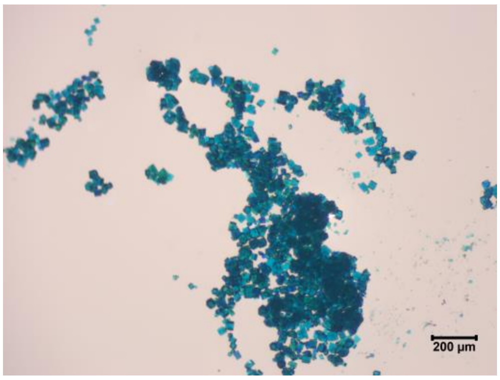

Figure 6.1 Optical micrograph of MUF-207 after water exchange.

- Recollection of the acetylene and ethylene isotherms of MUF-207 could also be performed to produce more reliable Q_{st} values.
- The PXRD patterns of MUF-209 displayed a shift in the framework structure at temperatures greater than 75 °C. More investigation on this framework shift could be done, such as determining a SCXRD structure and determining what was the exact framework structure that the gas adsorption studies were performed on.
- The calculated and experimentally determined ASA values of MUF-210 were considerably different to each other, which provides scope for future work to investigate why there is such a difference.
- UC-MUF-201, MUF-207 and MUF-210 all displayed high uptakes for propylene and propane, however, these isotherms lacked data points in the very low pressure regions. This made reliable Q_{st} calculations difficult. Therefore, these isotherms could be recollected with more low pressure points, and Q_{st} redetermined.
- Whilst making the copper-based MOFs with the OFEJAM synthesis, a few more ligands were tried (structures below in Figure 6.2). These all resulted in the formation of MOFs which had different PXRD patterns to the MUF-207-209 series. The middle MOF had a PXRD pattern very similar to UC-MUF-201 and TAGQUQ, suggesting another possible analogue. Due to time constraints, these MOFs were not investigated any further. It would be interesting to continue investigating these MOFs and their gas adsorption properties as they are more exotic H_2ipa derivative ligands.

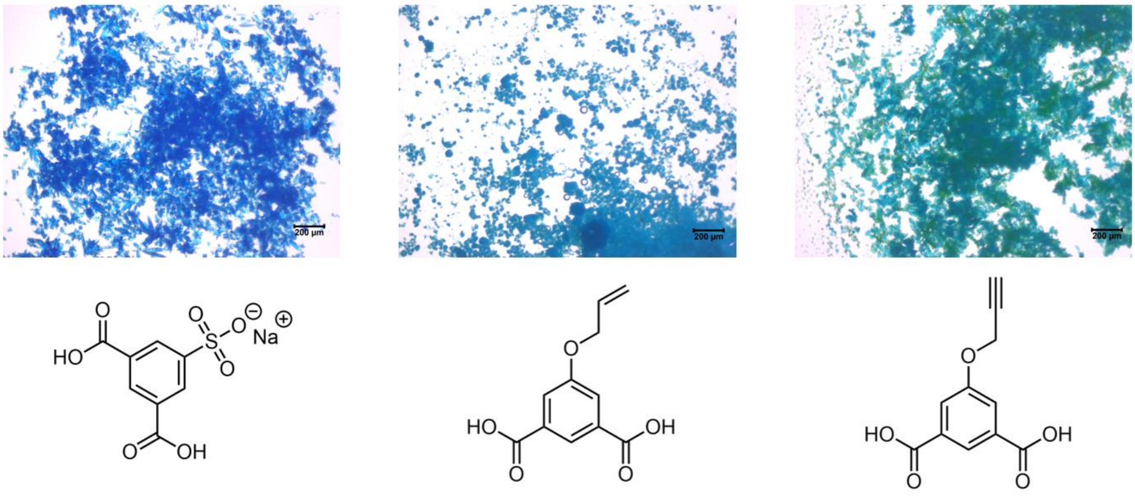

Figure 6.2 Optical micrographs of copper MOFs made with the corresponding ligand below.

- The isophthalic acids used for this project are only a small number of potential 5′ isophthalic acids that could be used. Thus future work could expand on the ligand reaction scope to include other 5′ derivative H_2ipa ligands such as F, Cl, I, CN, or PO_3H
- As mentioned throughout this thesis, many of the MOFs on the ‘Priority List’ and the ‘Larger Pore List’ could not be made. Many had several attempts however due to time contains, some only had a few. Therefore, more work could be done on these MOFs had only a few synthesis attempts, to see if they could be made in the future.
- Also due to time constraints, gas breakthrough analysis was not performed on any of the successful MOFs in this project. Many of them, such as UC-MUF-201, MUF-208 and MUF-209, could display very interesting breakthrough profiles. To achieve this, the syntheses should be scaled up (to ≈ 1 g) and breakthrough experiments conducted using the setup in our laboratory.

Chapter 7 – References

1. Lin, R.-B.; Xiang, S.; Zhou, W.; Chen, B. Microporous Metal-Organic Framework Materials for Gas Separation. *Chem* **2020,** *6* (2), 337-363.

2. Li, H.; Li, L.; Lin, R.-B.; Zhou, W.; Zhang, Z.; Xiang, S.; Chen, B. Porous Metal-Organic Frameworks for Gas Storage and Separation: Status and Challenges. *EnergyChem* **2019,** *1* (100006), 1-39.

3. Blackman, A.; Bottle, S. E.; Schmid, S.; Mocerino, M.; Wille, U.; Brady, J. E.; Senese, F.; Brown, W. H.; Poon, T.; Olmstead, J.; Williams, G. M. *Chemistry*. 3rd ed.; John Wiley & Sons Australia: Milton QLD Australia, 2016.

4. Anslyn, E. V. *Modern Physical Organic Chemistry*. 1st ed.; University Science Books: Sausalito, CA, 2005.

5. Nave, C. R. Electric Quadrupole. http://hyperphysics.phy-astr.gsu.edu/hbase/electric/elequad.html (accessed 8th March).

6. Qazvini, O. T.; Babarao, R.; Telfer, S. G. Selective Capture of Carbon Dioxide from Hydrocarbons Using a Metal-Organic Framework. *Nat. Commun.* **2021,** *12* (1).

7. Schrobilgen, G. J. Noble Gas. https://www.britannica.com/science/noble-gas/additional-info#history (accessed 13th August).

8. Mehio, N.; Dai, S.; Jiang, D.-E. Quantum Mechanical Basis for Kinetic Diameters of Small Gaseous Molecules. *J. Phys. Chem. A* **2014,** *118* (6), 1150-1154.

9. Yoon, T.-U.; Baek, S. B.; Kim, D.; Kim, E.-J.; Lee, W.-G.; Singh, B. K.; Lah, M. S.; Bae, Y.-S.; Kim, K. S. Efficient Separation of C_2 Hydrocarbons in a Permanently Porous Hydrogen-Bonded Organic Framework. *Chem. Commun.* **2018,** *54* (67), 9360-9363.

10. Khraisheh, M.; Almomani, F.; Walker, G. High Purity/Recovery Separation of Propylene from Propyne Using Anion Pillared Metal-Organic Framework: Application of Vacuum Swing Adsorption (VSA). *Energies* **2021,** *14* (3), 609.

11. Yang, Y.; Burke, N.; Ali, S.; Huang, S.; Lim, S.; Zhu, Y. Experimental Studies of Hydrocarbon Separation on Zeolites, Activated Carbons and MOFs for Applications in Natural Gas Processing. *RSC Adv* **2017,** *7* (21), 12629-12638.

12. Chen, L.; Reiss, P. S.; Chong, S. Y.; Holden, D.; Jelfs, K. E.; Hasell, T.; Little, M. A.; Kewley, A.; Briggs, M. E.; Stephenson, A.; Thomas, K. M.; Armstrong, J. A.; Bell, J.; Busto, J.; Noel, R.; Liu, J.; Strachan, D. M.; Thallapally, P. K.; Cooper, A. I. Separation of Rare Gases and Chiral Molecules by Selective Binding in Porous Organic Cages. *Nat. Mater.* **2014,** *13* (10), 954-960.

13. Poulsen, T. D.; Ogilby, P. R.; Mikkelsen, K. V. Polarizabilities of the First Excited (a1Δg) and Ground ($X^{3\Sigma}$) States of Molecular Oxygen. *J. Phys. Chem. A* **1998,** *102* (45), 8970-8973.

14. Lin, R.-B.; Xiang, S.; Xing, H.; Zhou, W.; Chen, B. Exploration of Porous Metal–Organic Frameworks for Gas Separation and Purification. *Coord. Chem. Rev.* **2019,** *378,* 87-103.

15. Bhatt, P. M.; Guillerm, V.; Datta, S. J.; Shkurenko, A.; Eddaoudi, M. Topology Meets Reticular Chemistry for Chemical Separations: MOFs as a Case Study. *Chem* **2020,** *6* (7), 1613-1633.

16. Kerry, F. G. *Industrial Gas Handbook*. CRC Press: Boca Raton, Florida, United States of America, 2007.

17. Speight, J. G., Unconventional Gas. In *Natural Gas*, Second ed.; Elsevier: Laramie, Wyoming, USA, 2018; pp 59-98.

18. Li, J.-R.; Ma, Y.; Mccarthy, M. C.; Sculley, J.; Yu, J.; Jeong, H.-K.; Balbuena, P. B.; Zhou, H.-C. Carbon Dioxide Capture-Related Gas Adsorption and Separation in Metal-Organic Frameworks. *Coord. Chem. Rev.* **2011,** *255* (15-16), 1791-1823.

19. Wang, T.; Lin, E.; Peng, Y.-L.; Chen, Y.; Cheng, P.; Zhang, Z. Rational Design and Synthesis of Ultramicroporous Metal-Organic Frameworks for Gas Separation. *Coord. Chem. Rev.* **2020,** *423*, 213485.

20. Ye, R.-P.; Ding, J.; Gong, W.; Argyle, M. D.; Zhong, Q.; Wang, Y.; Russell, C. K.; Xu, Z.; Russell, A. G.; Li, Q.; Fan, M.; Yao, Y.-G. CO_2 Hydrogenation to High-Value Products Via Heterogeneous Catalysis. *Nat. Commun.* **2019,** *10* (1).

21. Osman, A. I.; Hefny, M.; Abdel Maksoud, M. I. A.; Elgarahy, A. M.; Rooney, D. W. Recent Advances in Carbon Capture Storage and Utilisation Technologies: A Review. *Environ. Chem. Lett.* **2021,** *19* (2), 797-849.

22. Li, H.; Wang, K.; Sun, Y.; Lollar, C. T.; Li, J.; Zhou, H.-C. Recent Advances in Gas Storage and Separation Using Metal–Organic Frameworks. *Mater. Today* **2018,** *21* (2), 108-121.

23. Huot, J.; Bose, T. K. Determination of the Quadrupole Moment of Nitrogen from the Dielectric Second Virial Coefficient. *J. Chem. Phys.* **1991,** *94* (5), 3849-3854.

24. Taddei, M.; Petit, C. Engineering Metal–Organic Frameworks for Adsorption-Based Gas Separations: From Process to Atomic Scale. *Mol. Syst. Des. Eng.* **2021,** *6*, 814-875.

25. Sanz-Pérez, E. S.; Murdock, C. R.; Didas, S. A.; Jones, C. W. Direct Capture of CO_2 from Ambient Air. *Chem. Rev.* **2016,** *116* (19), 11840-11876.

26. Matar, S.; Hatch, L. F. *Chemistry of Petrochemical Processes*. Second ed.; Gulf Publishing Company: Houston, Texas, USA, 2000.

27. Wang, B.; Xie, L.-H.; Wang, X.; Liu, X.-M.; Li, J.; Li, J.-R. Applications of Metal–Organic Frameworks for Green Energy and Environment: New Advances in Adsorptive Gas Separation, Storage and Removal. *Green Energy Environ.* **2018,** *3*, 191-228.

28. Harris, P. D.; Barnes, R. The Uses of Helium and Xenon in Current Clinical Practice. *Anaesthesia* **2008,** *63* (3), 284-293.

29. Rochelle, G. T. Amine Scrubbing for CO_2 Capture. *Science* **2009,** *325* (5948), 1652-1654.

30. Chowdhury, F. A.; Yamada, H.; Higashii, T.; Goto, K.; Onoda, M. CO_2 Capture by Tertiary Amine Absorbents: A Performance Comparison Study. *Ind. Eng. Chem. Res.* **2013,** *52* (24), 8323-8331.

31. Choi, S.; Drese, J. H.; Jones, C. W. Adsorbent Materials for Carbon Dioxide Capture from Large Anthropogenic Point Sources. *ChemSusChem* **2009,** *2* (9), 796-854.

32. Patil, G. N.; Vaidya, P. D.; Kenig, E. Y. Reaction Kinetics of CO_2 in Aqueous Methyl- and Dimethylmonoethanolamine Solutions. *Ind. Eng. Chem. Res.* **2012,** *51* (4), 1592-1600.

33. Shaw, D. Behind Shell Technologies: Canslov SO_2 and CO_2 Capture with Devin Shaw. https://www.shell.com/business-customers/catalysts-technologies/resources-library/behind-shell-technologies-cansolv-so2-and-co2-capture-with-devin-shaw.html (accessed 24th February).

34. Aaron, D.; Tsouris, C. Separation of CO_2 from Flue Gas: A Review. *Sep. Sci. Technol.* **2005,** *40* (1-3), 321-348.

35. Weisend, J. G. Cryogenic Technology. *Kirk-Othmer Encyclopedia of Chemical Technology* **2012**. https://doi.org/10.1002/0471238961.0318251501071801.a01.pub3

36. Evans, T.; Grynia, E. *Carbon Capture – Purpose and Technologies*; Gas Liquids Engineering: Calgary, Alberta, Canada, 2020; pp 1-44.

37. Wang, Y.; Peh, S. B.; Zhao, D. Alternatives to Cryogenic Distillation: Advanced Porous Materials in Adsorptive Light Olefin/Paraffin Separations. *Small* **2019,** *15* (25), 1900058.

38. Naik, S.; Schornak, B.; Seadeek, C.; Wesorick, S.; Robertson, M.; Nalbandian, A.; Cotton, S.; Hoffman, N.; Potter, A. Distillation Columns. https://encyclopedia.che.engin.umich.edu/Pages/SeparationsChemical/DistillationColumns/DistillationColumns.html (accessed 23rd March).

39. Hinchliffe, A. B.; Porter, K. E. A Comparison of Membrane Separation and Distillation. *Chem. Eng. Res. Des.* **2000,** *78* (2), 255-268.

40. Bernardo, P.; Drioli, E.; Golemme, G. Membrane Gas Separation: A Review/State of the Art. *Ind. Eng. Chem. Res.* **2009,** *48* (10), 4638-4663.

41. Pandey, P.; Chauhan, R. S. Membranes for Gas Separation. *Prog. Polym. Sci.* **2001,** *26* (6), 853-893.

42. Baker, R. W.; Low, B. T. Gas Separation Membrane Materials: A Perspective. *Macromolecules* **2014,** *47* (20), 6999-7013.

43. Baker, R. W. Future Directions of Membrane Gas Separation Technology. *Ind. Eng. Chem. Res.* **2002,** *41* (6), 1393-1411.

44. Fain, D. E. Membrane Gas Separation Principles. *MRS Bull.* **1994,** *19* (4), 40-43.

45. Li, J.-R.; Kuppler, R. J.; Zhou, H.-C. Selective Gas Adsorption and Separation in Metal–Organic Frameworks. *Chem. Soc. Rev.* **2009,** *38* (5), 1477-1504.

46. Slater, A. G.; Cooper, A. I. Function-Led Design of New Porous Materials. *Science* **2015,** *348* (6238).

47. Wang, X.; Cheng, H.; Ye, G.; Fan, J.; Yao, F.; Wang, Y.; Jiao, Y.; Zhu, W.; Huang, H.; Ye, D. Key Factors and Primary Modification Methods of Activated Carbon and Their Application in Adsorption of Carbon-Based Gases: A Review. *Chemosphere* **2021**, 131995.

48. Ackley, M. W.; Rege, S. U.; Saxena, H. Application of Natural Zeolites in the Purification and Separation of Gases. *Microporous Mesoporous Mater.* **2003,** *61* (1-3), 25-42.

49. Khaleque, A.; Alam, M. M.; Hoque, M.; Mondal, S.; Haider, J. B.; Xu, B.; Johir, M. A. H.; Karmakar, A. K.; Zhou, J. L.; Ahmed, M. B.; Moni, M. A. Zeolite Synthesis from Low-Cost Materials and Environmental Applications: A Review. *Environ Advances* **2020,** *2*, 100019.

50. International Zeolite Association Framework Type Mor. https://europe.iza-structure.org/IZA-SC/framework.php?STC=MOR (accessed 25th November).

51. Çeçen, F., Activated Carbon. In *Kirk-Othmer Encyclopedia of Chemical Technology*, John Wiley & Sons: New York, 2014; pp 1-34.

52. Manocha, S. M. Porous Carbons. *Sadhana* **2003,** *28* (1-2), 335-348.

53. Batten, S. R.; Champness, N. R.; Chen, X.-M.; Garcia-Martinez, J.; Kitagawa, S.; Öhrström, L.; O'Keeffe, M.; Suh, M. P.; Reedijk, J. Terminology of Metal–Organic Frameworks and Coordination Polymers (IUPAC Recommendations 2013). *Pure Appl. Chem.* **2013,** *85* (8), 1715-1724.

54. Yaghi, O. M.; Kalmutzki, M. J.; Diercks, C. S. *Introduction to Reticular Chemistry*. Wiley-VCH: Weinheim, Germany, 2019.

55. Gropp, C.; Canossa, S.; Wuttke, S.; Gándara, F.; Li, Q.; Gagliardi, L.; Yaghi, O. M. Standard Practices of Reticular Chemistry. *ACS Cent. Sci.* **2020,** *6* (8), 1255-1273.

56. Howarth, A. J.; Peters, A. W.; Vermeulen, N. A.; Wang, T. C.; Hupp, J. T.; Farha, O. K. Best Practices for the Synthesis, Activation, and Characterization of Metal–Organic Frameworks. *Chem. Mater.* **2017,** *29* (1), 26-39.

57. Chui, S. S. A Chemically Functionalizable Nanoporous Material $[Cu_3(TMA)_2(H_2O)_3]_N$. *Science* **1999,** *283* (5405), 1148-1150.

58. Mondloch, J. E.; Bury, W.; Fairen-Jimenez, D.; Kwon, S.; Demarco, E. J.; Weston, M. H.; Sarjeant, A. A.; Nguyen, S. T.; Stair, P. C.; Snurr, R. Q.; Farha, O. K.; Hupp, J. T. Vapor-Phase Metalation by Atomic Layer Deposition in a Metal–Organic Framework. *J. Am. Chem. Soc.* **2013,** *135* (28), 10294-10297.

59. Yaghi, O. M.; Li, H. Hydrothermal Synthesis of a Metal-Organic Framework Containing Large Rectangular Channels. *J. Am. Chem. Soc.* **1995,** *117* (41), 10401-10402.

60. Li, Z.; Zhang, J.; Luo, T.; Tan, X.; Liu, C.; Sang, X.; Ma, X.; Han, B.; Yang, G. High Internal Ionic Liquid Phase Emulsion Stabilized by Metal–Organic Frameworks. *Soft Matter* **2016,** *12* (43), 8841-8846.

61. Li, H.; Eddaoudi, M.; Groy, T. L.; Yaghi, O. M. Establishing Microporosity in Open Metal−Organic Frameworks: Gas Sorption Isotherms for Zn(BDC) (BDC = 1,4-benzenedicarboxylate). *J. Am. Chem. Soc.* **1998,** *120* (33), 8571-8572.

62. Li, H.; Eddaoudi, M.; O'Keeffe, M.; Yaghi, O. M. Design and Synthesis of an Exceptionally Stable and Highly Porous Metal-Organic Framework. *Nature* **1999,** *402* (6759), 276-279.

63. Yaghi, O. M.; O'Keeffe, M.; Ockwig, N. W.; Chae, H. K.; Eddaoudi, M.; Kim, J. Reticular Synthesis and the Design of New Materials. *Nature* **2003,** *423* (6941), 705-714.

64. Eddaoudi, M.; Kim, J.; Rosi, N.; Vodak, D.; Wachter, J.; O'Keeffe, M.; Yaghi, O. M. Systematic Design of Pore Size and Functionality in Isoreticular MOFs and Their Application in Methane Storage. *Science* **2002,** *295* (5554), 469-472.

65. Mai, Z.; Liu, D. Synthesis and Applications of Isoreticular Metal–Organic Frameworks IRMOFs-N (N = 1, 3, 6, 8). *Cryst. Growth Des.* **2019,** *19* (12), 7439-7462.

66. Rosi, N. L.; Kim, J.; Eddaoudi, M.; Chen, B.; O'Keeffe, M.; Yaghi, O. M. Rod Packings and Metal−Organic Frameworks Constructed from Rod-Shaped Secondary Building Units. *J. Am. Chem. Soc.* **2005,** *127* (5), 1504-1518.

67. Dietzel, P. D. C.; Panella, B.; Hirscher, M.; Blom, R.; Fjellvåg, H. Hydrogen Adsorption in a Nickel Based Coordination Polymer with Open Metal Sites in the Cylindrical Cavities of the Desolvated Framework. *Chem. Commun.* **2006,** (9), 959.

68. Dietzel, P. D. C.; Morita, Y.; Blom, R.; Fjellvåg, H. An In Situ High-Temperature Single-Crystal Investigation of a Dehydrated Metal-Organic Framework Compound and Field-Induced Magnetization of One-Dimensional Metal-Oxygen Chains. *Angew. Chem. Int. Ed.* **2005,** *44* (39), 6354-6358.

69. Dietzel, P. D. C.; Blom, R.; Fjellvåg, H. Base-Induced Formation of Two Magnesium Metal-Organic Framework Compounds with a Bifunctional Tetratopic Ligand. *Eur. J. Inorg. Chem.* **2008,** *2008* (23), 3624-3632.

70. Sanz, R.; Martínez, F.; Orcajo, G.; Wojtas, L.; Briones, D. Synthesis of a Honeycomb-Like Cu-Based Metal–Organic Framework and its Carbon Dioxide Adsorption Behaviour. *Dalton Trans.* **2013,** *42* (7), 2392-2398.

71. Wang, L. J.; Deng, H.; Furukawa, H.; Gándara, F.; Cordova, K. E.; Peri, D.; Yaghi, O. M. Synthesis and Characterization of Metal–Organic Framework-74 Containing 2, 4, 6, 8, and 10 Different Metals. *Inorg. Chem.* **2014,** *53* (12), 5881-5883.

72. Zhao, S.-N.; Wang, G.; Poelman, D.; Van Der Voort, P. Luminescent Lanthanide MOFs: A Unique Platform for Chemical Sensing. *Materials* **2018,** *11* (4), 572.

73. Furukawa, H.; Cordova, K. E.; O'Keeffe, M.; Yaghi, O. M. The Chemistry and Applications of Metal-Organic Frameworks. *Science* **2013,** *341* (6149), 1230444.

74. Liu, L.; Zhou, T.-Y.; Telfer, S. G. Modulating the Performance of an Asymmetric Organocatalyst by Tuning Its Spatial Environment in a Metal–Organic Framework. *J. Am. Chem. Soc.* **2017,** *139* (39), 13936-13943.

75. Anbu, N.; Dhakshinamoorthy, A. Regioselective Ring Opening of Styrene Oxide by Carbon Nucleophiles Catalyzed by Metal–Organic Frameworks under Solvent-Free Conditions. *J. Ind. Eng. Chem.* **2018,** *58*, 9-17.

76. Chen, Y.; Ma, S. Biomimetic Catalysis of Metal–Organic Frameworks. *Dalton Trans.* **2016,** *45* (24), 9744-9753.

77. Cornelio, J.; Zhou, T.-Y.; Alkaş, A.; Telfer, S. G. Systematic Tuning of the Luminescence Output of Multicomponent Metal–Organic Frameworks. *J. Am. Chem. Soc.* **2018,** *140* (45), 15470-15476.

78. Qazvini, O. T.; Babarao, R.; Telfer, S. G. Multipurpose Metal–Organic Framework for the Adsorption of Acetylene: Ethylene Purification and Carbon Dioxide Removal. *Chem. Mater.* **2019,** *31* (13), 4919-4926.

79. Qazvini, O. T.; Macreadie, L. K.; Telfer, S. G. Effect of Ligand Functionalization on the Separation of Small Hydrocarbons and CO_2 by a Series of MUF-15 Analogues. *Chem. Mater.* **2020,** *32* (15), 6744-6752.

80. Adil, K.; Belmabkhout, Y.; Pillai, R. S.; Cadiau, A.; Bhatt, P. M.; Assen, A. H.; Maurin, G.; Eddaoudi, M. Gas/Vapour Separation Using Ultra-Microporous Metal–Organic Frameworks: Insights into the Structure/Separation Relationship. *Chem. Soc. Rev.* **2017,** *46* (11), 3402-3430.

81. Wang, Y.; Zhao, D. Beyond Equilibrium: Metal–Organic Frameworks for Molecular Sieving and Kinetic Gas Separation. *Cryst. Growth Des.* **2017,** *17* (5), 2291-2308.

82. Li, B.; Wang, H.; Chen, B. Microporous Metal-Organic Frameworks for Gas Separation. *Chem. Asian J.* **2014,** *9* (6), 1474-1498.

83. Bastin, L.; Bárcia, P. S.; Hurtado, E. J.; Silva, J. A. C.; Rodrigues, A. E.; Chen, B. A Microporous Metal−Organic Framework for Separation of CO_2/N_2 and CO_2/CH_4 by Fixed-Bed Adsorption. *J. Phys. Chem. C* **2008,** *112* (5), 1575-1581.

84. Chen, B.; Liang, C.; Yang, J.; Contreras, D. S.; Clancy, Y. L.; Lobkovsky, E. B.; Yaghi, O. M.; Dai, S. A Microporous Metal–Organic Framework for Gas-Chromatographic Separation of Alkanes. *Angew. Chem. Int. Ed.* **2006,** *45* (9), 1390-1393.

85. Noro, S.-i.; Kitagawa, S.; Kondo, M.; Seki, K. A New, Methane Adsorbent, Porous Coordination Polymer [{$CuSiF_6$(4,4-bipyridine)$_2$}$_N$]. *Angew. Chem. Int. Ed.* **2000,** *39* (12), 2081-2084.

86. Nugent, P.; Belmabkhout, Y.; Burd, S. D.; Cairns, A. J.; Luebke, R.; Forrest, K.; Pham, T.; Ma, S.; Space, B.; Wojtas, L.; Eddaoudi, M.; Zaworotko, M. J. Porous Materials

with Optimal Adsorption Thermodynamics and Kinetics for CO_2 Separation. *Nature* **2013,** *495*, 80-84.

87. Qazvini, O. T.; Babarao, R.; Shi, Z.-L.; Zhang, Y.-B.; Telfer, S. G. A Robust Ethane-Trapping Metal–Organic Framework with a High Capacity for Ethylene Purification. *J. Am. Chem. Soc.* **2019,** *141* (12), 5014-5020.

88. Thommes, M.; Kaneko, K.; Neimark, A. V.; Olivier, J. P.; Rodriguez-Reinoso, F.; Rouquerol, J.; Sing, K. S. W. *Physisorption of Gases, with Special Reference to the Evaluation of Surface Area and Pore Size Distribution (IUPAC Technical Report)*; IUPAC Division of Physical and Biophysical Chemistry Division: Pure and Applied Chemistry, **2015**; pp 1-19.

89. Rouquerol, F.; Rouquerol, J.; Sing, K. S. W.; Llewellyn, P.; Maurin, G. *Adsorption by Powders and Porous Solids: Principles, Methodology and Applications*. 2nd ed.; Academic Press: **2013**. https://www.sciencedirect.com/book/9780080970356/adsorption-by-powders-and-porous-solids

90. Elaiopoulos, K., Uses of Natural Zeolites in Operations Involving Organic Gases and Vapors. In *Handbook of Natural Zeolites*, Inglezakis, V. J.; Zorpas, A. A., Eds. Bentham Books: **2012**; pp 238-287.

91. Sarkisov, L.; Bueno-Perez, R.; Sutharson, M.; Fairen-Jimenez, D. Materials Informatics with Poreblazer v4.0 and the CSD MOF Database. *Chem. Mater.* **2020,** *32* (23), 9849-9867.

92. Walton, K. S.; Millward, A. R.; Dubbeldam, D.; Frost, H.; Low, J. J.; Yaghi, O. M.; Snurr, R. Q. Understanding Inflections and Steps in Carbon Dioxide Adsorption Isotherms in Metal-Organic Frameworks. *J. Am. Chem. Soc.* **2008,** *130* (2), 406-407.

93. Bourrelly, S.; Llewellyn, P. L.; Serre, C.; Millange, F.; Loiseau, T.; Férey, G. Different Adsorption Behaviors of Methane and Carbon Dioxide in the Isotypic Nanoporous Metal Terephthalates MIL-53 and MIL-47. *J. Am. Chem. Soc.* **2005,** *127* (39), 13519-13521.

94. Tun, H.; Chen, C.-C. Isosteric Heat of Adsorption from Thermodynamic Langmuir Isotherm. *Adsorption* **2021,** *27* (6), 979-989.

95. Nuhnen, A.; Janiak, C. A Practical Guide to Calculate the Isosteric Heat/Enthalpy of Adsorption Via Adsorption Isotherms in Metal–Organic Frameworks, MOFs. *Dalton Trans.* **2020,** *49* (30), 10295-10307.

96. Myers, A. L.; Prausnitz, J. M. Thermodynamics of Mixed-Gas Adsorption. *AlChE J.* **1965,** *11* (1), 121-127.

97. Walton, K. S.; Sholl, D. S. Predicting Multicomponent Adsorption: 50 Years of the Ideal Adsorbed Solution Theory. *AlChE J.* **2015,** *61* (9), 2757-2762.

98. Simon, C. M.; Smit, B.; Haranczyk, M. Pyiast: Ideal Adsorbed Solution Theory (IAST) Python Package. *Comput. Phys. Commun.* **2016,** *200*, 364-380.

99. Bojdays, M. J. Prediction of Gas Adsorption Selectivity by Ideal Adsorption Solution Theory (IAST). *Comprehensive Manuals* **2013,** (1), 1-4.

100. Krishna, R.; Van Baten, J. M. How Reliable Is the Ideal Adsorbed Solution Theory for the Estimation of Mixture Separation Selectivities in Microporous Crystalline Adsorbents? *ACS Omega* **2021,** *6* (23), 15499-15513.

101. Van Heest, T.; Teich-Mcgoldrick, S. L.; Greathouse, J. A.; Allendorf, M. D.; Sholl, D. S. Identification of Metal–Organic Framework Materials for Adsorption Separation of Rare Gases: Applicability of Ideal Adsorbed Solution Theory (IAST) and Effects of Inaccessible Framework Regions. *J. Phys. Chem. C* **2012,** *116* (24), 13183-13195.

102. Chen, H.; Sholl, D. S. Efficient Simulation of Binary Adsorption Isotherms Using Transition Matrix Monte Carlo. *Langmuir* **2006,** *22* (2), 709-716.

103. Gonçalves, I. K. V.; Oliveira, W. X. C.; Almeida, F. B. d.; Marinho, M. V.; Pim, W. D. d.; Silva-Caldeira, P. P. The Versatile Coordination Chemistry of 1,3-benzenedicarboxylate in the Last 20 Years: An Investigation from the Coordination Modes to Spectroscopic Insights. *Polyhedron* **2021,** *198* (115068), 1-31.

104. Zhou, R.-S.; Cui, X.-B.; Song, J.-F.; Xu, X.-Y.; Xu, J.-Q.; Wang, T.-G. Syntheses, Structures and Luminescence Properties of Lanthanide Coordination Polymers with Helical Character. *J. Solid State Chem.* **2008,** *181*, 2099-2107.

105. Liu, C.-B.; Wang, S.-S.; Che, G.-B.; Zhao, H.; Li, W.-W.; Li, X.-Y.; Xu, Z.-L. Hydrothermal Syntheses and Crystal Structures of Pb^{II} Coordination Polymers Based on a N,O-Donor Ligand. *Inorg. Chem. Commun.* **2013,** *27*, 69-75.

106. Kim, E. Y.; Song, Y. J.; Koo, H. G.; Lee, J. H.; Park, H. M.; Kim, C.; Kwon, T.-H.; Huh, S.; Kim, S.-J.; Kim, Y. 1-D, 2-D and 3-D Coordination Polymers Assembled from Polynuclear Co^{II} Units Based on the isophthalate(-2) Ligand. *Polyhedron* **2010,** *29*, 3335-3341.

107. Luo, F.; Batten, S. R.; Che, Y.; Zheng, J.-M. Synthesis, Structure, and Characterization of Three Series of 3d–4f Metal-Organic Frameworks Based on Rod-Shaped and (6,3)-Sheet Metal Carboxylate Substructures. *Chem. Eur. J.* **2007,** *13* (17), 4948-4955.

108. Deng, M.; Ling, Y.; Xia, B.; Chen, Z.; Zhou, Y.; Liu, X.; Yue, B.; He, H. Synthesis of Isoreticular Zinc(II)-phosphonocarboxylate Frameworks and Their Application in the Friedel-Crafts Benzylation Reaction. *Chem. Eur. J.* **2011,** *17* (37), 10323-10328.

109. Badiane, I.; Freslon, S.; Suffren, Y.; Daiguebonne, C.; Calvez, G.; Bernot, K.; Camara, M.; Guillou, O. High Brightness and Easy Color Modulation in Lanthanide-Based Coordination Polymers with 5-methoxyisophthalate as Ligand: Toward Emission Colors Additive Strategy. *Cryst. Growth Des.* **2017,** *17* (3), 1224-1234.

110. Zhu, X.; Chen, Q.; Yang, Z.; Li, B.-L.; Li, H.-Y. Tuning Zinc(II) Coordination Polymers Based on bis(1,2,4-triazol-1-yl)ethane and 5-Substituted 1,3-benzenedicarboxylates: Syntheses, Structures and Properties. *CrystEngComm* **2013,** *15* (3), 471-481.

111. Reinsch, H.; Van Der Veen, M. A.; Gil, B.; Marszalek, B.; Verbiest, T.; De Vos, D.; Stock, N. Structures, Sorption Characteristics, and Nonlinear Optical Properties of a New Series of Highly Stable Aluminum MOFs. *Chem. Mater.* **2013,** *25* (1), 17-26.

112. Reinsch, H.; Waitschat, S.; Stock, N. Mixed-Linker MOFs with CAU-10 Structure: Synthesis and Gas Sorption Characteristics. *Dalton Trans.* **2013,** *42* (14), 4840.

113. Wang, H.-N.; Meng, X.; Wang, X.-L.; Yang, G.-S.; Su, Z.-M. Auxiliary Ligand Induced Structural Allomorphism in Nanotubular Microporous Metal–Organic Frameworks Based on Discrete Magnesium Clusters. *Dalton Trans.* **2012,** *41* (8), 2231-2233.

114. Chen, P.-K.; Che, Y.-X.; Zheng, J.-M.; Batten, S. R. Heteropolynuclear Metamagnet Showing Spin Canting and Single-Crystal to Single-Crystal Phase Transformation. *Chem. Mater.* **2007,** *19* (9), 2162-2167.

115. He, J.; Yu, J.; Zhang, Y.; Pan, Q.; Xu, R. Synthesis, Structure, and Luminescent Property of a Heterometallic Metal−Organic Framework Constructed from Rod-Shaped Secondary Building Blocks. *Inorg. Chem.* **2005,** *44* (25), 9279-9282.

116. Bauer, S.; Stock, N. Synthesis and Characterization of Three Zinc Phosphonates Based on 5-phosphonoisophthalic acid, $(HO_2C)_2C_6H_3PO_3H_2$. *Z. Anorg. Allg. Chem.* **2008,** *634* (1), 131-136.

117. Qazvini, O. T.; Telfer, S. G. MUF-16: A Robust Metal–Organic Framework for Pre- and Post-Combustion Carbon Dioxide Capture. *ACS Appl. Mater. Interfaces* **2021,** *13* (10), 12141-12148.

118. Qazvini, O. T.; Scott, V.-J.; Bondorf, L.; Ducamp, M.; Hirscher, M.; Coudert, F.-X.; Telfer, S. G. Flexibility of a Metal–Organic Framework Enhances Gas Separation and Enables Quantum Sieving. *Chem. Mater.* **2021,** *33* (22), 8886-8894.

119. Lv, D.; Shi, R.; Chen, Y.; Wu, Y.; Wu, H.; Xi, H.; Xia, Q.; Li, Z. Selective Adsorption of Ethane over Ethylene in PCN-245: Impacts of Interpenetrated Adsorbent. *ACS Appl. Mater. Interfaces* **2018,** *10* (9), 8366-8373.

120. Liao, P.-Q.; Zhang, W.-X.; Zhang, J.-P.; Chen, X.-M. Efficient Purification of Ethene by an Ethane-Trapping Metal-Organic Framework. *Nat. Commun.* **2015,** *6* (1), 8697.

121. Sarkisov, L.; Kim, J. Computational Structure Characterization Tools for the Era of Material Informatics. *Chem. Eng. Sci.* **2015,** *121*, 322-330.

122. Sarkisov, L.; Harrison, A. Computational Structure Characterisation Tools in Application to Ordered and Disordered Porous Materials. *Mol. Simul.* **2011,** *37* (15), 1248-1257.

123. Ma, D.-Y.; Qin, L.; Lei, J.-M.; Liang, Y.-Q.; Lin, W.-J.; Yan, J.-J.; Ding, W.-Q.; Guo, H.-F.; Ling, Y. Structural Diversity of a Series of Coordination Polymers Built from 5-Substituted isophthalic acid with or without a Methyl-Functionalized N-Donor Ligand. *CrystEngComm* **2016,** *18* (8), 1363-1375.

124. Cheng, X.-N.; Xue, W.; Chen, X.-M. Synthesis, Structures, and Magnetic Properties of Two Cobalt(II) isophthalate Coordination Polymers. *Eur. J. Inorg. Chem.* **2010,** *2010* (24), 3850-3855.

125. Lal, G.; Gelfand, B. S.; Lin, J.-B.; Banerjee, A.; Trudel, S.; Shimizu, G. K. H. Three Sequential Hydrolysis Products of the Ubiquitous Cu_{24} isophthalate Metal–Organic Polyhedra. *Inorg. Chem.* **2019,** *58* (15), 9874-9881.

126. Feng, D.; Wang, K.; Wei, Z.; Chen, Y.-P.; Simon, C. M.; Arvapally, R. K.; Martin, R. L.; Bosch, M.; Liu, T.-F.; Fordham, S.; Yuan, D.; Omary, M. A.; Haranczyk, M.; Smit, B.; Zhou, H.-C. Kinetically Tuned Dimensional Augmentation as a Versatile Synthetic Route Towards Robust Metal–Organic Frameworks. *Nat. Commun.* **2014,** *5* (1), 5723.

127. Yang, Y.; Yan, L.-T.; Luo, X.-J.; Qin, R.-H.; Duan, W.-G. Three Coordination Polymers of 5-aminoisophthalic acid with Similar benzimidazole Derivative Ligands: Synthesis, Structure and DNA-Binding Studies. *Supramol. Chem.* **2012,** *24* (11), 810-818.

128. Che, G.-B.; Liu, C.-B.; Wang, L.; Cui, Y.-C. Solvothermal Syntheses, Structures, and Luminescence of Two Heterometallic Metal-Organic Frameworks Constructed from *m*-BDC (*m*-BDC = 1,3-benzene-dicarboxylate). *J. Coord. Chem.* **2007,** *60* (18), 1997-2007.

129. Zhang, T.-z.; Lu, Y.; Li, Y.-g.; Zhang, Z.; Chen, W.-l.; Fu, H.; Wang, E.-b. Metal–Organic Frameworks Constructed from Three Kinds of New Fe-Containing Secondary Building Units. *Inorg. Chim. Acta* **2012,** *384*, 219-224.

130. Ye, J.; Liu, Y.; Zhao, Y.; Mu, X.; Zhang, P.; Wang, Y. Porous Lanthanide–Copper Coordination Frameworks Exhibiting Reversible Single-Crystal-to-Single-Crystal Transformation Based on Variable Coordination Number and Geometry. *CrystEngComm* **2008,** *10* (5), 598.

131. Al-Terkawi, A.-A.; Scholz, G.; Prinz, C.; Zimathies, A.; Emmerling, F.; Kemnitz, E. Hydrated and Dehydrated Ca-Coordination Polymers Based on benzene-dicarboxylates: Mechanochemical Synthesis, Structure Refinement, and Spectroscopic Characterization. *CrystEngComm* **2018,** *20* (7), 946-961.

132. Hill, M. D.; El-Hankari, S.; Chiacchia, M.; Tizzard, G. J.; Coles, S. J.; Bradshaw, D.; Kitchen, J. A.; Keene, T. D. Additive Effects in the Formation of Fluorescent Zinc Metal–Organic Frameworks with 5-hydroxyisophthalate. *Cryst. Growth Des.* **2015,** *15* (3), 1452-1459.

133. Zeng, M.-H.; Zou, H.-H.; Hu, S.; Zhou, Y.-L.; Du, M.; Sun, H.-L. Unique (3,13)-Connected Coordination Framework Based on Pentacobalt Clusters Constructed from the (3,12)-Connected Analogue and 4,4-bipyridyl Spacer: Structural and Magnetic Aspects. *Cryst. Growth Des.* **2009,** *9* (10), 4239-4242.

134. Luo, F.; Zheng, J.-M.; Long, G. J. Unique Anionic Eight-Connected Net with $3^6 4^{18} 5^3 6$ Topology Derived from a Rare $Co_6(M_3\text{-}OH)_2(M\text{-}H_2O)(CO_2)_{12}$ Building Block. *Cryst. Growth Des.* **2009,** *9* (3), 1271-1274.

135. Qiao, C.; Zhao, Y.; Ren, Y.; Gao, X.; Zhang, M.; Zhou, C.; Zhang, G.; Chen, S.; Gao, S. Synthesis, Photoluminescence and Thermodynamics of Two Lanthanide Coordination Polymers with 5-nitroisophthalate. *J. Solid State Chem.* **2019,** *270*, 443-449.

136. Vodak, D. T.; Braun, M. E.; Kim, J.; Eddaoudi, M.; Yaghi, O. M. Metal–Organic Frameworks Constructed from Pentagonal Antiprismaticand Cuboctahedral Secondary Building Units. *Chem. Commun.* **2001,** (24), 2534-2535.

137. Gao, Q.; Wu, M.-Y.; Huang, Y.-G.; Chen, L.; Wei, W.; Zhang, Q.-F.; Jiang, F.-L.; Hong, M.-C. Double-Walled Tubular Metal–Organic Frameworks Constructed from Bi-Strand Helices. *CrystEngComm* **2009,** *11* (9), 1831.

138. Günay, H.; Çolak, A. T.; Temel, E.; Bayraktar, Ö. S.; Çolak, F.; Büyükgüngör, O. Syntheses, Structural Characterizations and Microbial Activities of Ni(II) and Zn(II) 5-aminoisophthalate Coordination Polymers. *J. Coord. Chem.* **2016,** *69* (9), 1499-1513.

139. Cheng, X. N.; Zhang, W. X.; Lin, Y. Y.; Zheng, Y. Z.; Chen, X. M. A Dynamic Porous Magnet Exhibiting Reversible Guest-Induced Magnetic Behavior Modulation. *Adv. Mater.* **2007,** *19* (11), 1494-1498.

140. Bu, F.; Xiao, S.-J. A 4-Connected Anionic Metal–Organic Nanotube Constructed from Indium isophthalate. *CrystEngComm* **2010,** *12* (11), 3385.

141. Gao, L.; Zhao, B.; Li, G.; Shi, Z.; Feng, S. Mixed Solvothermal Synthesis and X-Ray Characterization of a Layered Copper Coordination Polymer, $Cu(H_2O)(1,3\text{-}BDC)\cdot H_2O$ (BDC=benzenedicarboxylate). *Inorg. Chem. Commun.* **2003,** *6* (9), 1249-1251.

142. Yang, Y.; Li, C.-G.; Luo, X.-J.; Luo, Z.-H.; Liu, R.-J.; Liang, W.-J. Synthesis and DNA Interaction of the Novel Mixed-Ligand Polymers That Incorporate bis(2-benzimidazolylmethyl) sulfide. *Supramol. Chem.* **2016,** *28* (3-4), 321-328.

143. Wang, H.-N.; Liu, F.-H.; Zhu, Y.-F.; Wang, X.-L.; Chen, Z.-H.; Su, Z.-M. Synthesis and Property Investigation of Two Hexa-Cobalt Cluster Based Porous Coordination Polymers. *CrystEngComm* **2013,** *15* (37), 7402.

144. He, Z.; Pang, Q.; Rankine, D.; Sumby, C. J.; Zhang, L.; Doonan, C. J.; Li, Q. Encapsulation of Polyoxometalates within Layered Metal–Organic Frameworks with Topological and Pore Control. *CrystEngComm* **2013,** *15* (45), 9340.

145. Xue, D.-X.; Lin, Y.-Y.; Cheng, X.-N.; Chen, X.-M. A Tetracarboxylate−Bridged Dicopper(II) Paddle-Wheel-Based 2-D Porous Coordination Polymer with Gas Sorption Properties. *Cryst. Growth Des.* **2007,** *7* (7), 1332-1336.

146. Hu, P.; Liu, H.; Wang, H.; Zhou, J.; Wang, Y.; Ji, H. Synergic Morphology Engineering and Pore Functionality within a Metal–Organic Framework for Trace CO_2 Capture. *J. Mater. Chem. A* **2022,** *10* (2), 881-890.

147. Zhou, J.; Ke, T.; Steinke, F.; Stock, N.; Zhang, Z.; Bao, Z.; He, X.; Ren, Q.; Yang, Q. Tunable Confined Aliphatic Pore Environment in Robust Metal–Organic Frameworks for Efficient Separation of Gases with a Similar Structure. *J. Am. Chem. Soc.* **2022,** *144* (31), 14322-14329.

148. Pei, J.; Gu, X.-W.; Liang, C.-C.; Chen, B.; Li, B.; Qian, G. Robust and Radiation-Resistant Hofmann-Type Metal–Organic Frameworks for Record Xenon/Krypton Separation. *J. Am. Chem. Soc.* **2022,** *144* (7), 3200-3209.

149. Ye, Y.; Xian, S.; Cui, H.; Tan, K.; Gong, L.; Liang, B.; Pham, T.; Pandey, H.; Krishna, R.; Lan, P. C.; Forrest, K. A.; Space, B.; Thonhauser, T.; Li, J.; Ma, S. Metal–Organic Framework Based Hydrogen-Bonding Nanotrap for Efficient Acetylene Storage and Separation. *J. Am. Chem. Soc.* **2022,** *144* (4), 1681-1689.

150. Sun, W.; Hu, J.; Duttwyler, S.; Wang, L.; Krishna, R.; Zhang, Y. Highly Selective Gas Separation by Two Isostructural Boron Cluster Pillared MOFs. *Sep. Purif. Technol.* **2022,** *283* (120220).

151. Wang, G. D.; Li, Y. Z.; Shi, W. J.; Hou, L.; Wang, Y. Y.; Zhu, Z. One‐Step C_2H_4 Purification from Ternary $C_2H_6/C_2H_4/C_2H_2$ Mixtures by a Robust Metal-Organic Framework with Customized Pore Environment. *Angew. Chem. Int. Ed.* **2022,** *61* (28).

152. Ding, Q.; Zhang, S. Recent Advances in the Development of Metal–Organic Frameworks for Propylene and Propane Separation. *Energy Fuels* **2022,** *36* (14), 7337-7361.

153. Butova, V. V.; Soldatov, M. A.; Guda, A. A.; Lomachenko, K. A.; Lamberti, C. Metal-Organic Frameworks: Structure, Properties, Methods of Synthesis and Characterization. *Russ. Chem. Rev.* **2016,** *85* (3), 280-307.

154. Bennett, T. D.; Goodwin, A. L.; Dove, M. T.; Keen, D. A.; Tucker, M. G.; Barney, E. R.; Soper, A. K.; Bithell, E. G.; Tan, J.-C.; Cheetham, A. K. Structure and Properties of an Amorphous Metal-Organic Framework. *Phys. Rev. Lett.* **2010,** *104* (11).

155. McKellar, S. C.; Moggach, S. A. Structural Studies of Metal–Organic Frameworks under High Pressure. *Acta Crystallogr. B. Struct. Sci. Cryst. Eng. Mater.* **2015,** *71* (6), 587-607.

156. Beveridge, S.; McAnally, C. A.; Nichol, G. S.; Kennedy, A. R.; Cussen, E. J.; Fletcher, A. J. Unexpected Selective Gas Adsorption on a ‘Non-Porous’ Metal Organic Framework. *Crystals* **2020,** *10* (6), 548.

157. Liu, J.-J. Multi-Responsive Host-Guest MOFs Derived from Ethyl Viologen Cations. *Dyes and Pigments* **2019,** *163*, 496-501.

158. Shuai, Q.; Chen, S.; Gao, S. Structural and Thermal Properties of Three Novel Alkaline Earth Metal Coordination Polymers Based on 5-hydroxyisophthalate Ligand. *Inorg. Chim. Acta* **2007,** *360* (5), 1381-1387.

159. Meekel, E. G.; Schmidt, E. M.; Cameron, L. J.; Dharma, A. D.; Windsor, H. J.; Duyker, S. G.; Minelli, A.; Pope, T.; Lepore, G. O.; Slater, B.; Kepert, C. J.; Goodwin, A. L. Truchet-Tile Structure of a Topologically Aperiodic Metal-Organic Framework. *arXiv (Condensed Materials, Materials Science)* **2022**.

160. Yuan, S.; Feng, L.; Wang, K.; Pang, J.; Bosch, M.; Lollar, C.; Sun, Y.; Qin, J.; Yang, X.; Zhang, P.; Wang, Q.; Zou, L.; Zhang, Y.; Zhang, L.; Fang, Y.; Li, J.; Zhou, H.

C. Stable Metal–Organic Frameworks: Design, Synthesis, and Applications. *Adv. Mater.* **2018,** *30* (37), 1704303.

161. Maghsoudi, H. Comparative Study of Adsorbents Performance in Ethylene/Ethane Separation. *Adsorption* **2016,** *22* (7), 985-992.

162. Sheldrick, G. M. Crystal Structure Refinement with *SHELXL*. *Acta Crystallogr. C Struct. Chem.* **2015,** *71* (1), 3-8.

Appendix

A.1 General Procedures

All reagents and solvents used were obtained from commercial sources and used without further purification.

A.1.1 Synthesis of XADDOX [124]

$Co(OAc)_2 \cdot 4H_2O$ (62.3 mg, 0.25 mmol), H_2ipa (66.6 mg, 0.40 mmol) and methanol (5 mL) was continuously stirred for 30 min in air, then transferred into a Teflon liner and sealed in an autoclave reaction vessel, which was heated to 160°C for 3 days. After cooling to room temperature, the small purple crystals were collected by decanting off the mother liquor and washing several times with fresh methanol.

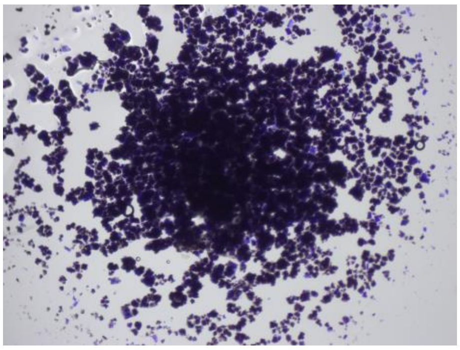

Figure A.1 Optical micrograph of XADDOX.

A.1.2 Synthesis of MUF-200

Under constant stirring, H_2ipa (83.0 mg, 0.50 mmol) then NaOH (40.4 mg, 1.01 mmol) then $Co(NO_3)_2 \cdot 6H_2O$ (146 mg. 0.50 mmol) were dissolved in DMF (12 mL). The pink solution was then transferred into a Teflon liner, sealed in an autoclave reaction vessel, and heated to 170°C for 2 days. After cooling to room temperature, the resultant purple crystals were collected by decanting off the mother liquor and washing well with fresh DMF.

To grow single crystals, a solvent mixture of *N*,*N*-diethylformamide AKA DEF (6 mL) and DMF (6 mL) was used instead of just DMF. Everything else remained the same.

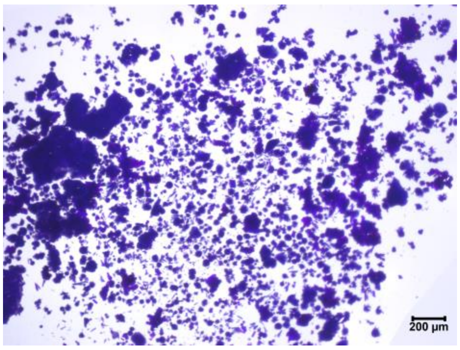

Figure A.2 Optical micrograph of MUF-200.

A.1.3 Synthesis of JETJOI [115]

Under constant stirring, H_2ipa (84.2 mg, 0.51 mmol) then NaOH (40.3 mg, 1.01 mmol) then $Zn(NO_3)_2{\cdot}6H_2O$ (145 mg, 0.49 mmol) were dissolved in DMF (8 mL). The solution was then transferred into a Teflon liner, sealed in an autoclave reaction vessel, and heated to 170°C for 2 days. After cooling to room temperature, the resultant colourless crystals were collected by decanting off the mother liquor and washing well with fresh DMF.

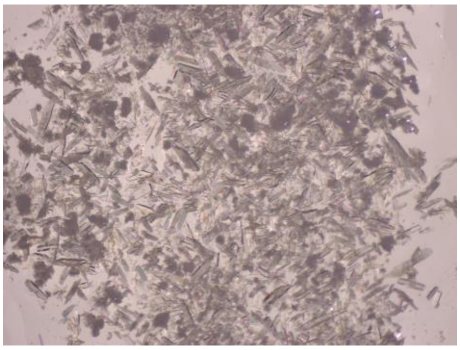

Figure A.3 Optical micrograph of JETJOI.

A.1.4 Synthesis of UC-MUF-201

Methanol (6 mL) and water (0.5 mL) were added to $Cu(OAc)_2{\cdot}H_2O$ (102 mg, 0.51 mmol) and H_2ipa (166 mg, 1.00 mmol) in a 20 mL vial. This was sonicated for 10 min and produced a bright blue suspension. This was transferred into a Teflon liner, sealed in an autoclave reaction vessel, and heated to 120°C for 2 days. Once cooled to room temperature, the bright blue crystals were collected by vacuum filtration, being washed several times with fresh methanol.

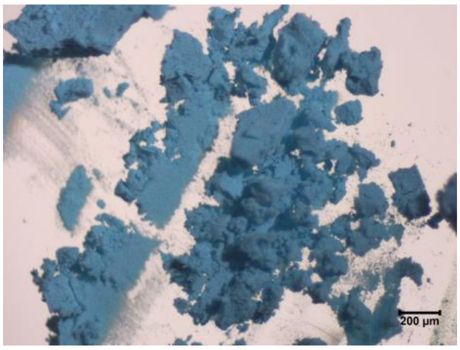

Figure A.4 Optical micrograph of UC-MUF-201.

A.1.5 Synthesis of EMIDEJ02 [131]

$Ca(OH)_2$ (167 mg, 2.25 mmol) and H_2ipa (374 mg, 2.25 mmol) were added to a ball mill with water (65 μL). Five medium sized zirconium balls were added, and the mixture was milled at 600 rpm for 1 hour. The white powder formed was collected by scraping off the sides of the mill.

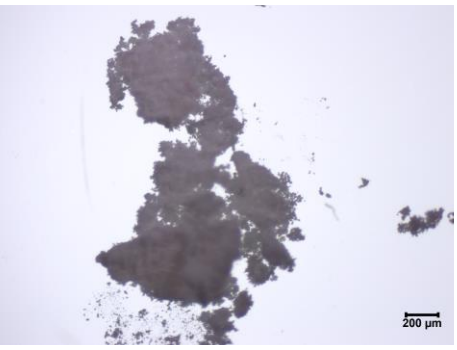

Figure A.5 Optical micrograph of EMIDEJ02.

A.1.6 Synthesis of WAMRIN [113]

$Mg(OAc)_2{\cdot}4H_2O$ (105 mg, 0.49 mmol) and H_2ipa-NH_2 (200 mg, 1.00 mmol) were added to a swirled mixture of DMA (5 mL), ethanol (2 mL) and water (1 mL) in a Schott bottle. This was heated to 110°C for 3 days. The mother liquor was decanted off whilst still warm and the crystals were washed well with fresh ethanol.

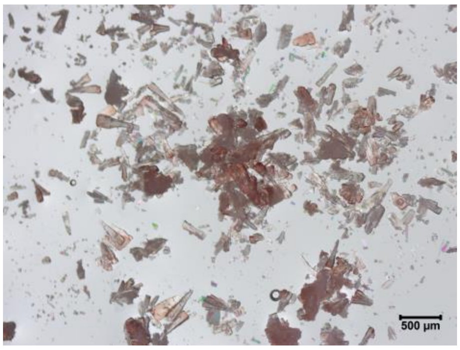

Figure A.6 Optical micrograph of WAMRIN.

A.1.7 Synthesis of EDOTUN [114]

$Zn(NO_3)_2 \cdot 6H_2O$ (298 mg, 1.00 mmol), $CoCl_2 \cdot 6H_2O$ (357 mg, 1.50 mmol), H_2ipa (333 mg, 2.00 mmol), and imidazole (68.5 mg, 1.00 mmol) were mixed in water (8 mL). Under constant stirring, the pH was adjusted to approximately 7 using 2 M KOH. Not all of the reactants appeared to dissolve. The mixture was then transferred into a Teflon liner, sealed in an autoclave reaction vessel, and heated to 180°C for 4 days. Once cooled to room temperature, the dark purple crystals were collected by decanting off the mother liquor and washing with fresh water several times.

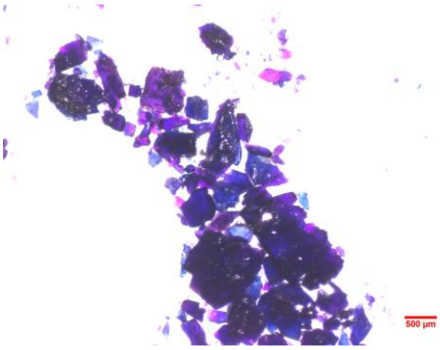

Figure A.7 Optical micrograph of EDOTUN.

A.1.8 Synthesis of RUGXUO [132]

A solution of H_2ipa-OH (73.0 mg, 0.04 mmol) in DMF (4 mL) was added to a solution of $Zn(NO_3)_2 \cdot 6H_2O$ (120 mg, 0.4 mmol) in DMF (4 mL) alongside $(CH_3)_4NCl$ (44.8 mg, 0.41 mmol) in a 25 mL Schott bottle. The Schott bottle was then put into a 120°C oven for 3 days. Afterward, the mother liquor was decanted off the yellow ‘sea-urchin’ crystal aggregate, then it was washed well with fresh DMF.

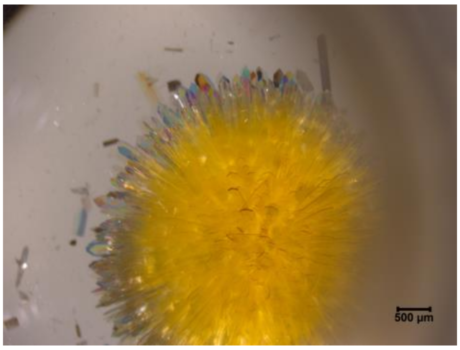

Figure A.8 Optical micrograph of RUGXUO.

A.1.9 Synthesis of MUF-202

$Co(OAc)_2 \cdot 4H_2O$ (125 mg, 0.50 mmol), H_2ipa-NO_2 (158 mg, 0.75 mmol), 1.5 mL isopropanol and 1.5 mL butan-1-ol was mixed in a ball mill with 15 small zirconium balls for 30 minutes at 30 Hz. After such time, a pink solution resulted. This was transferred into a Teflon liner with another 1.5 mL isopropanol and 1.5 mL butan-1-ol. 0.5 mL water was also added. After sealing in an autoclave reaction vessel, the vessel was put into a 120°C oven for approximately 20 hours. After cooling to room temperature, the pink crystals were collected by decanting off the mother liquor and washing with isopropanol. A small amount of a pale pink phase formed but almost was able to be picked out.

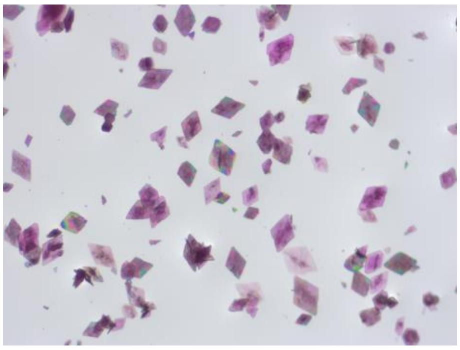

Figure A.9 Optical micrograph of MUF-202.

A.1.10 Synthesis of MUF-203

H_2ipa (39.8 mg, 0.24 mmol) and $Zn(NO_3)_2 \cdot 6H_2O$ (131 mg, 0.44 mmol) were dissolved in a solution of DMF (5 mL) and acetonitrile (5 mL) in a 20 mL vial. This was heated to 85°C for

48 hours. The colourless crystals were collected by decanting off the mother liquor while warm and washing with fresh acetonitrile.

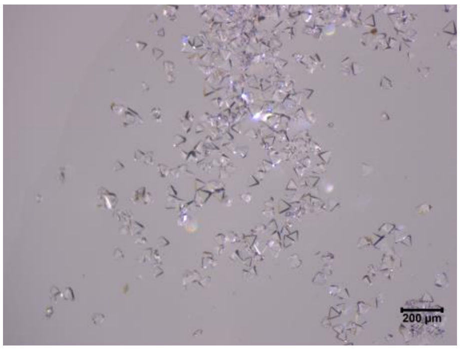

Figure A.10 Optical micrograph of MUF-203.

A.1.11 Synthesis of MUF-204

Mg(OAc)$_2$·4H$_2$O (105 mg, 0.49 mmol) and H$_2$ipa-NH$_2$ (90.2 mg, 0.49 mmol) was added to a stirred mixture of DMA (5 mL), ethanol (2 mL) and water (1 mL). The suspension was transferred into a Teflon liner and sealed in an autoclave reaction vessel which was heated to 110°C for 3 days. After cooling to room temperature, the pale peach crystals were collected by decanting off the mother liquor and washing well with fresh ethanol.

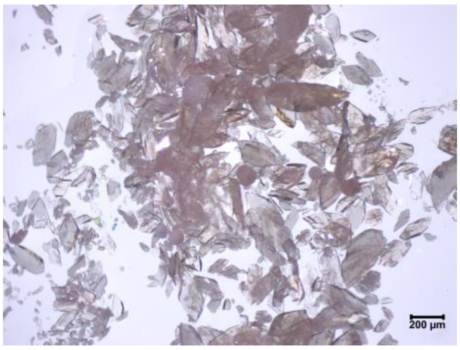

Figure A.11 Optical micrograph of MUF-204.

A.1.12 Synthesis of MUF-205

Mg(OAc)$_2$·4H$_2$O (105 mg, 0.49 mmol) and H$_2$ipa-Br (270 mg, 1.10 mmol) were combined dry then added to a Schott bottle containing solution of DMA (5 mL), ethanol (2 mL) and water (1 mL). The reactants were mixed by swirling before the bottle was heated in an oven to 110°C for 2 days. The mother liquor was then decanted off the colourless crystals whilst still warm and the crystals were washed with fresh ethanol several times.

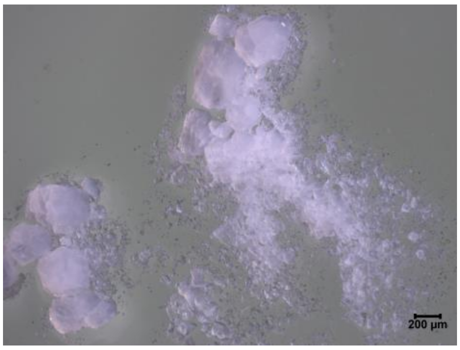

Figure A.12 Optical micrograph of MUF-205.

A.1.13 Copper/H_2ipa-NO_2 MOF

$Cu(NO_3)_2·3H_2O$ (20 mg, 0.084 mmol) and H_2ipa-NO_2 (18 mg, 0.083 mmol) was combined dry then dissolved in a solution of DMF (0.75 mL), ethanol (0.75 mL) and water (0.5 mL) by swirling, in a 4 mL vial. This vial was then tightly capped and put into an 85°C oven for around 24 hours. The mother liquor was then decanted off whilst still warm and the turquoise crystals were washed with fresh ethanol several times.

Figure A.13 Optical micrograph of the Copper/H_2ipa-NO_2 MOF.

A.1.14 Copper/H_2ipa-NH_2 MOF

H_2ipa-NH_2 (15 mg, 0.084 mmol) was dissolved in DMF (0.75 mL) then the $Cu(NO_3)_2·3H_2O$ solution* (0.75 mL, 0.083 mmol) and H_2O (0.5) were added. The pale blue solution was put into a 65°C dry bath for 6 hours. The mother liquor was then decanted off and the light green crystals were collected by washing several times with fresh ethanol.

*See note at the end of the section

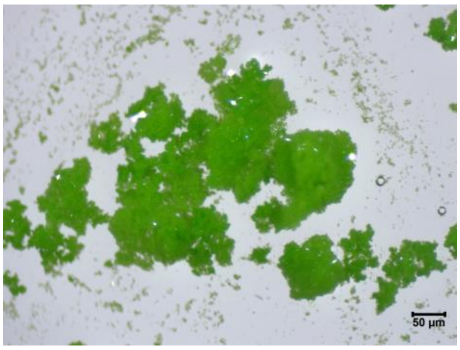

Figure A.14 Optical micrograph of the Copper/H_2ipa-NH_2 MOF.

A.1.15 Synthesis of MUF-206

$Cu(NO_3)_2 \cdot 3H_2O$ (20 mg, 0.084 mmol) and H_2ipa-NH_2 (15 mg, 0.085 mmol) was combined dry then dissolved in DMF (1 mL) and a drop of ethanol, in a 4 mL vial. This vial was put into a 100°C dry bath for around 4 hours. The mother liquor was then decanted off whilst still warm and the dark green crystals were washed with fresh ethanol several times.

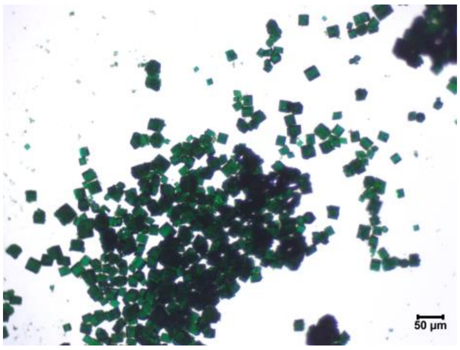

Figure A.15 Optical micrograph of MUF-206.

A.1.16 Synthesis of MUF-207

$Cu(NO_3)_2 \cdot 3H_2O$ (20 mg, 0.084 mmol) and H_2ipa-CH_3 (15 mg, 0.083 mmol) was combined dry then dissolved in a solution of DMF (0.75 mL), ethanol (0.75 mL) and water (0.5 mL) by swirling, in a 4 mL vial. This vial was then tightly capped and put into an 85°C oven for around 24 hours. The mother liquor was then decanted off whilst still warm and the bright blue crystals were washed with fresh ethanol several times.

Instead of $Cu(NO_3)_2{\cdot}3H_2O$ and ethanol, a copper solution (0.75 mL) can be used. See note at the end of this section.

To grow single crystals, a quarter scale of the reagents was used; $Cu(NO_3)_2{\cdot}3H_2O$ (5 mg, 0.02 mmol) and H_2ipa-CH_3 (4 mg, 0.0 mmol). Also, DEF (0.75 mL) was used instead of DMF. Everything else remained the same.

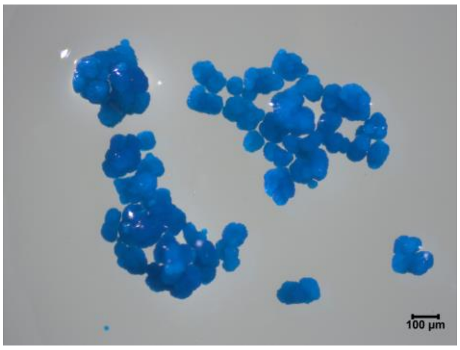

Figure A.16 Optical micrograph of MUF-207.

A.1.17 Synthesis of MUF-208

$Cu(NO_3)_2{\cdot}3H_2O$ (20 mg, 0.084 mmol) and H_2ipa-OMe (16 mg, 0.083 mmol) was combined dry then dissolved in a solution of DMF (0.75 mL), ethanol (0.75 mL) and water (0.5 mL) by swirling, in a 4 mL vial. This vial was then tightly capped and put into an 85°C oven for around 24 hours. The mother liquor was then decanted off whilst still warm and the bright blue crystals were washed with fresh ethanol several times.

Instead of $Cu(NO_3)_2{\cdot}3H_2O$ and ethanol, a copper solution (0.75 mL) can be used. See note at the end of this section.

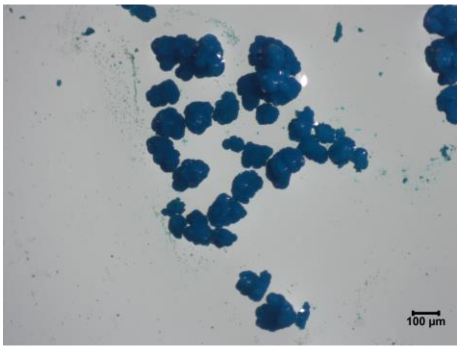

Figure A.17 Optical micrograph of MUF-208.

A.1.18 Synthesis of MUF-209

$Cu(NO_3)_2\cdot 3H_2O$ (20 mg, 0.084 mmol) and H_2ipa-Br (21 mg, 0.084 mmol) was combined dry then dissolved in a solution of DMF (0.75 mL), ethanol (0.75 mL) and water (0.5 mL) by swirling, in a 4 mL vial. This vial was then tightly capped and put into an 85°C oven for around 24 hours. The mother liquor was then decanted off whilst still warm and the bright blue crystals were washed with fresh ethanol several times.

Instead of $Cu(NO_3)_2\cdot 3H_2O$ and ethanol, a copper solution (0.75 mL) can be used. See note at the end of this section.

To grow single crystals, benzoic acid (10.3 mg, 0.084 mmol) was added to the synthesis and DMF was replaced with DEF (0.75 mL). Everything else remained the same.

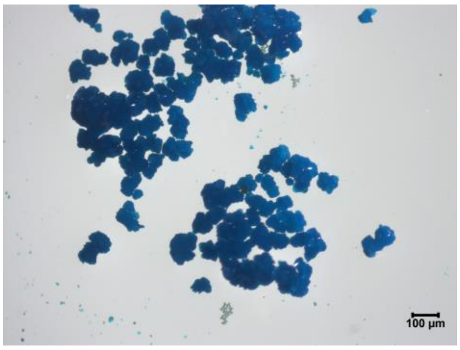

Figure A.18 Optical micrograph of MUF-209.

A.1.19 Synthesis of MUF-210

H_2ipa-OH (15 mg, 0.084 mmol) dissolved in a solution of DMF (0.75 mL) and $Cu(NO_3)_2\cdot 3H_2O$ solution* (0.75 mL, 0.083 mmol), in a 4 mL vial. This vial was then tightly capped and put into an 85°C oven for around 48 hours. The mother liquor was then decanted off whilst still warm and the green crystals were washed with fresh ethanol several times.

*See note at the end of the section.

To grow single crystals, the vial was rinsed with Sigmacote then water before putting in all the reagents as per above.

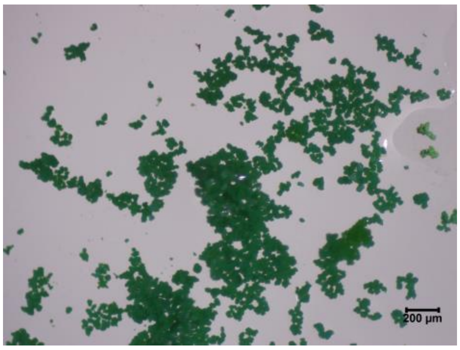

Figure A.19 Optical micrograph of MUF-210.

Note

For the MOFs described in sections A.1.13 to A.1.19, a $Cu(NO_3)_2{\cdot}3H_2O$ solution can replace the $Cu(NO_3)_2{\cdot}3H_2O$ salt and ethanol. A stock solution was made by dissolving $Cu(NO_3)_2{\cdot}3H_2O$ (533 mg, 2.21 mmol) in ethanol (20 mL) so that 0.75 mL of this solution would have the equivalent of 20 mg of $Cu(NO_3)_2{\cdot}3H_2O$.

A.2 Single Crystal X-ray Diffraction (SCXRD)

All SCXRD data was collected using a Bruker Venture D8 diffractometer equipped with a Microfocus generator (Cu_α radiation, 1.54178 Å) using a Photon III detector.

The SCXRD data collection and structure refinement details for all of the low porosity MOFs can be found in Table A.1. Olex2 was used for structural refinement.[162]

Table A.1 SCXRD data collection and structure refinement details for MUF-202 to MUF-206 using a CuKα (λ = 1.54178) radiation source.

	MUF-202	MUF-203	MUF-204	MUF-205	MUF-206
Formula	$[Co(ipa\text{-}NO_2)(H_2O)_3]$	$[Zn_4O(ipa)_3]$	$[Mg(ipa\text{-}NH_2)(H_2O)_2]$	$[Mg_3(ipa\text{-}Br)_3(H_2O)(DMA)_2(EtOH)]\cdot H_2O$	$[Cu_2(ipa\text{-}NH_2)_2(DMF)_2]$
Empirical formula	$C_8H_9CoNO_9$	$C_{0.25}H_{0.08}O_{0.19}Zn_{0.06}$	$C_8H_{10}MgNO_6$	$C_{34}H_{35}Br_3Mg_3N_2O_{17}$	$C_6H_{6.5}Cu_{0.5}NO_{2.5}$
Formula weight	322.09	49.98	240.48	4225.19	164.39
Temperature (K)	296.0	297.0	295.0	200.0	293.15
Crystal system	monoclinic	cubic	triclinic	monoclinic	orthorhombic
Space group	*P2₁/c*	*F$\bar{4}$3m*	*P-1*	*P2₁/n*	*Pmna*
a (Å)	11.1475(10)	15.4516(5)	7.5542(8)	9.4930(4)	14.989(4)
b (Å)	14.0328(13)	15.4516(5)	8.1914(8)	22.0659(10)	7.741(2)
c (Å)	7.5636(7)	15.4516(5)	8.9297(9)	20.3859(9)	10.645(2)
α (°)	90	90	99.207(3)	90	90
β (°)	108.974(4)	90	100.847(3)	100.567(2)	90
γ (°)	90	90	116.261(2)	90	90
Volume ($Å^3$)	1118.89(18)	3689.1(4)	467.75(8)	4197.8(3)	1235.2(5)
Z	4	56	2	4	8
ρ_{calc} (g/cm^3)	1.912	1.260	1.707	1.671	1.768
μ (mm^{-1})	12.525	3.349	1.853	4.652	2.728
F(000)	652.0	1368.0	250.0	2120.0	672.0
2Θ range for data collection (°)	8.388 to 117.782	9.914 to 129.26	10.494 to 148.896	5.958 to 144.742	10.192 to 129.662
Index ranges	$-11 \leq h \leq 12$, $-15 \leq k \leq 15$, $-8 \leq l \leq 8$	$-16 \leq h \leq 18$, $-17 \leq k \leq 18$, $-17 \leq l \leq 16$	$-9 \leq h \leq 8$, $-10 \leq k \leq 10$, $-11 \leq l \leq 11$	$-11 \leq h \leq 11$, $-26 \leq k \leq 25$, $-23 \leq l \leq 25$	$-11 \leq h \leq 17$, $-9 \leq k \leq 8$, $-10 \leq l \leq 12$
Reflections collected	8091	3189	11525	61048	5879
Independent reflections	1583 [R_{int} = 0.0701, R_{sigma} = 0.0554]	354 [R_{int} = 0.0231, R_{sigma} = 0.0166]	1866 [R_{int} = 0.0367, R_{sigma} = 0.0312]	7991 [R_{int} = 0.0495, R_{sigma} = 0.0328]	1017 [R_{int} = 0.0745, R_{sigma} = 0.0640]
Data/restraints/parameters	1583/0/175	354/0/33	1866/0/162	7991/33/601	1017/45/99
Goodness-of-fit on F^2	1.701	1.317	1.081	1.151	1.209
Final R indexes [I>=2σ (I)]	R_1 = 0.1217, wR_2 = 0.3461	R_1 = 0.0788, wR_2 = 0.2186	R_1 = 0.0380, wR_2 = 0.1064	R_1 = 0.1764, wR_2 = 0.3912	R_1 = 0.1930, wR_2 = 0.4340
Final R indexes [all data]	R_1 = 0.1240, wR_2 = 0.3486	R_1 = 0.0810, wR_2 = 0.2207	R_1 = 0.0387, wR_2 = 0.1069	R_1 = 0.1796, wR_2 = 0.3924	R_1 = 0.2001, wR_2 = 0.4367
Largest diff. peak/hole (e $Å^{-3}$)	1.63/-1.74	0.84/-0.51	0.22/-0.59	2.22/-1.71	1.91/-2.42
Flack parameter	-	0.5	-	-	-

A.3 Powder X-ray Diffraction (PXRD)

All PXRD data was collected at room temperature, except for the temperature variable PXRD patterns of MUF-209, using a Bruker Venture D8 diffractometer equipped with a Microfocus generator (Cu$_\alpha$ radiation, 1.54178 Å) using a Photon III detector.

Sample preparation involved dropping a small amount of the MOF in solvent onto the slide. If the solvent was volatile, once it has mostly evaporated, a small drop of oil was placed on top then the MOF was mounted onto a nylon loop for analysis. If the solvent was non-volatile, the MOF could be mounted onto the loop without oil.

The PXRD patterns for all known, synthesized MOFs and all of the low porosity MOFs can be found in Figure A.20 to Figure A.30. The after gas adsorption PXRD patterns for EMIDEJ02, WAMRIN, and RUGXUO (Figure A.22, Figure A.23, and Figure A.25) were done several months after the gas adsorption experiments took place. Therefore, the patterns can not conclusively say if the MOF collapsed from activation or from being left dry for several months.

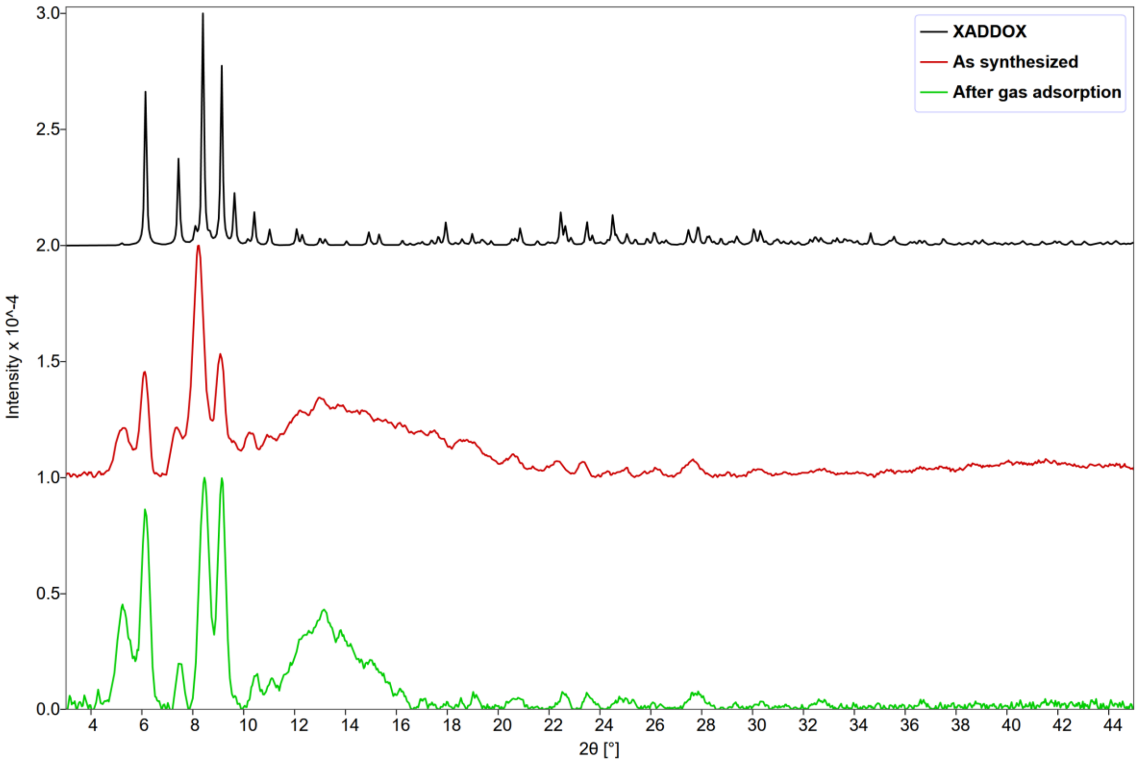

Figure A.20 PXRD patterns of XADDOX simulated (black), as synthesized (red), after gas adsorption (lime).

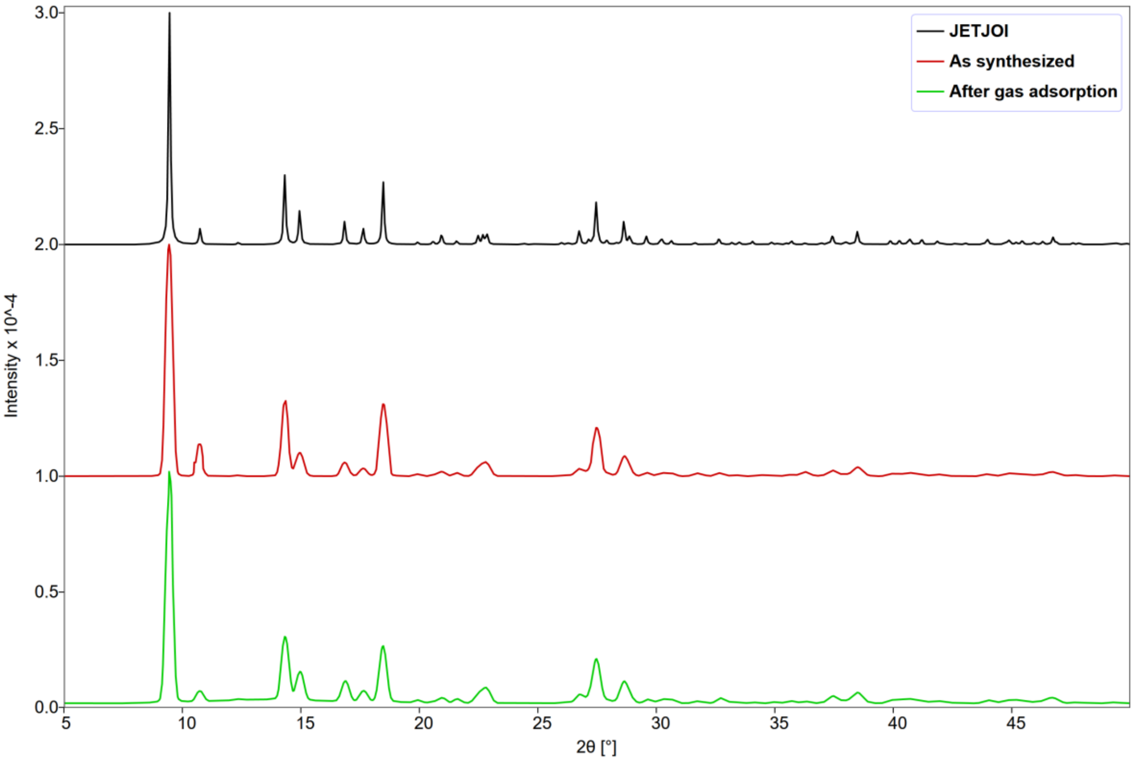

Figure A.21 PXRD patterns of JETJOI simulated (black) and as synthesized (red), and after gas adsorption (lime).

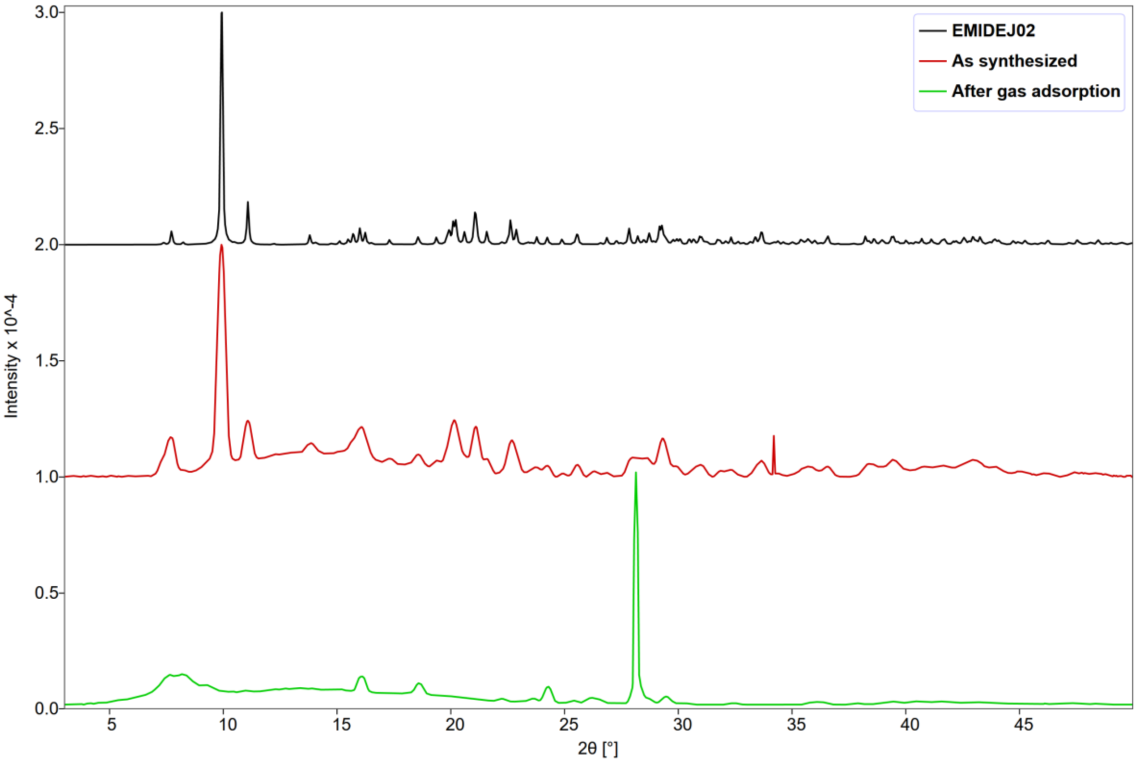

Figure A.22 PXRD patterns of EMIDEJ02 simulated (black) and as synthesized (red), and after gas adsorption (lime).

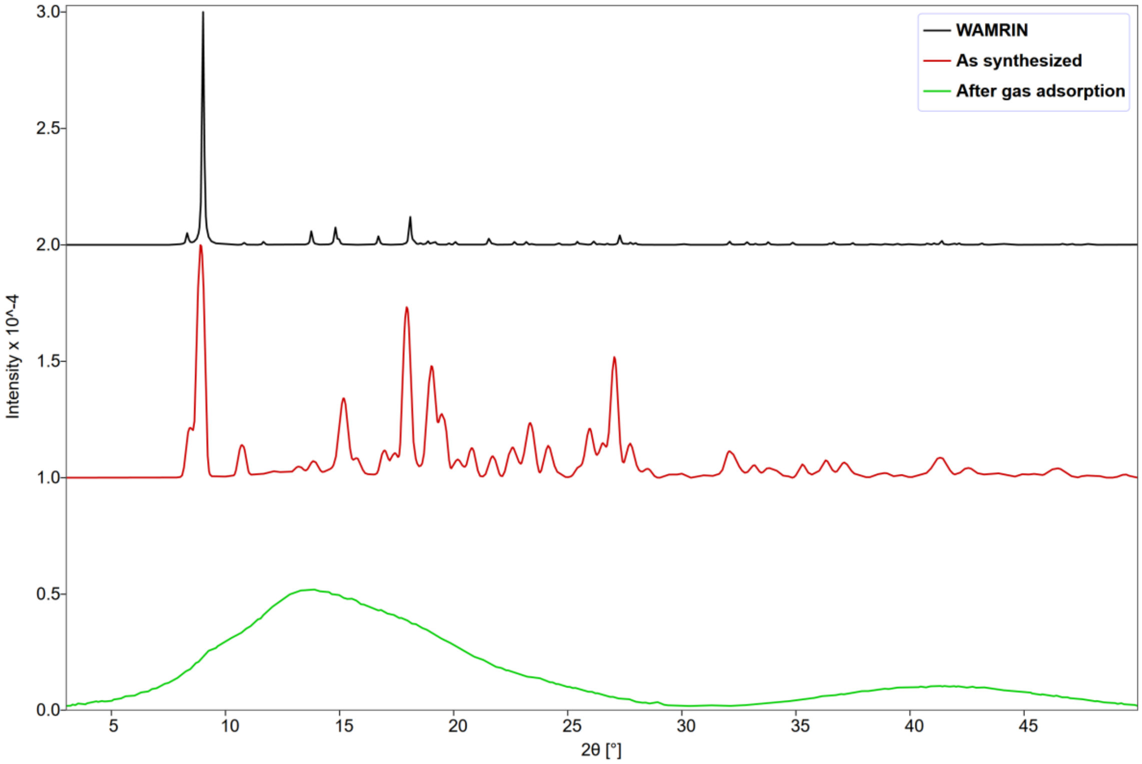

Figure A.23 PXRD patterns of WAMRIN simulated (black) and as synthesized (red), and after gas adsorption (lime).

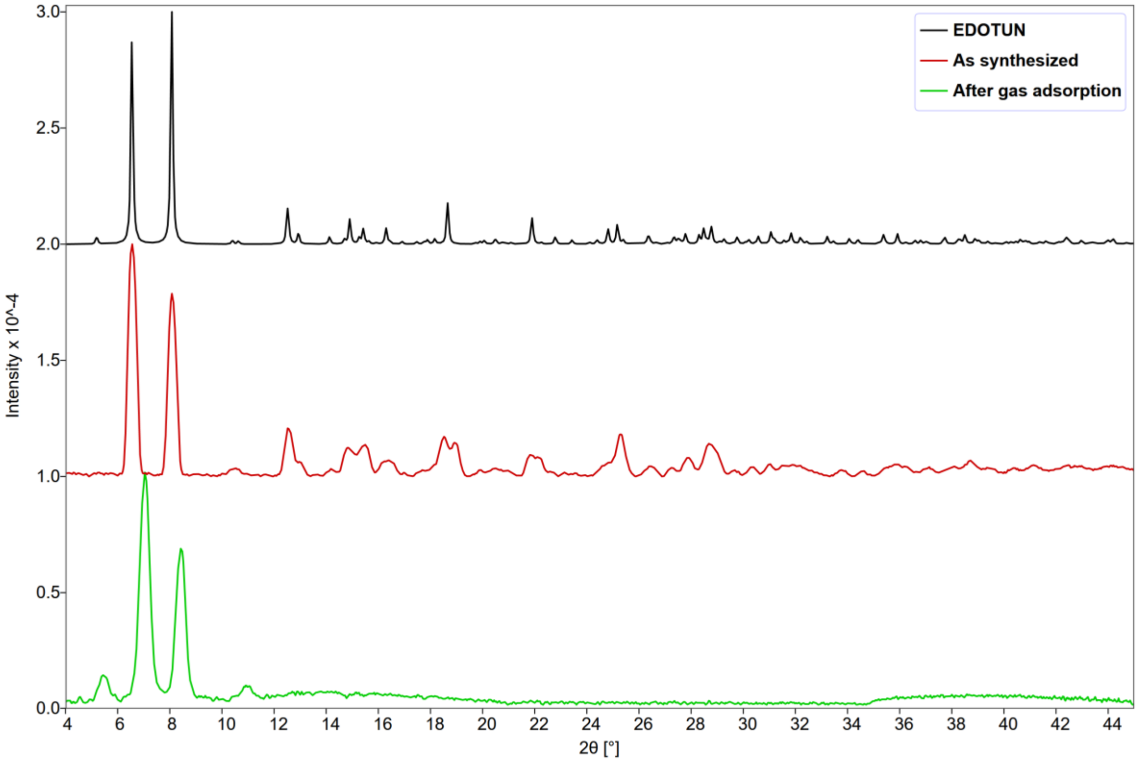

Figure A.24 PXRD patterns of EDOTUN simulated (black) and as synthesized (red), and after gas adsorption (lime).

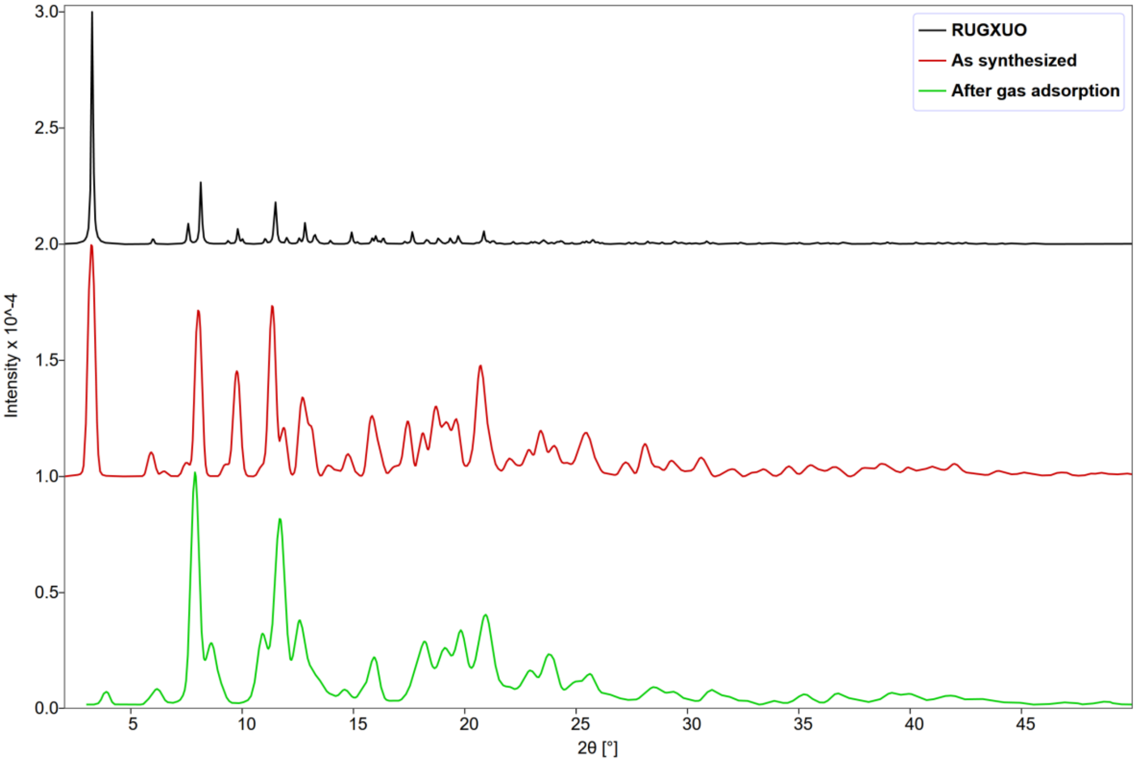

Figure A.25 PXRD patterns of RUGXUO simulated (black) and as synthesized (red), and after gas adsorption (lime).

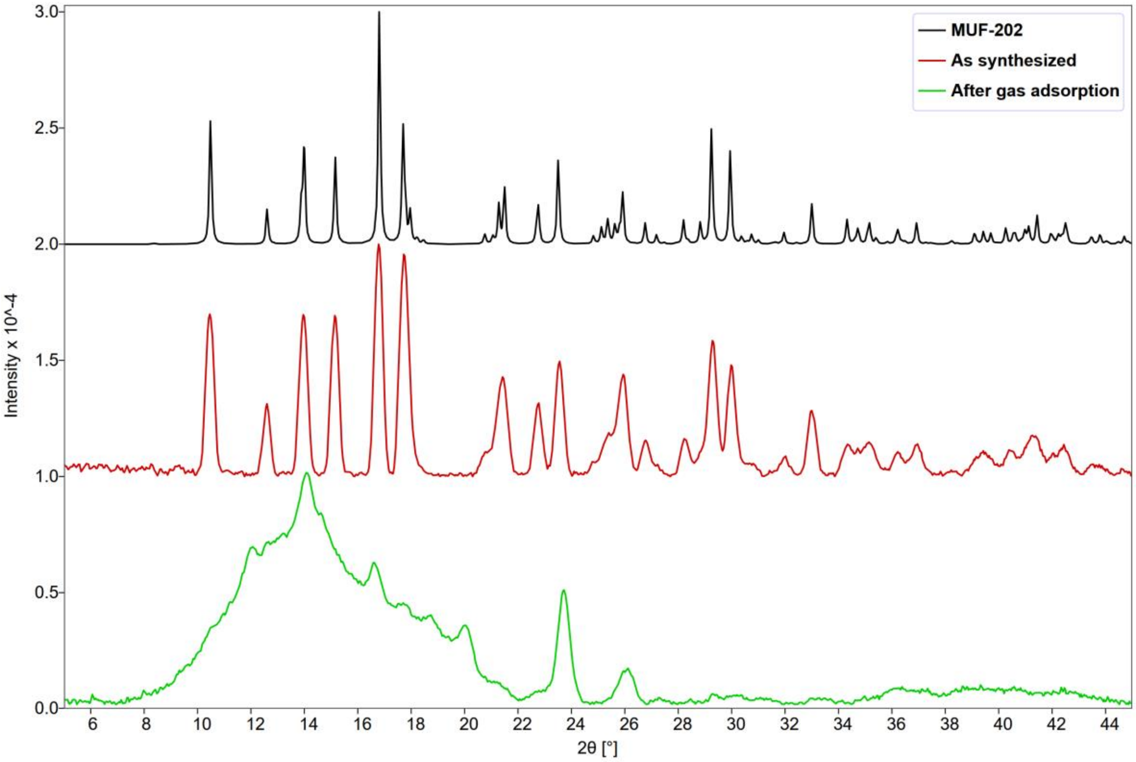

Figure A.26 PXRD patterns of MUF-202 simulated (black), as synthesized (red), and after gas adsorption (lime).

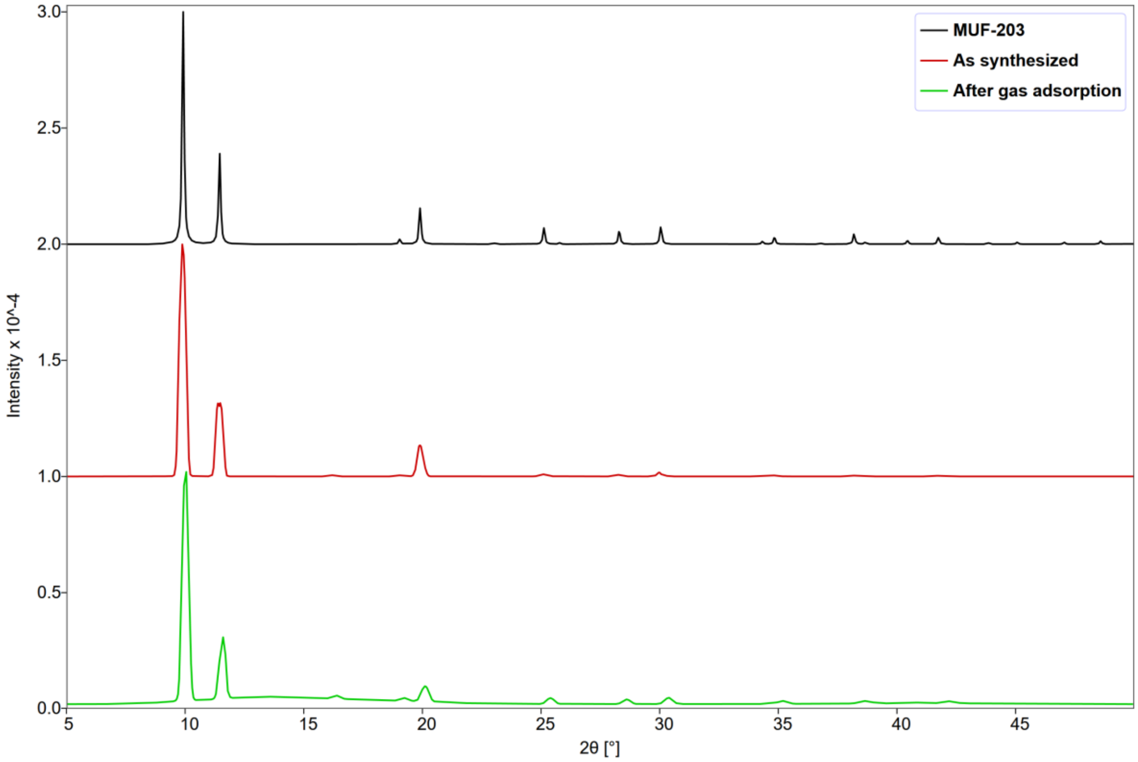

Figure A.27 PXRD patterns of MUF-203 simulated (black), as synthesized (red), and after gas adsorption (lime).

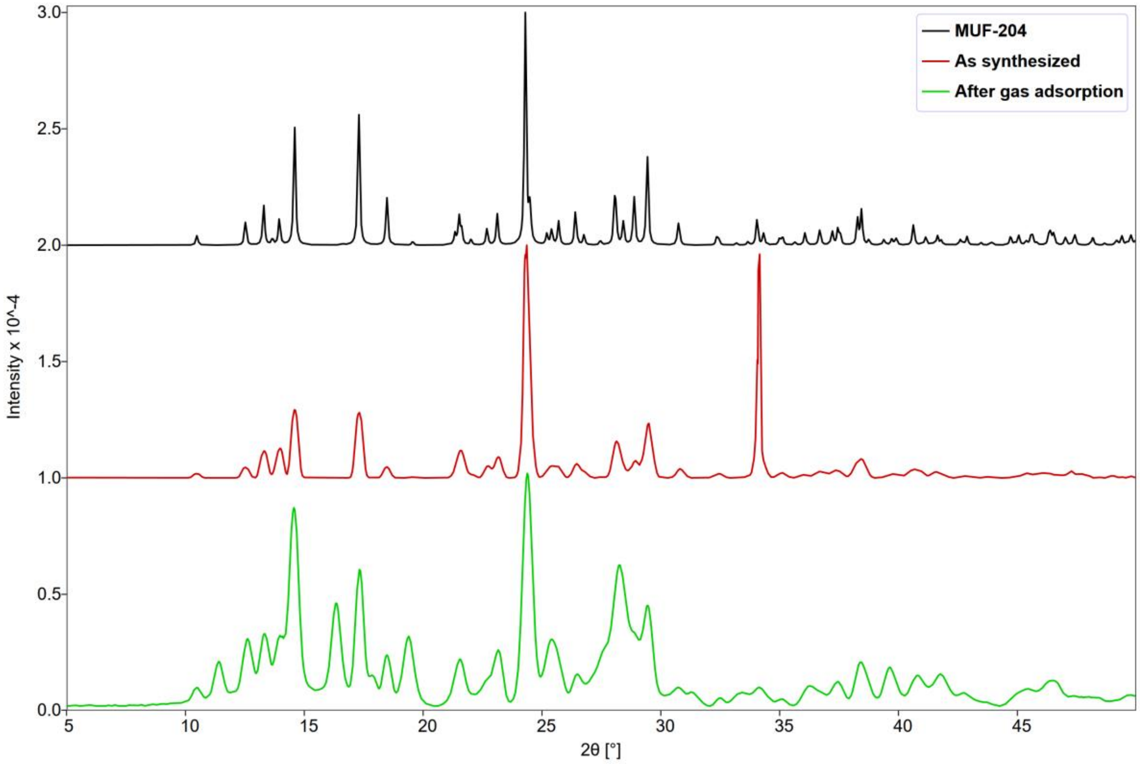

Figure A.28 PXRD patterns of MUF-204 simulated (black) and as synthesized (red), and after gas adsorption (lime).

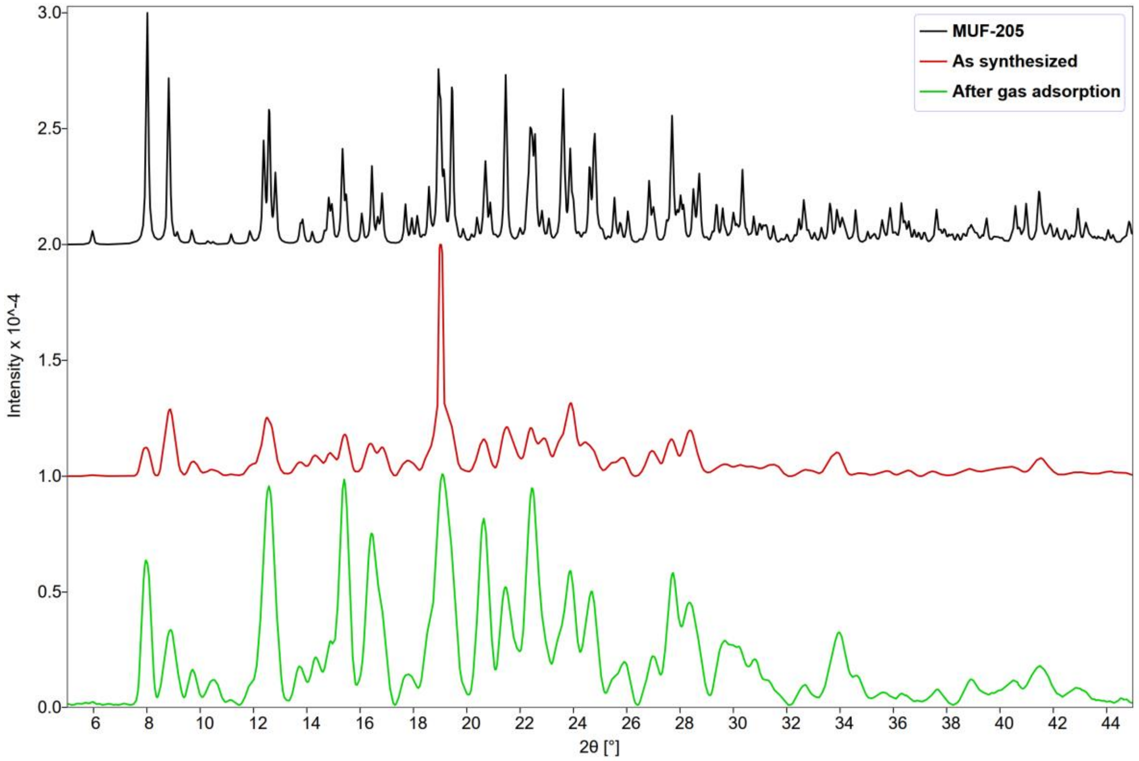

Figure A.29 PXRD patterns of MUF-205 simulated (black), as synthesized (red), and after gas adsorption (lime).

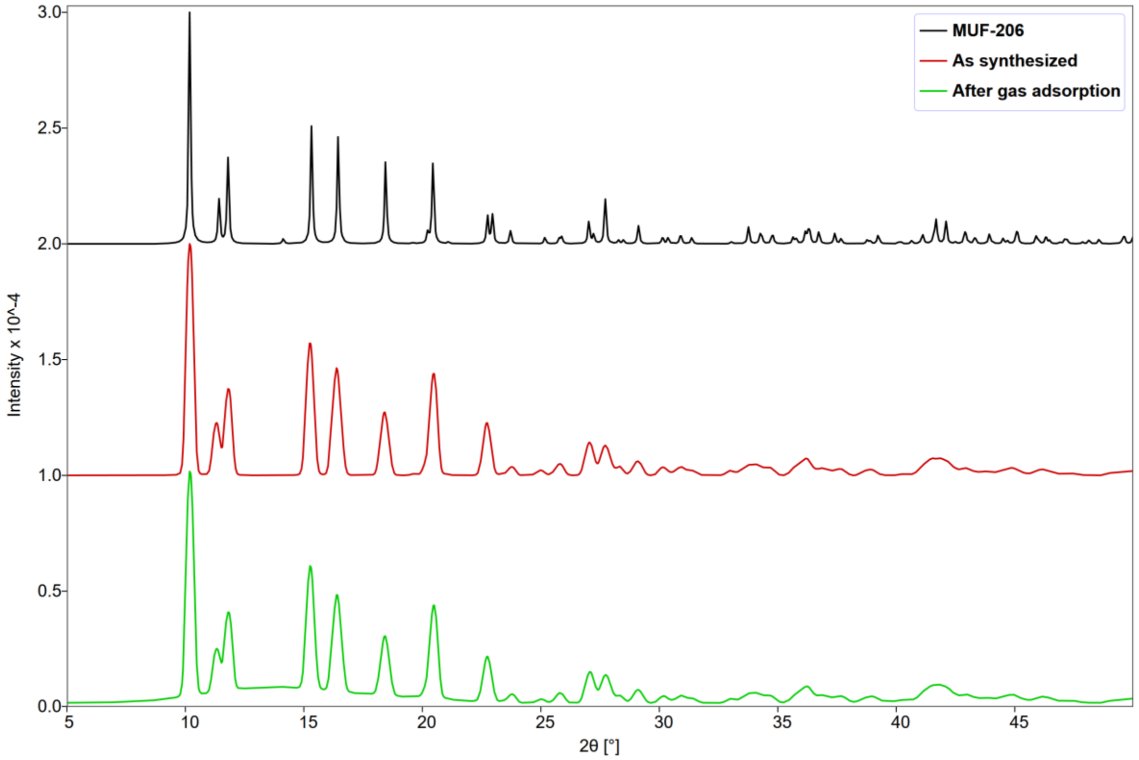

Figure A.30 PXRD patterns of MUF-205 simulated (black), as synthesized (red), and after gas adsorption (lime).

A.4 Thermogravimetric Analysis (TGA)

Thermogravimetric analysis (TGA) was performed using a TA Instruments Q50 instrument with 1-5 mg of activated sample (generally after gas adsorption studies were performed) under a N_2 flow with a heating rate of 5°C/min. For MUF-200 and MUF-209, the samples were pre-treated at 50°C before the TGA was measured. Low temperature weight loss is attributed to the loss of solvent that was trapped in the pores.

A.5 Stability Tests

A small amount of sample (1-10 mg) was placed into a 2 mL vial. For air stability tests, a needle was inserted into the rubber portion of the lid of the vial, allowing the sample to be exposed to the air. This was left on the benchtop. For water stability tests, approximately 1 mL of Milli-Q water was added to the vial.

A.6 Gas Adsorption

The isotherms were measured using a volumetric adsorption Quantachrome Autosorb iQ2 instrument. High purity gases were used a received from BOC Gases. Approximately 30-150 mg of as synthesized sample was either solvent- or dry-loaded into a pre-weighed sample tube. The sample was then activated, generally at 100°C for 24 hours at a heating rate of 5°C/min under a dynamic vacuum. The accurate sample mass was then recorded with the activated sample after the sample tube was backfilled with N_2. For 273 K and 293 K measurements, the temperatures were controlled with a circulating thermostat controlled bath filled with a mixture of water and ethylene glycol. For 77 K measurements, a dewar filled with liquid N_2 was used. For 195 K measurements, a dewar filled with dry ice and acetone was used.

For all isotherms in this appendix, coloured circles represent adsorption points and open circles represent desorption points.

The isotherms for all the low uptake MOFs can be found in Figure A.31 to Figure A.41.

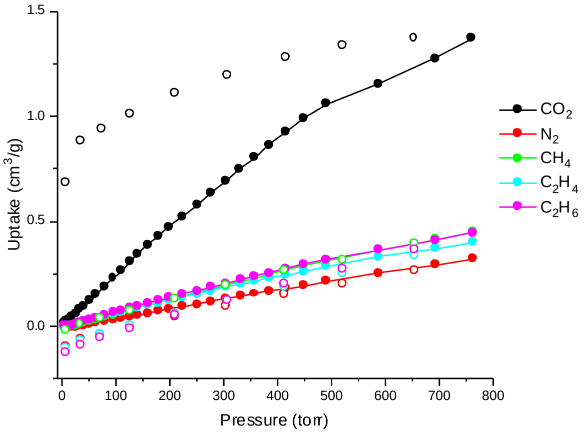

Figure A.31 Adsorption isotherms of EMIDEJ02 at 293 K.

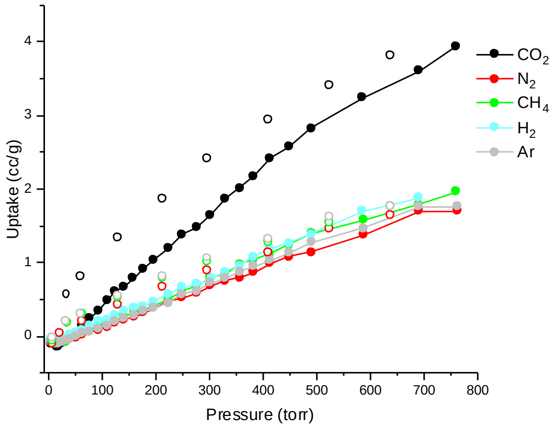

Figure A.32 Adsorption isotherms of WAMRIN at 293 K.

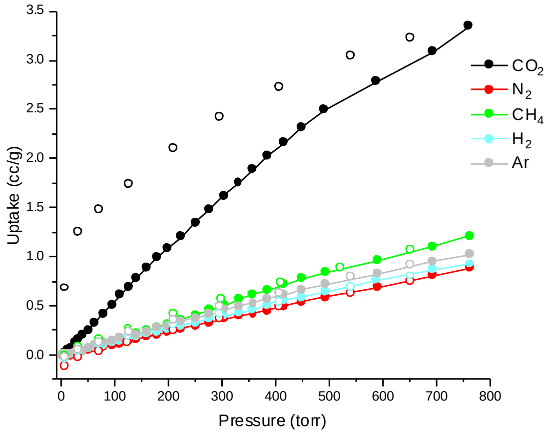

Figure A.33 Adsorption isotherms of EDOTUN at 293 K.

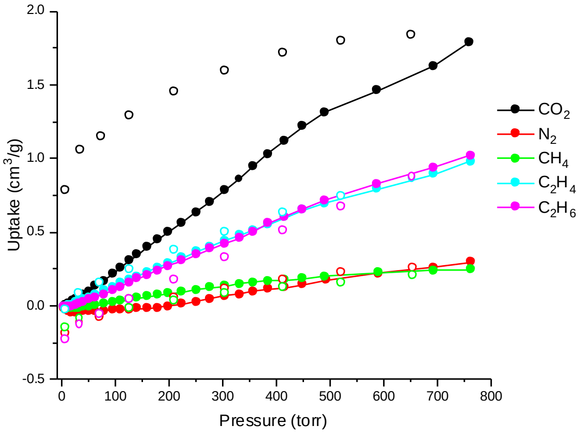

Figure A.34 Adsorption isotherms of RUGXUO at 293 K.

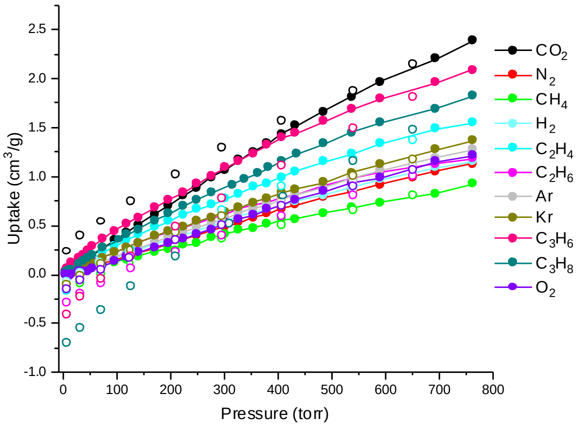

Figure A.35 Adsorption isotherms of MUF-202 at 293 K.

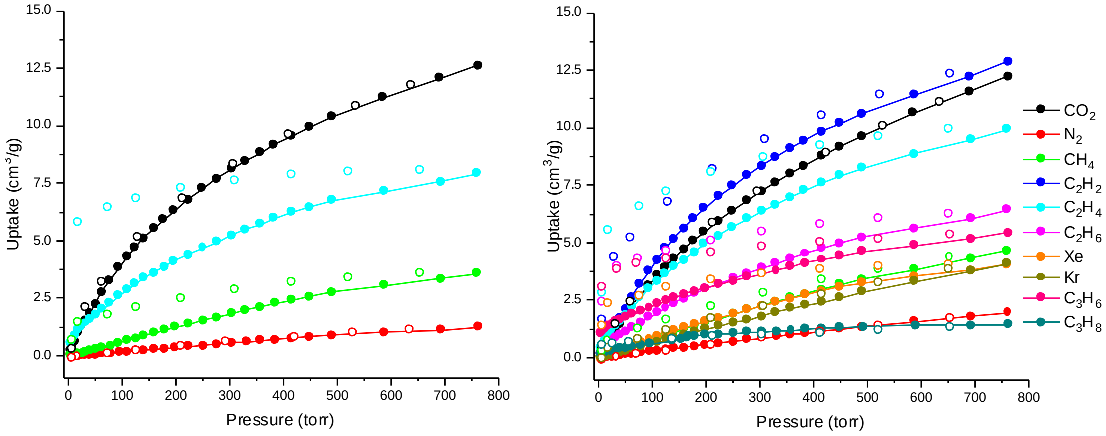

Figure A.36 Adsorption isotherms of MUF-203 at 273 K (left) and 293 K (right).

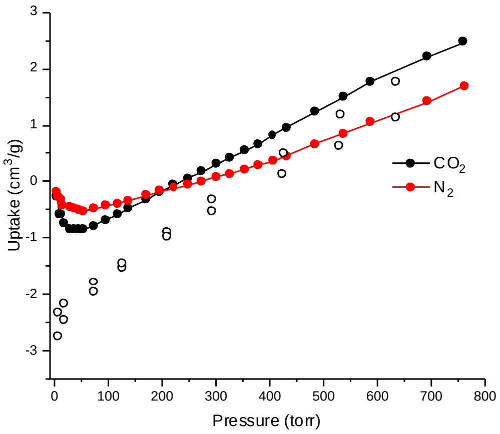

Figure A.37 Adsorption isotherms of MUF-204 at 293 K.

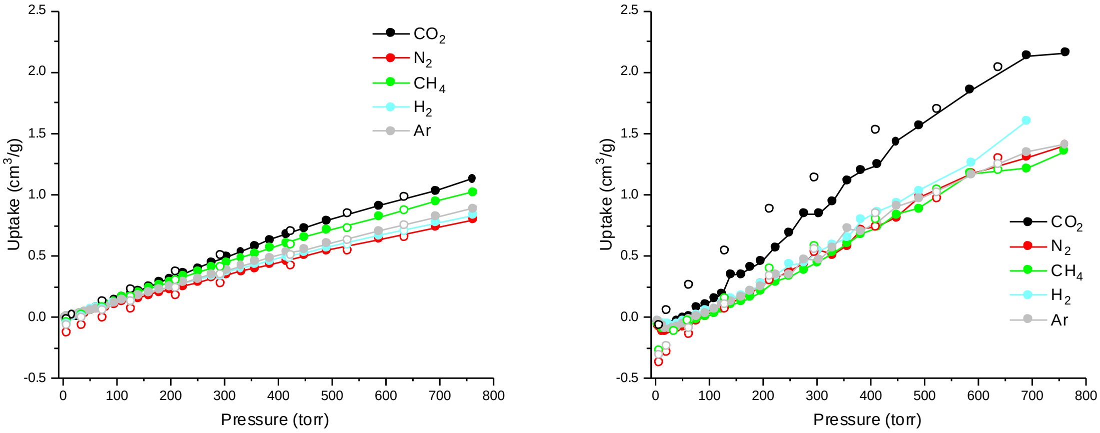

Figure A.38 Adsorption isotherms of MUF-205 (left) activated from ethanol and (right) activated from acetone. Both sets were measured at 293 K.

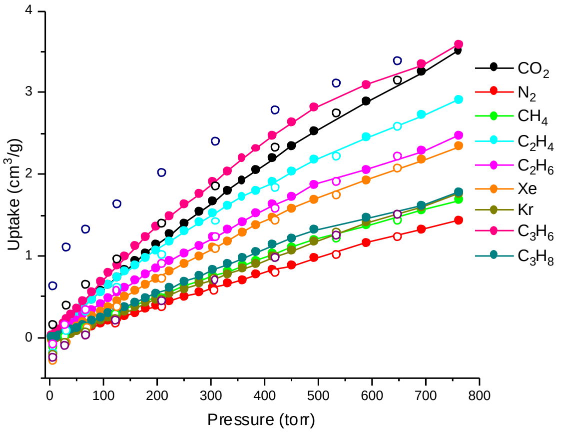

Figure A.39 Adsorption isotherms of Copper/H$_2$ipa-NO$_2$ MOF at 293 K.

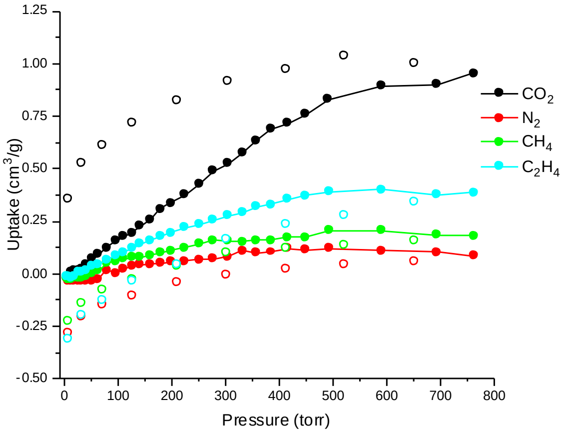

Figure A.40 Adsorption isotherms of Copper/H_2ipa-NH_2 MOF at 293 K.

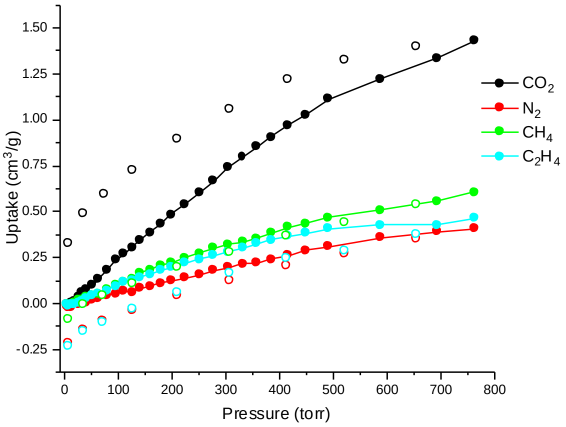

Figure A.41 Adsorption isotherms of MUF-206 at 293 K.

BET fittings using N_2 at 77 K isotherms can be found in Figure A.42 to Figure A.44.

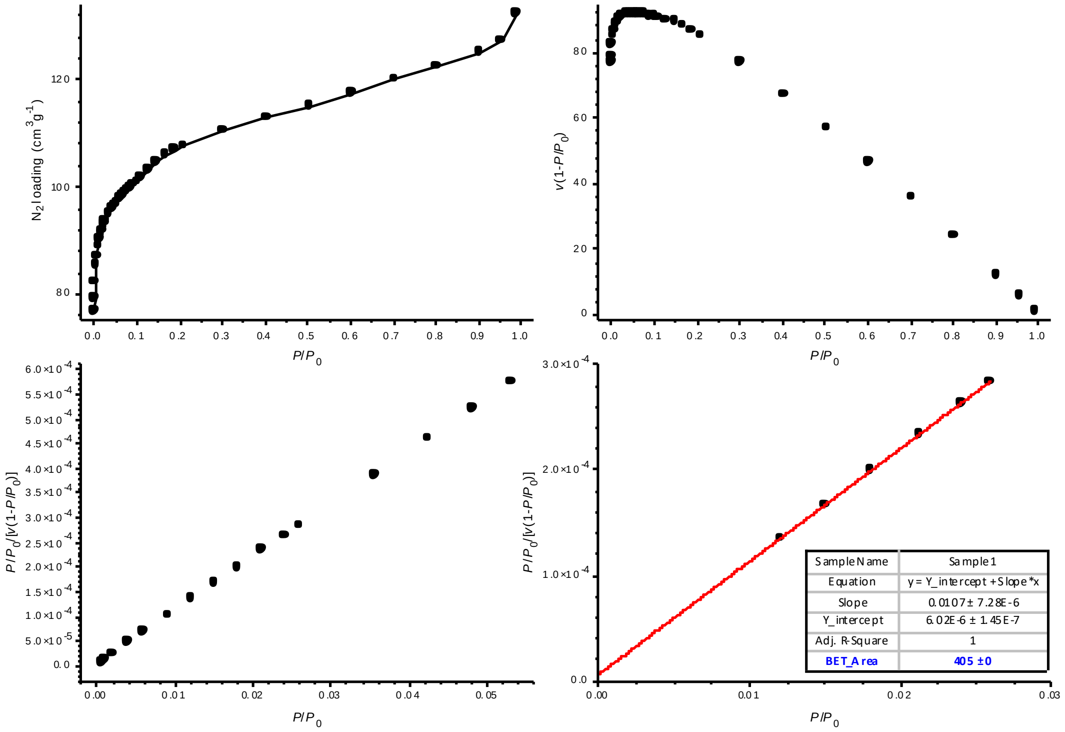

Figure A.42 N$_2$ adsorption isotherm at 77 K alongside the BET surface area plots of MUF-200.

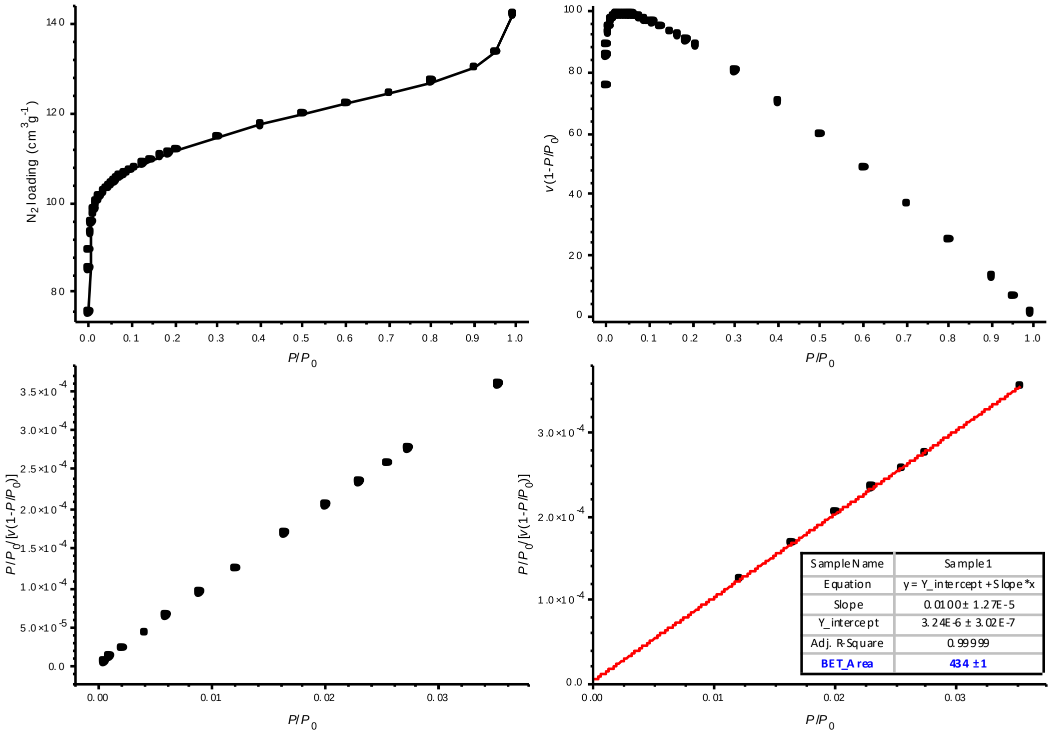

Figure A.43 N$_2$ adsorption isotherm at 77 K alongside the BET surface area plots of UC-MUF-201.

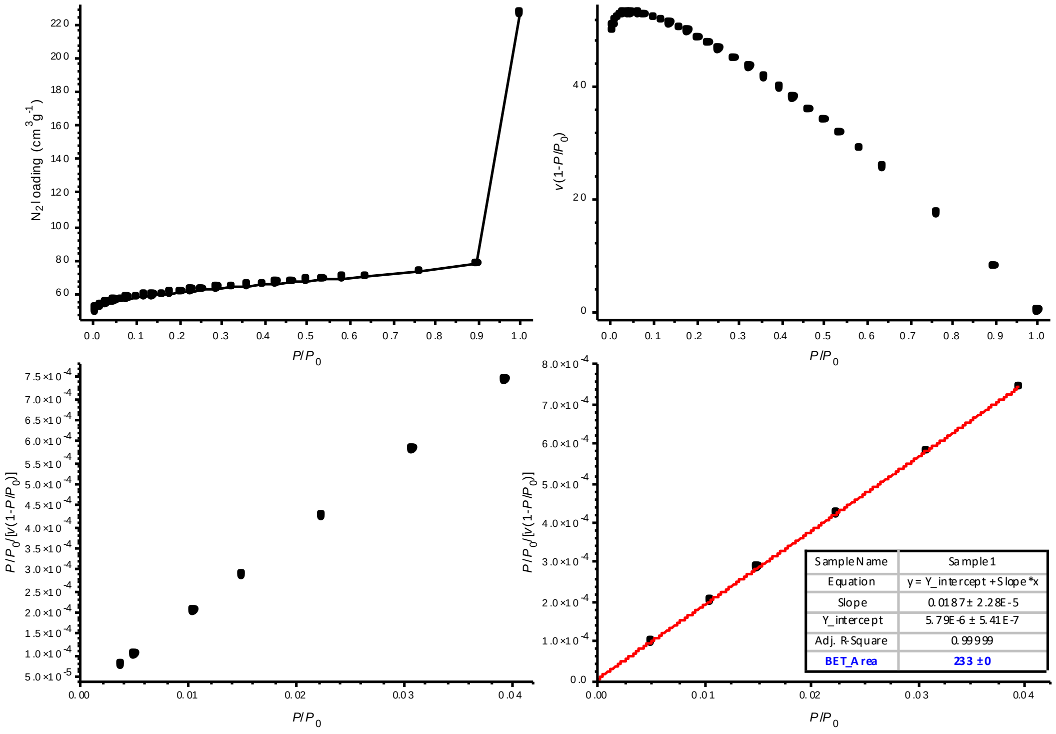

Figure A.44 N$_2$ adsorption isotherm at 77 K alongside the BET surface area plots of MUF-210.

The pore size distribution (PSD) was calculated using a NLDFT model with a CO$_2$ at 273 K isotherm. The results of this calculation can be found in Figure A.45.

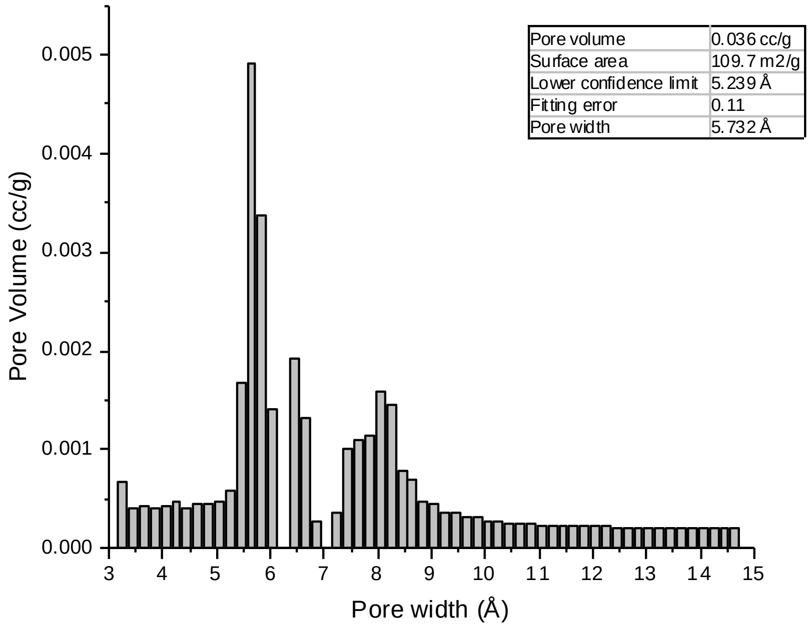

Figure A.45 PSD of MUF-210.

A.7 Isosteric Heat of Adsorption (Q_{st})

Isosteric heat of adsorption (Q_{st}) values were calculated using isotherms measured at 273 and 293 K. For more information about the fitting and calculation process, see Chapter 1, section 1.4.3.3. Fitting parameters for MOFs with Q_{st} analyses are found below (Table A.2 to Table A.9), including those calculated by Elnaz Jangodaz (noted in their respective tables).

A.7.1 Q_{st} data for XADDOX

Table A.2 Virial equation fitting parameters for the Q_{st} plots of XADDOX.

	Xe	CO_2 *	C_2H_6	C_3H_6	C_3H_8
a0	-4060 ± 550	-3340 ± 1380	-3900 ± 112	-6110 ± 382	-15400 ± 161
a1	10.8 ± 22.8	-17.0 ± 63.5	-5.36 ± 3.65	27.4 ± 9.97	345 ± 55.6
a2	1.12 ± 0.284	0.680 ± 0.540	0.279 ± 0.0455	0.446 ± 0.140	0.802 ± 0.962
a3	-0.0106 ± 3.74×10^{-3}	-5.84×10^{-3} ± 6.22×10^{-3}	-2.75×10^{-4} ± 5.33×10^{-4}	-7.08×10^{-4} ± 1.29×10^{-3}	-4.49×10^{-4} ± 0.0104
b0	17.2 ± 1.93	14.7 ± 4.87	14.8 ± 0.389	19.9 ± 1.28	51.8 ± 5.18
b1	-0.142 ± 0.0777	-0.0104 ± 0.218	1.83×10^{-3} ± 0.0122	-0.102 ± 0.0285	-1.23 ± 0.134
R^2	0.96544	0.80628	0.99915	0.998	0.98079

* Low R^2 value however increasing the number of parameters used did not improve the fit.

A.7.2 Q_{st} data for JETJOI

Table A.3 Virial equation fitting parameters for the Q_{st} plots of JETJOI.

	CO_2
a0	-4150 ± 43.0
a1	275 ± 11.3
a2	-11.5 ± 0.624
a3	0.503 ± 0.0437
b0	17.5 ± 0.150
b1	-0.553 ± 0.0375
R^2	0.99984

A.7.3 Q_{st} data for MUF-200

Table A.4 Virial equation fitting parameters for the Q_{st} plots of MUF-200.

	Xe	CO_2	C_2H_2	C_3H_6	C_3H_8
a0	-3050 ± 24.4	-3800 ± 20.9	-3710 ± 34.8	-6620 ± 225	-6910 ± 305
a1	-13.4 ± 1.37	21.0 ± 1.20	1.09 ± 1.40	33.9 ± 8.67	78.6 ± 13.8
a2	0.177 ± 0.0222	-0.200 ± 0.0159	-0.278 ± 0.0194	1.10 ± 0.193	-0.915 ± 0.386
a3	$1.47 \times 10^{-3} \pm 3.88 \times 10^{-4}$	$3.01 \times 10^{-3} \pm 2.60 \times 10^{-4}$	$6.57 \times 10^{-3} \pm 2.63 \times 10^{-4}$	$-5.38 \times 10^{-4} \pm 2.42 \times 10^{-3}$	$0.0360 \pm 5.23 \times 10^{-3}$
b0	12.5 ± 0.0853	14.9 ± 0.0733	14.0 ± 0.121	21.6 ± 0.744	21.5 ± 0.996
b1	$0.0602 \pm 4.63 \times 10^{-3}$	$-0.0194 \pm 4.09 \times 10^{-3}$	$0.0378 \pm 4.67 \times 10^{-3}$	-0.147 ± 0.0234	-0.151 ± 0.0341
R^2	0.99994	0.99996	0.9999	0.99957	0.99933

A.7.4 Q_{st} data for UC-MUF-201

Table A.5 Virial equation fitting parameters for the Q_{st} plots of UC-MUF-201.

	C_3H_6	C_3H_8	Xe**	C_2H_4**	C_2H_6**
a0	-4890 ± 374	-4760 ± 276	-2170 ± 113	-2510 ± 190	-3570 ± 203
a1	33.9 ± 9.00	46.3 ± 7.78	-8.29 ± 3.84	-23.6 ± 5.49	35.4 ± 7.92
a2	-1.23 ± 0.111	-1.54 ± 0.127	1.61 ± 0.170	1.54 ± 0.199	-0.0474 ± 0.240
a3	$0.0100 \pm 8.00 \times 10^{-4}$	$0.0166 \pm 1.11 \times 10^{-3}$	$-0.0233 \pm 2.24 \times 10^{-3}$	$-0.0161 \pm 2.14 \times 10^{-3}$	$-2.7 \times 10^{-3} \pm 2.26 \times 10^{-3}$
b0	12.5 ± 1.22	12.8 ± 0.911	7.82 ± 0.377	9.12 ± 0.619	10.1 ± 0.607
b1	0.118 ± 0.0241	0.0715 ± 0.0206	-	-	-
R^2	0.99779	0.99856	0.99511	0.98738	0.988

** Calculated by Elnaz Jangodaz

A.7.5 Q_{st} data for MUF-207

Table A.6 Virial equation fitting parameters for the Q_{st} plots of MUF-207.

	CO_2	Xe**
a0	-2920 ± 94.3	-1280 ± 64.4
a1	35.7 ± 3.97	1.39 ± 3.32
a2	-0.361 ± 0.0116	1.49 ± 0.227
a3	-	$-0.260 \pm 4.57 \times 10^{-3}$
b0	9.473 ± 0.327	5.31 ± 0.219
b1	0.0166 ± 0.0132	-
R^2	0.99949	0.99827

** Calculated by Elnaz Jangodaz.

A.7.6 Q_{st} data for MUF-208

Table A.7 Virial equation fitting parameters for the Q_{st} plots of MUF-208.

	C_3H_6	CO_2	C_2H_4	C_2H_2
a0	-8120 ± 442	-4350 ± 32.3	-4270 ± 83.3	-4730 ± 90.9
a1	437 ± 37.5	68.8 ± 1.99	164 ± 17.2	66.5 ± 4.26
a2	-17.5 ± 1.48	$-0.18 \pm 5.68 \times 10^{-3}$	-4.25 ± 0.771	-0.489 ± 0.0308
a3	0.450 ± 0.0454	-	$0.0192 \pm 1.93 \times 10^{-3}$	$2.86 \times 10^{-3} \pm 3.20 \times 10^{-4}$
a4	$-6.51 \times 10^{-3} \pm 7.35 \times 10^{-4}$	-	-	-
a5	$3.65\ 10^{-5} \pm 4.43 \times 10^{-6}$	-	-	-
b0	24.7 ± 1.42	16.9 ± 0.112	16.5 ± 0.290	17.5 ± 0.316
b1	-0.746 ± 0.0998	$-0.176 \pm 6.73 \times 10^{-3}$	-0.410 ± 0.0594	-0.136 ± 0.0142
b2	$9.91 \times 10^{-3} \pm 1.49 \times 10^{-3}$	-	$9.65 \times 10^{-3} \pm 2.58 \times 10^{-3}$	-
R^2	0.99785	0.99989	0.99974	0.9992

A.7.7 Q_{st} data for MUF-209

Table A.8 Virial equation fitting parameters for the Q_{st} plots of MUF-209.

	CO_2	C_2H_2	C_2H_4	C_2H_6
a0	-13500 ± 102	-7510 ± 43.1	-17100 ± 252	-8180 ± 73.2
a1	435 ± 12.7	306 ± 5.70	742 ± 30.5	9.89 ± 12.2
a2	-3.54 ± 0.172	-8.90 ± 0.186	-5.83 ± 0.606	1.92 ± 0.32
a3	0.0385 ± 4.47 x 10^{-3}	0.223 ± 6.76 x 10^{-3}	0.0556 ± 0.0190	-0.0963 ± 0.0130
b0	47.4 ± 0.344	26.1 ± 0.146	58.0 ± 0.840	29.4 ± 0.0380
b1	-1.13 ± 0.0397	-0.482 ± 0.0176	-1.92 ± 0.0929	0.243 ± 0.0380
R^2	0.99983	0.99994	0.99957	0.99987

A.7.8 Q_{st} data for MUF-210

Table A.9 Virial equation fitting parameters for the Q_{st} plots of MUF-210.

	Xe	CO_2	C_2H_2	C_2H_4	C_3H_6**
a0	-3450 ± 37.0	-4180 ± 48.2	-5280 ± 119	-5440 ± 92.4	-3090 ± 1230
a1	16.1 ± 1.88	50.3 ± 2.09	65.2 ± 3.93	92.5 ± 4.03	-3200 ± 3020
a2	0.301 ± 0.0428	-0.202 ± 0.0344	-0.711 ± 0.0666	-0.506 ± 0.0876	3820 ± 2460
a3	4.05 x 10^{-3} ± 8.22 x 10^{-4}	4.01 x 10^{-3} ± 5.12 x 10^{-4}	9.36 x 10^{-3} ± 7.33 x 10^{-4}	0.0103 ± 1.29 x 10^{-3}	-940 ± 657
b0	13.2 ± 0.130	15.3 ± 0.167	16.8 ± 0.399	17.9 ± 0.312	12.2 ±0.639
b1	-0.0383 ± 6.48 x 10^{-3}	-0.113 ± 6.78 x 10^{-3}	-0.0897 ± 0.011	-0.194 ± 0.0117	-
R^2	0.9999	0.99982	0.99957	0.99973	0.98599

** Calculated by Elnaz Jangodaz.

A.8 Ideal Adsorbed Solution Theory (IAST)

IAST values were calculated using isotherms measured at 293 K. For more information about the fitting and calculation process, see Chapter 1, section 1.4.3.4. Fitting parameters for all MOFs with IAST analysis can be found in the tables below (Table A.10 to Table A.16)

A.8.1 IAST data for MUF-200

Table A.10 Fitting parameters for the IAST plots of MUF-200.

Gas	Model	q1	b1	t1	q2	b2	t2	R^2
CO_2	DSL	7.12 ± 0.255	$0.0875 \pm 2.64 \times 10^{-3}$	1 ± 0	49.6 ± 0.104	$9.87 \times 10^{-3} \pm 1.57 \times 10^{-4}$	1 ± 0	1
N_2	SSL	31.2 ± 1.22	$1.09 \times 10^{-3} \pm 4.58 \times 10^{-5}$	1 ± 0	0 ± 0	0 ± 0	1 ± 0	0.99993
CH_4	SSL	58.2 ± 1.64	$1.98 \times 10^{-3} \pm 6.30 \times 10^{-5}$	1 ± 0	0 ± 0	0 ± 0	1 ± 0	0.99989
Xe	SSLF	42.1 ± 0.114	$0.0230 \pm 8.91 \times 10^{-5}$	$0.981 \pm 2.23 \times 10^{-3}$	0 ± 0	0 ± 0	1 ± 0	0.99999
Kr	SSL	44.8 ± 0.589	$2.67 \times 10^{-3} \pm 4.12 \times 10^{-5}$	1 ± 0	0 ± 0	0 ± 0	1 ± 0	0.99996
C_2H_2	DSL	4.44 ± 1.05	0.147 ± 0.0272	1 ± 0	50.5 ± 0.871	$0.0258 \pm 7.66 \times 10^{-4}$	1 ± 0	0.9998
C_2H_4	DSL	35.4 ± 0.170	$0.0434 \pm 1.63 \times 10^{-4}$	1 ± 0	21.2 ± 1.82	$2.26 \times 10^{-3} \pm 3.19 \times 10^{-4}$	1 ± 0	1

A.8.2 IAST data for JETJOI

Table A.11 Fitting parameters for the IAST plots of JETJOI.

Gas	Model	q1	b1	t1	q2	b2	t2	R^2
CO_2	DSL	1.21 ± 0.0724	0.144 ± 0.0107	1 ± 0	15.3 ± 0.256	$5.96 \times 10^{-3} \pm 2.47 \times 10^{-4}$	1 ± 0	0.99997
N_2	SSL	9.09 ± 0.864	$1.85 \times 10^{-3} \pm 1.98 \times 10^{-4}$	1 ± 0	0 ± 0	0 ± 0	1 ± 0	0.99908

A.8.3 IAST data for UC-MUF-201

Table A.12 Fitting parameters for the IAST plots of UC-MUF-201.

Gas	Model	q1	b1	t1	q2	b2	t2	R^2
CO_2	SSL	58.2 ± 0.378	$0.0176 \pm 2.13\ 10^{-4}$	1 ± 0	0 ± 0	0 ± 0	1 ± 0	0.99978
N_2	SSLF	12.1 ± 1.18	$8.55 \times 10^{-4} \pm 6.05 \times 10^{-5}$	0.686 ± 0.0210	0 ± 0	0 ± 0	1 ± 0	0.99881
CH_4	SSL	45.8 ± 0.792	$7.27 \times 10^{-3} \pm 1.79 \times 10^{-4}$	1 ± 0	0 ± 0	0 ± 0	1 ± 0	0.99961
Xe	SSLF	65.1 ± 7.34	$0.108 \pm 9.39 \times 10^{-3}$	1.76 ± 0.127	0 ± 0	0 ± 0	1 ± 0	0.99187
Kr	SSL	49.0 ± 1.37	$66.6 \times 10^{-3} \pm 2.58 \times 10^{-4}$	1 ± 0	0 ± 0	0 ± 0	1 ± 0	0.99911
C_3H_6	DSL	47.6 ± 0.983	$0.0739 \pm 5.17 \times 10^{-3}$	1 ± 0	20.9 ± 1.23	3.93 ± 0.939	1 ± 0	0.99834
C_3H_8	DSL	17.8 ± 1.11	2.89 ± 0.523	1 ± 0	39.6 ± 0.912	$0.0956 \pm 5.78 \times 10^{-3}$	1 ± 0	0.99913

A.8.4 IAST data for MUF-207

Table A.13 Fitting parameters for the IAST plots of MUF-207.

Gas	Model	q1	b1	t1	q2	b2	t2	R^2
CO_2	DSL	15.3 ± 0.246	0.496 ± 0.0168	1 ± 0	46.1 ± 0.823	$9.65 \times 10^{-3} \pm 4.51 \times 10^{-4}$	1 ± 0	0.99986
N_2	SSL	34.0 ± 0.288	$1.93 \times 10^{-3} \pm 1.84 \times 10^{-5}$	1 ± 0	0 ± 0	0 ± 0	1 ± 0	0.99999
CH_4	SSL	33.1 ± 0.153	$7.50 \times 10^{-3} \pm 4.99 \times 10^{-5}$	1 ± 0	0 ± 0	0 ± 0	1 ± 0	0.9997
Xe	DSL	41.2 ± 0.658	$3.52 \times 10^{-3} \pm 9.39 \times 10^{-5}$	1 ± 0	20.8 ± 0.0566	$0.135 \pm 4.76 \times 10^{-4}$	1 ± 0	1
Kr	SSL	22.3 ± 0.114	$5.90 \times 10^{-3} \pm 4.08 \times 10^{-5}$	1 ± 0	0 ± 0	0 ± 0	1 ± 0	0.99998

A.8.5 IAST data for MUF-208

Table A.14 Fitting parameters for the IAST plots of MUF-208.

Gas	Model	q1	b1	t1	q2	b2	t2	R^2
CO_2	DSL	69.1 ± 1.50	$4.38 \times 10^{-3} \pm 2.19 \times 10^{-4}$	1 ± 0	9.32 ± 0.383	$0.0743 \pm 2.86 \times 10^{-3}$	1 ± 0	0.99999
N_2	SSL	63.4 ± 7.91	$9.27 \times 10^{-4} \pm 1.23 \times 10^{-4}$	1 ± 0	0 ± 0	0 ± 0	1 ± 0	0.9995
C_2H_2 ***	DSLF	124 ± 23.2	$0.0159 \pm 2.79 \times 10^{-3}$	1.42 ± 0.0256	$5.23 \times 10^{5} \pm 1.70 \times 10^{10}$	$2.10 \times 10^{-14} \pm 6.81 \times 10^{-10}$	0.231 ± 0.85	0.99995
C_2H_4	DSL	47.3 ± 0.860	$5.26 \times 10^{-3} \pm 2.02 \times 10^{-4}$	1 ± 0	5.22 ± 0.160	$0.156 \pm 6.39 \times 10^{-3}$	1 ± 0	0.99997
C_3H_6	DSLF	97.6 ± 35.2	0.0643 ± 0.0227	1.92 ± 0.296	16.6 ± 2.79	$2.24 \times 10^{-4} \pm 3.11 \times 10^{-4}$	0.262 ± 0.0435	0.99892
C_3H_8	DSL	43.8 ± 1.55	$7.17 \times 10^{-3} \pm 4.49 \times 10^{-4}$	1 ± 0	4.36 ± 0.132	2.74 ± 0.448	1 ± 0	0.99928

*** Due to the isotherm not reaching saturation, we struggled to get a good fit that converged. Thus this fit was the best we could obtain.

A.8.6 IAST data for MUF-209

Table A.15 Fitting parameters for the IAST plots of MUF-209.

Gas	Model	q1	b1	t1	q2	b2	t2	R^2
CO_2	DSL	9.04 ± 0.126	1.36 ± 0.062	1 ± 0	22.0 ± 0.332	0.0143 ± 6.40 x 10^{-4}	1 ± 0	0.99966
N_2	SSL	9.84 ± 0.0981	4.47 x 10^{-3} ± 5.69 x 10^{-5}	1 ± 0	0 ± 0	0 ± 0	1 ± 0	0.99994
Xe	DSL	2.81 ± 0.565	0.190 ± 0.0409	1 ± 0	7.62 ± 0.336	0.0189 ± 3.37 x 10^{-3}	1 ± 0	0.99926
Kr	SSL	7.49 ± 0.0541	0.0129 ± 1.55 x 10^{-4}	1 ± 0	0 ± 0	0 ± 0	1 ± 0	0.99983
C_2H_4	DSL	10.73 ± 0.186	0.0281 ± 2.10 x 10^{-3}	1 ± 0	8.87 ± 0.155	3.76 ± 0.338	1 ± 0	0.99825
C_2H_6	DSL	10.5 ± 0.103	0.0252 ± 1.25 x 10^{-3}	1 ± 0	7.02 ± 0.122	1.13 ± 0.0502	1 ± 0	0.99966

A.8.7 IAST data for MUF-210

Table A.16 Fitting parameters for the IAST plots of MUF-210.

Gas	Model	q1	b1	t1	q2	b2	t2	R^2
CO_2	DSL	44.8 ± 0.240	0.0105 ± 3.67 x 10^{-4}	1 ± 0	16.6 ± 0.427	0.123 ± 3.17 x 10^{-3}	1 ± 0	0.99999
N_2	SSL	46.1 ± 2.08	1.21 x 10^{-3} ± 5.91 x 10^{-5}	1 ± 0	0 ± 0	0 ± 0	1 ± 0	0.99989
CH_4	SSL	44.9 ± 0.361	4.63 x 10^{-3} ± 4.80 x 10^{-5}	1 ± 0	0 ± 0	0 ± 0	1 ± 0	0.99996
Xe	DSL	17.3 ± 3.45	4.19 x 10^{-3} ± 1.92 x 10^{-3}	1 ± 0	28.7 ± 0.887	0.0669 ± 1.84 x 10^{-3}	1 ± 0	0.99996
Kr	SSL	46.1 ± 0.887	4.87 x 10^{-3} ± 1.22 x 10^{-4}	1 ± 0	0 ± 0	0 ± 0	1 ± 0	0.99974
C_2H_2	DSL	35.1 ± 0.480	0.292	1 ± 0	20.8 ± 0.737	0.699 ± 0.0468	1 ± 0	0.99961
C_3H_6	DSL	24.8 ± 0.197	4.48 ± 0.212	1 ± 0	15.8 ± 0.284	0.0256 ± 1.83 x 10^{-3}	1 ± 0	0.99868
C_3H_8	DSLF	5.22 ± 1.24	8.45 x 10^{-3} ± 5.98 x 10^{-3}	0.738 ± 0.105	24.0 ± 1.17	1.58 ± 0.195	1.61 ± 0.123	0.99977

A.9 ^{1}H Nuclear Magnetic Resonance (NMR) Spectroscopy

A Bruker Avance 500 MHz NMR was used to collect the ^{1}H NMR spectroscopic data. The activated samples were digested in 1 mL of a NaOH/D_2O solution (0.1 mL NaOD in 0.9 mL D_2O). Some samples contained copper or cobalt (which are paramagnetic and not desired in an NMR solution) which often precipitated out, the supernatant was taken for NMR analysis. The resulting spectra are found below (Figure A.46 to Figure A.48).

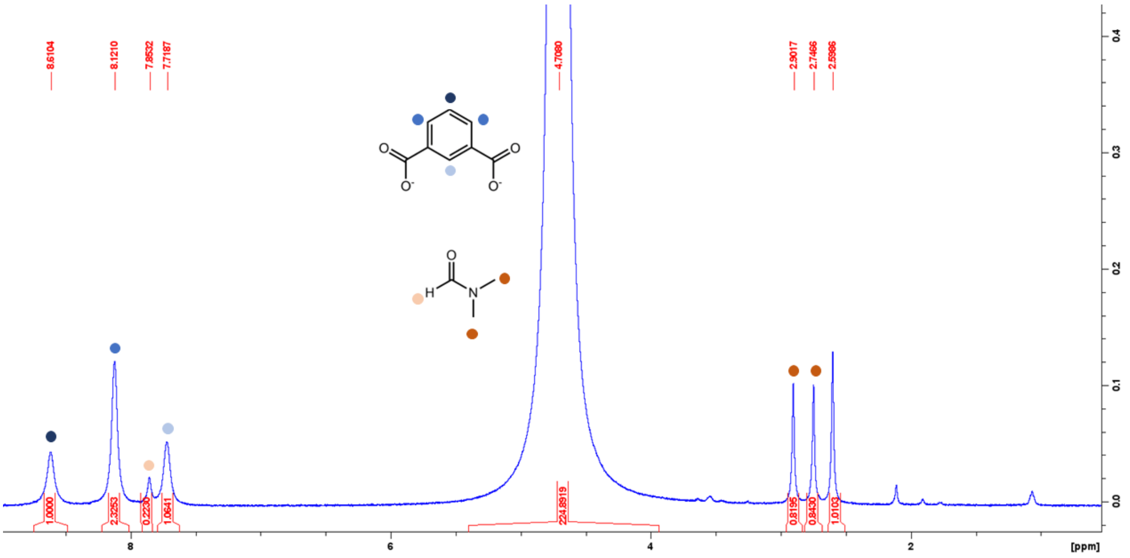

Figure A.46 ^{1}H NMR spectrum of activated MUF-200 digested in NaOD/D_2O.

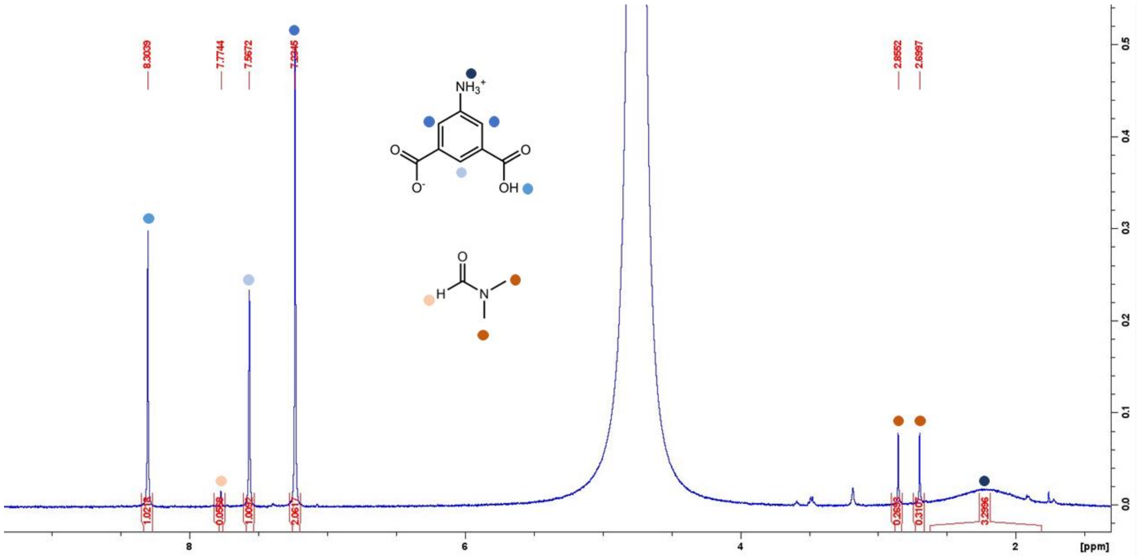

Figure A.47 ^{1}H NMR spectrum of activated MUF-206 digested in NaOD/D_2O.

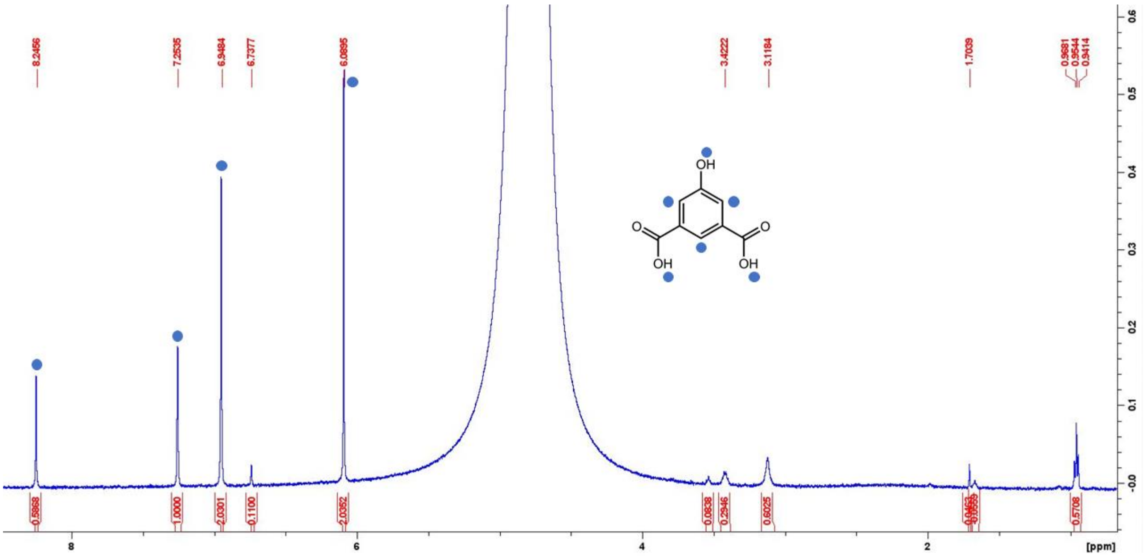

Figure A.48 ^{1}H NMR spectrum of activated MUF-210 digested in NaOD/D_2O.

A.10 Infrared (IR) Spectroscopy

A Thermo Scientific Nicolet iS5 IR with iD7 ATR accessory was used to collect the IR spectroscopic data. The sample used was either exchanged into acetone (from its original solvent) then vacuum dried briefly or it was activated on the iQ2. The resulting spectra are found below (Figure A.49 to Figure A.52).

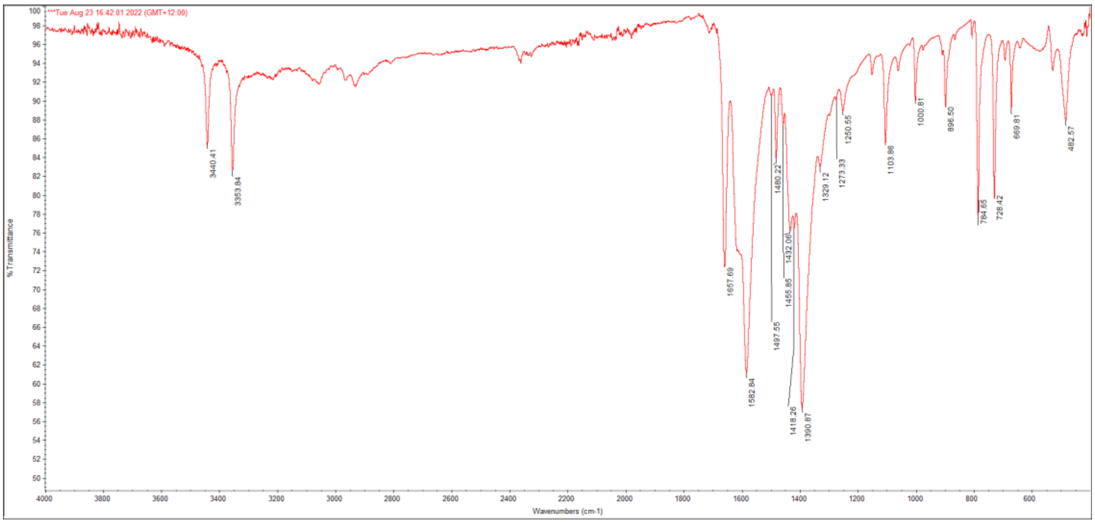

Figure A.49 IR spectrum of vacuumed dried MUF-206.

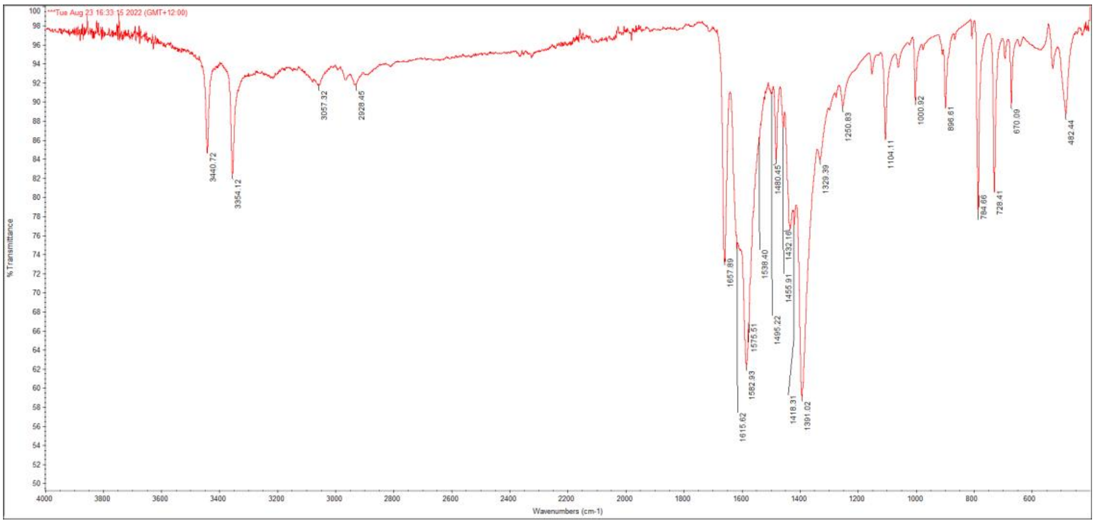

Figure A.50 IR spectrum of activated MUF-206.

Figure A.51 IR spectrum of vacuumed dried MUF-210.

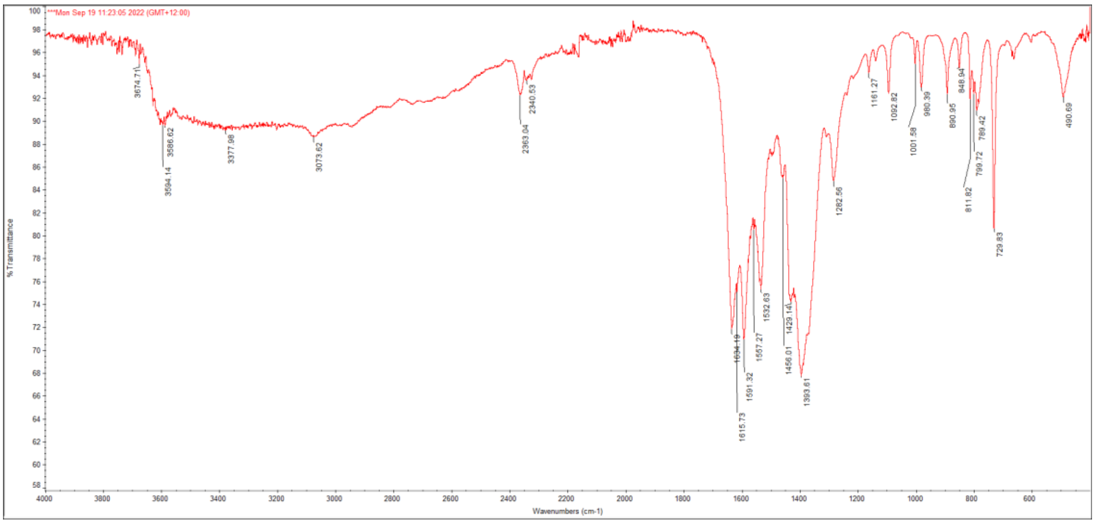

Figure A.52 IR spectrum of activated MUF-210.